Porosity engineering of Starbon® materials

Han Li

PhD

University of York

Chemistry

September 2021

Abstract

Hierarchically porous Starbon® based materials have been prepared from initially highly mesoporous Starbons®. Mesoporous Starbons® were prepared from three different biopolymers: starch, alginic acid and pectin and each was then activated using three different activating agents: potassium hydroxide, carbon dioxide and oxygen to give a set of hierarchically porous Starbons®. The properties of the hierarchically porous Starbons® were tailored by variation of precursors, activating agents and activation conditions. Potassium hydroxide activation is favourable in engineering micropores, while carbon dioxide and oxygen activation led to the development of both micropores and mesopores. The textural, physical and chemical properties of the series of hierarchically porous materials were characterised using nitrogen porosimetry, CHN analysis, ICP-OES, XPS, SEM and TEM imaging.

The activated Starbons® with finely tuned textual properties displayed higher adsorption ability towards carbon dioxide and methylene blue than either mesoporous Starbons® or microporous activated carbon. Systematic in-depth investigation of the relationship between the porosities of the materials and their adsorption capacities for carbon dioxide and methylene blue was conducted. The carbon dioxide adsorption capacity at ambient pressure is mainly determined by the micropore surface area and ultramicroporosity, while at high pressure it is determined by the total surface area and pore volume. Adsorption of methylene blue depends predominantly on the micropore volume and surface area and to some extent also on the combination of these with the presence of mesopores. The analysis of adsorption selectivity and adsorption kinetics, isotherms and thermodynamics further provided a comprehensive understanding of the factors that influence the carbon dioxide and methylene blue adsorption processes.

List of Contents

List of Tables

Chapter 3

Chapter 4

Appendix

List of Figures

Chapter 3

Chapter 4

Appendix

Acknowledgements

Four years of PhD study is coming to an end. I would like to first thank the support from Prof. James Hanley Clark and Prof. Michael North for offering me the fantastic opportunity to study at Green Chemistry Centre of Excellence in University of York. Special thanks to Mike, who is a dedicated supervisor; leading me into the research field of Starbons®, providing me with guidance and support throughout my whole research, and revising my thesis word by word. The scenes in the group meeting when he inspires us, summarizes the key points and gives constructive suggestions have become unforgettable memories, which will also have great impact in my future academic career. Great thanks to my co-supervisor Dr. Vitaliy Budarin, for answering my doubts, helping me with many challenges that I faced and guiding me during my in-depth research. Great thanks also to my co-supervisor Prof. James Clark for giving valuable suggestions for my research progress and my thesis. I would also like to thank Dr. Duncan Macquarrie for being my thesis advisory panel member and for his suggestions during my TAP meetings. Thanks to Dr. Xiao Wu who is not only my advisory supervisor but also my good friend, who not only helped me in the research but also brought me joy in my life.

I would also like to thank the technician team: Dr. Paul Elliot, Dr. Maria Garcia Gallarreta, Dr. Richard Gammons, Dr. Hannah Briers, Dr. Suranjana Bose, Dr. Tabitha Petchey for training and helping me with kindness and patience and maintaining the instruments during my study. Without their support many parts of this research would have been difficult to progress. Similarly, thanks to the administrators Sophie Palmer and Katy Brooke for their help. Thanks to Dr Joseph Houghton for his training on using the porosimeters and the product specialist Chris Pilkington at Micromeritics for his wisdom and suggestions for the analysis of microporous samples using porosimeter. Thanks to Dr Jon

Barnard at York JEOL Nanocentre for his support and training on using the Scanning electron microscope (SEM) and Transmission electron microscope (TEM). Thanks to John Angus at the Biorenewables Development Centre for the inductively coupled plasma-optical emission spectrometry (ICP-OES) analysis, to Dr David Morgan at the University of Cardiff for XPS analysis and to Cheng Li at the Fudan University for measuring the carbon dioxide and nitrogen adsorption isotherms.

Thanks to everyone else in the Green Chemistry Centre of Excellence, for being a good friend or helping me here and there during my studies: Roxana Milescu, Jaspreet Kaur, Florent Bouxin, Eksuree Saksornchai, Liping Guo, Yang Gao, Yanrui Ran, Qingwei Meng, Ryan Barker, Dr Katie Lamb, Dr Ian Ingram etc. Finally, deep thanks to my family: my mother, my father, my sister and my nephews. It is their love and support that inspired me to move forward bravely in a foreign country. A special thanks to my husband Jincheng Tong, who loves me, accompanies me, supports me and brings me happiness.

Author’s Declaration

I declare that this thesis is a presentation of original work and I am the sole author. This work has not previously been presented for an award at this, or any other, University. All sources are acknowledged as References.

Han Li

2021

Chapter 1: Introduction

1.1 Porous Materials

A porous material is a solid matrix comprised of a network of interconnected pores that are filled with gas or liquid. Porosity provides materials with lower density and higher surface area compared to dense materials, and thus endows them with the ability to interact with atoms, ions and molecules not only at their outer and inner surfaces, but also throughout the bulk of the material.[1,2]

To meet the increasing demands for renewable energy and a clean environment, a wide range of porous solids have been developed including: zeolites,[3] metal oxides,[4] metal organic frameworks (MOFs),[5] covalent organic frameworks (COFs),[6] porous organic polymers (POPs)[7] and others. The porous structures (pore sizes, shapes and volumes) of these solids, coupled with other characteristics such as stability, sorption kinetics and processability make them good candidates for applications in adsorption, separation, catalysis, purification and energy storage.[8]

In 1985, the International Union of Pure and Applied Chemistry (IUPAC) recommended that porous materials be classified into three categories based on their pore diameters: macroporous greater than 50 nm, mesoporous 2~50 nm and microporous less than 2 nm.[9] Due to the development of nanoporous materials during subsequent years, IUPAC further supplemented the classification of porous materials in 2015. Nanoporous materials have a pore diameter of up to 100 nm, thus covering the range of microporous, mesoporous and even macroporous materials. Microporous materials were further classified into supermicroporous with diameters of 0.7~2 nm and ultramicroporous with diameters less than 0.7 nm.[10,11] Much progress has been made recently in developing porous materials containing all these pore regimes (e.g. hierarchical Zeolites, metal–organic frameworks, metals and

carbons etc.), as shown in **Figure 1.1**, for applications that require not only high specific surface areas and large pore volumes but also a wide pore size distribution.[12]

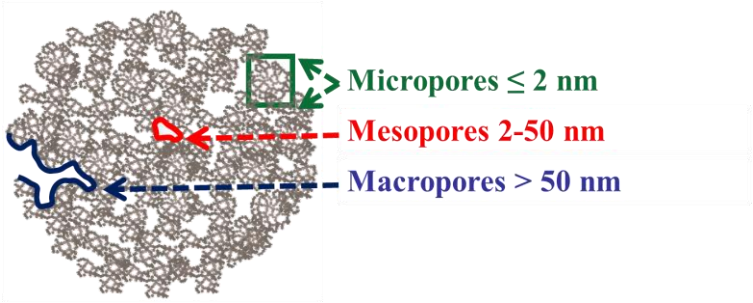

Figure 1.1 Schematic drawing of a hierarchical porous structure including micropores, mesopores and macropores.

In general, micropores, mesopores and macropores have different functions within a given application. It is well established that micropores are well-suited to applications relating to small molecules: such as molecular sieving, adsorption and catalysis. Micropores can provide active sites for guest molecules (e.g. reactants, intermediates and products) with accurate size and shape selectivities. Especially for ultramicropores, the interaction energy (e.g. short-range attractive, van-der-Waals and repulsive forces) in the extraordinarily fine pores between the adsorbent and adsorbate is reinforced due to the overlapping of potential fields from neighbouring walls.[13-16] High surface areas provide a large number of reaction or interaction sites in surface or interface-related processes such as adsorption of large hydrophobic molecules (e.g. dyes, vitamins and polymers), chromatographic separations and supporting bulky catalysts for converting chemicals (e.g. carbon dioxide) into valuable products. Large pore volumes, meso- and macropore channels facilitate the transport of atoms, ions and large molecules through the bulk of the material, thereby increasing the number of active sites with high accessibility to large components. The size restriction encountered with microporous materials is overcome by meso- and macropores.[17,18]

1.1.1Mesoporous Materials

Over the last three decades, mesoporous solids have become appealing materials with a wide application scope including: adsorption,[19,20] separation,[21,22] catalysis,[23,24] energy conversion and storage.[25] This is due to their satisfactory surface areas and pore volumes; large accessible pore networks and controllable pore sizes, shapes and channels.

A wide variety of mesoporous solids and compositions have been synthesised via various methods, including soft-templating, hard-templating or template-free approaches. The manifold shapes; architectures (e.g. nanomaterials, composites); structure dimensions (e.g. mesoporous); and pore geometries (e.g. cylindrical, spherical, cage-type) of materials can be controlled by varying the synthesis routes, reaction conditions, type of template and precursor sources used.[26-28]

Historically, the ordered mesoporous aluminosilicate molecular sieve family (M41S) were first synthesised via the soft template method by Mobil scientists in the 1990s.[32,29] Surfactant liquid crystals were introduced as structure-directing templates (SDA) in a sol–gel synthesis medium, the subsequent removal of the surfactant by extraction or calcination generates an ordered mesostructured composite. After that, diverse mesoporous materials were prepared by surfactant assisted soft-templating approaches by various synthetic processes including sol-gel, hydrothermal, evaporation-induced self-assembly (EISA) (non-aqueous process) and chemical or physical vapour deposition. The soft-templating method was further developed for the synthesis of silica-based mesoporous solids (e.g. SBA-15/16,[30] KIT-6,[31] AMS,[32] FDU-12,[33] organic-inorganic hybrid silica[34] and periodic mesoporous organosilica[35]) and non-silica based mesoporous solids (e.g. metal oxides,[26,36] metal sulphides,[37] metal phosphates,[38] mesoporous polymers[39] and MOFs[40]) by employing various soft templates, including ionic or non-ionic surfactant micelles or block copolymers.[41-43]

However, phase transitions of some non-siliceous precursors result in hydrolysis and thermal breakdown of structural integrity of some ordered porous metals.[44] Alternatively, some metal oxides,[45] mesoporous carbon[48] and organic polymers[46] have been synthesised by a 'nanocasting' method which involves using preformed mesoporous materials such as mesoporous silica, carbon or aggregates of nanoparticles as hard templates. The use of a hard template avoids the assembly and condensation of guest precursors with surfactants and ensures that the mesochannels are completely filled. As a result, hard templating can prepare highly crystalline materials due to the protection offered by rigid templates at high temperatures.

Both soft templates (e.g. surfactant and polymers) and hard templates (e.g. metal oxides, carbon and carbonates) can be burned-off or dissolved at an appropriate temperature or pH, giving rise to controlled mesoporosity in solids. The advantage of these methodology is their ability to precisely control the pore structure and surface chemistry of mesoporous materials. However, the templated synthetic routes have limitations because they involve many complex synthetic steps, which is energy intensive and the removal of the template results in the generation of waste which is not environmentally friendly. Also, it is still a challenge to keep the integrity of the structure stable because the removal of templates often results in the collapse of mesopores.[48,49]

Template free methods are widely implemented in the fabrication of mesoporous materials. The mesoporosity can be generated by: the formation of a gas during the synthesis process (e.g. hydrogen evolution approach); selective etching of a composite material or alloy (e.g. dealloying method); or aggregation of nanoscale building blocks (e.g. template-free packing method).[47-49] Using this method is difficult to obtain ordered mesostructure, but it does not require any hard or soft template; allows the creation of products with high crystallinity; and is easily scalable and processable. To date, this approach has been

extensively used to synthesise mesoporous materials based on carbon, metals oxides and metals sulphides.

1.1.2 Mesoporous Carbon Materials

Carbon materials such as fullerenes, carbon tubes, graphene, and porous carbons, have advantages including: abundance of raw materials; low cost; rich morphologies; high conductivity; good chemical and mechanical stability; and ease of processing and modification.[50] Porous carbons are distinguished from traditional carbons by their additional characteristics of diverse particle sizes (ranging from nanometer to micrometer scales) and adjustable pore sizes (ranging from micropores to mesopores and macropores).[51-54] Thus, they exhibit great potential in catalysis; gas adsorption and separation; purification; electrochemistry; and energy conversion and storage.[55,56] Mesoporous carbons, which can be synthesised from porous templates, polymers or biomass resources stood out owing to their large and accessible pore networks, controllable mesoporosity and channels which can be adjusted to favour the requirements of various applications (as mentioned in section 1.1.1).

Since the first report of synthesising ordered mesoporous carbon (OMC) using mesoporous silica (MCM-48) as a hard template and sucrose as a carbon source by Ryoo *et al* in 1999,[57] a wide spectrum of mesoporous carbons and corresponding composites have been discovered and created via either template carbonisation or template free methods. The specific synthetic routes, carbon sources, synthesis/activation conditions and types of templates/catalysts employed can all be used to influence the morphology, architecture and porosity of the final material. Templating methods are the most straightforward ways to fabricate uniformly distributed mesopores in carbon materials. In the hard-templating approach, pre-existing, ordered, mesoporous solids are introduced as hard templates. Carbonisation and removal of the template allows the replication of their internal frameworks

into the porous carbon structure with well-distributed mesoporosity.[58] In the soft-templating approach, the mesoporous framework structure is achieved by the cooperative assembly of block copolymer surfactants (structure directing agents) and organic carbon precursors. In this case, the mesoporosity is generated upon removal of the surfactants by a calcination process at high temperatures.[59,60]

Disordered mesoporous carbons with wide pore size distribution can be synthesised via both direct carbonisation methods and activation methods. Direct pyrolysis of carbon precursors at elevated temperatures; etching processes in catalytic activation with a physical activator (e.g. steam, carbon dioxide and air) or a chemical activator (e.g. metal and metal oxides), enables the escape of gases and results in the formation of a disordered pore structure.[56,61] Conventional carbon precursors used to synthesise mesoporous carbons are fossil derived (e.g. methane, pitch, resorcinol, phloroglucinol and formaldehyde cross-linked phenol). The exploitation and utilisation of fossil fuels has caused environmental pollution, climate change and energy shortage crisis. The synthesis process also requires harsh and energy intensive conditions (e.g. electric-arc discharge, chemical vapor deposition or laser ablation) or requires the use of toxic reagents (e.g. potassium permanganate and sulfuric acid) and always produces large volumes of hazardous waste.[62] Therefore, it is highly desirable to produce carbon materials derived from sustainable, economic and environmentally friendly resources instead of fossil feedstocks. It has been suggested that biomass is a reliable alternative source for the synthesis of chemicals and fuels.[15,51] Biomass is abundant, sustainable and is distributed widely in nature. The utilisation of biomass waste offers solutions for the management of solid waste, can reduce the cost of raw materials and does not complete with existing food resources. Moreover, the routes used to prepare mesoporous carbons from waste biomass are relatively easy, inexpensive and typically biocompatible.[55]

Polysaccharides (including cellulose, alginic acid, pectin and chitosan) extracted from natural sources have been used as alternatives to synthetic polymers as mesoporous carbon precursors especially for biomedical and electrochemical applications due to their inherent merits of: ready availability; low cost; green features; high mechanical strength; and richness in functional groups (alcohols, ketones and acids etc).[63] Native polysaccharides are however essentially non-porous and have a low surface area, which limits their use where diffusion and surface interactions are critical to function in applications.[64] For example, both non-ionic polysaccharides (such as starch) and anionic polysaccharides (such as alginic acid) are restricted as adsorbents for dyes by their low surface area (<1 m^2g^{-1}), low degree of mesoporosity and electrostatic repulsion between the polymer surface and dyes.[65]

In the late 1990s, it had been demonstrated that native starch could be expanded to generate porous polysaccharide xerogels with higher specific surface areas (<145 m^2g^{-1}).[66,67] The expansion process involves thermal gelation; retrogradation of starch; solvent replacement by a lower surface tension solvent and finally a supercritical carbon dioxide ($scCO_2$) drying processes. The porous polysaccharide network is stabilised by dense hydrogen-bonding between chains and local domains, and thus the inherent hydrophilicity of these polymeric networks results in poor stability in the presence of protic reagents.[55] Therefore, following the expansion of the polysaccharides into porous aerogels, maintaining the porosity into the final sustainable porous carbons with high porosity stabilisation is vital for high value applications which demand efficient diffusion and surface interactions.[68-70]

1.1.3 Starbon® Materials

1.1.3.1 Synthesis and characterisation of Starbon® materials

Starch is widely available in many foods (e.g. potatoes, corn, rice, wheat and cassava) and food wastes (e.g. potato peel). It is a polymeric polysaccharide consisting of linear amylose and branched amylopectin units. As shown in **Figure 1.2**, amylose is made up of α-D-glucose linked by (1→4) glycosidic bonds and the branch of amylopectin is linked by (1→6) glycosidic bonds. Alginic acid and pectin are acidic structural polysaccharides that are abundant in the cell walls of seaweed and citrus fruit peels, respectively. Alginic acid is a linear copolymer consisting of β-D-mannuronic acid (M) and α-L-guluronic acid (G) monomers with (1→4) glycosidic bonds linking the monomers. The linear chain is formed with homopolymeric G-blocks, M-blocks or alternating blocks of M and G. Pectin is a heteropolysaccharide primarily made up of D-galacturonic acid linked by (1→4) glycosidic bonds, existing as protonated, methoxylated and carboxylate forms. L-rhamnose generally incorporates in the main chain and forms branched chains with other pectin monomers (e.g. arabinan, galectin, D-glucuronic acid, D-glucose, D-mannose and D-xylose). There are generally two pectins commercially available depending on their esterification degree (≤50% and >50%). The structural components of starch, alginic acid and pectin are shown in **Figure 1.2**.

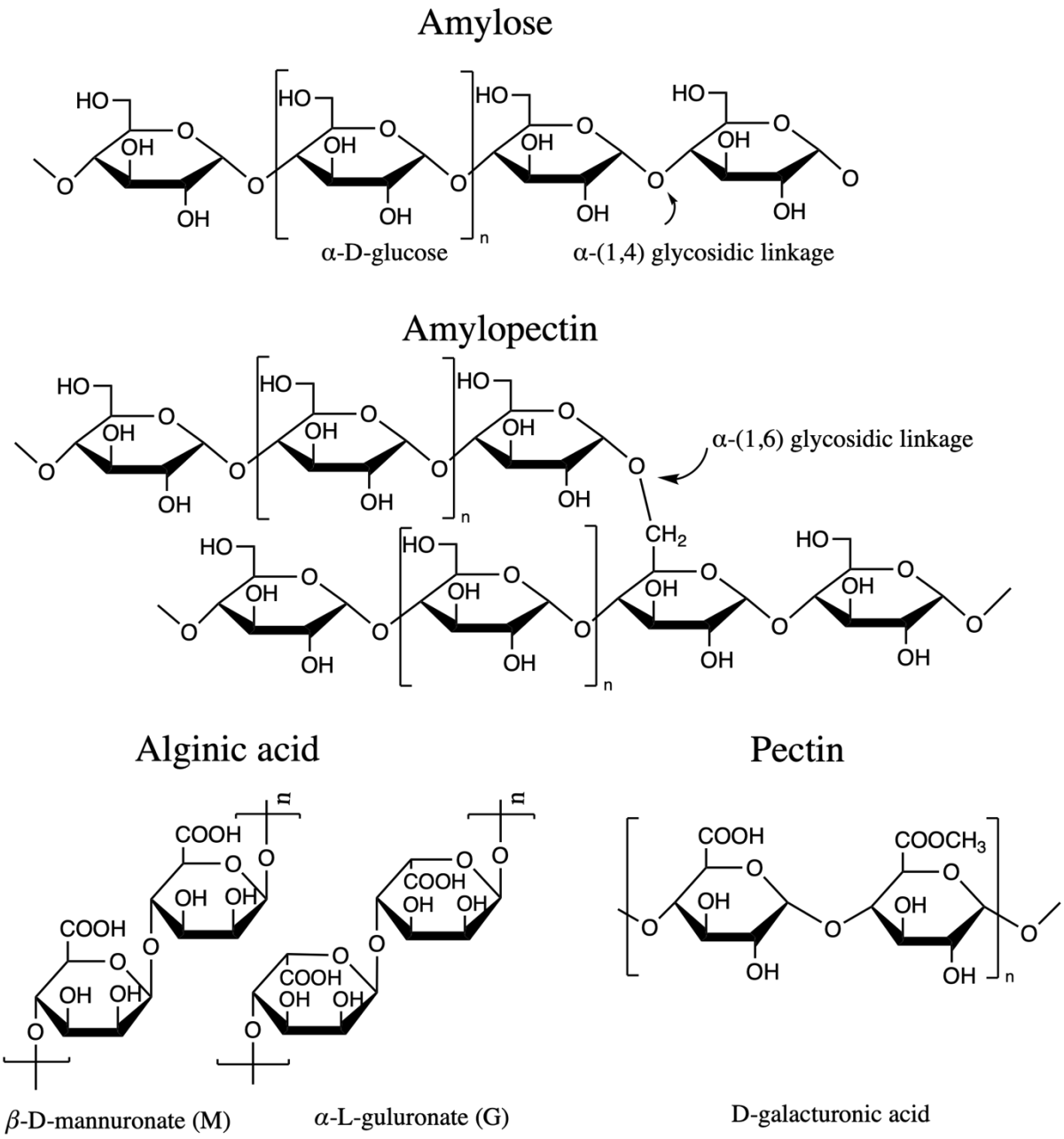

Figure 1.2 Structure of the components of starch, alginic acid and pectin.

In 2006, Clark and co-workers at the Green Chemistry Centre of Excellence of the University of York first demonstrated that starch can be converted into mesoporous carbonaceous derivatives via a direct carbonisation method (expansion, drying and carbonisation). This family of mesoporous carbon materials has been named as Starbons®.[71] It was subsequently established that other helix-forming polysaccharides (e.g. alginic acid[72,73] and pectin[68]) with flexible glycosidic bond linkages,[69] are also able to be transformed into

mesoporous Starbon® materials (these are informally referred to as Algibons if derived from alginic acid and Pecbons if derived from pectin). Extending this synthetic approach to other polysaccharides offers a green alternative route to traditional hard or soft templating methods and opens access to the production of various porous carbons.

The Starbon® synthesis process is inexpensive and environmentally friendly. The lack of a template avoids wasteful processing steps and use of harmful chemicals and enables materials to be prepared at any desired temperature. A polysaccharide aqueous gel is first prepared by a gelatinisation and retrogradation process. Gelatinisation in water disorders the dense biopolymer network and retrogradation allows the recrystallisation of the network.[70] The gelatinisation of the precursors is determined by the structural complexity of the precursors (e.g. self-association, surface charge and esterification degree) and the arrangement of chain segments, which then influences the porosity of the polysaccharide gel. Following gelatinisation, a mesoporous aerogel is obtained by a solvent exchange drying process. The network structure can be maintained without collapse by exchange of water with a lower surface-tension solvent (e.g. ethanol, acetone and hexane). Subsequent supercritical carbon dioxide ($scCO_2$) drying enables formation of the product possessing high surface area and pore volume.

Another drying method: freeze-drying, with addition of tert-butanol (TBA) to the hydrogels before drying, was later shown to provide a simpler and solvent saving route although an organic waste stream is inevitably produced. This method overcomes the surface tension issues and offers some control over the meso/macropore distribution of the resulting material.[74] Tert-butanol has low toxicity, high vapor pressure, high viscosity and a low melting point, making it an ideal freeze-drying medium.[75] It has been extensively investigated and used in crystal templating since its phase equilibrium as a function of temperature and pressure are compatible with the ice-templating conditions.[76] By gelling polysaccharides in

the presence of tert-butanol, mesoporous aerogels can be successfully prepared via freeze-drying. The fine structured eutectic crystals formed enable the preservation of the mesopore structure.[74] Finally, the mesoporous aerogel is thermal carbonised under a non-oxidising atmosphere at a desired temperature (generally between 300 and 1200 °C) to produce a predominantly mesoporous Starbon®.

When starch is used as the precursor, the resultant neutral starch aerogel needs to be doped with a catalytic amount of an organic acid (e.g. p-toluenesulfonic acid) in the final carbonisation stage. Starch is thermally stable at temperatures below 300 °C which is lower than the melting point of the hydrogen-bonded polymer network. The introduction of the acid catalyst leads to the formation of intermolecular crosslinks and the dehydration of hydroxyls at low temperature and thus facilitates the conversion of the porous polysaccharide into a stable nanostructured porous carbon.[69] The uneven distribution of the acid catalyst at the surface of the polysaccharide results in non-uniform thermal decomposition of the polysaccharide. Compared to starch, the thermal decomposition of the inherently acidic polysaccharides (alginic acid and pectin) is more uniform when preparing Algibons and Pecbons.

The flexibility of the preparation temperature provides a controllable surface chemistry in the Starbon® material.[71] As the carbonisation temperature increases, hydroxyl groups in the polysaccharides are converted into ethers, ketones, isolated aromatics and finally aromatic rings (**Figure 1.3a**). Hence, there is a progressive increase in the hydrophobicity of the functional groups and the tolerance towards harsh condition of the samples as the carbonisation temperature increases. In addition, the porous structures (surface area, pore volume and micropore:mesopore ratio etc.) of expanded starch, alginic acid and pectin aerogels derived from the expansion and drying processes are maintained and developed

during the final carbonisation stage for the resultant Starbons®. The porous structures are tuneable by varying the carbonisation temperature (**Figure 1.3b**).

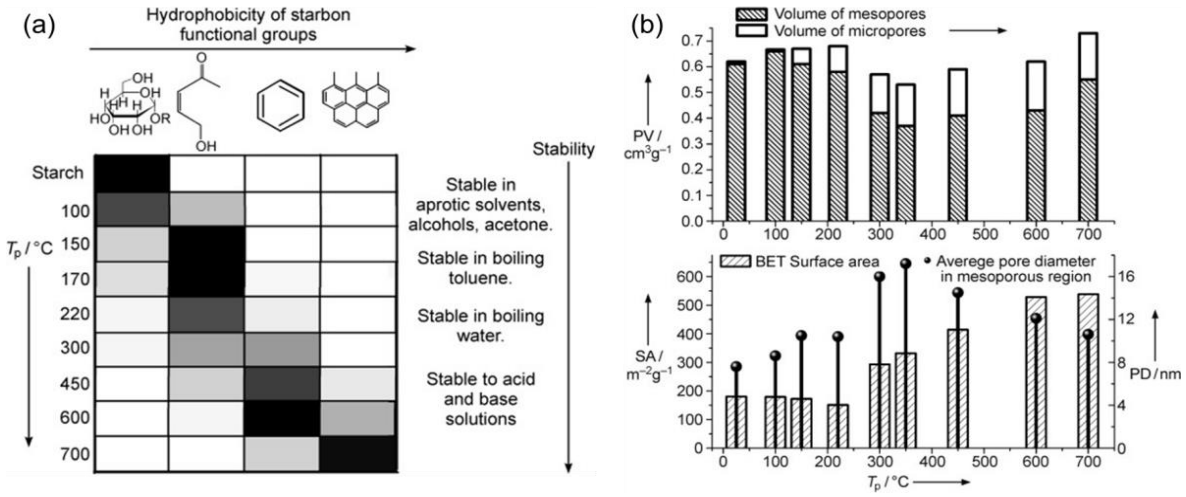

Figure 1.3 (a) Type and quantity variation of functional groups in Starbons® prepared by the solvent exchange method at various carbonisation temperatures (the darker the colour, the higher the content). (b) Porous structure of Starbons® (PV=pore volume, SA=surface area, PD=pore diameter, T_p=temperature of preparation). Adapted with permission from reference 71.

The porous structure of Starbon® materials is also determined by the polysaccharide precursors. In all cases, increasing the carbonisation temperature results in the formation of micropores and higher surface areas. However, alginic acid and pectin derived Starbons® (A800/P800) produce larger mesopore volumes compared to starch derived Starbon® (S800) (**Figure 1.4 G-I**).[77] It is postulated that this is related to the different self-associations and electron densities associated with the amylose homopolymer in starch and the polyuronide block copolymer in alginic acid/pectin.[55,72] Due to the different kinetics between a surface-initiated acid catalysed decomposition (organic acid additive catalysed starch) and a uniform bulk direct thermal decomposition (inherently acidic alginic acid/pectin) process, Algibon and Pecbon show lower microporosity as a function of temperature compared to Starbon®.[72]

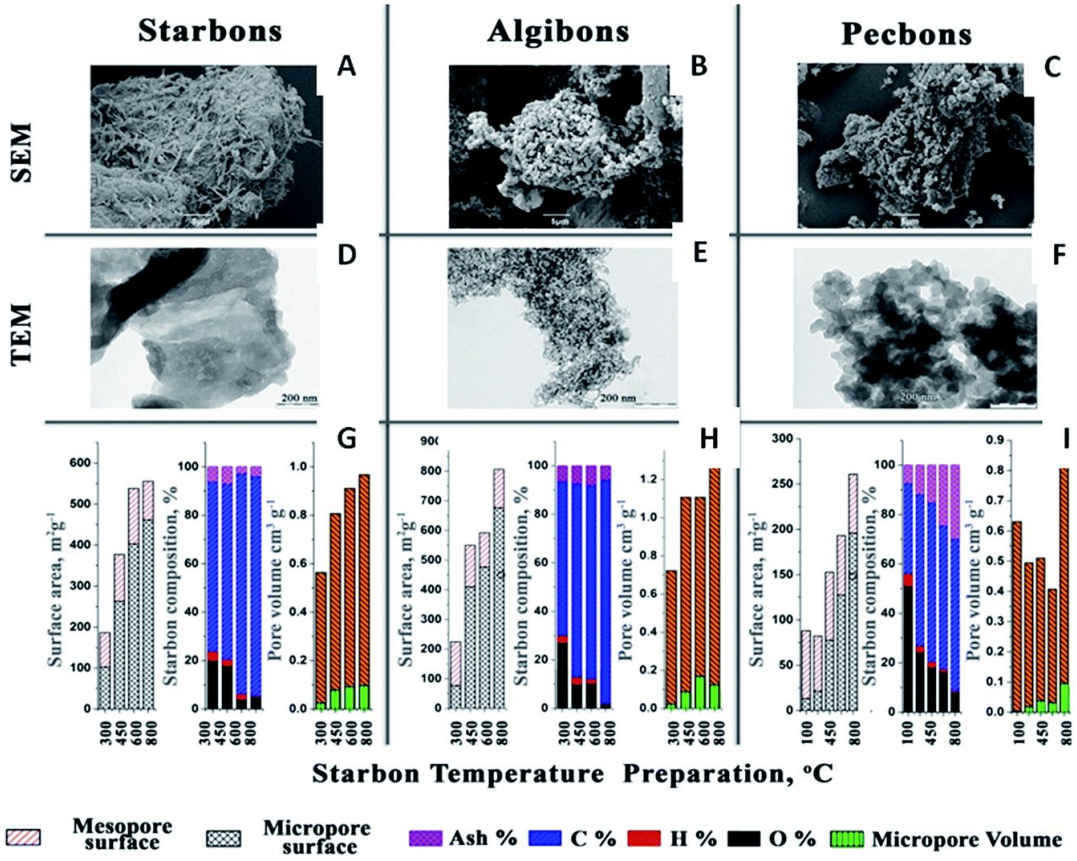

Figure 1.4 SEM images, TEM images, N_2 sorption data, ash content and elemental composition of starch, alginic acid and pectin-derived materials: (A, D, G) Starbons®, (B, E, H) Algibons and (C, F, I) Pecbons. Adapted with permission from reference 77.

In addition, the morphology of Starbon® materials is also affected by the choice of polysaccharide precursor with S800 showing a more amorphous structure, whilst A800 exhibits a more heterogeneous fine fibrous structure and P800 contains nanostructured platelets or spheres (**Figure 1.4 A-F**). In summary, the morphology, surface chemistry, and textural porosity of these nanoporous Starbon® materials can be controlled through varying: the temperature of preparation (during both gelatinisation and carbonisation), drying technique and polysaccharide precursor.

1.1.3.2 Applications of Starbon® materials

Starbon® materials obtained by the solvent exchange method have already demonstrated great promise in catalysis, chromatography, purification and adsorption applications. Starbon aerogels or solids prepared at relatively low temperatures (250-700 °C) possess highly accessible oxygenated functionalities and are ideal to act as catalysts or catalyst supports.[59] For example, Starbon® acids (e.g. Starbon-supported-SO_3H) has act as a heterogeneous catalyst in esterification and transesterification of waste oils to produce biodiesel and glycerol;[78,79] acylation of primary and secondary amines to produce amides[80,82]; and alkylations of aromatics.[83]

Starbons® generated at high temperatures have been successfully used as an adsorbent in liquid or solid adsorption and separation due to their high hydrophobicity and good textural properties. For example A1000 has performed well in the liquid phase separation of polar sugar analytes owing to its large mesopore volumes and polarisable graphitic structure.[72] Calcium alginic acid-derived mesoporous carbon spheres (AMCS) with highly defined spherical morphology and extensive mesoporous networks (90% mesoporosity) also demonstrated superior efficiency compared to commercially available porous graphitic carbon (PGC) in the separation of polar carbohydrate analytes.[81] S800 and A800 have been demonstrated to be efficient adsorbents for the recovery of phenolic compounds from aqueous solution[82]; removal of dyes (e.g. methylene blue and acid blue)[64] and detergent residues[83] from wastewater; selective desorption of plant growth promoters[84]; and selective adsorption and separation of critical metals (Au^{3+}, Pt^{2+} and Pd^{2+}) from a mixture also containing earth abundant elements (Ni^{2+}, Cu^{2+} and Zn^{2+})[85].

As recyclable carbon dioxide adsorbents, Starbons® (e.g. S800) with large specific area and high mesoporosity have shown both high carbon dioxide adsorption capacity and large carbon dioxide versus nitrogen adsorption selectivity compared to microporous

activated carbon.[86] As an adsorbent for toxic acidic or basic gases, the functionality/surface chemistry of Starbons® enables them to selectively adsorb acidic or basic gases. Acidic gases (e.g. hydrogen sulphide and sulphur dioxide) adsorb better onto a hydrophobic surface (P800). In contrast, the basic gas ammonia adsorbs best onto a hydrophilic surface (uncarbonised alginic acid-derived material) due to acid-base interactions of basic gas ammonia with oxygen containing groups.[87]

Starbons® have also proved their potential in photochemical and electrochemical applications. For example TiO_2/S800 has shown improved activity compared to TiO_2/activated carbon and TiO_2/graphene oxide as a photocatalysis support in the aqueous phase total mineralisation of phenol under mild conditions because of its high crystallinity and hydrophobicity.[88] A mesoporous Starbon®-graphite composite monolith has been successfully applied in a supercapacitor electrode with enhancement of the stability, conductivity and capacitance retention.[89] Starbon® can act not only as a carbon additive in lithium-ion battery negative electrodes[90] but also as the negative electrode itself[91] and has shown good electrochemical performance. The large pore volumes and pore diameters in the interconnected pore network can provide both efficient pathways for lithium ions/electrons and high accessibility for the electrolyte.

1.2 Pore Engineering of Carbon Materials

To meet the demands associated with applying porous carbon materials in real industrial applications, it is necessary to optimise their multiple functionalities and engineer their porous structures.[51,53] The distribution of pores and the specific surface area in a porous structure can provide the space needed for its functionalisation such as surface modification (e.g. oxidation, halogenation, sulfonation and diazonium grafting), metal incorporation, non-metal heteroatom doping (e.g. oxygen, nitrogen, sulphur or boron), and graphitisation. The uniform distribution of the resulting functionalities enables the production of porous carbons with elevated stability, selectivity, processability, mechanical properties, and thermal properties; allowing them to be used for many different applications.[92-94]

Therefore, it is desired to achieve a hierarchically porous structure with high porosity; interconnected pores ranging in size from micro to meso to macro; and large surface area, which would be favourable for various applications from both kinetic and thermodynamic perspectives. Great efforts have been devoted to engineer the pore structures of carbon materials by either directly carbonising porous precursors,[95-97] "templating" synthesis via replication of a porous template[98,99] or chemical/physical activation[97] of carbons.

The direct carbonisation and template methods offer the possibility to construct porous carbons with fine control of morphologies and structures by either selecting, inheriting and developing the porous structure of precursors (e.g. MOFs, ZIFs and modified carbon black etc), or by replication of rigid templates (e.g. mesoporous silicates, colloidal particles and MOFs etc) which possesses inherent porosity.[100] For instance, highly porous carbons could be generated from porous MOFs via appropriate thermolysis with the MOF acting as the sacrificial template in the presence of an additional carbon source (e.g. furfuryl alcohol or glucose).[101] In addition, some organic species contained in the scaffolds of MOFs also enable

MOFs to be used as carbon precursors for the preparation of nanoporous carbons through direct carbonisation.[102] However, direct carbonisation of biomass precursors usually leads to carbon materials with low porosity. In these cases, the use of an activation process has proved to be an effective strategy for structure optimisation and the fabrication of porous carbons. This approach is especially well-developed for the production of mesoporous carbons with improved porosity and pore size distribution. There are two kinds of activation methods: physical activation[103, 104] and chemical activation[105] as listed in **Table 1.1**.

Table 1.1 Comparison of activation methods for carbon-based materials and the resulting textural properties.

Activation method	Activating agent	Activation temperature	Produced S_{BET}	Produced porosity
Chemical activation	KOH, NaOH, K_2CO_3, $KHCO_3$, $ZnCl_2$, H_3PO_4 etc	400-900 °C	1000-4000 $m^2 g^{-1}$	High degree of microporosity with some small mesopores
Physical activation	CO_2, steam, O_2	700-1200 °C (CO_2 and steam activation) 400-700 °C (O_2 activation)	500-3000 $m^2 g^{-1}$	Less and broadened microporosity but more mesoporosity

Different activation routes can lead to porous carbons with diverse porosity and microstructure; wettability; and electrical conductivity.[106] What the various activation methods have in common is that certain parts of a carbonaceous material are prone to be dehydrated and oxidised during the activation process, leading to the creation and development of micro- and mesopores. Variation of the ratio of the activator and precursor, activation temperature or hold time can be used to adjust the porosity for both chemical and physical activations, although a highly degree activation always leads to a significant decrease in carbon yield. Therefore, selecting appropriate activation conditions is crucial in

balancing the yield and pore texture.

1.2.1 KOH Activation

Chemical activation is conducted by co-carbonisation of carbonaceous precursors with an activating agent such as potassium hydroxide (KOH),[107] sodium hydroxide (NaOH),[108] potassium carbonate (K_2CO_3),[109] potassium bicarbonate ($KHCO_3$),[110] zinc chloride ($ZnCl_2$)[111] or phosphoric acid (H_3PO_4)[112] etc. at 400 to 900 °C. It allows for the conversion of biomass into highly porous carbon in a one-step carbonisation/activation process, whereby porosity is generated through simultaneous dehydration and oxidation reactions with the assistance of the chemical activator, which greatly simplifies the manufacturing process.[113,114] Two-stage chemical activation processes have also been developed by mixing the dehydrating (e.g. zinc chloride or phosphoric acid) or oxidation (e.g. potassium hydroxide or sodium hydroxide) activator with previously carbonised material (char). The intrinsic pore structure in the char permits adequate penetration and diffusion of the activator towards the interior structure of the precursor and hence sufficient reaction of the activator with the carbon.[115,116]

The various activators show different characteristics during activation.[117,118] Among the various activating agents, potassium hydroxide has been shown to be one of the efficient agents for generating activated carbons with large surface areas (up to 4000 $m^2\ g^{-1}$), high pore volumes (up to 2.7 $cm^3\ g^{-1}$), tuneable and narrow pore size distributions (PSD) through control of the activating conditions. In contrast, other activating agents (such as zinc chloride and phosphoric acid) always produce a material with a relatively broad pore size distribution and poor porous structure with the surface areas and pore volumes less than 2000 $m^2\ g^{-1}$, and 1.5 $cm^3\ g^{-1}$ respectively.[119,120]

A typical potassium hydroxide activation process involves impregnation of the precursors with potassium hydroxide solution and subsequent carbonisation of the dry

mixture at elevated temperature.[60] The inherent mechanism underlying potassium hydroxide activation is complex, but it is generally accepted that during potassium hydroxide activation, potassium carbonate is generated from the reaction of potassium hydroxide and carbon as shown in Eq. (1.1) at around 400 °C. The potassium hydroxide will be consumed by the time the temperature reaches 600 °C. The formed potassium carbonate decomposes into carbon dioxide and potassium oxide at 700 °C to 800 °C as shown in Eq. (1.2). The generated carbon dioxide and potassium containing compounds can be reduced by gasification processes to form carbon monoxide and metallic potassium at temperatures over 700 °C as shown in Eq. (1.3), (1.4) and (1.5).[103,104,121]

$$6KOH + 2C \rightarrow 2K + 3H_2 + 2K_2CO_3 \quad (1.1)$$

$$K_2CO_3 \rightarrow K_2O + CO_2 \quad (1.2)$$

$$CO_2 + C \rightarrow 2CO \quad (1.3)$$

$$K_2CO_3 + 2C \rightarrow 2K + 3CO \quad (1.4)$$

$$K_2O + C \rightarrow 2K + CO \quad (1.5)$$

The development of pore structures is attributed by potassium etching and oxidative removal of carbon atoms. The generated metallic potassium efficiently intercalates into the carbon lattices. This penetrating and vaporising of potassium within the carbon matrix results in expansion of the lattice and formation of the pore network. Generation of gases (steam, carbon monoxide and carbon dioxide) from carbon and water during the activation process further expands these pores. Finally, removal of residual potassium compounds that intercalated within the lattice structure by washing further promotes the development of microporosity.

It is well established that the conventional potassium hydroxide activation processes produce predominately micropores and some mesopores with diameters less than 4 nm in porous carbons. However, in addition to micropores, both large mesopores and macropores

have been observed in materials produced by potassium hydroxide activation processes. It is agreed that there are several factors that leads to the formation of a hierarchical pore structure: macropores are partly inherited from the precursor, while micro- and mesopores are created by potassium hydroxide activation;[122,123] the aggregation of micropores can also lead to the formation of mesopores and macropores;[124] phase separation of water and hydrophobic carbon at relatively low pyrolytic temperatures during the activation process may also contribute to the additional pores;[125] the removal of potassium hydroxide during activation and the subsequent washing process allows opening of closed and bottlenecked pores. Therefore, the porous structure and pore size distribution of the resultant materials can be generated and controlled by potassium hydroxide activation. Activation conditions (such as activation temperature, activation time and amounts of the activating reagents) contribute greatly to regulating the textural properties of the resultant materials. In general, harsh activation conditions lead to the development of more porosity resulting in higher surface areas and larger pore volumes; whereas excessive elimination of carbon and heteroatoms from the framework always result in reduced ultramicro- and microporosity, a widening of the pore size distribution and shrinkage or collapse of the structure.[126-128]

Materials activated by potassium hydroxide have been widely used in applications such as gas adsorption and storage,[129-131] water treatment[132,133] and electrochemical supercapacitors[127,134] etc. For instance, it has been demonstrated that mild conditions with a mass ratio of potassium hydroxide and carbon in the range of 2.5-3.5 and a temperature around 700-900 °C are more appropriate for activating carbonaceous adsorbents for carbon dioxide capture because the resulting carbon products have a high ultramicro-/micro-porosity, moderate mesopore volume and high specific surface area.[129] The effects of activation temperature (600-800 °C) and mass ratios (0.1-3) of potassium hydroxide and rice husk (RH) on hierarchically structured microporous biocarbons in terms of the textural properties and

carbon dioxide adsorption behaviour were investigated by Snape et al.[126] The ultramicropore volumes increased with the increase of the activation temperature and the amount of potassium hydroxide used due to the enhanced activation effect. However, the associated pore creating and widening effect results in a decrease of the ultramicroporosity (ultramicropore volume as a fraction of micropore volume). As a result, the carbon dioxide uptake of the resultant materials was affected substantially by the activation conditions: samples prepared at 600 and 700 °C showing the best carbon dioxide adsorption performance; HC-600-2 exhibited the highest carbon dioxide adsorption capacities, consistent with it having the highest ultramicroposity compared with other samples produced at the same activation temperature of 600 °C but from different mass ratios.

1.2.2 CO_2 Activation

Most chemical activation methods suffer from drawbacks such as that the preparation process is corrosive, costly and hazardous due to the use of large amounts of corrosive activating agents (typical weight ratio of potassium hydroxide to precursor is 2-4). In addition, in order to remove the residual chemicals and impurities from the structures, extensive washing processes are needed which lead to secondary pollution problems and cause a significant environmental disadvantage.[135]

Compared to chemical activation, physical activation or gas activation is potentially a cleaner and greener process for achieving a high purity product due to the absence of non-volatile chemical agents during the preparation. By contacting the carbonized raw material with activation gases, it is possible to produce activated carbons with broadened microporosity, a small degree of mesoporosity, moderate surface areas and desirable physical characteristics.[136,137] Owing to these advantages, physical activation is widely adopted in industry.

Physical activation is commonly carried out in a two-step process including pyrolysing the carbonaceous precursors at 400-900 °C under an inert atmosphere, followed by a further heat treatment at a temperature of 700-1200 °C with controlled gasification in a stream of oxidising gases, such as carbon dioxide, steam, oxygen or a combination of these gaseous reactants.[103] In addition, single-step activation of biomass with steam,[138] carbon dioxide[139] or oxygen[140] has also shown the ability to produce biomass-based activated carbons with similar or even better characteristics than those obtained by the two-step procedure. The reactions between carbonaceous materials and activating agents are:

$$C+CO_2 = 2CO \ (CO_2 \text{ as the activating agent, } \Delta H = +173 \text{ kJ/mol}) \quad (1.6)$$

$$C+H_2O = H_2 + CO \ (\text{steam as the activating agent, } \Delta H = +132 \text{ kJ/mol}) \quad (1.7)$$

$$C+O_2 = CO_2 \ (O_2 \text{ as the activating agent, } \Delta H = -395 \text{ kJ/mol}) \quad (1.8)$$

$$C+1/2\ O_2 = CO \ (O_2 \text{ as the activating agent, } \Delta H = -111 \text{ kJ/mol}) \quad (1.9)$$

Reactions of carbon dioxide or steam with carbon require high temperatures (above 600 °C) to eliminate carbon atoms due to their endothermic nature as shown in Eq. (1.6) and (1.7).[104] In contrast, due to the exothermic nature of the reaction of oxygen with carbon as shown in Eq. (1.8) and (1.9), the oxygen activation process can be realised at lower temperatures (below 450 °C), which saves considerable energy compared to activation with carbon dioxide or steam.

The generation of pore structure in a physical activation process generally starts with the initial devolatilisation/carbonisation process under an inert gas to produce carbon-enriched samples (char), during which new pores can be created and blocked pores can be re-opened due to the elimination of both impurities and volatile matter. With further activation, the microporous structure is developed, and the existing pores are widened due to the oxidation or gasification of reactive areas of the carbon skeleton with the oxidising gas (e.g. carbon dioxide, steam or oxygen), which results in the consumption of carbon; formation of

gaseous oxides (carbon monoxide or carbon dioxide); and burning-off of walls between adjacent pores. In addition, venting of the gaseous oxides gives rise to the formation and development of larger pores.

The oxidising agents and carbon precursors as well as the activation conditions employed in physical activation determine the final yield; composition; and chemical and physical nature of the resulting carbon material. These factors allow activated carbons with moderate to high porosity as well as varied surface chemistry (e.g. type and amount of oxygen groups) to be obtained.[120] It is believed that activating agents (carbon dioxide, steam) with different molecular size and reactivity play different roles in determining the final porosity and pore size distributions of the resultant materials.[141-144] Carbon dioxide activation has potential to form narrow micropores and extensive microporosity. However, the molecular size of water is lower than that of carbon dioxide, so the reactivity of steam at a given temperature is greater than that of carbon dioxide, which permits its faster diffusion and greater accessibility into the micropore network. Therefore, the steam activation process can be performed at a lower temperature and for a shorter time, and results in the widening of micropores which leads to lower micropore volumes but more ordered mesoporosity.[145]

As a general trend, the more severe gasification conditions lead to lower total carbon yields but with larger surface areas and a higher degree of porosity development. However, higher porosity developments are usually accompanied by a broadening of the pore size distribution. Since a higher temperature accelerates the removal of volatile compounds from the carbon framework, a longer activation time enables more oxidising gases to burn the carbon and organic compounds away. Eventually, excessive burning-off of walls between adjacent pores leads to the broadening of pores.[53,54,146]

The porous structure of the carbon precursor influences the way gasification proceeds from the exterior to the interior of the precursor. Intrinsic pores in materials can provide

active sites for reaction and also diffusion routes for gas transfer. Due to the existence of intrinsic pores, carbon atoms can be removed from the interior of the material, while the diffusion resistance of gas through the particle is smaller than the gasification resistance. These factors result in the creation of micropores, opening up of closed micropores and enlargement of micropores.[147-149] The surface areas were found to be dependent on the carbon dioxide activation temperature and hold time. The maximum BET and micropore surface areas were found to be 1410 m^2 g^{-1} and 942 m^2 g^{-1} respectively at the optimum carbon dioxide flow-rate of 100 cm^3 min^{-1}, activation temperature of 850 °C and hold time of 2 h.[150] Chang et al. proposed that the BET surface area, pore volume, and average pore diameter of the resulting activated carbon generally increase with the extent of burn-off during carbon dioxide activation at a given temperature. The BET surface area of high temperature (900 °C) prepared activated carbons reached 1705 m^2 g^{-1} when the burn-off wt% of the precursors was 71%. This overcame the drawbacks of a longer activation period at a lower temperature and gave material with a high adsorption capacity.[151]

Apart from the above advantages, the carbon dioxide activation process is considered to be a cheap and simple way to activate carbons from the perspective of real applications, as the carbon dioxide flow can easily be regulated from a gas cylinder without the utilisation of an additional steam generator or a metering pump; whereas these are needed in the steam activation process.

1.2.3 O_2 Activation

Oxygen is economically attractive as an activating agent, with the advantage of inexhaustibility, easy handling and ready availability from air. In addition, as a result of the exothermic nature of oxygen reactions with carbon; oxygen activation meets industrial requirements well since it allows lower activation temperatures and shorter activation times

and thus requires less energy and reduces cost.[152,153] Oxygen activation has been used in the oxidation of carbon materials to modify their porous structure[154,155] or surface chemistry.[156]

However, the exothermic nature of the reactions also makes the oxygen activation process difficult to control owing to its high reactivity, which always results in non-uniform activation, excessive burn-off of carbon and reduction of yield. The burning of carbon occurs not only in the internal pore structures but also on the exterior surface of particles and thus leads to great losses of external carbon and the reduction of surface area.[135] To circumvent these limitations of oxygen as an activating agent the oxidation rate can be controlled by lowering the temperature or reducing the oxygen partial pressure.[157] Plaza et al. proposed performing oxygen activation at low temperatures (preferably lower than 650 °C), with low activation times and with use of diluted oxygen (3-5% oxygen in nitrogen) rather than purified oxygen in order to avoid excessive combustion. Compared to conventional activation with carbon dioxide or steam, this process reduces the energy required, but the obtained activated carbons still possess narrow microporosity, tailored pore size distribution and good carbon dioxide adsorption capacity (1.36 and 3.1 mmol g^{-1} at 0.1 and 1 bar, respectively).[140] The requirement of a reduced oxygen concentration in the gas mixture opens the door to using residual hot gas streams such as power station flue gas, which contains excess oxygen not consumed by the combustion process, for carbon activation.

Bathia[158] studied the variation of pore structure of coal chars (coals pyrolysed at 900-1150 °C) during gasification in air and carbon dioxide. Gasification in air was performed at 380 °C, whereas carbon dioxide gasification proceeded at 800 °C. It is suggested that in carbon dioxide gasification, the surface area and pore volume of pores of all sizes increase with an increase of the gasification time. However, in air activation, the positive effect on porosity development only occurs for larger pores (pore sizes of 1 to 5 nm) not for small pores (pore sizes below 1 nm). There is a rapid initial increase of pore volume and surface

area for pore sizes below 1 nm at the beginning of the heat treatment, but no significant variation after a certain level of conversion. This initial rapid increase is attributed to the high degree of re-opening of closed micropores by oxygen. Since oxygen is more reactive than carbon dioxide, it can react more rapidly with heavy atoms and functional groups that are present after the carbonisation process.

Ganan[159] et al. and Osswald et al.[160] observed an increase in surface area and pore volume with an increase of activation time and temperature in air gasification processes. Ganan prepared high-quality activated carbons from almond tree prunings by air gasification at 190-260 °C. The surface area (up to 560 m^2 g^{-1}) and pore volume (up to 0.31 cm^3 g^{-1}) increased with an increase of the gasification temperature and time. Osswald et al. demonstrated that the increase of both parameters was moderate (10%) and accompanied by a rapid enlargement of micropores into mesopores and a large weight loss.

1.3 Applications of Hierarchically Porous Carbon Materials

As mentioned above, the synthesis and applications of hierarchically porous materials has attracted rapidly increasing interest.[29] The structural, morphological and component level advantages of these materials gives them high performance in applications such as: adsorption, separation, purification and energy conversion and storage.[56,61] The micro- and mesoporosities of hierarchically porous materials provide high surface areas for high active site dispersion of guest molecules and accurate size and shape selectivity of reactants, intermediates and products. The meso- and macroporous networks provide high accessibilities for even most large molecules, minimise diffusion barriers and enhance mass transport.[65]

Hierarchical porous carbons stand out from the family of hierarchically porous materials since they not only possess the merits mentioned above but can also be synthesised from abundant biomass resources.[161] This has added additional momentum to their sustainable, economic and environmentally compatible applications.

1.3.1 Carbon Dioxide Capture

1.3.1.1 Current state of carbon dioxide capture

Urgent action is required to prevent the continued emission of the greenhouse gas carbon dioxide into the atmosphere, which is the main reason for global warming and the acidification of oceans. Various approaches have been devised to reduce carbon dioxide emissions: such as energy utilisation efficiency improvements, renewable energy substitution

and carbon dioxide capture and sequestration (CCS).[162] However, there is still a challenge for renewable energy sources such as solar energy, wind and biomass in replacing fossil fuels on a large scale. Fossil fuel fired power plants and other human activities related combustion processes are still leading causes of carbon dioxide emissions and account for approximately 33-40% of carbon dioxide emissions.[163]

Three complementary strategies are considered crucial for large scale carbon dioxide emission reduction through CCS.[164] These are: carbon dioxide pre-combustion capture from fuel gas (high pressure, separation of 60-80% hydrogen and 20-40% carbon dioxide), sweetening of natural gas and landfill gas (high pressure, predominantly carbon dioxide and methane separation with carbon dioxide concentration over 80%) and post-combustion separation from power plant flue gas (low carbon dioxide concentration of 3-20% and more than 70% nitrogen, predominantly carbon dioxide and nitrogen separation at 1 bar pressure). In particular, significant investigations have been directed towards post-combustion separation for efficient carbon dioxide emissions reduction due to its ability to be retro-fitted to existing power plants which are responsible for a substantial proportion of global carbon dioxide emissions.[165-167]

1.3.1.2 Methods for carbon dioxide capture

Methods of carbon dioxide capture and sequestration (CCS) are diverse (as listed in **Table 1.2**) and the requirements for methods vary with different application types and depend on the composition and pressure of the gas mixture. Amongst them, chemical absorption, physical adsorption, membrane separation and cryogenic distillation are the most practical technologies to reduce the carbon dioxide emissions.[168]

Table 1.2 CO_2 capture methods and their characteristics.

CO_2 capture method	Agent or technology	Advantages	Disadvantages
Chemical absorption	Aqueous amine solutions: monoethanolamine (MEA), diethanolamine (DEA) or methydiethanolamine (MDEA); or alkaline solvents: $Ca(OH)_2$ or NaOH	High CO_2 capture efficiency from flue gas via chemical reactions with fast kinetics	Equipment corrosion; solvent loss; thermal or oxidative degradation of the amine; high energy requirements for regeneration
Physical adsorption	Porous carbons, zeolites, mesoporous silica, MOFs, COFs and metal oxide frameworks	Low energy requirement; low cost; property variability; fast diffusion; reversible; insensitivity to moisture; high adsorption efficiency and good reusability	Insufficient selectivity over other components present (e.g. N_2, O_2, H_2O, SO_X, NO_X, etc)
Membrane separation	Polymeric or inorganic membranes	Low energy requirements; environmental friendliness and high selectivity at elevated pressures	Expensive; poor stability; competitive relationship between flux and high selectivity
Cryogenic distillation	Cyclic distillation, heat-integrated distillation columns, reactive distillation, and thermally coupled columns	No chemical reagents are needed	High energy requirements for CO_2 desublimation

The most widely used chemical absorption methods which utilise amine-based or hydroxide-based compounds such as monoethanolamine (MEA), diethanolamine (DEA), methydiethanolamine (MDEA), calcium hydroxide and sodium hydroxide as absorbents are the industrial standard for removing carbon dioxide from post-combustion flue gases.

However, they suffer from a series of drawbacks including high heat capacity of aqueous amine solutions, considerable energy requirements for regeneration of solvent and severe thermal or oxidative degradation of the amine. The capture process alone can increase the consumption of energy from the power plant by 25-40% and leads to additional costs of 70%.[169] The regeneration constitutes about 60-80% of the required energy for carbon capture, which increases the electricity usage by approximately 81%.[170]

Polymeric or inorganic membranes have been studied extensively and used commercially due to their low energy requirements, environmental friendliness and high selectivity at elevated pressures. Membranes used for carbon dioxide separation are usually operated under continuous steady-state conditions and the separation of carbon dioxide is realised by selectively filtering the gas due to a pressure difference across the membrane. Therefore, membranes are not efficient for separating mixtures with low carbon dioxide partial pressure. Due to the low pressure of flue gas streams, the application of membrane technology for post-combustion carbon dioxide capture is very challenging and improvements are still required to achieve high stability with good carbon dioxide capture capacity and selectivity simultaneously.[171,172]

Cryogenic distillation processes are based on process integration and intensification techniques. They utilise the dew and sublimation points of gas stream constituents and no chemical reagents are needed. Nevertheless, a pre-treatment step is essential to remove impurities such as NO_X and SO_X in the flue gas to increase the carbon dioxide concentration, as lower concentrations of carbon dioxide will cause higher cooling energy requirements for carbon dioxide de-sublimation.[173,174]

The problems with aqueous amine based carbon capture can be avoided by use of solid carbonaceous adsorbents to physisorb carbon dioxide in a pressure swing process. Compared with the other methods, adsorption on solids is one of the most promising alternative

processes for carbon dioxide capture from gases even at low carbon dioxide partial pressure at pilot plant scale. The carbon-based adsorbents have potential advantages of having wide availability, reliable producibility on a large scale, high adsorption capacity, high selectivity for carbon dioxide over nitrogen, low regeneration energy requirements and long-term stability at ambient conditions.[175-177]

1.3.1.3 Adsorbents for carbon dioxide capture

In general, to be a good candidate for efficient carbon dioxide separation, materials should have high specific surface areas, pore volumes and micropore volumes, as well as a well-defined pore size distribution. Other influence factors should also be considered in effective adsorption/separation processes, which include high adsorption and desorption kinetics; tolerance towards moisture and impurities; low energy consumption for regeneration; and long-term stability in multi-cycle processes.[172] Steady progress of developing diverse ranges of adsorbents has been made over recent years to meet the requirements for carbon dioxide capture, such as: zeolites, mesoporous silicas, MOFs, COFs, metal oxide frameworks and carbon-based materials (e.g. activated carbon, carbon nanotubes, carbon nanofibers and graphene etc.)[135,178].

Zeolites and activated carbons hold great potential in commercial applications due to their economic and environmental friendliness. However, the application of zeolites is restricted as their surface areas are relatively low and their tolerance of moisture is poor. Activated carbons possess large surface areas, however, they show low carbon dioxide capture selectivity when separating carbon dioxide from other combustion flue gases. In addition, neither of these materials is suitable for high temperature applications since their capture capacity decreases rapidly with increasing temperature.[178] MOFs possess significant advantages in gas separation because of their unique structural properties, including large

surface area, adjustable chemical functional groups and pore characteristics within the metal–organic framework, enabling them to have high carbon dioxide capacity at high pressures (>10 bar).[179] However, although the synthesis of MOFs with particular functional groups enhanced their affinity to carbon dioxide; most MOFs exhibit unfavourable adsorption and low carbon dioxide selectivity at low carbon dioxide partial pressures.[180] Hence, the majority of MOFs are considered more appropriate for carbon dioxide storage than for separation. In addition, the long-term stability and tolerance to moisture of MOFs remain problematical.[180,181]

Thus, most of these adsorbents for post combustion carbon dioxide capture still suffer from problems, such as poor performance retention over multiple cycles; intensive energy consumption; and insufficient selectivity. Therefore, it is still a great challenge to develop adsorbents with high carbon dioxide adsorption capacity and selectivity, fast adsorption kinetics, mild conditions for regeneration, high stability and low cost for carbon dioxide capture and sequestration.

1.3.1.4 Factors that determine carbon dioxide capture efficiency

Adsorption or separation of carbon dioxide is attained via selective adsorption of carbon dioxide at the surface, or within the pore network, of adsorbents. Generally, two stages are included in this technology: carbon dioxide is physically (physisorption, via van der Waals interactions) or chemically (chemisorption, via a covalent bonding interaction) bonded by solid adsorbents; then, after equilibration, the adsorbents are regenerated by increasing the operating temperature in thermal swing systems (TSA) or reducing the pressure in pressure swing systems (PSA).[53] As a result, carbon dioxide molecules are adsorbed and then desorbed from the adsorbents and thus the adsorbents can be regenerated for use in subsequent cycles.

In real applications, the direct use of mostly reported activated carbons (with particle sizes in the range of micrometers) in fluidized bed and moving bed on large scales is greatly restricted. Particle size affects carbon dioxide capture performance to some extent by influencing the carbon dioxide mass transfer resistance. The mass transfer coefficient for carbon dioxide adsorption decreases as the particle size in a fixed bed reactor increases. For example, Ding reported that the mass transfer coefficient onto crushed hydrotalcite (mean particle size of 0.5 mm) increased ten fold compared to the parent material (particle size of 2.75 mm) for carbon adsorption at 673 K under wet conditions.[182] Thus, to assess the effect of the porous structure of adsorbents on carbon dioxide capture performance, a preliminary particle size screening is needed for granulometrically heterogeneous adsorbents.[183]

In addition, in a practical application of gas separation and storage, the adsorbent is confined in a given volume of a capture system. When the adsorption capacity is reported on a volumetric basis, both the textural property and the density of the adsorbent affect the gas adsorption capacity. Most adsorbents have low bulk densities of below 1 g cm^{-3} due to their high porosity. It is essential to maximize the textural property whereas maintain the density of the adsorbent, because if an adsorbent has a higher density, a higher amount of the adsorbent can be confined in the limited volume and thus a higher storage capacity can be realised.[184]

Separation of carbon dioxide and nitrogen in flue gas at relatively low pressure requires the adsorbent to exhibit a large carbon dioxide adsorption capacity and high carbon dioxide/ nitrogen selectivity, which depends on the interactions between the adsorbent and adsorbate.[185] Thermodynamic equilibrium, molecular sieving and the adsorption kinetics are principally responsible for these interactions and for the affinity between the adsorbate and adsorbents and thus influence the carbon dioxide capture.

One of the parameters that influences the thermodynamic equilibrium between the

sorbate and sorbent in gas adsorption processes is the free adsorption enthalpy, which is proportional to the polarity/polarisability of both materials. Carbon dioxide has a polarisability of 26.3×10^{-25} cm^3, which is 50% higher than that of nitrogen (17.6×10^{-25} cm^3). In addition, the quadrupole moment of the carbon dioxide molecule is a higher than N_2, at 13.4×10^{-40} cm^2 versus 4.7×10^{-40} cm^2 (**Figure 1.5A**).

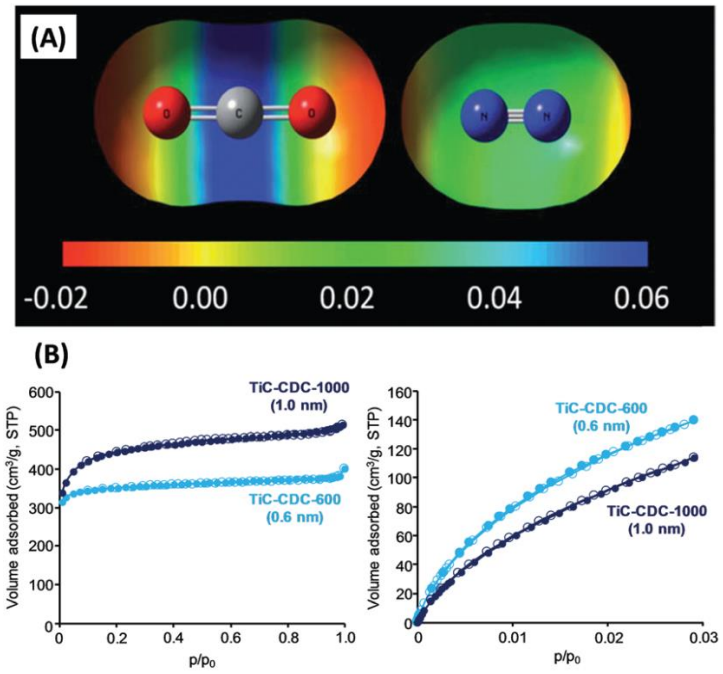

Figure 1.5 (A) Electrostatic potentials of CO_2 and N_2 mapped against the isoelectron density value of 0.005 a.u.[129] (B) N_2 (77 K, left) and CO_2 (273 K, right) adsorption/desorption isotherms on carbon adsorbents with different micropore sizes.[182] Adapted with permission from reference 129 and 182.

Although these differences are small, the selective adsorption of carbon dioxide over nitrogen can be achieved by adjusting the polarisability of the sorbent and can be further enhanced by functionalising adsorbents with extra cations or polar groups within the framework to give stronger dipole-quadrupole interactions. Based on this principle, modification and functionalisation of adsorbents by introducing polarisability has been extensively investigated to enhance carbon dioxide capture. Approaches include nitrogen[93] or

sulphur[94] doping in porous carbons and incorporation of extra cations in the framework of zeolites[186,187] and MOFs etc.[188,189]

Separating gases by a molecular sieving effect exploits differences in the pore size of the adsorbent and the kinetic diameters of the adsorbate components. The kinetic diameters of carbon dioxide, nitrogen and methane are 0.330 nm, 0.364 nm and 0.380 nm respectively.[190] For example, if the pore sizes of an adsorbent are larger than the kinetic diameter of carbon dioxide but smaller than the kinetic diameters of nitrogen or methane, the adsorbent will exhibit excellent diffusion of carbon dioxide from gas mixtures, resulting in efficient adsorption of carbon dioxide. An ideal "molecular sieve" adsorbent is hard to produce due to the small differences between the kinetic diameters of carbon dioxide and other gases. Nevertheless, significant diffusion selectivity can be achieved if there is a slight difference between the pore sizes of the adsorbent and the diameter of the larger gas molecules in the gas mixtures.

It is well established that compared to larger supermicropores or mesopores; ultramicropores (pore diameter less than 0.7 nm) possess stronger carbon dioxide adsorption potential. As a result, carbon dioxide fills these pores preferentially at low-pressure (**Figure 1.5B**).[182,191] This effect is due to the van der Waals force from the walls of ultramicropores which provides favourable interactions between the carbon structure and carbon dioxide molecules. Therefore, at low pressure, it is the ultramicropore volume and ultramicropore surface area, rather than the total pore volume and overall surface area that determine the carbon dioxide adsorption capacity and selectivity.

In addition to the thermodynamic equilibrium and molecular sieving effects, the adsorption kinetics can also affect the carbon dioxide capture behaviour of an adsorbent.[192] For example, if the pore size of an adsorbent is slightly larger than the kinetic diameter of larger component of the gas mixture (nitrogen or methane), the separation of carbon dioxide

from the gaseous mixture can still be achieved due to the different diffusion rates of the gases within the pore space. In addition, when the pore sizes are sufficiently large for molecules of two different gases to readily diffuse into the pores, the two gases in a mixture may be separated by differences in their equilibrium adsorption. Thus, although narrow pores have great potential to selectively "sieve" large gas components, if the pore sizes are extremely small, adsorption of carbon dioxide and filling of the pores will become increasingly slow due to the effect of adsorption kinetics.

In reality, carbon dioxide adsorption behaviour is in most cases determined by a synergistic combination of these effects. It is believed that adsorbents which possess a strong interaction and affinity with carbon dioxide; a suitable pore size configuration composed of both: large amounts of ultramicropores to effectively "sieve" large gas components; and larger micro-, meso- or macropores to provide faster diffusion kinetics will exhibit excellent carbon dioxide capture behaviour. For example, microporous MOFs have been utilised as precursors, followed by further pyrolysis, to produce new fabricated porous structures. In this case, the micropores are retained together with newly generated mesopores and macropores. As a consequence, the newly defined porous carbons exhibited excellent textural properties and great potential for carbon dioxide storage applications.[193] It was shown that micropores contribute greatly to the high specific surface area and thermal and mechanical stability of the material; whereas additional types of pores facilitate gas transportation, providing rapid access to adsorption sites, and thus enhance the carbon dioxide capacity and selectivity. In addition, Choma et al.[194] reported that porous materials with distributed micropores and additional mesopores are suitable for adsorption of gas molecules. Micropores within the material enhance the interactions between the carbon surface and gaseous molecules and enlarge the specific surface area. The mesopores provide space for mass transfer and facilitate diffusion, and thus relieve the problem of limited diffusion seen for most conventional

absorbents with high micropore density.

Therefore, it is desirable to have a hierarchical pore structure that has a suitable pore size configuration of ultramicro-, micro-, meso- and macropores with a significant amount of uniform ultramicropores to favour carbon dioxide capture from both the thermodynamic and kinetic perspectives. However, there remain a series of questions: what size of "transportation pores" is most appropriate to promote selective adsorption of carbon dioxide in reasonable conditions and to fully utilise the entire volume of pores in carbon dioxide capture? What is the most suitable proportion of narrow pore volume to "transportation" pore volume?

1.3.1.5 Potential of Starbons® in CO_2 capture

Amongst the various solid adsorbents, biomass-derived carbonaceous materials have received significant consideration because of their low raw material costs, extensive availability, potentially tuneable porous structure and reusability.[195] In particular, mesoporous carbonaceous materials referred to as Starbons®, which are derived from low-value bio-resources, such as starch, alginic acid and pectin have become a research hot-spot over recent years due to their outstanding textural properties. These include an adjustable specific BET surface area (can be varied between 200 and 1000 m^2/g) and high total pore volume (up to 4 $cm^3\ g^{-1}$) composed predominately of mesopores.[55,59] Moreover, by controlling the degree of carbonisation, a controlled pyrolysis from polysaccharides to graphite-like Starbons® with a progressive increase in the hydrophobicity of the remaining functional groups can be achieved.[71] This hydrophobicity gives Starbons® the potential advantage of avoiding an additional step for moisture removal prior to gas adsorption and a better tolerance to moisture, which is crucial in carbon dioxide physisorption.

A systematic analysis made by our group indicated that Starbons® made by the solvent exchange process are good candidates as recyclable carbon dioxide adsorbents.[86] As shown in

Figure 1.6c, compared with the representative microporous material, Norit activated carbon, Starbons® adsorb up to 65% more carbon dioxide, and show 3~4 times higher selectivity for carbon dioxide adsorption over nitrogen adsorption, even though they have much lower microporosities (8~32% versus 73% for active carbon). It was also shown that Starbon® materials retain up to 90% of their carbon dioxide adsorption capacity when the carbon dioxide is saturated with water, whereas activated carbon retains only 80% of its carbon dioxide adsorption capacity. It was proposed that the presence of interconnected micropores and mesopores and a high porosity is responsible for the enhanced carbon dioxide adsorption.

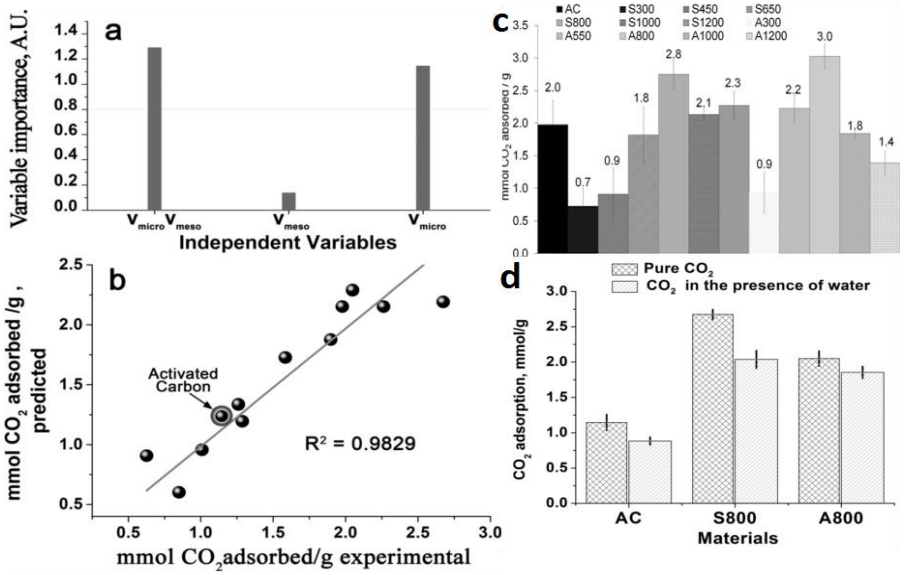

Figure 1.6 (a) Analysis of the importance of micropore and mesopore volume in CO_2 adsorption by Starbons®. (b) The correlation of experimental and predicted CO_2 adsorption data estimated from a mathematical model. (c) CO_2 adsorption data for activated carbon (AC) and Starbons®. (d) Comparison of dry and wet CO_2 adsorption of samples. Adapted with permission from reference 86.

As shown in **Figure 1.6a**, carbon dioxide physisorption of Starbons® depends principally on $V_{micro}V_{meso}$, where mesopores facilitate diffusion and mass transfer and indirectly enhance interactions between the carbon surface and the gaseous molecules. To a

lesser extent, carbon dioxide physisorption depends on just V_{micro}, where carbon dioxide directly accesses the micropores without passing through mesopores.

However, as discussed above, the design of an optimal adsorbent for carbon dioxide should include a hierarchical pore structure with a considerable amount of uniform and highly interconnected ultramicropores and a suitable pore size configuration with meso- and macropores.[196-199] The porosities of the initially prepared Starbons® obtained from the expansion and carbonisation processes are not sufficient and the amount of micropores in the Starbons® is thought to be lower than optimal. Therefore, it is very attractive to prepare a new generation of Starbons®, which possess more micropores coupled with the mesoporous regions and with tailored micro-, meso- and macroporosities. This may also allow correlation of the textural properties of Starbons® with changes in their carbon dioxide adsorption capacity and selectivity.

1.3.2 Dye Adsorption

1.3.2.1 Dyes and dye adsorption

Dyes are coloured chemicals that can attach to surfaces or fabrics to impact colour.[200] Synthetic dyes are widely used in industries such as textiles, paper, leather, rubber, food processing, plastics, cosmetics and printing.[201-204] In order to withstand degradation on contact with strong light, water, detergents or any other washing agents, a synthetic dye should have high and stable colour intensity. Synthetic dye molecules are generally created by the presence of chromophores (colour giving groups) and auxochromes (colour intensifying groups).[205] Chromophores generally have a carbon-carbon conjugated structure, or a heteroatom containing conjugated structure, such as C=C-C=C，C=C，C=O，-COOH，Ph-, -NO_2，-$CONH_2$，-COX，-COOR, which can undergo π-π and n-π transitions. When

non-bonded electrons of auxochromes such as -OH, -OR, -NH_2, -NHR, -NR_2 and -X connect with double bonds or conjugated systems, a p-π conjugated system is formed. Thus, the range of delocalisation of the electrons is enlarged, absorption shifts to longer wavelengths and the colour is deepened.[206]

Pollutants in textile and other industrial wastewater include dyes, toxic heavy metals, organic acids, pesticides, halogenated and phenolic compounds etc. Amongst them, the removal of methylene blue (MB, a basic and cationic dye) in the effluents has raised great concern since it represents a large source of environment contamination due to its extensive use in textiles, printing, biology and chemistry.[207,212] As a large heterocyclic aromatic compound, (as shown in **Figure 1.7**) methylene blue is used extensively to evaluate the porous structure and the adsorption capacity of activated carbons, as the available surface of a certain activated carbon (adsorbent) for a large molecule (MB as the adsorbate) is limited due to the pore screening or molecular sieving effect.[208]

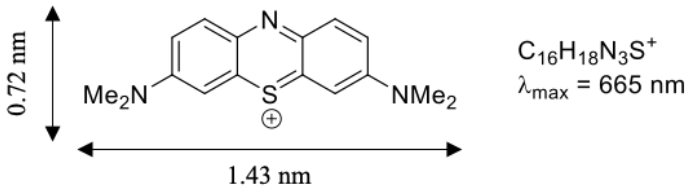

Figure 1.7 Chemical structure and characteristics of methylene blue (MB).

The discharge of dyes into environmental water bodies creates a major source of pollution and has detrimental effects on human and aquatic life due to their toxic, potential carcinogenic, recalcitrant and poorly biodegradable nature.[209,210] Therefore, permanent removal of dye molecules from water sources has become a significant concern and a challenge to environmentalists and scientists.[211]

Various techniques have been explored to remove dyes from wastewater, such as biological treatment (e.g. algal degradation, enzyme degradation and aerobic-anaerobic digestion etc.); chemical treatment (e.g. oxidation, precipitation, coagulation, irradiation,

photocatalytic and electrochemical processes etc.) and physical treatment (e.g. adsorption, distillation, ion exchange, irradiation, reverse osmosis and membrane filtration etc.).[212,213] Adsorption has become the most favourable approach due to its ease of operation and high efficiency. It has the ability to remove almost any type of dye and no secondary pollutants are produced during the adsorption process.[206,214,215]

Adsorption is a mass transfer process whereby a solid surface is contacted by a surrounding gaseous or liquid substance, resulting in a lowering of the non-bound concentration of the substance.[216] The adsorption process is illustrated in **Figure 1.8** and generally involves four steps: (1) external diffusion: migration of adsorbate from the bulk of the adsorbate to the surface of adsorbent; (2) adsorption of the adsorbate at an active site on the surface of adsorbent; (3) intra-particle diffusion: diffusion the adsorbate to the available pores of the adsorbent; and (4) occupancy of all the available exposed active sites by either physisorption or chemisorption. Once the sites of the adsorbent get saturated, the adsorption and desorption rates are equal, and the system reaches a dynamic equilibrium.[224,225]

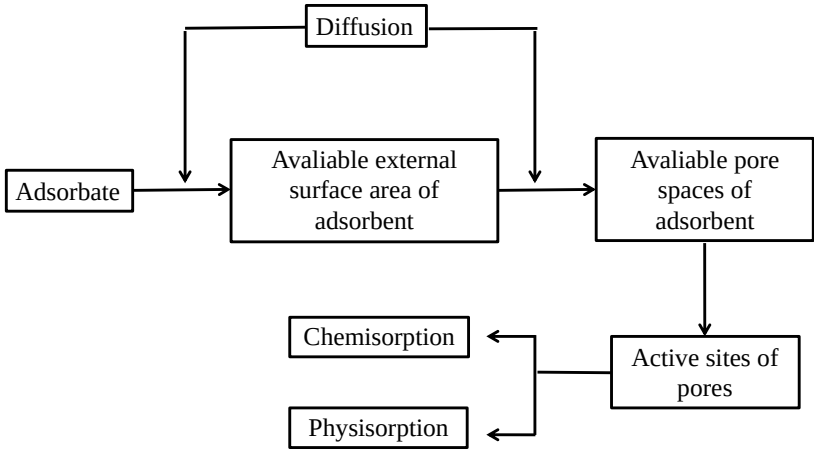

Figure 1.8 Pathway of adsorption process.

In most cases, physisorption is a reversible process. In physisorption, the adsorbate sticks to the surface of the adsorbent through weak intermolecular interactions such as Van der Waals forces, hydrogen bonding, polarity, hydrophobicity, static interactions, dipole-

dipole interactions and π-π interactions. In contrast, chemisorption is generally an irreversible process, which occurs due to the formation of a chemical bond through electron exchange between molecules or ions of adsorbate and adsorbent surface.[217]

1.3.2.2. Factors that influence dye adsorption

To be a favourable adsorbent for the removal of dyes from wastewater, a material should not only be effective in adsorption performance but should also be economically viable and readily available.[212] For example, commercial activated carbons, derived from coal, have been considered as highly efficient adsorbents due to their large specific surface areas, controllable microporous structure, thermal stability and low acid/base reactivity. However, the high costs of the raw material and process operations limits its large scale use.[218,219] Hence, a wide variety of non-conventional and low-cost materials such as natural materials (e.g. wood, bark, clays and zeolites etc.), agricultural waste (e.g. leaves, fibres, fruits peels and seeds etc.), industrial by-products (e.g. sludge, fly ash and red mud etc.), biomass (e.g. chitin, seaweed, fungi, yeast, algal waste, cellulosic materials, chitosan etc.) and biomass based activated carbon have been extensively explored for this application.[214,220-223] These low-cost materials are obtained from renewable sources and their conversion into activated carbon partly reduces the volume of by-products or waste and also provides alternatives to existing commercial activated carbons with a reduced cost.[218] The adsorption process based on these low-cost adsorbents is therefore cost effective.

The adsorption capacity of an activated carbon depends on the source of the raw material as these possess different carbon contents and surface functional groups (e.g. alcohol, phenol, aldehyde, carboxyl and ketone etc.) in their polymer chains.[224] By heat treatment and activation of biomass precursors, their surface functional groups and pore structures can be maintained and developed due to the removal of moisture and volatiles. Treatment methods

(e.g. physical activation and chemical activation) as well as treatment conditions (e.g. pyrolysis temperature, activation time etc.) have a significant impact on the particle size, surface areas, pore structures and surface chemistry; and as a result, affect the adsorption performance of the resultant materials.[225,226]

Studies have shown that the adsorption capacity of adsorbents can be affected and enhanced by changes to its functional group composition and porosity. Increasing the number of functional groups on adsorbents creates more active sites for bonding and strengthens electrostatic attraction and hydrogen bonding between adsorbents and dyes.[227,228] Increasing the hydrophobicity of an adsorbent may also enhance the hydrophobic interactions between dyes and the hydrophobic adsorbent surface.[229] High specific surface areas produced by micropores provide accessible sites for dye adsorption; mesopores and macropores facilitate fast mass transport for dye diffusion, and macropores act as reservoirs for minimising the diffusion distances.[230-233] Therefore, it is reasonable to expect that hierarchically porous carbon materials with high specific surface areas and multipored porous structures will be favourable in dye adsorption.

In addition to considering the chemical and physical properties of adsorbents; optimisation of the adsorption conditions is also important to ensure the achievement of a desired rate of adsorption and maximum efficiency of dye removal to establish industrially relevant dye removal conditions. The adsorption conditions include pH of the solution, temperature of the solution, adsorbent dosage, dye concentration and contact time between the adsorbate and the adsorbent.

The pH of solution plays a vital role in determining the adsorption process since it can change both the surface characteristics of the adsorbent and the specific charge of exchange sites in the adsorbate.[206] In general, the adsorbent will be positively charged under the influence of a high concentration of hydrogen ions at low pH values (acidic conditions), thus

high removal of anionic dyes (e.g. acid blue 25 and acid orange 95) occurs due to the electrostatic attraction between the anionic dye and the positively charged surface of the adsorbent. Conversely, at high pH values (basic conditions), there is an electrostatic attraction between negatively charged adsorbent sites and cationic dyes (e.g. methylene blue), therefore the adsorption capacity for cationic dyes can be enhanced under basic conditions.[234,235] High removal effectiveness of an adsorbent can be achieved by applying the minimum adsorbent dosage.[206] However, dye removal efficiency is directly proportional to the adsorbent dosage, since the higher the adsorbent dosage amount, the more available adsorption sites are available which can take up more dye ions.[236-238]

The amount of dye adsorbed and the removal percentage increase with the adsorption time until equilibrium is reached. The adsorption rate is dependent on the contact time of the adsorbate and adsorbent. In general, there is a fast adsorption during the initial stage of adsorption followed by a slow adsorption process prior to reaching equilibrium.[239] The rapid initial uptake is due to the rapid diffusion of dye molecules from aqueous solution to the adsorbent external surface. As the external surface adsorption sites are gradually occupied by dyes, more dye molecules are transported from the bulk phase to the inner surface of adsorbents which is more difficult and slower. Thus, the diffusion process and the adsorption rate decrease.[240]

The temperature of the aqueous solution also plays a role in determining the adsorption rate and capacity. The adsorption rate increases with increasing temperature since the diffusion of adsorbate from aqueous solution to the adsorbent external surface and then inner surface of adsorbent can be accelerated at a higher temperature.[241] The type of adsorption can be revealed by the variation of adsorption capacity with temperature. For example, when the adsorption capacity increases with temperature, the adsorption is an endothermic process and conversely, if the adsorption capacity decreases with increasing temperature then the

adsorption is an exothermic process.[242]

A higher initial concentration of dyes is also of benefit in increasing the adsorption amount, since the driving force provided by the initial concentration of dye is helpful to overcome the resistance of mass transfer of dye from bulk solution to the particle surface.[241] However, the percentage of dye removed will be lower at a higher initial dye concentration as the number of adsorption sites becomes the limiting factor. In contrast, the majority of the dye molecules can be taken up by an adsorbent at a lower initial dye concentration due to the relatively higher number of adsorption sites, leading to a higher percentage removal.[243]

1.3.3 Adsorption Kinetics, Isotherms and Thermodynamics

A plot of the increase of adsorbate uptake on an adsorbent versus reaction time can be described by the adsorption kinetics. Kinetic parameters are important for determining the adsorption rate and predicting the adsorption mechanism. Various kinetic models have been established (**Table 1.3**) to interpret the resulting data including: pseudo-first order, pseudo-second order and intra-particle diffusion etc.[211]

Table 1.3 Kinetic models for adsorption.

Kinetic model	Equation form	Plot
Pseudo-first order	$\ln(q_e - q_t) = \ln q_e - k_1 t$	$q_t = q_e(1 - e^{-k_1 t})$
Pseudo-second order	$\frac{t}{q_t} = \frac{1}{k_2 q_e^2} + \frac{t}{q_e}$	$q_t = \frac{k_2 q_e^2 t}{(1 + k_2 q_e t)}$
Elovich	$q_t = {}^{1}/_{\beta} \ln(\alpha\beta) + {}^{1}/_{\beta} \ln(t)$	$q_t \; vs \; \ln(t)$
Intra-particle diffusion	$q_t = k_3 t^{1/2} + C$	$q_t \; vs \; t^{1/2}$

In a solid-liquid adsorption system, k_1 (min^{-1}), k_2 (g mg^{-1} min^{-1}) and k_3 (mg g^{-1} $min^{1/2}$) are rate constant of the pseudo-first order, pseudo-second order and intra-particle diffusion

models respectively; α (mg g^{-1} min^{-1}) represents the initial rate of adsorption and β (g mg^{-1}) represents the extent of surface coverage, where the value of 1/β indicates the available number of adsorption sites; C indicates the thickness of the boundary layer and t is adsorption time. The unit of k_2, k_3, α and β should be g $mmol^{-1}$ min^{-1}, mmol g^{-1} $min^{1/2}$, mmol g^{-1} min^{-1} and g $mmol^{-1}$, respectively, when the kinetic model is used for analysing a gas adsorption system.

The pseudo-first order model assumes that adsorption is controlled by the diffusion step and that the diffusion rate is proportional to the concentration of adsorbate.[236] Pseudo-second order kinetics takes into account diffusion of the external surface, surface adsorption and intra-particle diffusion processes. The adsorption rate is determined by the number of unoccupied adsorption vacancies on the adsorbent surface.[226, 244] The Elovich kinetic equation is commonly used to describe the chemisorption process.[229] According to Weber and Morris, the intraparticle diffusion model assumes that the amount of adsorption varies almost proportionally with $t^{1/2}$ as observed for most adsorption process.[245]

The initial adsorption rates (h, mg $g^{-1}min^{-1}$ or mmol $g^{-1}min^{-1}$) can be determined from the pseudo-first or second order rate constants according to Eq. (1.10) and (1.11).[200] The linear regression correlation coefficient R^2 and the Sum of Squared Error (SSE) calculated based on Eq. (1.12)[246] can be used to verify which kinetic model is applicable: where $q_{t,exp}$ and $q_{t,cal}$ are the experimental and calculated adsorption capacity, respectively. A higher value of R^2 and a lower value of SSE, represent a goodness of fit.

$$h_1 = k_1 q_e \quad (1.10)$$

$$h_2 = k_2 q_e^2 \quad (1.11)$$

$$SSE = \sum\left[(q_{t,exp} - q_{t,cal})\right]^2 \quad (1.12)$$

At a constant temperature, when the solute concentration or the gas adsorbed amount

(at a gas pressure) remains unchanged, the equilibrium for the adsorption has been reached. A plot of the amount of adsorbate take up on the adsorbent as a function of the solute equilibrium concentration or a gas pressure at a constant temperature is the adsorption isotherm.[247] The adsorption isotherm provides information which can be used to predict the adsorption mechanism, optimise adsorption parameters and quantitatively compare adsorption capacities.[248] Various equilibrium isotherm models have been formulated in recent years as listed in **Table 1.4**.[249] The Langmuir and Freundlich isotherm are the most common models applied in dye adsorption and carbon dioxide adsorption studies.

Table 1.4 Adsorption isotherm models.

Kinetics model	Non-linear equation form	Linear equation form
Langmuir	$q_e = \frac{q_m K_L C_e}{1 + K_L C_e}$	$\frac{C_e}{q_e} = \frac{1}{q_0} K_L + \frac{1}{q_0} C_e$
Freundlich	$q_e = K_F C_e^{1/n}$	$\ln q_e = \ln K_F + \frac{1}{n} \ln C_e$
Tempkin	$q_e = B \ln(K_T C_e)$	$q_e = B \ln(K_T C_e)$

In a solid-liquid adsorption system, q_0 (mg g^{-1}) is the monolayer adsorption capacity; q_m (mg g^{-1}) is the maximum adsorption capacity; K_L (L mg^{-1}) is the Langmuir isotherm constant; K_F (mg g^{-1}(L $mg^{-1})^{1/n}$) is the Freundlich isotherm constant; n is the intensity of adsorption constant for Freundlich; B is the Temkin isotherm constant and K_T (L mg^{-1}) is the Temkin isotherm equilibrium binding constant.[249,250] C_e in the equation should be replaced by P when the isotherm is used for analysing a gas adsorption system. The units of q_0 (and q_m), K_L, K_F and K_T should be mmol g^{-1}; atm^{-1}; mmol g^{-1} $atm^{-1/n}$ and atm^{-1}.

The Langmuir adsorption isotherm which was originally developed to describe gas adsorption onto activated carbon, has generally been used to quantify and contrast the properties of bio-based adsorbents.[251] It assumes that the adsorption is a monolayer adsorption process, whereby the adsorption localised on specific homogeneous surface sites. The adsorption sites are of fixed number and identical and no lateral interactions or steric

hindrance exists between the adsorbed molecules and adjacent sites. The affinity for the adsorbate is equal with all molecules possessing the same enthalpy and sorption activation energy. Hence, there is no transmigration of the adsorbate in the surface plane.[252] An equilibrium saturation is reached and a plateau is shown in the isotherm once a molecule occupies a site and no further adsorption takes place.[248]

The Freundlich model is an empirical relationship between the quantity of a gas (or concentration of a solute) adsorbed onto a unit mass of solid adsorbent and the gas pressure (or solute concentration). It is applicable for describing non-ideal and reversible adsorption and presumes that multilayer adsorption processes occur on a heterogeneous surface with non-uniform distribution of adsorption heat and affinities over the heterogeneous surface.[253] Adsorption occurs first in stronger binding sites, the adsorption energies exponentially decrease with the progress of the adsorption process and the adsorption amount is the summation of adsorption on all sites.[249]

The Temkin isotherm was developed to describe the adsorption of hydrogen onto platinum electrodes within acidic solutions.[254] The isotherm takes the interactions of adsorbent and adsorbate into consideration, ignores extremely low and large values of concentrations and assumes that there is a linear decrease in heat of adsorption of all molecules in the layer with coverage. The Temkin equation is applicable for predicting the gas phase equilibrium but not appropriate for complex adsorption systems which includes liquid-phase adsorption isotherms.[255]

Thermodynamic parameters including Gibbs free energy ($\Delta G°$, KJ mol^{-1}), enthalpy ($\Delta H°$, KJ mol^{-1}) and entropy ($\Delta S°$, J mol^{-1} K^{-1}) of adsorption acquired at different temperatures can be used to estimate the effect of temperature on adsorption and provide an insight into the adsorption mechanism. The change in free energy $\Delta G°$ can be determined using Eq. (1.13) and (1.14):[206] where R (8.314 J $mol^{-1}K^{-1}$) is the universal gas constant, T (K)

is the temperature and K_{eq} is the equilibrium constant. By combining Eq. (1.16) and (1.17), K_{eq} can be expressed in terms of entropy change (ΔS°) and enthalpy change (ΔH°) as a function of temperature as given in Eq. (1.15), which is known as van't Hoff equation.[211] ΔS° and ΔH° can be calculated from the intercept and slope of a linear plot of ln K_{eq} vs 1/T. Negative values of ΔG° indicate that the adsorption is spontaneous and feasible; the lower the value of ΔG° the more favourable the adsorption.[256] Positive values of ΔH° suggest the adsorption is endothermic and positive values of ΔS indicate a rise in disorder at the adsorbent and adsorbate interface.[257]

$$\Delta G = -RT \ln K_{eq} \quad (1.13)$$

$$\Delta G = \Delta H - T\Delta S \quad (1.14)$$

$$\ln K_{eq} = \Delta S/R - \Delta H/RT \quad (1.15)$$

Based on the determination of the appropriate isotherm model, kinetics and thermodynamics, the physicochemical parameters and the underlying assumptions provide an insight into the adsorption mechanism, surface properties and the degree of affinity of the adsorbates and adsorbents.[211]

1.4 Characterisation of Porous Carbon materials

A comprehensive characterisation of carbon materials is crucial in screening their properties, understanding their behaviours and evaluating their potential for specific applications. Structural, textural, physicochemical and morphological features are particularly important in the fields of adsorption, separation and purification.[258,259] Therefore, a detailed description of porous carbon materials must include: (i) porous architecture (i.e. porosity and textural properties); (ii) thermal properties (e.g. thermal stability and pyrolysis mechanisms); (iii) physicochemical properties (e.g. surface chemistry, functionalities and component analysis); and (iv) adsorption properties (e.g. carbon dioxide, hydrogen, methylene blue or phenol adsorption).[260,261]

1.4.1 Gas Physisorption Characterisation of Porous Carbons

Porous architecture characterisation is particularly important because it describes the pore morphology (geometry of pores and roughness of surface), porosity (ratio of pore volume in a particular size to total pore volume) and textural properties (surface area and pore size distribution) of porous materials. These properties control transport processes and diffusional rates and determine selectivity in catalytic reactions and adsorption processes.[262]

Techniques for the characterisation of the porous architecture of solids include physical adsorption of probe gases (nitrogen, argon and carbon dioxide etc.), mercury porosimetry, small angle neutron (SAN) or X-ray scattering (SAX), electron scanning and transmission microscopy (SEM and TEM), tunnel microscopy, immersion calorimetry and NMR-based methods etc.[263] In general, each method has its limitations in pore size analysis. Gas

adsorption measurement is the most accepted method of providing numerical parameters, which allow the determination of specific surface areas and pore size distributions over a wide range, covering micropores and mesopores (up to 50 nm).[262] As a complimentary technique, mercury porosimetry is the most extensively used method for macropore analysis (50 nm-500 μm).[264] Mercury porosimetry makes use of the non-wetting property (contact angle >90^{o}) of mercury; pressure must be applied to force mercury enter the pores. There is an inverse relationship between the applied pressure and the pore width. The amount of mercury entering into the pore under a particular external pressure determines the pore volume and the corresponding pore size. The purity of the mercury, appropriate evalustion of the contact angle of mercury on a sample surface and equilibration times are critical for a reliable textural analysis of the sample.[264]

1.4.1.1 Gas adsorption mechanism

Compared with other methods, gas adsorption has the advantages of easy of operation, low cost and of being capable of measuring all surfaces including internal surfaces and irregular surfaces in open pores.[262] Gas adsorption measurement is normally based on inert gases and can be regarded as primarily a physisorption process. The filling mechanisms of micropores and mesopore are very different. For micropores, the whole accessible volume can be considered as adsorption space. The adsorption process in micropores is primarily micropore filling. In most cases, micropore filling is a continuous process and takes place at a low relative pressure range. For narrow micropores (i.e. ultramicropores), the pores filling occurs at $P/P_0 < 0.01$ and the adsorption mechanism is based on fluid-solid interactions. For wider micropores (i.e. supermicropores), the pore filling process occurs at a higher relative pressure range of $P/P_0 = 0.01\sim0.15$. The adsorption is governed by a cooperative fluid-solid and fluid-fluid interactions. There are various factors that could impact on the interactions

during micropore filling, such as the nature and dimensions of the adsorptive molecules; and the shape, width and accessibility of pores.[265]

The adsorption behaviour in mesopores also depends on fluid-wall and fluid-fluid interactions. In particular, the significant and attractive fluid-fluid interaction always results in multilayer adsorption as well as capillary condensation. Multilayer surface coverage takes place on the walls of mesopores or open macropores and includes three distinct stages: all adsorbate molecules contact with the surface layer of the adsorbent by a monolayer adsorption; more than one layer of adsorbate molecules is accommodated on the surface by multilayer adsorption; pore (capillary) condensation occurs followed by multilayer adsorption. A vapour-liquid phase transition occurs in finite-pore systems at a pressure P which is less than the bulk liquid's saturation pressure P_0.[262]

1.4.1.2 Gas adsorption isotherm

The relationship between the amount adsorbed and the equilibrium pressure of the gas at constant temperature gives an adsorption isotherm. As the adsorption temperature is below the critical temperature of the adsorptive (e.g. 77 K for nitrogen), the pressure is usually plotted as relative pressure P/P_0, where P is the equilibrium pressure and P_0 is the saturation vapour pressure of the pure adsorptive at this temperature. In contrast, when the adsorption temperature is above the critical temperature, no condensation occurs and no P_0 exists; therefore the equilibrium pressure P must be used to plot the isotherm.[265] A complete pore size analysis covering the range of micropores and mesopores requires that a physisorption experiment span a whole range of relative pressures starting from an extremely low P/P_0 of 10^{-7} to 1.

Prior to the physisorption, all species adhered to the surface of the solid should be removed by outgassing to minimise the error of the measurement. The recommended

outgassing method for microporous materials is pumping the system under vacuum (P/P_0 ~10^{-7}) at elevated temperature (e.g. ~300 °C). The outgassing conditions (time, heating programme and pressure) required should be selected carefully according to the nature of the adsorbent to avoid irreversible changes.[263]

The evaluation of gas adsorption isotherms requires a model to interpret the experimental data. The selection of the model determines the level of accuracy of characterisation. Over the years, a wide variety of adsorption isotherm models have been formulated for predicting the equilibrium distribution of adsorbate on the adsorbent as a function of pressure. The most commonly used isotherms are the Langmuir isotherm, the Freundlich isotherm, the Dubinin–Radushkevich isotherm and the Temkin isotherm.[249] The assumptions, formulation and range of application of each isotherm model has been discussed in section 1.3.3.

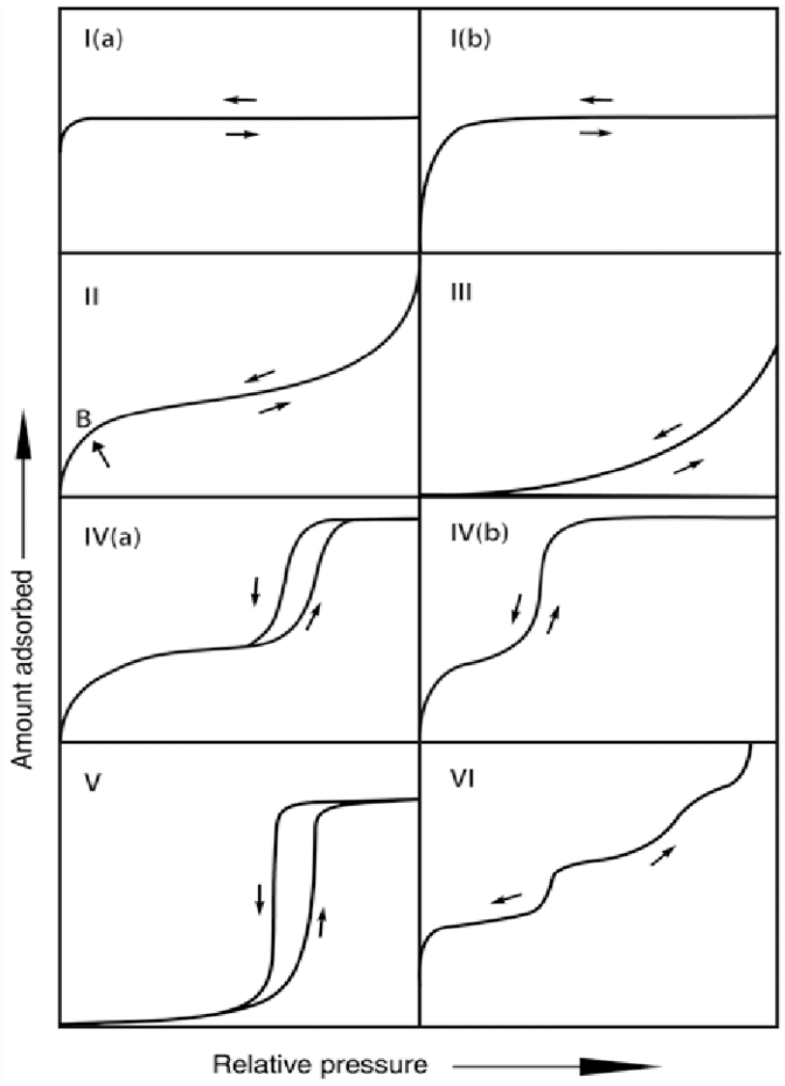

Figure 1.9 Classification of physisorption isotherms.

The adsorption/desorption isotherm has been classified and then refined into six types (**Figure 1.9**) according to the recommendations of IUPAC in 1985 and 2015, providing criteria for the characterisation of the porous texture of materials.[9,265] Type I represents microporous materials: filling of the micropores results in a steep uptake at very low P/P_0. Type II represents nonporous or macroporous materials: showing unrestricted monolayer-multilayer adsorption until high P/P_0; point B corresponds to the completion of monolayer coverage and the beginning of multilayer adsorption. Type III represents nonporous or macroporous materials with no identifiable monolayer formation. Type IV represents

mesoporous adsorbents: it shows initial monolayer-multilayer adsorption followed by pore condensation and a final saturation plateau which is variable in length. Type V represents water adsorption on hydrophobic microporous and mesoporous adsorbents; and Type VI isotherm represents layer-by-layer adsorption on a highly uniform nonporous surface.

1.4.1.3 Choice of adsorptive gas

The selection of adsorptive gas affects the characterisation of porous materials because the shape and dimensions of adsorptive molecules determine their accessibility to pores due to packing and molecular sieve effects. Nitrogen has been accepted as a standard adsorptive gas for both micropore and mesopore sizes analysis with an assumption that the value of its cross-sectional area σ_m(nitrogen) is 0.162 nm^2 in compact monolayer adsorption. N_2 adsorption at its boiling temperature (77 K) covers a relative pressure (P/P_0) range from 10^{-6} to 1 and can provide information about the whole porosity of the material. However, due to the quadrupolar nature of nitrogen, the specific interaction of nitrogen molecules with functional groups and ions that are exposed on the surface of the adsorbent results in changes of orientation of adsorbed nitrogen molecules on the adsorbent surface.[266] As a result, the nitrogen adsorption pressure is not correlated with the pore size in a straightforward way. In particular, for the micropore filling process, the initial relative pressure of physisorption shifts to an extremely low value of 10^{-7}. The rate of diffusion is low, so the measurement of equilibrium at such a low pressure is difficult. Therefore, the determination of microporosity by nitrogen adsorption requires a high vacuum and a long equilibrium time.

The problems encountered with nitrogen at 77 K can be avoided by argon adsorption at 87 K (liquid argon temperature). There are no specific interactions of argon with the adsorbents surface due to the absence of a quadrupole moment. The cross-sectional area σ_m(argon) is less sensitive to the surface and is assumed to be 0.142 nm^2. Therefore,

compared to nitrogen adsorption at 77 K, argon adsorption at 87 K can fill micropores at higher relative pressures, whereby diffusion is accelerated and equilibration is achieved more rapidly.[262]

The use of carbon dioxide as the adsorptive at 273 K can complement the shortcoming of the kinetic restrictions associated with both argon and nitrogen at cryogenic temperatures (87 and 77 K) in the characterisation of narrow microporosity.[266] The saturation vapour pressure of carbon dioxide is very high (3.5 MPa) at 273 K and thus a short relative pressure range (10^{-6}~ 0.03) is required for micropore analysis. The relatively high temperatures and pressures facilitate the diffusion of molecules and the ability of molecules to access narrow pores (width smaller than 1 nm). However, carbon dioxide adsorption is not recommended for pore size analysis of adsorbents with polar surfaces (e.g. zeolites, MOFs or carbons with oxidised functionalities). The quadrupole moment of carbon dioxide is even larger than that of nitrogen, so specific interactions can lead to an indirect correlation of pore filling pressure and pore size.[267]

1.4.1.4 Determination of surface area

The surface of porous adsorbents includes both external and internal surfaces. In general, the internal surface is defined as the surface of all pore walls and the external surface refers to the surface outside the pores. In the presence of microporosity, the external surface can thus be defined as the non-microporous surface.

The initially used theory for surface area determination is the Langmuir equation which assumes that there is a monolayer adsorption of gas molecules onto the adsorbate.[251] By modification of the Langmuir isotherm, Brunauer, Emmett, and Teller put forward a BET method in 1938.[268] This is a multiple layer model and has been widely used in gas and solid adsorption systems for evaluating the surface area of porous materials. The application of the

BET method requires a transformation of the physisorption isotherm into a "BET" plot by selecting a proper pressure range in the isotherm. The BET equations (Eq. 1.16 and 1.17) are generally applied in a linear form:

$$\frac{p/p^0}{n\,(1-p/p^0)} = \frac{1}{n_m C} + \frac{C-1}{n_m C}\,(p/p^0) \quad (1.16)$$

and

$$S_{BET} = n_m \cdot L \cdot \frac{\sigma_m}{m} \quad (1.17)$$

Where n is the specific amount adsorbed at the relative pressure P/P_0, n_m is the specific BET monolayer capacity, σ_m is the molecular cross-sectional area, S_{BET} is the BET specific area (can be regarded as probe accessible area or available effective area) of adsorbent, L is Avogadro constant and the C value represents the degree of interaction between the adsorbate and the adsorbent. The correct calculation of S_{BET} depends on the operational temperature, the choice of adsorptive and the pressure range used for the BET equation.

The BET method was originally developed and applied to nonporous, mesoporous or macroporous materials which give rise to a Type II or Type IV isotherm. The selection of the relative pressure range in the isotherm always lies within 0.05~0.30 for multilayer adsorption systems. However, when micropores are present in materials (i.e. Type I isotherm or a combination of Types I and II or IV isotherms), or the adsorption energy is high (i.e. the surface is energetically homogeneous or crystalline), the linear BET range is shifted to a lower P/P_0 range of 0.01~0.2 for monolayer coverage. For microporous adsorbents, it is difficult to separate the processes of micropore filling and monolayer-multilayer adsorption (completed at low P/P_0 of less than 0.1). The linear range of a BET plot is often narrow and difficult to locate. To address this difficulty in evaluating the BET monolayer capacity, Rouquerol et al. suggested some criteria:[268] (i) the value of C should be positive (a negative intercept of the BET plot indicates the selected range is not appropriate); (ii) $n(1- P/P_0)$

should continuously increase with P/P_0; (iii) P/P_0 and the corresponding n_m value should be within the BET range. In addition, the BET area calculated for a microporous material should not be considered as the realistic probe accessible surface area but rather as an "apparent" or "equivalent" surface area.

1.4.1.5 Determination of microporosity

Various methods have been proposed to evaluate the pore volume and pore size distribution of porous materials. For purely microporous materials which exhibit a type I isotherm, a plateau region is shown on the isotherm at the high relative pressure range. The total pore volume (V_{total}) can be simply calculated based on the limiting adsorbed amount derived at the horizontal relative pressure range according to the Gurvich rule.[269] The Gurvich rule assumes that micropores are filled with bulk liquid adsorptive, but it ignores the molecular packing effect in a confined space. In practice, most microporous materials contain additional mesopores with appreciable external surface areas. In this case the micropore volume can be obtained by another macroscopic thermodynamic procedure (e.g. t-method, α_s method) or by a statistical mechanics method (e.g. molecular simulation or density functional theory).

The empirical methods (t-method or α_s method) allow the determination of both the micropore volume and the external (non-microporous) surface area by empirically comparing the experimental isotherm with the isotherm of a nonporous reference material which has similar chemical composition. The curve of the t-method describes the change in adsorbed amount with the statistical thickness of adsorption layer. The calculation of the t-method depends on the application of BET method. Compared to the t-method, the α_s method is preferable as it provides a more refined analysis of micropores due to its utilisation of high-resolution standard isotherm data at very low relative pressures. The analysis is not dependent

on BET results and there is no requirement for the evaluation of monolayer adsorption capacity.[270]

Other frequently used methods for calculating the micropore volume and distribution of micropores are Dubinin-Radushkevich (DR), Dubinin-Astakov (DA), and Dubinin-Stoeckli (DS) approaches, which are based on Dubinin's theory of micropore volume filling.[271] The DR equation describes the adsorption in micropores with a wide pore size distribution. It assumes that the adsorption occurs on a homogeneous structure. The DA equation assumes that heterogeneous adsorption occurs in micropores which have a narrow pore size distribution. Stoeckli et al. proposed that the overall DR isotherm equations can be described as a relationship of the parameters in the adsorption isotherm and the distribution of micropore sizes. The DR derived equation must be fitted as a straight line in the micropore range of 10^{-4}~0.1 and the extrapolation of this line gives rise to the volume of micropores. Although linear DR plots have often been reported, sometimes the linear region was absent or restricted to a limited range of low relative pressures, which limits the applicability of DR derived methods.[258]

Some more advanced semi-empirical methods, including the HK method (proposed by Horvath and Kawazoe), and the later developed SF method (proposed by Saito and Foley) allow for the characterisation of microporous carbons by considering the shape of pores as slit, cylindrical or spherical.[272] The HK model is formulated based on the nitrogen adsorption (at 77 K) of some carbon molecular sieves and activated carbons and it is only applicable for nitrogen adsorption. It enables the calculation of micropore widths up to 2 nm. The further extended SF method can be used to calculate the effective pore size distributions in zeolite molecular sieves by both nitrogen adsorption (at 77 K) and argon adsorption (at 87 K). In contrast to the Gurvich rule, plot methods and DR derived methods; the HK and SF methods employ a realistic adsorption potential by considering the effect of pore shape and the

interaction of adsorbate with adsorbent. However, HK derived methods still assume that the pores are filled by bulk liquid like adsorbate, which neglects the inhomogeneity and molecular packing effect of the adsorbed molecules in the micropores.

1.4.1.6 Determination of mesoporosity

If no macropores exist in a mesoporous material (type IV isotherm with a horizontal plateaux at the upper range of P/P_0), the total pore volume can be obtained from the adsorbed amount at P/P_0 close to 1 (e.g. 0.95~ 0.99) by simply applying the Gurvich rule.[269] However, when macropores are present, the isotherm shows a combination of type II and type IV (non-horizontal at P/P_0 close to 1), so the evaluation of total pore volume in this way is no longer accurate.[273] Other methods of analysing the pore size and pore size distribution of mesoporous materials, including BJH (Barett, Joyner, Halenda) method, Broeckhoff method and de Boer method, which are all based on a modified Kelvin equation.[9] The Kelvin equation is dependent upon macroscopic, thermodynamic assumptions. It describes that there is a relationship between the pore diameter and the pore condensation pressure.

The BJH method assumes: pores have regular shapes (slit or cylindrical) and the pore channels are rigid; no micropores exist; all the pores that need to be measured have been filled by adsorbate; and the pore radius is equal to the sum of the Kelvin radius and the thickness of the adsorbed film. However, the assessment of film thickness is always problematic when the pore diameter is very small. In addition, the Kelvin equation also cannot describe the thermodynamic properties of adsorbed fluids in confined pores, which is different to that of the bulk fluid. Therefore, the BJH method is not applicable for analysing narrow mesopores. To avoid underestimation when the pore size is below 10 nm, the recommended range of relative pressures in BJH is 0.35~1.[274] In order to obtain a complementary pore size analysis including the range of 2~10 nm, a series of MCM-silicas

with known pore diameters can be used. This allows the relationship between the capillary condensation pressure and the pore size to be established and used to obtain an empirically corrected Kelvin equation.[275] However, the BJH method is still only valid over a limited pore size range.

The problem of macroscopic methods of ignoring the effect of adsorbed fluids in confined pore spaces has been solved by some newly developed microscopic, molecular dynamics methods such as molecular simulation or density functional theory (DFT).[262] Based on the fundamental principles of statistical mechanics, these methods consider the configuration of the adsorbed phase. They are powerful in describing the phase behaviour of confined fluids and the distribution of adsorbed molecules in pores on a molecular level. Essential features including micropore filling, mesopore condensation and hysteresis are all considered in these methods, which makes them more reliable in providing pore size analysis across the whole pore size range.[276] Based on the intermolecular potential energy of fluid-fluid and fluid-solid interactions, different DFT models have been developed for various materials (e.g. carbons, silicas, zeolites) with different pore shapes (e.g. slit, cylinder, or spherical geometries and hybrids). The adsorption isotherm models provide both a microscopic description of the adsorption process and a thermodynamic description of fluid behaviour in pores.[265]

The widely used DFT based methods include local DFT (LDFT), nonlocal DFT (NLDFT), two-dimensional DFT (2D-NLDFT) and quenched solid DFT (QSDFT) methods. The first developed local DFT (LDFT) showed great promise in describing the adsorption of pores compared to the macroscopic methods, but it is unreliable in describing the adsorption of narrow micropores.[277] In contrast to the LDFT method, NLDFT was established based on the behaviour of non-homogeneous fluids at a solid interface and made great progress in the precise analysis of pore size distribution. Initially, NLDFT was reported for analysing

microporous carbons.[278] After further refinement of the correlation of molecular properties of adsorbed gases with their adsorption properties in different pore sizes, it is capable of analysing both micropores and mesopores.[279] However, the NLDFT method has a limitation in the characterisation of disordered or amorphous carbon materials since it regards the surface of a solid as molecularly smooth and homogeneous. Ignoring the roughness and heterogeneity of surface could affect the shape of the adsorption isotherms and generate a gap (~1 nm) in the NLDFT pore size distribution.[280]

The drawbacks of the conventional NLDFT method can be solved by the well-developed 2D-NLDFT or QSDFT approaches.[281,282] These two methods take into account the effects of geometrical curvature and energetic heterogeneity on the surface of carbon pores, and the QSDFT approach accounts for the heterogeneous effects in a practical way. A roughness parameter is employed in the QSDFT model to represent the characteristic width of surface corrugations at a molecular level. The QSDFT method was originally developed assuming slit-shaped pores in microporous carbons, but has been expanded to cage-like or channel-like pores in micro-mesoporous carbons.[283] It is worth emphasising that the chosen DFT conditions should be consistent with the features of the given material. In that case, an accurate evaluation of the pore size distribution can be acquired by these models.

Due to the diversity and complexity of porous materials, there is no unified standard for determining the pore parameters.[284] Each method has its own scope of application: both the older macroscopic thermodynamic methods (e.g. t-method, α_s, DR and HK series and BJH) and the more modern microscopic methods (e.g. molecular simulation or DFT based methods). The choice of the model, as well as the corresponding parameters applied in the model, all have significant impacts on the results. Therefore, careful consideration needs to be given to the assumptions of the model and the experimental conditions used to accurately analyse the structural properties of the material.

1.4.2 Gas Adsorption Measurement

The techniques used for determination of gas adsorption isotherms are volumetric (or manometric) methods and gravimetric methods. The adsorption isotherm is constructed point-by-point by following the variation of the amount adsorbed with change in pressure. The variation is obtained by applying a volumetric or gravimetric technique by admission of successive charges of gas to the system at a slow and constant rate with the aid of a dosing technique.[265]

1.4.2.1 Volumetric gas adsorption method

Volumetric (or manometric) gas adsorption is the most generally used technique for measuring gas adsorption isotherms at cryogenic temperatures (e.g. nitrogen adsorption at 77 K and argon adsorption at 87 K) for determining the surface area and porosity of porous solids. Due to the kinetic restrictions of argon and nitrogen at these cryogenic temperatures, adsorption of carbon dioxide at 273 K has become another accepted method for the characterisation of carbonaceous materials with very narrow micropores. Gas adsorption isotherms at various temperatures are generally measured using static volumetric systems (e.g. Micromeritics ASAP2020, ASAP2420, and TriStar etc.) coupled with a dewar filled with liquid nitrogen or argon; or a circulating water bath, to control the adsorption temperature.

In the volumetric method, the adsorbed quantities at each measurement are not determined directly; they are calculated from pressure changes over the sample in a known fixed volume as shown in **Figure 1.10**. The calculation is achieved using Eq. 1.18 to 1.20:[285]

$$n_1 = \frac{V_{prc}}{\upsilon_a\,(T_1, P_1)} \quad (1.18)$$

$$n_2 = \frac{V_{prc} + V_{ads}}{\upsilon_a\,(T_2, P_2)} \quad (1.19)$$

$$n_{ads} = \frac{n_1 - n_2}{m_{sample}} \quad (1.20)$$

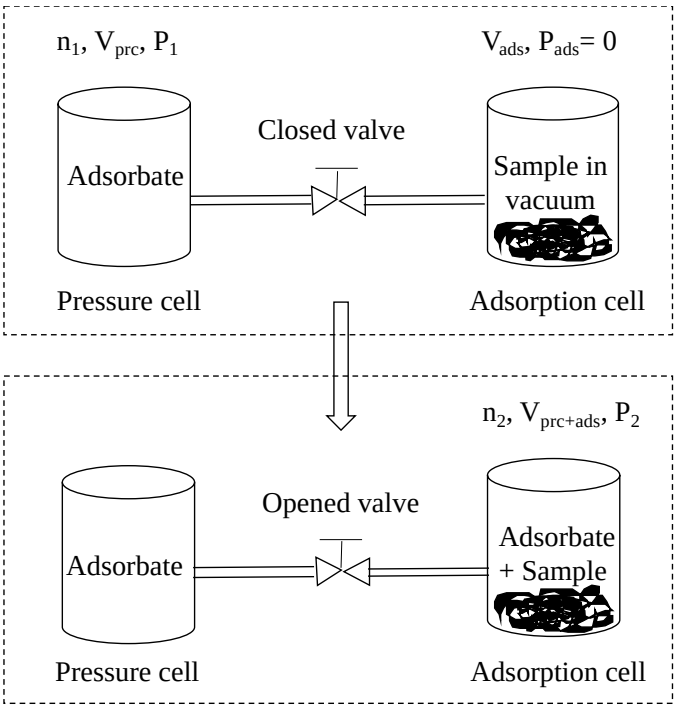

Figure 1.5 General procedure of volumetric method.

In the first stage, the valve between the pressure cell and the adsorption cell is closed, the pressure cell is filled with gas adsorbate and the adsorption cell is under vacuum. n_1, P_1 and V_{prc} represent the number of moles of adsorbate, the pressure and the volume in the pressure cell before adsorption, respectively. P_{ads} and V_{ads} are the pressure and volume of the adsorption cell. P_{ads}= 0 KPa and V_{ads} is predetermined in a separate helium calibration step, subtracting the volume occupied by sample. In the second stage, the valve is opened, the gas fills the adsorption cell. Here n_2 is the number of moles of adsorbate remaining in the gas phase after adsorption, P_2 is the equilibrium pressure in both cell cells, υ_a (T, P) (calculated by an equation of state) is the molar volume of adsorbate in the gas phase at temperature T and pressure P, where T_1 is equal to T_2. n_{ads} is the number of moles adsorbed per unit mass of the adsorbent, and m_{sample} is the mass of the adsorbent.[286]

1.4.2.2 Gravimetric gas adsorption method

The gravimetric method is convenient for vapour measurements (e.g. water vapour or some organic adsorptives) at temperatures close to ambient. However, it is difficult to measure the exact temperature of the adsorbent and control the convection effects at low temperatures particularly at cryogenic temperatures. The gravimetric method allows the direct measurement of the adsorbed amount. In this method, a clean adsorbent sample is exposed to a pure gas at constant temperature and the adsorbed amount is determined based on the change in the weight of the adsorbent as well as the pressure and temperature before and after adsorption.[285] The weight change is measured by an analytical balance. The adsorbed mass is calculated according to Eq. (1.21)[287].

$$n_{ads} = \frac{m_2 - m_1}{m_{sample} M_{ads}} \quad (1.21)$$

Where n_{ads} is the number of moles adsorbed per unit mass of adsorbent, m_1 (crucible, sample) and m_2 (crucible, sample and adsorbed phase) are the mass of the system before and after adsorption, respectively. m_{sample} is the mass of the sample. M_{ads} is the molar mass of the adsorbate. In reality, due to the different buoyancy effects on the system before and after adsorption, the m_1 and m_2 measured by the balance are not the absolute masses, but the rough masses Ω_1 and Ω_2.

$$\Omega_i = m_i - \rho_i(T_i, P_i) V_{syst} \quad (1.22)$$

Where i= 1, 2; P_1 = 0 kPa and P_2 is the pressure in the adsorption chamber after adsorption. T_1 and T_2 are the experimental temperature before and after adsorption ($T_1 = T_2$). ρ is the gas density calculated by an equation of state, V_{syst} is the volume of the system which is subject to buoyancy effects. It is estimated by exposing a clean adsorbent sample to helium at increasing pressures. Therefore, the degree of accuracy of the gravimetric method is

determined by the precise acquisition of the values of ρ, T, P, m_{sample} and V_{syst}. V_{syst} is considered the most important source of errors.

1.4.2.3 High pressure gas adsorption

High pressure adsorption measurements are important in the fields of gas storage and separation. Keeping the temperature constant is important for high pressure adsorption because the higher pressures have a magnifying effect on volumetric errors and a small change in temperature may lead to large uncertainties in determining the amounts adsorbed. Both volumetric and gravimetric methods can be used for a high-pressure adsorption measurement. The measurement can generate full adsorption and desorption isotherms over a wide range of pressures and temperatures.[288] However, unlike cryogenic adsorption at low pressure (e.g. nitrogen adsorption at 77 K below 1 bar), the measurement at high pressure under supercritical conditions is always associated with surface excess adsorption which may cause overestimation, because the voids are filled with un-adsorbed gas whose density continually increases as the pressure increases.[289]

1.4.3 Thermal Analysis of Porous Carbons

Thermal analysis techniques can be used to determine the physical and chemical properties of a system (element, compound or mixture) as a function of increasing temperature under a controlled programme. The commonly used techniques involve thermogravimetric analysis (TGA, mass change over temperature or time), differential scanning calorimetry (DSC, heat flow change over temperature or time), differential thermal analysis (DTA, temperature difference over temperature or time) and simultaneous thermal analysis (STA, simultaneous application of TGA and DSC in one experiment) etc.[290]

1.4.3.1 Thermogravimetric analysis (TGA)

Thermogravimetric analysis (TGA) is essential in material characterisation, processing and production. It is a method of measuring the mass change of a sample as a function of temperature or time under a specified atmosphere. The typical curve is plotted as the mass or percentage of initial mass as the y-axis versus either time or temperature as the x-axis. A typical TG analyser consists of a precision balance with a sample pan located inside a furnace. The thermal reaction occurs in the furnace. Various atmospheres (e.g. air, vacuum, inert gas, oxidising/reducing gases and vapours of liquids etc.) and pressures (e.g. high vacuum and high pressure) can also be used during the analysis.

Rich information can be provided by this technique, including physical phenomena: such as phase transitions, absorption and desorption; as well as chemical phenomena: such as desolvation (e.g. dehydration), decomposition, and solid-gas reactions (e.g. chemisorption). For a typical thermal analysis of a carbon-based material, the weight losses in different temperature ranges can be used to evaluate the amounts of moisture, volatiles, carbon and ash contents. The upper temperature limit of the material can also be determined by an observable degradation over a temperature range.[291] In addition, TGA can be used to perform activation studies by examining the reactivity of carbon materials under an atmosphere of oxidising gas (e.g. air, carbon dioxide, or steam). The activation rate can be controlled by varying the experimental conditions (e.g. temperature, time, heating rate and flow rate).[259]

1.4.3.2 Thermogravimetric-Fourier transform infrared spectroscopy coupled analysis (TG-FTIR)

Fourier-transform infrared spectroscopy (FTIR) is a technique of measuring the interaction of infrared radiation with a solid, liquid or gas. The FTIR adsorption spectrum is

formed when a sample is irradiated by infrared light; the functional groups within the sample adsorb radiation at energies consistent with specific vibrational frequencies. The vibration of molecular groups causes a change in the dipole moment, which results in an energy level transition from the ground state to an excited state. In addition to qualitative characterisation, FTIR spectroscopy can also be used for quantitative analysis as the concentration of most species is related to the magnitude of absorption observed in the spectrum.[258]

In recent years, the coupling of thermogravimetric analysis (TGA) and Fourier transform infrared spectroscopy (FTIR) has been successfully applied in biomass pyrolysis and gasification research.[292,293] In a TG-FTIR analysis, the sample is introduced to the TGA instrument and any gases generated in the TGA are transferred by a heated transfer-line to an on-line FTIR cell. This allows a complete quantitative and qualitative characterisation of materials in one thermal treatment. The TGA technique permits a quantitative assessment of the material by measuring the weight loss whilst the FTIR provides identification of gaseous products formed at all stages during the analysis.[294,295]

In addition to facilitating the characterisation of thermal properties and pyrolysis mechanisms of materials, TG-FTIR can also be used to analyse activation studies involving the gasification of a carbon material in a stream of oxidising gas. The thermal treatment of the precursor material is conducted in the TGA and the composition of the produced gases is monitored online by the FTIR gas cell. As a consequence, the optimal activation conditions can be investigated by controlling the parameters of the thermal treatment and monitoring the gaseous products formed during activation.

1.4.3.3 Simultaneous thermal analysis (STA, combination of TGA and differential scanning calorimetry)

Differential scanning calorimetry (DSC) is another thermal analysis technique in which the heat changes occurring in a sample and a reference are monitored as a function of temperature. Generally, the temperature of sample holder increases linearly as a function of time. The DSC curve is plotted as heat flow versus temperature or time, a peak in the curve represents a change in the differential heat flow caused by absorption or evolution of heat in sample. The area under the peak is proportional to the enthalpic change and the direction determines whether it is exothermic or endothermic.[296]

Simultaneous thermal analysis (STA) is a technique that combines both TGA and DSC, the test conditions (atmosphere, heating program, gas flow rate and gas pressure etc.) are identical for the TGA and DSC analyses. It is capable of simultaneously providing information of mass change in TGA and energy change (due to mass change or transformation of structural phase) in DSC as a function of temperature.[297-299] Taking advantage of the combination of a calorimeter and a gas dosing system, which is able to accurately estimate the heat of adsorption,[300] STA has previously been employed in the characterisation of CO_2 adsorption onto mesoporous Starbon® materials by estimation of the heat of adsorption as the ratio of the mass and heat flow changes during adsorption and desorption.[86]

1.4.4 Electron Microscopy

Electron microscopies apply a high energy electron beam as an immolation source and have been widely used to provide insights into morphology, topology, chemical structure and composition of different types of materials. As shown in **Figure 1.11**, when the electron

beam focuses on a specimen, different types of interactions can occur. In principle, all of these signals can be used to obtain useful information from the specimen. Most commonly, scanning electron microscopy (SEM) and transmission electron microscopy (TEM) work by reconstruction of images based on secondary electrons and transmitted electrons, respectively.

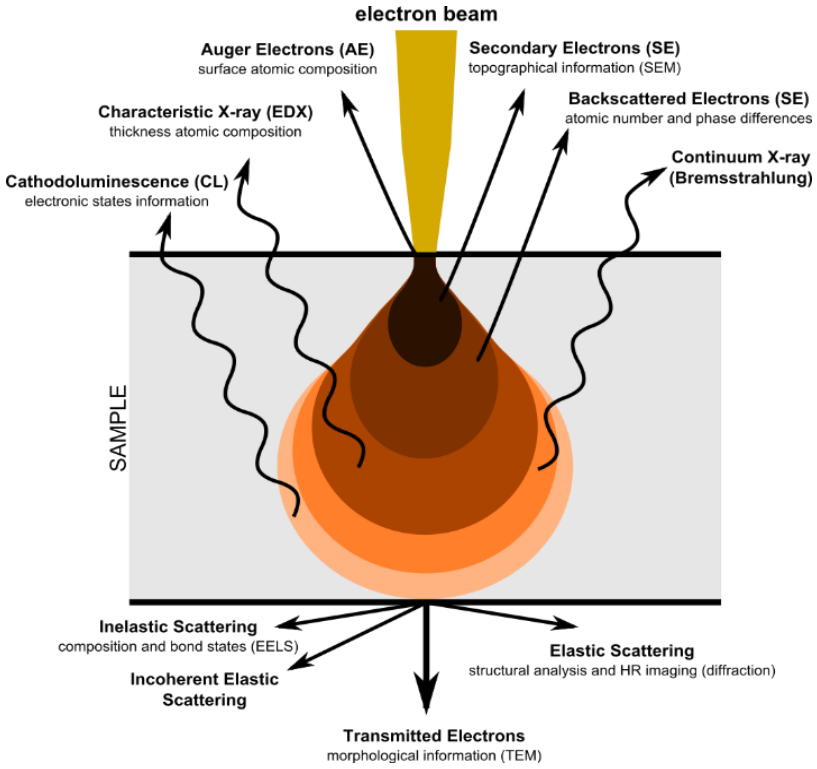

Figure 1.6 Schematic illustration of the theory for electron-matter interactions arising from the effect of an electron beam onto a specimen.

For SEM, an electron beam voltage of 5, 10 or 15 KV is typically used and a spatial resolution of less than 10 nm can be obtained. The high energy electron beam is scanned over the surface of the specimen; secondary electrons are collected by a secondary electron detector and used to form an image on the display screen. Secondary electrons usually have low energies (on the order of 50 eV), which can only escape from the top few nanometres of the surface of a sample. The different emission of secondary electrons across the surface can thus reflect the morphology and surface topography. SEM also has the advantage of high depth of field, which can produce images of the three-dimensional surface shape of the sample, and thus for porous materials the aggregates and pores on the surface can be readily

observed.[258] As shown in **Figure 1.11**, characteristic X-rays are also emitted when a higher-energy electron fills the shell after the electron beam removes the inner shell electron from the atom. The energy of these characteristic X-rays is determined by the chemical element they come from and can be measured by Energy-dispersive X-ray spectroscopy (EDX). Thus, EDX can be used to measure the abundance of elements and map their distribution in samples.

The spatial resolution of electron microscopy is determined by the wavelength of the electron beam. TEM usually applies a much higher electron beam voltage (100 KV) than that used in SEM, and thus it provides a higher resolution (less than 1 nm) and is able to visualise the pore structures of porous materials at nanometre scale resolution. The TEM image is a result of diffraction contrast for the electron beam from point to point where some of the beam is transmitted but another part is diffracted based on the local structural variation in the sample. Previous work has shown that TEM can provide additional information on the mechanism of formation of mesopores in Starbons® by comparison of images derived from expanded starch and Starbons® produced at a range of temperatures.[71]

1.4.5 X-ray Photoelectron Spectroscopy (XPS)

X-ray photoelectron spectroscopy (XPS) is a quantitative spectroscopic technique that measures the surface chemical structure of a material based on the photoelectric effect.[301] When a sample surface is irradiated by monoenergetic X-rays, electrons from the core or valence orbitals will be excited to continuum levels via photoabsorption and emitted from the surface (less than 10 nm depth).[302] For XPS measurement, the energy (hν) of incident X-ray is known, the emitted photoelectron's kinetic energy (E_K) can be measured by the detector, and thus the atomic core level binding energy (E_B) can be determined using the Eq. 1.23:

$$E_B = \mathrm{h}\nu - E_K - \phi \quad (1.23)$$

where ϕ is the work function which is dependent on both the material and the spectrometer. The elemental identity, chemical state, and quantity of a detected element can be determined from the binding energy, which is reflected by the position and intensity of the peaks in an XPS spectrum. In an XPS system, the precision of elemental quantification is typically within ±5%.[303] To obtain the chemical state of the material, high-resolution XPS spectra with a short scan range are usually performed. Chemical shifts of the excited electrons which are ascribed to small changes in the binding energy (0~3 eV) can be observed as the binding energy is highly dependent on the chemical environment of the atom. Therefore, XPS is powerful in studying the surface chemistry of various materials.

1.4.6 UV-vis Spectroscopy

UV-Vis spectroscopy is widely used to determine the concentration of different analytes in solution. As a result of the possible electronic transitions from ground states to excited states ($\pi \rightarrow \pi^*$, $n \rightarrow \pi^*$, $\sigma \rightarrow \sigma^*$, and $n \rightarrow \sigma^*$), some molecules can adsorb ultraviolet or visible light.[304] To perform the experiment, a light source with wavelengths in the UV-visible range of the spectrum is passed through the solution and the spectrometer measures the amount of adsorbed light. The Beer–Lambert law[305] (Eq. 1.24) is used to determine the concentrations of the analyte in solution. The absorbance (A) of a solution is proportional to the concentration (c) of the analyte in the solution and the path length (l). The equation is:

$$A = \varepsilon c l \quad (1.24)$$

where ε is the absorption coefficient, a fundamental molecular property of the analyte in a given solvent at a particular temperature and pressure. ε can be obtained by plotting a calibration curve by using solutions with known concentrations. By using a cell with known pathlength (l), and measuring A, the concentration (c) of analyte in an unknown solution can thus be obtained.

1.5 Aims of the Project

In this thesis, the overall project aim is to prepare a new generation of Starbons®, that is hierarchical Starbons® with tuneable micro- and mesoporosities, by using chemical and physical activation methods (Chapter 2). To gain insight into the correlation of the porous structure with their functionalities in applications, the hierarchical Starbons® were applied to carbon dioxide adsorption (Chapter 3) and methylene blue adsorption (Chapter 4).

In Chapter 2: the preparation of Starbon® materials is described in section 2.1: the influence of polysaccharide precursors, freeze-drying technique and carbonisation temperature in the preparation of Starbons® are systematically investigated. In sections 2.2-2.4, three activation strategies (potassium hydroxide in section 2.2, carbon dioxide in section 2.3 and oxygen in section 2.4) are employed to enhance the porosity of Starbons®. Direct comparisons of precursors and activation parameters are carried out in these sections. We aimed to produce hierarchical Starbons® with diverse pore sizes, pore shapes and a wide range of micro- and mesopore volumes for meeting the requirements of various applications.

In Chapter 3 and Chapter 4, we aimed to study the adsorption performance of carbon dioxide (Chapter 3) and methylene blue (Chapter 4) onto the resultant non-activated Starbons®, Algibons and Pecbons and the corresponding activated materials prepared in Chapter 2. In both Chapters, to verify their suitability for practical applications in carbon dioxide and methylene blue adsorption, systematic investigations of adsorption capacity, adsorption selectivity, adsorption kinetics, recyclability and heats of adsorption were carried out. In Chapter 3 and Chapter 4, we also aimed to acquire an in-depth understanding of the dependence of micro- and mesoporosities on the carbon dioxide and methylene blue adsorption performance and thus produce materials that are competitive in adsorption applications.

Chapter 2: Preparation and Characterisation of Hierarchically Porous Starbon® Materials

2.1 Preparation and Characterisation of Starbons®

2.1.1 Introduction

As previously reported, the preparation of Starbon® materials includes gelatinisation, retrogradation, drying and carbonisation processes as shown in **Figure 2.1**.[71]

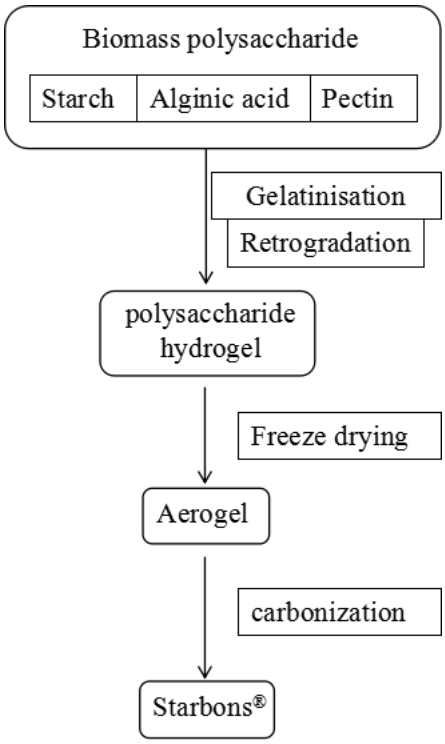

Figure 2.1 Schematic illustration of the preparation of Starbon® materials.

A polysaccharide aqueous gel is first prepared by a gelatinisation and retrogradation process. During thermal gelatinisation, polysaccharide granules dissolve and swell in water as the intermolecular bonds in the semi-crystalline polysaccharide network are broken. The disruption of the crystallinity promotes the solvation of the polysaccharide chains.[306] Retrogradation of the polysaccharide gel occurs on cooling, it allows reformation of the intermolecular associations between the polysaccharide chains as well as partial recrystallisation of the network.[70]

In previous work, a solvent exchange process was employed following the retrogradation to transform the polysaccharide hydrogel into an aerogel. The solvent exchange method is conducted by exchanging the aqueous phase by a lower surface tension solvent (e.g. ethanol, acetone or hexane), which facilitates the retention of the porous network.[71,86] However, this solvent often needs to be removed by the use of $scCO_2$, which is complicated in operation. Therefore, in this work, the polysaccharide hydrogel was dried by utilising a simpler, more recently developed method based on freeze drying. Addition of tert-butanol (TBA) to the hydrogel, overcomes issues associated with surface tension during freeze drying and ensures that the meso/macropore distribution of the resulting polysaccharide aerogel is controlled.[74]

The final stage for the production of mesoporous Starbons® is to carbonise the polysaccharide aerogel under a non-oxidising atmosphere at a desired temperature. For starch derived Starbon®, the neutral mesoporous starch is doped with a catalytic amount of an organic acid (e.g. p-Toluenesulfonic acid) to assist the carbonisation, but this is not necessary for the production of the naturally acidic alginic acid or pectin derived Starbons® (Algibons® or Pecbons®).[69] The yield of product in **Section 2.1** was obtained by dividing the mass of the product by the mass of precursor used (starch, alginic acid or pectin).

2.1.2 Results and Discussion

2.1.2.1 Starch derived Starbons®

Herein, starch was converted into mesoporous Starbons® based on the previously reported procedures. The polysaccharide aerogel was carbonised at 300, 600, 800 and 1000 °C, denoted as S300, S600, S800 and S1000, respectively. The textural properties of these materials were investigated by measuring their nitrogen adsorption-desorption

isotherms at 77 K. The textural property and yield of the samples are presented in **Table 2.1**. The BET model was applied for determination of surface area; the total pore volume (V_{total}) was estimated at a relative pressure of 0.99; the Barrett-Joyner-Halenda (BJH) method was used for determination of mesopore volume and mesopore size distribution. Although the t-plot method is useful in acquiring the micropore volume, it is limited in providing detailed information on the micropore size and distribution as it requires high-resolution nitrogen adsorption at low-pressure. Therefore, the HK method for carbon materials with slit-shaped pores was applied for determination of micropore volume (V_{micro}), ultramicropore volume ($V_{ultramicro}$) and micropore size distribution.

Table 2.1 Textural properties of starch derived Starbons®.

Material	**S_{BET} (m^2g^{-1})**	**V_{micro} ($V_{ultramicro}$) (cm^3g^{-1}) HK**	**$V_{mesopore}$ (cm^3g^{-1}) BJH**	**V_{total} (cm^3g^{-1}) P/P_0=0.99**	**Percentage of micro (ultramicro) (%)**	**Yield (%)**
S300	305	0.13 (-)	0.22	0.35	37.1 (-)	44.3
S600	627	0.25 (0.18)	0.34	0.59	42.4 (30.5)	29.3
S800	619	0.24 (0.19)	0.35	0.59	40.7 (32.2)	26.8
S1000	520	0.20 (0.15)	0.39	0.59	33.9 (25.4)	25.5

As expected, the data in **Table 2.1** shows that all of the materials have relatively low microporosity (the micropore volume accounts for 34~42% of the total pore volume), indicating that they are predominantly mesoporous materials. The carbonisation temperature plays a crucial role in determining the porosity of Starbons®. There is a trade-off between reduced yields and increased porosity with the increase of the carbonisation temperature from 300 °C to 600 °C: the surface areas and micropore volumes increase gradually up to pyrolysis temperatures of 600 °C and mesopore volumes keep increasing until 1000 °C. The dehydration, decomposition and expulsion processes contribute to the development of pores, especially ultramicropores during pyrolysis processes up to 800 °C. However, over burn off of carbon occurs at the high pyrolysis temperature of 1000 °C when preparing S1000, which

results in the expansion of micropores to mesopores and hence the reduction of micropore volume, ultramicro- and microporosity and surface area.

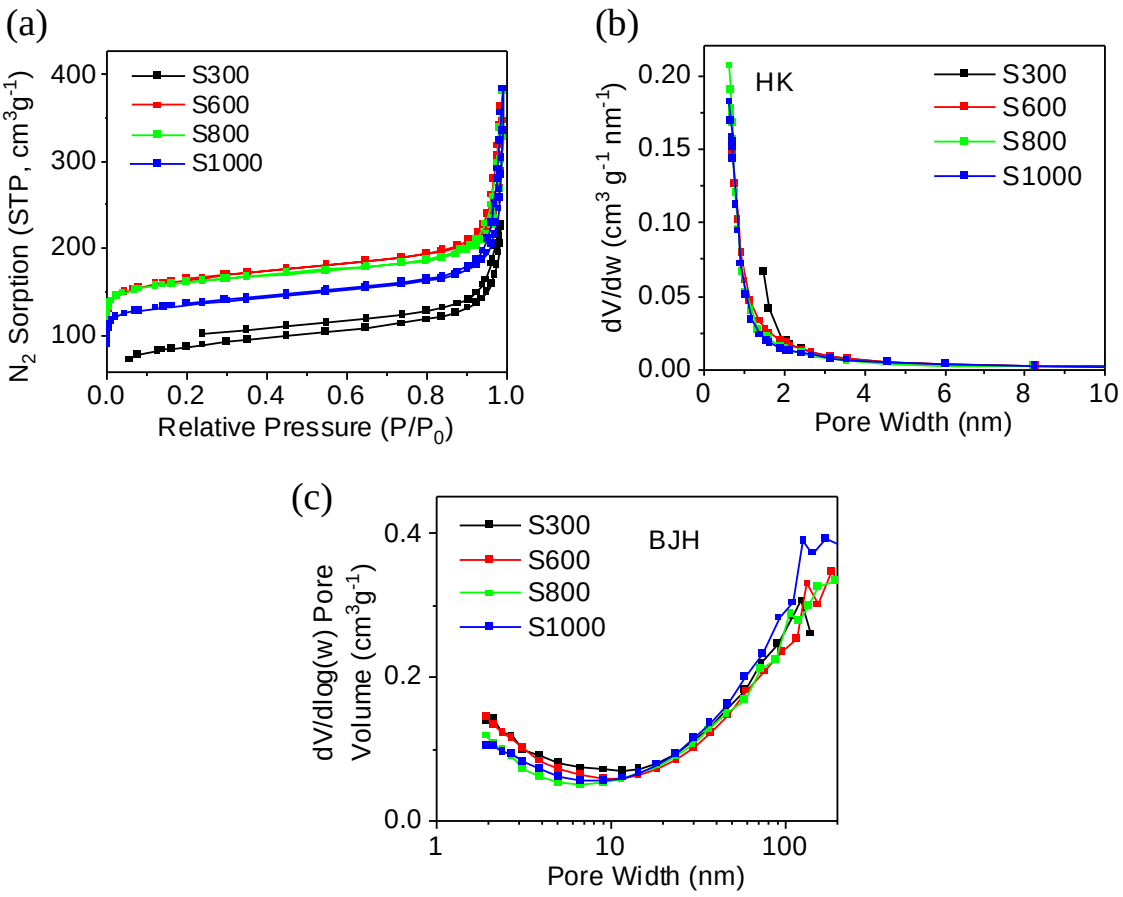

Figure 2.2 (a) N_2 adsorption and desorption isotherms at 77 K, (b) pore size distribution in micropore region determined by HK method and (c) pore size distribution in the mesopore region determined by BJH model of Starbons®.

Due to their mesoporous structure and disordered slit-shaped pores, starch derived Starbons® display type IV adsorption isotherms accompanied by type H3 hysteresis loops (**Figure 2.2a**). The higher P/P_0 range corresponds to capillary condensation in the mesopores. The increased magnitude of nitrogen adsorption in S600 and S800 compared to S300 (**Figure 2.2a**) is consistent with the increased porosity (**Table 2.1**). The distribution of pore sizes shown in **Figure 2.2b,c** demonstrates that these materials are predominantly mesoporous in

structure. Thus, the freeze-drying method combined with pyrolysis carbonisation allow the preparation of Starbons® with diversification in textural properties for further studies.

The reproducibility in textural properties of Starbons® was studied across five batches of S800 as shown in **Table 2.2**. Each batch was carbonised from different batches of S300 and subjected to porosimetry analysis to determine the variation. The data indicates that surface areas and pore volumes do vary across the five batches of materials, but the variation is not significant. Extra burn off results in a slightly increase of porosity. The variations of surface area and microporosity are 507~722 m^2 g^{-1} and 36~44%, respectively. The high mesoporosity (above 56%) and limited microporosity of all the materials is indicative of their predominantly mesoporous character.

Table 2.2 Textural properties of five batches of starch derived Starbons® (S800).

Material	S_{BET} (m^2g^{-1})	V_{micro} ($V_{ultramicro}$) (cm^3g^{-1}) HK	$V_{mesopore}$ (cm^3g^{-1}) BJH	V_{total} (cm^3g^{-1}) P/P_0=0.99	Percentage of micro (ultramicro) (%)	Yield (%)
S800-1	619	0.24 (0.19)	0.35	0.59	40.7 (32.2)	26.8
S800-2	507	0.20 (0.14)	0.35	0.55	36.4 (25.5)	29.0
S800-3	627	0.25 (0.20)	0.37	0.62	40.3 (32.3)	24.5
S800-4	702	0.28 (0.22)	0.37	0.65	43.1 (33.8)	23.2
S800-5	722	0.28 (0.23)	0.36	0.64	43.8 (35.9)	23.8

Overall, Starbons® prepared in batches have good reproducibility with acceptable variations in textural properties. However, the variation could have an impact in applications where performance is directly dependent on the surface area and porosity of the material. Therefore, to make results more reliable, careful consideration was taken when selecting materials in this study and material that was used for each modification or application came from the same batch.

2.1.2.2 Alginic acid and pectin derived Algibons and Pecbons

The textural properties of alginic acid and pectin derived Algibons and Pecbons were also investigated by measuring nitrogen adsorption-desorption isotherms at 77 K. The textural properties and yields are presented in **Table 2.3**. Up to 80% mesoporosity was obtained, which, along with the Type IV nitrogen sorption isotherms and mesopore size distributions shown in **Figure 2.3**, demonstrates the predominantly mesoporous nature of both Algibons and Pecbons. This is consistent with the previously reported materials produced by the solvent exchange method.[87,307]

Table 2.3 Textural properties of alginic acid and pectin derived Algibons and Pecbons.

Material	S_{BET} (m^2g^{-1})	V_{micro} ($V_{ultramicro}$) (cm^3g^{-1}) HK	$V_{mesopore}$ (cm^3g^{-1}) BJH	V_{total} (cm^3g^{-1}) P/P_0=0.99	Percentage of micro (ultramicro) (%)	Yield (%)
A300	168	0.01 (0)[a]	0.76	0.77	1.3 (0)[a]	39.4
A800	322	0.13 (0.07)	0.68	0.81	16.0 (8.6)	23.6
P300	65	0.01 (0) [a]	0.37	0.38	2.6 (0) [a]	36.8
P800	262	0.11 (0.06)	0.43	0.54	20.4 (11.1)	24.9

a) Determined by t-plot method as the microporosity was too low to analyse by HK method.

A higher carbonisation temperature of 800 °C leads to lower yields of products and produces larger porosities (BET surface area and pore volume) for both Algibons and Pecbons compared to the 300 °C derived A300 and P300 as shown in **Table 2.3**. This changing porosity trend is seen by comparing the nitrogen adsorption isotherms in **Figure 2.3a,c**, where the higher microporosity in A800 and P800 results in higher adsorption of nitrogen at low P/P_0 due to micropore filling. Compared to Starbons®, Algibons and Pecbons have considerably larger mesopore volumes and mesoporosity. This has been attributed to phase separation and self-association in the polysaccharide precursors as a result of their surface charge and helical domains.[55] The type of hysteresis loop in the isotherms is

associated with the shape of the pores in materials. Algibons show a narrow pore size distribution and the type H3/H1 hysteresis loops indicate a cylindrical pore shape. Pecbons exhibit type H3 hysteresis loops, corresponding to slit shaped pores.

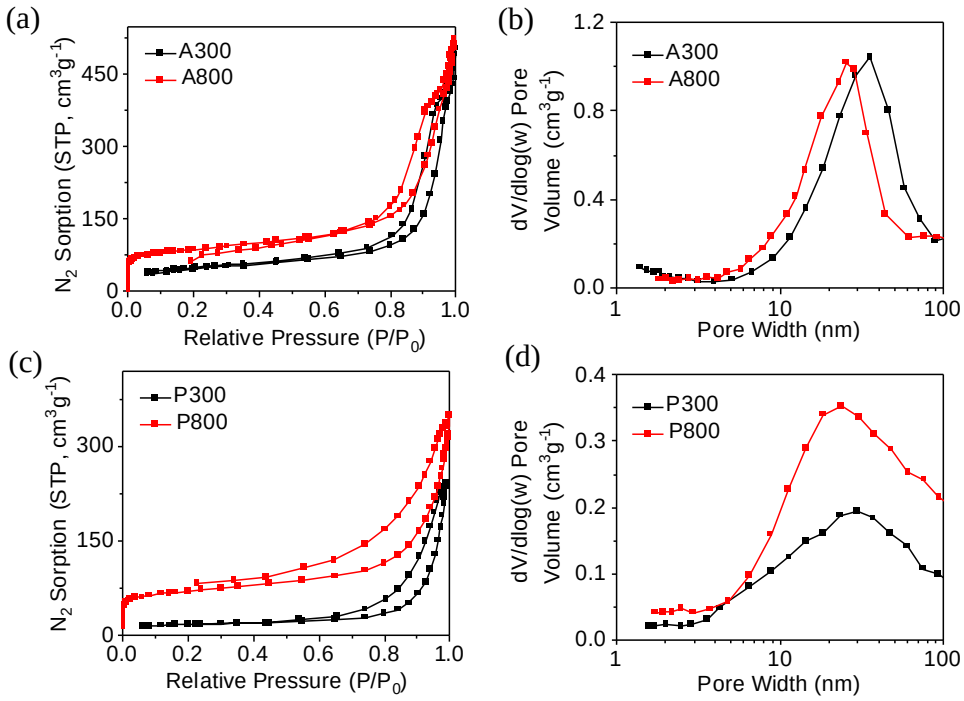

Figure 2.3 N_2 adsorption and desorption isotherms (a,c) and BJH pore size distribution plots in the mesoporous region (b,d) of Algibons and Pecbons.

2.1.3 Summary

The freeze-drying method combined with pyrolysis carbonisation is a promising way to prepare Starbons® with diverse textural properties and on a scale that can provide sufficient material for subsequent activation studies. The carbonisation temperature plays a crucial role in determining the porosity of the materials. In addition, materials derived from different biomass sources have different textural properties. Compared to Starbons®, Algibons and Pecbons have larger mesopore volumes and mesoporosities. The high mesoporosity (above 56%) and limited microporosity of all the materials (Starbons®, Algibons and Pecbons) is indicative of their predominantly mesoporous nature.

2.2 Preparation and Characterisation of KOH Activated Starbons®

2.2.1 Introduction

Given the widespread use of the potassium hydroxide activation process in engineering the microporosity of materials, potassium hydroxide activation was employed first in this study according to the processes illustrated in **Figure 2.4**. The activation precursors applied in this study are S300, A300 and P300, because they are considered to have relatively stable porous structures but retain oxygen-containing functionalities. The existence of oxygen-containing functional groups in the carbon materials is conducive to enhancing the etching behaviour of potassium hydroxide by inducing local charge redistributions and improving the binding affinity between the activators and the carbon atoms.[308]

The activation parameters are key variables which regulate the textural properties of materials. Therefore, various activation parameters such as: activation temperature (600~1000 °C) and amount of activating reagent (mass ratio of Starbon®: potassium hydroxide of 1:1~1:5) were investigated to maximise the textural properties of Starbon®. In addition, the effect of the precursors (S300, A300 and P300) on the pore structure of activated Starbons® are also described, allowing a new type of Starbons® to be prepared with high diversification in textural properties.

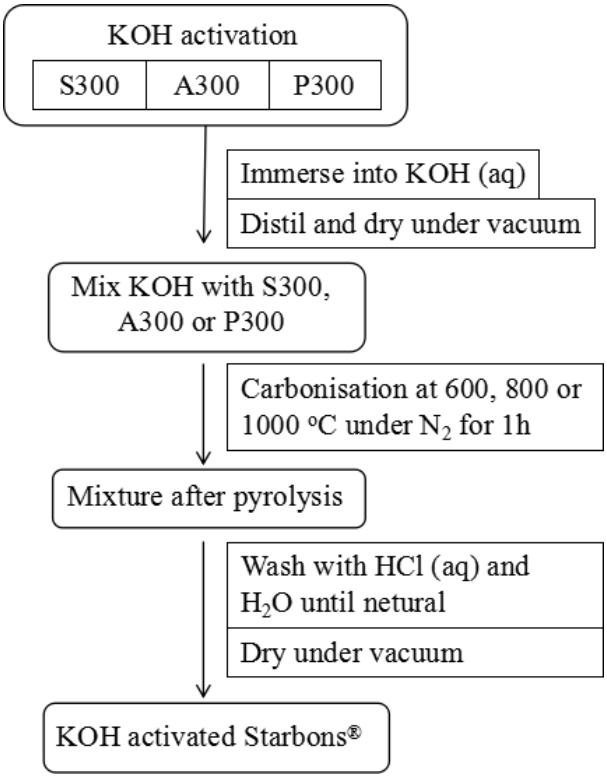

Figure 2.4 Schematic illustration of the KOH activation steps for synthesis of KOH activated Starbon® materials.

All samples prepared after potassium hydroxide activation are denoted as SxKy, AxKy or PxKy, where S, A, P represent the activation precursor: S300, A300 or P300, respectively; K represents potassium hydroxide activation; x represents the activation temperature (600, 800 or 1000 °C) and y represents the mass ratio of potassium hydroxide to precursor (1, 2, 3, 4 or 5). For example, S800K4 indicates that S300 was activated at 800 °C using a 4:1 mass ratio of potassium hydroxide to S300. The yield of product (including S800, A800 and P800) in **Section 2.2** was obtained by dividing the mass of the product by the mass of the precursor (e.g. S300, A300 or P300).

2.2.2 Results and Discussion

2.2.2.1 Textural properties of KOH activated Starbons®

2.2.2.1.1 Comparison of KOH activated Starbons® prepared at different temperatures

Activation temperature is one of the most important parameters that affects the properties of the products. Therefore, the effect of temperature on activation of Starbons® in terms of engineering their textural properties was firstly investigated. The activation was conducted by pyrolyzing S300 with potassium hydroxide using a mass ratio of 1:4 at 600, 800 and 1000 °C. The textural properties of the resulting samples were investigated by measuring nitrogen adsorption-desorption isotherms at 77 K and are detailed in **Table 2.4**. All the materials were derived from one batch of S300 and yields of samples are shown in Table 2.4.

Table 2.4 Textural properties of KOH activated Starbon® materials prepared at different temperatures.

Material	S_{BET} (m^2g^{-1})	V_{micro} ($V_{ultramicro}$) (cm^3g^{-1}) HK	V_{meso} (cm^3g^{-1}) BJH	V_{total} (cm^3g^{-1}) P/P_0=0.99	Percentage of micro (ultramicro) (%)	Yield (%)
S800	507	0.20 (0.14)	0.36	0.55	36.4 (25.5)	60.5
S600K4	1890	0.73 (0.50)	0.13	0.84	86.9 (59.5)	39.0
S800K4	2299	0.91 (0.46)	0.07	0.98	92.9 (46.9)	28.4
S1000K4	1503	0.62 (0.28)	0.23	0.84	73.8 (33.3)	17.1

The potassium hydroxide activation process is very effective in producing micropores. S600K4, S800K4 and S1000K4 show significantly increased BET surface area and micropore volume compared to the nonactivated S600, S800 and S1000 as shown in **Table 2.4** and **Table 2.1**. Mesopores were degraded probably due to the burning off of interconnected carbon walls among mesopores leading to the enlargement of mesopores to

macropores. A higher activation temperature results in a lower yield of product due to a higher degree of burning off, which leads to greater development of micropores in S600K4 and S800K4. S800K4 was found to be the sample with the highest BET surface area (2299 $m^2 g^{-1}$), micropore volume (0.91 $cm^3 g^{-1}$) and total pore volume (0.98 $cm^3 g^{-1}$). Compared to S800K4, the higher activation temperature of 1000 °C results in the formation of S1000K4 with the lowest product yield and an inferior development of ultramicro- and micropores, but a better development of mesopores since the over burn off leads to the expansion of small pores. Nitrogen adsorption on S800 results in a type IV isotherm (**Figure 2.5a**), indicative of predominant mesoporosity with limited microporosity. The isotherm of S800K4 is type I, due to its dominant microporous structure, whereas S600K4 and S1000K4 exhibit a combination of type I and type IV isotherms because of the coexistence of micropores and mesopores. S800 exhibits an obvious mesopore size distribution as shown in **Figure 2.5c**.

The more intense and broader peak within the micropore range of activated Starbons® in **Figure 2.5b** demonstrates the development of microporosity in these activated materials. In contrast, the weakened peaks in the (8-100) nm region of S600K4, S800K4 and S1000K4 in **Figure 2.5c** reveal the reduction of large mesopores in their structures. In addition, **Figure 2.5c** shows that smaller mesopores with pore sizes in the range of (2-8) nm were developed after KOH activation compared to non-activated S800.

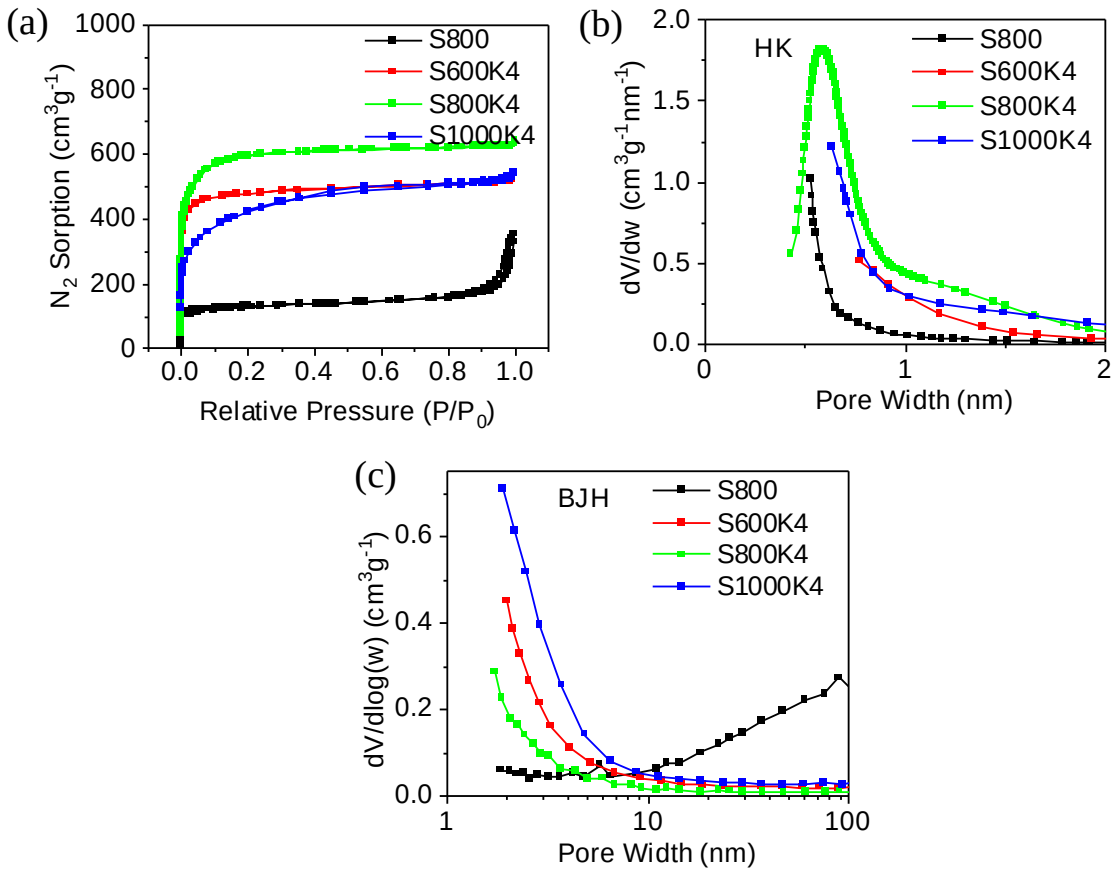

Figure 2.5 (a) N_2 adsorption isotherms at 77 K, (b) pore size distributions in the micropore region determined by HK method and (c) pore size distributions in the mesopore region determined by BJH method of S800 and KOH activated Starbons®.

Density functional theories (DFTs) are widely accepted in describing pore sizes across the whole pore size range. Therefore, for comparison, a DFT method assuming a slit pore model and a non-local DFT method (NLDFT) assuming a non-homogeneous fluid at a solid interface in a slit pore model were also applied for the characterisation of the pore volume in the potassium hydroxide activated Starbons®. The comparison of t-plot, HK, DFT and NLDFT models of analysing the micropore volumes; BJH, DFT and NLDFT models of analysing the mesopore volumes and HK (P/P_0=0.99), DFT and NLDFT models of analysing the total pore volumes is presented in **Table (7.1-7.3)** and **Figure (7.1-7.3)** in **Appendix 7.1**. The various models were found to give consistent results and to show the same trend from

sample to sample.

2.2.2.1.2 Comparison of KOH activated Starbons® prepared at different mass ratios of S300 to KOH

The investigation of activation temperature showed that a temperature of 800 °C optimises the textural properties of the resultant materials with highest surface area and microporosity. Therefore, the effect of amount of activator on the textural properties of Starbons® was further investigated at 800 °C. All the precursor S300s (from one batch) were activated at 800 °C, whilst the mass ratio of S300 to potassium hydroxide was varied from 1:1 to 1:5. Two batches of S800K2, S800K3 and S800K4 were prepared separately to study the reproducibility in textural properties of potassium hydroxide activated Starbons®. The repeated samples were named as S800K2R, S800K3R and S800K4R.

The textural properties and yields of samples are shown in **Table 2.5**, the yield of sample inversely correlates to its total porosity. The variation of porosity and yield across the two batches of S800K2, S800K3 and S800K4 is not significant. The specific surface area, micropore volume and microporosity increased as the amount of activating agent increased. The mesoporous Starbon® (type IV isotherm) was converted into a hierarchical (a combination of type I and IV isotherm) or a microporous Starbon® (type I isotherm) by creating additional micropores and degrading some mesopores in the structure (**Figure 2.6**). Activation of S300 with an equivalent amount of potassium hydroxide results in the formation of a hierarchical structure in S800K1. A plateau at low relative pressures of $P/P_0<0.15$ and a pronounced hysteresis at higher relative pressures of $P/P_0>0.45$ are observed in the isotherm (a combination of type I and IV in **Figure 2.6a**), indicating that both the micropores and the mesopores were well developed. Due to its well-developed total porosity, the yield of the S800K1 is relatively low compared to S800K2 and S800K3.

Table 2.5 Textural properties of S800 and KOH activated Starbons® prepared with S300 to KOH mass ratios of 1:1 to 1:5.

Material	S_{BET} (m^2g^{-1})	V_{micro} ($V_{ultramicro}$) (cm^3g^{-1}) HK	V_{meso} (cm^3g^{-1}) BJH	V_{total} (cm^3g^{-1}) P/P_0=0.99	Percentage of micro (ultramicro) (%)	Yield (%)
S800	507	0.20 (0.14)	0.36	0.55	36.4 (25.5)	60.5
S800K1	1214	0.48 (0.32)	0.58	1.06	45.3 (30.2)	26.5
S800K2	1294	0.49 (0.39)	0.10	0.59	83.1 (66.1)	43.2
S800K3	1633	0.62 (0.45)	0.14	0.77	80.5 (58.4)	49.8
S800K4	2299	0.91 (0.46)	0.07	0.98	92.9 (46.9)	28.4
S800K5	2452	1.00 (0.57)	0.09	1.09	91.7 (52.3)	25.2
S800K2R	1281	0.49 (0.37)	0.16	0.65	75.4 (56.9)	43.8
S800K3R	1676	0.64 (0.48)	0.14	0.78	82.1 (61.5)	43.2
S800K4R	2101	0.84 (0.44)	0.04	0.88	95.5 (50.0)	33.1

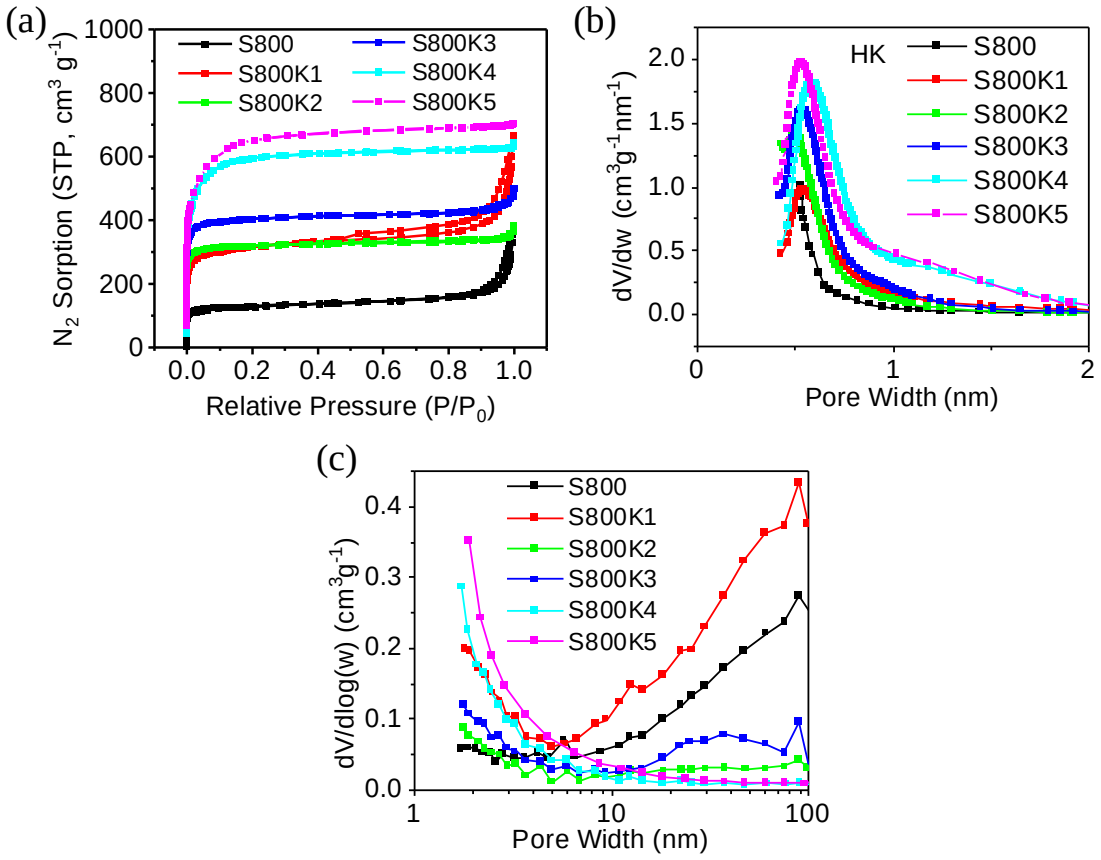

Figure 2.6 (a) N_2 adsorption isotherms at 77 K, (b) pore size distributions in the micropore region determined by the HK method and (c) pore size distributions in the mesopore region determined by the BJH method of S800 and KOH activated Starbons®.

More micropores were created by applying more potassium hydroxide in the activation, which is visualised as intensified plateaus at low relative pressure in the nitrogen adsorption isotherms (**Figure 2.6a**) and obvious pore size distributions in the micropore region (**Figure 2.6b**). As a result, S800K4 and S800K5 became typical microporous materials with a few mesopores preserved in the structures. S800K5 has the highest ultramicropore volume of 0.57 $cm^3\ g^{-1}$, micropore volume of 1.00 $cm^3\ g^{-1}$, total pore volume of 1.09 $cm^3\ g^{-1}$ and specific surface area of 2452 $m^2\ g^{-1}$ (**Table 2.5**) and its highest porosity correlates to its lowest yield.

Both ultramicropores (pore sizes less than 0.7 nm) and supermicropores (pore sizes of 0.7~2.0 nm) were simultaneously developed for the potassium hydroxide activated Starbons® (**Table 2.5** and **Figure 2.6b**). However, the increase in supermicropores is higher than that of ultramicropores for highly activated Starbons® (S800(K2~K5)). Particularly notable is S800K2 which exhibits the highest ultramicroporosity of 66.1% (**Table 2.5**) and its pore size distribution in the ultramicropore region is clearly enhanced (**Figure 2.6b**). The pore size distributions in the micropore region were broadened as the amount of potassium hydroxide used increased. In addition, some smaller mesopores were also developed by potassium hydroxide activation as demonstrated by the intensified mesopore size distributions in the region of 2-8 nm in **Figure 2.6c**. In contrast, the weakened peak in the 8-100 nm region of S800(K2~K5) reveals the reduction of the number of large mesopores (8-100 nm) in their structures. Comparison of the various models for analysing these micropore, mesopore and total pore volumes of the samples is also presented in **Table 7.1-7.3** and **Figure 7.1-7.3** in **Appendix 7.1**. Consistent results and the same trend are observed from sample to sample.

2.2.2.2 Textural properties of KOH activated Algibons and Pecbons

The effects of temperature, amount of activator and activation precursor (A300 or P300) on the pore structure of the activated Algibons and Pecbons are described in this section. The

activation was conducted by 92yrolyzing the precursor with potassium hydroxide in a mass ratio of 1:1~ 1:5 at 600, 800 or 1000 °C for 1 hour under pure nitrogen.

2.2.2.2.1 Comparison of KOH activated Algibons prepared at different temperatures

Consistent with the results of potassium hydroxide activated Starbons®, A600K2, A800K2 and A1000K2 show significantly increased BET surface area and microporosity compared to the non-activated A600, A800 and A1000 as shown in Table 2.6. Activating A300 at 800 °C leads to A800K2 with the highest BET surface area of 1392 $m^2\ g^{-1}$, ultramicropore volume of 0.43 $cm^3\ g^{-1}$ and micropore volume of 0.53 $cm^3\ g^{-1}$. Compared to A800K2, the higher activation temperature of 1000 °C results in better development of mesoporosity, but an inferior development of ultramicro- and micropores.

Table 2.6 Textural properties of A800 and KOH activated Algibons prepared at different temperatures.

Material	S_{BET} (m^2g^{-1})	V_{micro} ($V_{ultramicro}$) (cm^3g^{-1}) HK	$V_{mesopore}$ (cm^3g^{-1}) BJH	V_{total} (cm^3g^{-1}) P/P_0=0.99	Percentage of micro (ultramicro) (%)	Yield (%)
A800	322	0.13 (0.08)	0.71	0.81	16.0 (9.9)	59.9
A600K2	687	0.27 (0.22)	0.08	0.36	75.0 (61.1)	37.9
A800K2	1392	0.53 (0.43)	0.15	0.67	79.1 (64.2)	37.2
A1000K2	1233	0.49 (0.33)	0.30	0.80	61.3 (41.3)	31.9

A800 exhibits a distinct mesoporous distribution as shown in **Figure 2.7b,c**, whereas pores of the potassium hydroxide activated Algibons are mainly distributed in micropore region. The variation of sample yield with increase of activation temperature for activated Algibons is the same as that of activated Starbons. A higher degree of burning off at a higher activation temperature results in a higher total porosity. In particular, A800K4 shows a greater developed microporosity but A1000K4 shows further developed mesoporosity.

Because of their dominant microporous structure, A600K2 and A800K2 exhibit a predominantly type I isotherm as shown in **Figure 2.7a**. A1000K2 exhibits a more obvious combination of type I and type IV isotherms due to the distinct coexistence of micropores and mesopores. The pore volumes in each region determined by various other models show the same trend as shown in **Table 7.1-7.3** and **Figure 7.1-7.3** in **Appendix 7.1**.

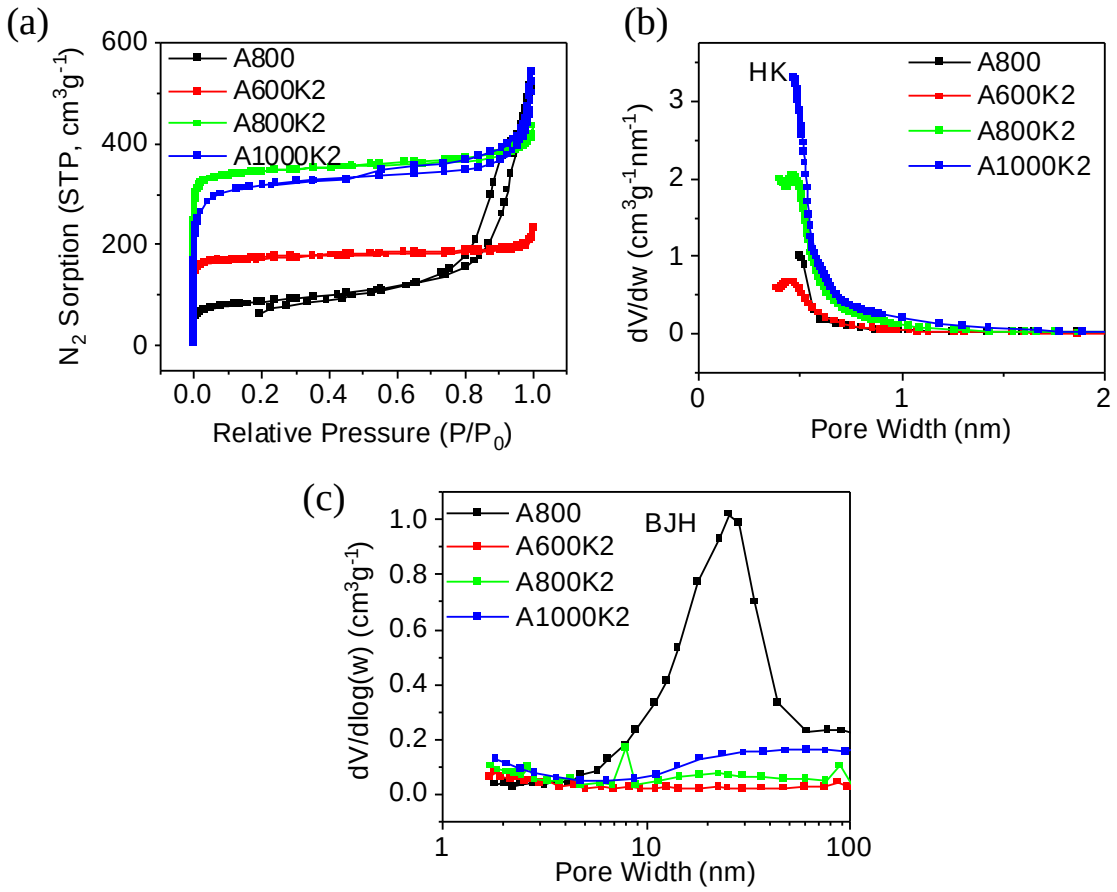

Figure 2.7 (a) N_2 adsorption isotherms at 77 K, (b) pore size distributions in the micropore region determined by the HK method and (c) pore size distributions in the mesopore region determined by the BJH method of A800 and KOH activated Algibons.

2.2.2.2.2 Comparison of KOH activated Algibons and Pecbons prepared at different mass ratios of A300 or P300 to KOH

The effect of activation temperature on the engineering of materials has been revealed

by investigation of both Starbons® and Algibons. An activation temperature of 800 °C has been demonstrated to be most capable of producing hierarchical materials by conserving mesoporous structures whilst extensively enhancing the microporosity. Therefore, the effect of the amount of activator on the activation of Algibons and Pecbons was investigated by activating the precursor A300 or P300 to 800 °C, whilst varying the mass ratio of A300 or P300 to KOH from 1:1 to 1:5.

Table 2.7 Textural properties of A800, P800 and KOH activated Algibons and Pecbons.

Material	S_{BET} (m^2g^{-1})	V_{micro} ($V_{ultramicro}$) (cm^3g^{-1}) HK	V_{meso} (cm^3g^{-1}) BJH	V_{total} (cm^3g^{-1}) P/P_0=0.99	Percentage of micro (ultramicro) (%)	Yield (%)
A800	322	0.13 (0.08)	0.71	0.81	16.0 (9.9)	59.9
A800K1	1117	0.46 (0.29)	0.82	1.31	35.1 (22.1)	27.0
A800K2	1392	0.53 (0.43)	0.16	0.67	79.1 (64.2)	37.2
A800K3	1952	0.75 (0.57)	0.09	0.85	88.2 (67.1)	32.5
A800K4	2419	0.95 (0.39)	0.18	1.15	82.6 (33.9)	26.2
A800K5	2414	1.01 (0.55)	0.10	1.09	92.7 (50.5)	14.4
P800	262	0.11 (0.07)	0.43	0.54	20.4 (13.0)	67.7
P800K2	1895	0.77 (0.52)	0.18	0.97	79.4 (53.6)	34.4
P800K3	1747	0.73 (0.47)	0.13	0.86	84.9 (54.7)	22.7
P800K5	1954	0.82 (0.43)	0.20	1.02	80.4 (42.2)	11.9

As shown in **Table 2.7 and Figure 2.8**, although deriving from different precursors (S300, A300 and P300), Starbons®, Algibons and Pecbons activated by potassium hydroxide show the same variation of porosity. Mild activation conditions with moderate amounts of potassium hydroxide (K2 and K3) leads to higher yields of products with lower porosities. In contrast, high total porosities in K1 materials due to high volumes of both micro and mesopores and in K5 materials due to high volumes of micropores result in their low yields. Similarly to Starbons®, the mesoporous Algibon and Pecbon were converted into hierarchical

(A800K1~K4, P800K2 and P800K3) or microporous material (A/P800K5) by potassium hydroxide activation, showing an intensified pore size distribution in the micropore region. The surface area of potassium hydroxide activated Algibons and Pecbons are increased significantly due to the well-developed microporosity in the structure.

An equivalent amount of potassium hydroxide to precursor results in the development of both micropores and mesopores in A800K1, leading to the formation of hierarchical structure. More potassium hydroxide (1:2~1:5 mass ratio) results in the development of additional microporosity and surface area, but a few mesopores are preserved in the resultant sample. Their mesopore volumes are even less than that of A300 and P300 precursors, which is possibly due to the burning off of interconnected carbon walls among mesopores during activation leading to the fragmentation of the intrinsic mesopores. As a result, by extensively developing micropores and preserving only a few mesopores, A/P800K5 is a typical microporous material. In addition, the highest ultramicroporosity is created when three mass equivalents of potassium hydroxide were applied in the activation. Further reaction of potassium hydroxide with carbon results in the enlargement of ultramicropores into supermicropores for highly activated A/P800K5.

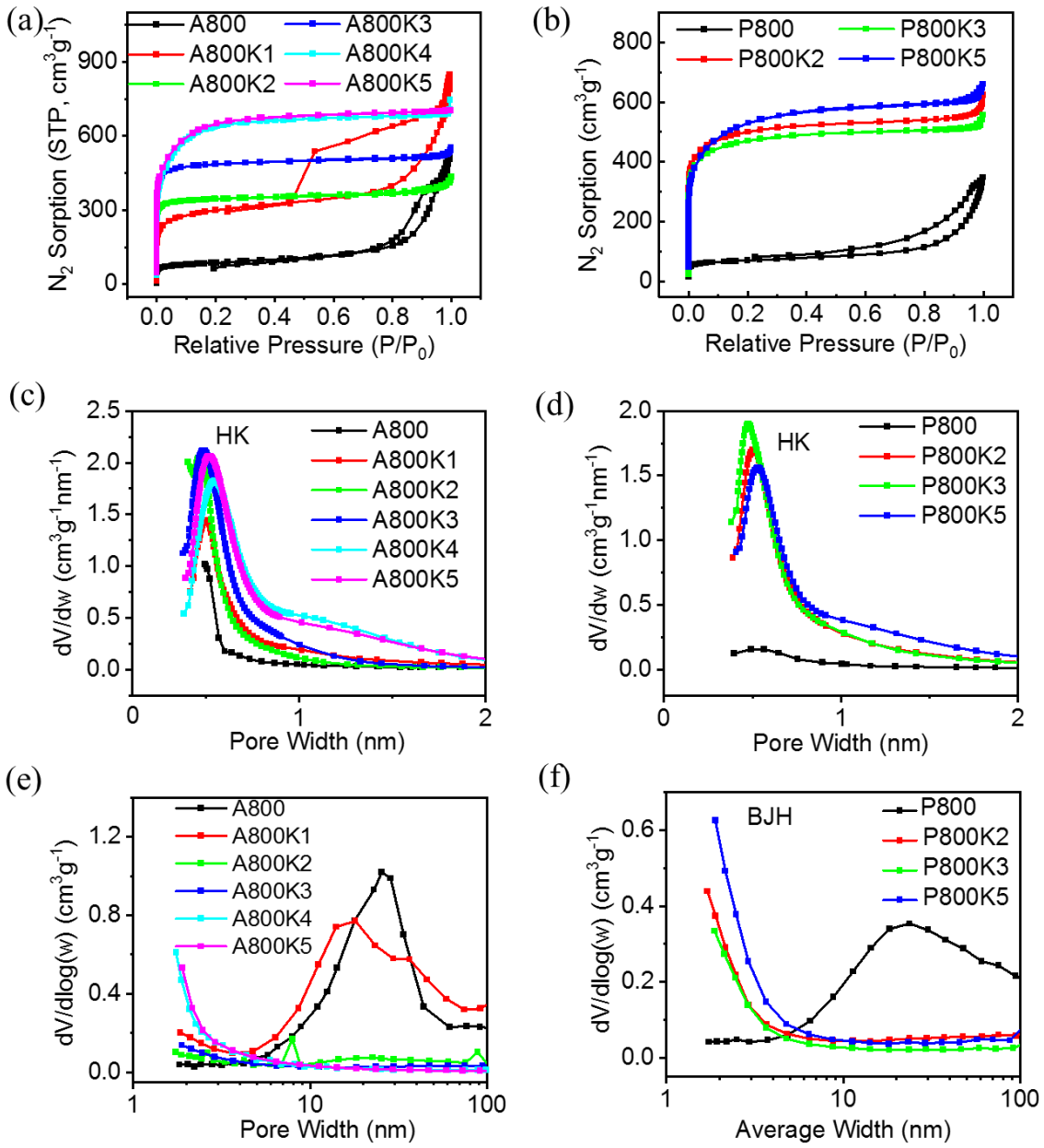

Figure 2.8 (a-b) N_2 adsorption isotherms at 77 K; (c-d) pore size distributions in the micropore region determined by the HK method and (e-f) pore size distributions in the mesopore region determined by the BJH method.

As with Starbons®, the more intense and broader peak within the micropore region of the activated Algibons and Pecbons suggests the presence of more ultramicro and micropores, and on the contrary, the smaller peak in the mesopore region of the highly activated Algibons and Pecbons reveals the reduction of mesopore content in these materials. Consistent results

and the same trend from sample to sample are observed by using other models to analyse the pore volumes as presented in **Table 7.1-7.3** and **Figure 7.1-7.3** in **Appendix 7.1**.

2.2.2.3 SEM and TEM characterisation

The surface morphology and porous structure evolution arising from potassium hydroxide activation of Starbon®, Algibon and Pecbon were revealed via SEM and TEM.

2.2.2.3.1 Starbons®

The SEM images and particle size distributions shown in **Figure 2.9** reveal that smaller particles were consumed, and bigger particles became dominant as a result of the activation. Activation of S300 with potassium hydroxide results in a larger average particle size of S800K1–5 (23-40 μm) than seen in S800 (14 μm). S800 exhibits a net structure with irregular cavities and edges. A large number of mesopores and macropores are non-uniformly distributed both on the rough surface and the slit-shaped interior. The pores appear to have disordered slit-shapes in good agreement with the H3-type adsorption isotherm observed by porosimetry. In contrast, materials prepared after activation all exhibit significant cylindrical macropores. The formation of pores with diameters of 20 nm~10 um was a result of the drastic activation. For highly activated samples, mesopores were observed to be degraded so that enlarged pores became dominant and the interconnected carbon walls were partly burnt out resulting in the formation of flakes associated with large pores.

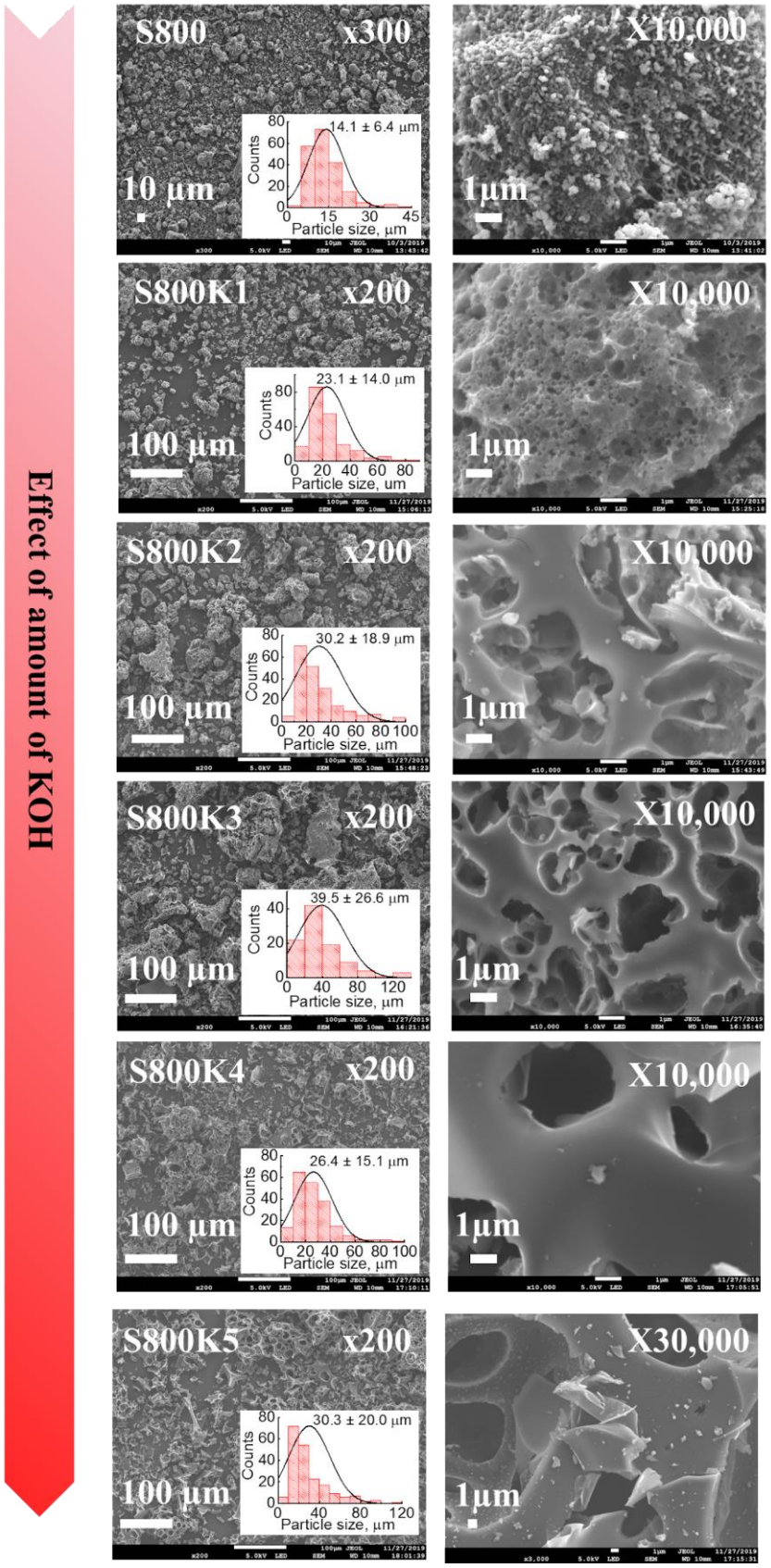

Figure 2.9 SEM images and the related particle size distributions of S800 and KOH activated Starbons®.

There is no doubt that micropores must be predominantly generated during the potassium hydroxide activation process. However, micropores cannot be observed by SEM due to its limited resolution. Therefore, TEM images (**Figure 2.10**) were obtained to provide additional information about the potassium hydroxide activation process. In **Figure 2.10** a network formed by the interlaced aggregation of the corrugated branches is observed for non-activated S800. The slit shaped mesopores are distinctly distributed in the structure. In comparison, the consumption of carbon during activation results in the development of micropores, degeneration of mesopores, corrosion of bulk structure and formation of a flimsy structure. Therefore, S800K2 shows a corroded bulk with circular voids in the structure. A larger quantity of micropores can be observed for S800K2, however, the mesopores were degraded by activation.

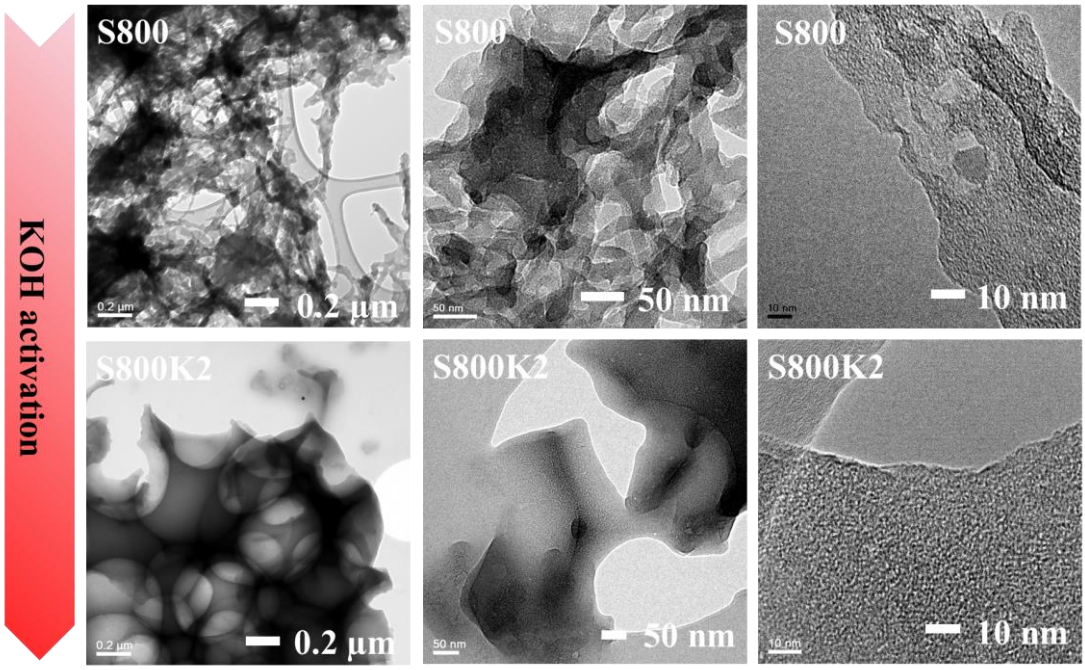

Figure 2.10 TEM images of S800 and S800K2 at different magnifications.

2.2.2.3.2 Algibons and Pecbons

The SEM images and particle size distributions of materials in **Figure 2.11** reveal that the average particle size of A800 (50 µm) is larger than that of S800 (14 µm, **Figure 2.9**) and

P800 (16 μm). Also in contrast to the particle morphology of S800 which was dominated by spheres, more particles of A800 exhibit amorphous structures and most P800 particles exhibit platelet morphology.

At the lowest temperature (600 °C), only the smallest particles are degraded during the activation, resulting in the average particle size of A600K2 (99 μm) being almost double that of A800 (50 μm). At 800 °C, the larger particles also undergo significant fragmentation and degradation to give A800K2-5 with a small average particle size (12-34 μm). Activation using small amounts of potassium hydroxide also gives material A800K1 with a larger average particle size (72 μm) than A800, due to selective destruction of the smallest particles during the activation. Finally, at 1,000 °C, the conditions are so harsh that small particles are completely eaten away almost as soon as they form, leaving only larger particles and resulting in the formation of A1000K2 with a larger average particle size (79 μm) than A800. However, activation of P300 with potassium hydroxide results in the formation of P800K2, P800K3 and P800K5 with the same average particle size (15-20 μm) as P800 (16 μm). This indicates that the thin, flat plate-like particles present in Pecbons are all attacked by potassium hydroxide at the same rate. Mesopores and macropores are non-uniformly distributed on the rough surface and interior of A800 and P800. Compared to A800 and P800, cylindrical macropores were additionally generated and further enlarged in potassium hydroxide activated Algibons and Pecbons. As a result, most mesopores were degraded and macropores became dominant for highly activated materials. The partial burning out of the interconnected carbon framework leads to the aggregation of flakes. Changing the activation temperature has a similar effect to varying the amount of activator, whereby, more macropores are developed under more severe activation conditions.

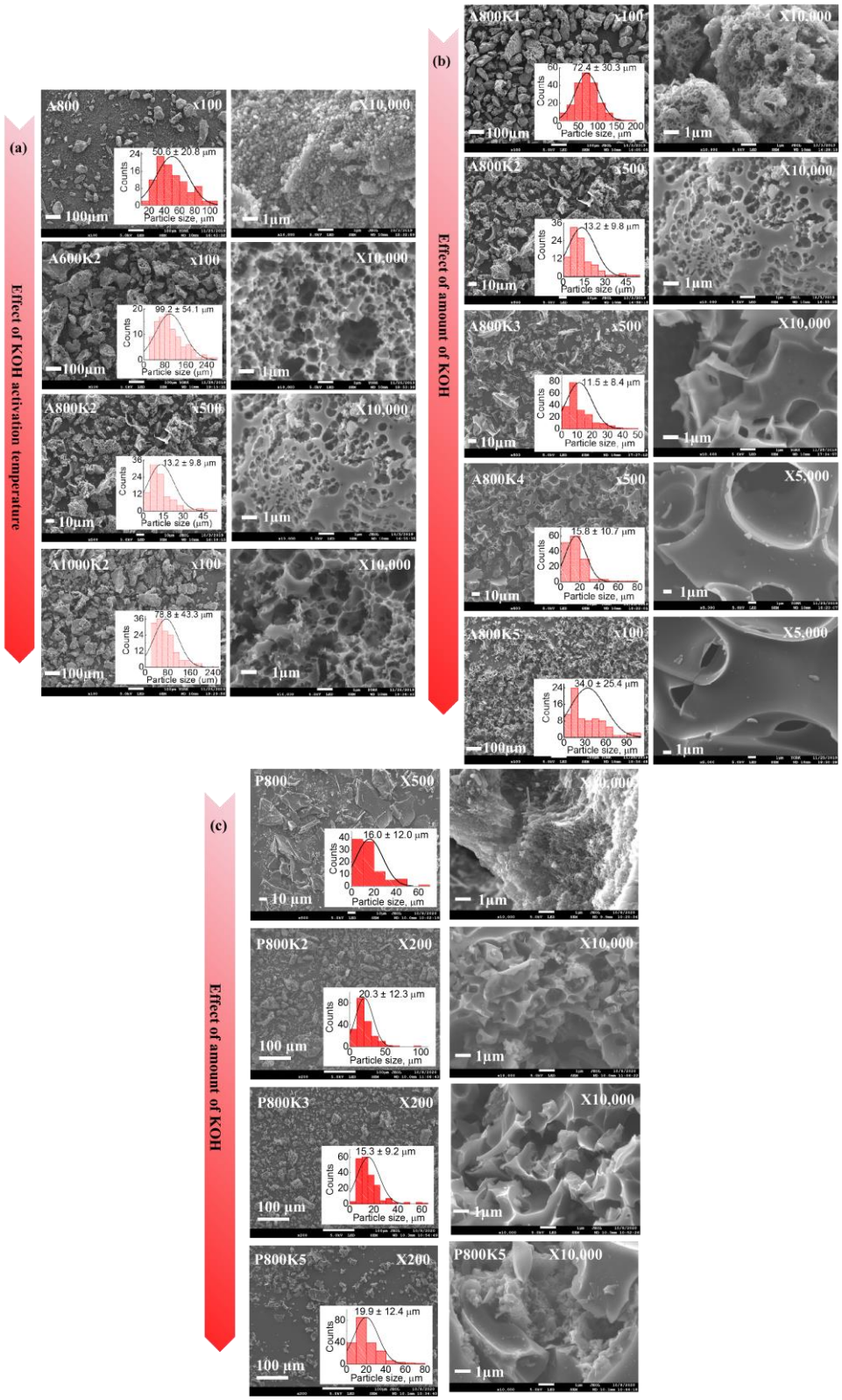

Figure 2.11 SEM images and related particle size distributions of (a) A800 and KOH activated Algibons prepared at different temperatures (b) KOH activated Algibons prepared at different mass ratios of A300 to KOH and (c) P800 and KOH activated Pecbons prepared at different mass ratios of P300 to KOH.

TEM images (**Figure 2.12**) were obtained to provide additional information about the potassium hydroxide activation of Algibons. In contrast to the amorphous network of S800 formed by corrugated branches, A800 has a more heterogeneous fibrous backbone. In addition, a corroded structure with circular voids and a porous structure with more micropores but less mesopores is again observed for the potassium hydroxide activated Algibons.

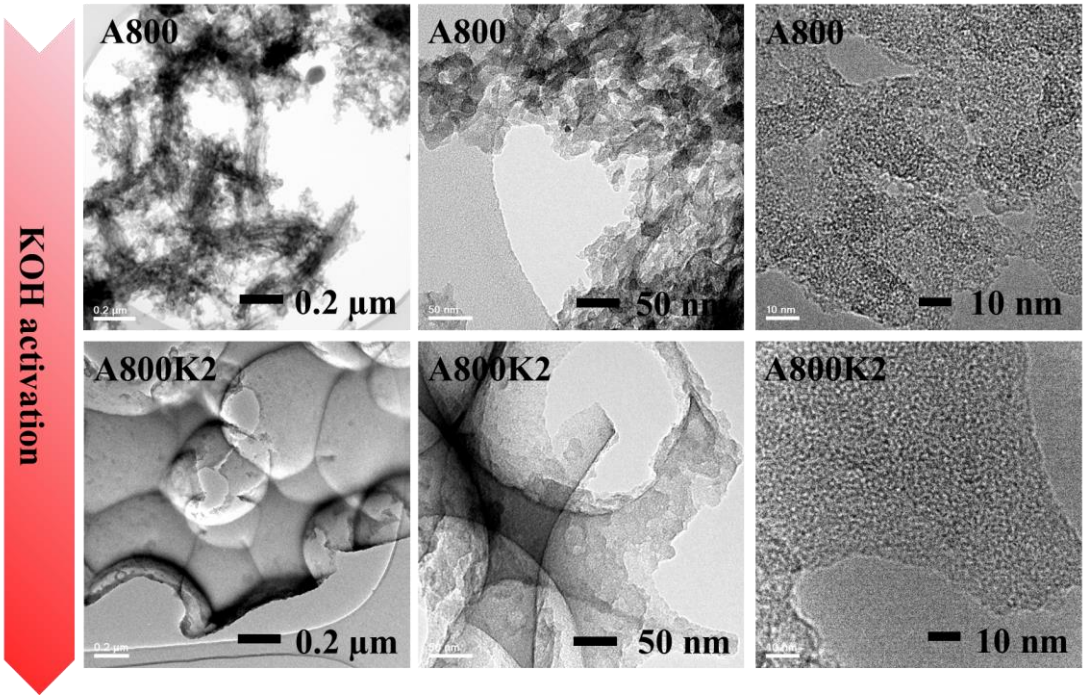

Figure 2.12 TEM images of A800 and A800K2 at different magnifications.

2.2.2.4 ICP-OES analysis

Any residual potassium salts intercalated in the carbon lattices of the potassium hydroxide activated materials may have an influence on the porosity and chemical properties of the materials and as a result on their absorption performance. Therefore, washing processes using hydrochloric acid and water were used after the carbonisation process to remove residual chemical agents. The composition of potassium (and other elements) in the nonactivated S800, A800, P800 and the potassium hydroxide activated Starbons®, Algibons

and Pecbons were determined by ICP-OES and are listed in **Table 2.8**.

There is negligible potassium content (0.007%) in the non-activated S800. The potassium contents in A800 (0.09%) and P800 (0.04%) are slightly higher than that of S800. In addition, A800 and P800 also contain significant calcium and sodium. The nonnegligible metallic contents in A800 and P800 come from their precursors of alginic acid and pectin which are originally extracted from brown seaweeds and citrus peels.

Table 2.8 Main metallic element and total trace element composition of nonactivated S800, A800, P800 and KOH activated Starbons®, Algibons and Pecbons.

Element (%)	K	Al	Ca	Fe	Mg	Na	Total
S800	0.0066	0.0046	0.1986	0.0134	0.0174	0.0695	0.70
A800	0.0861	0.0776	5.3668	0.1109	0.1398	0.5669	8.10
P800	0.0431	0.0184	0.2839	0.0451	0.0796	5.0110	6.72
S600K4	0.0117	0.0074	0.2727	0.0249	0.0215	0.0424	0.89
S1000K4	0.0306	0.0129	0.4657	0.0337	0.0324	0.0692	1.71
S800K1	0.0219	0.0007	0.0937	0.0096	0.0090	0.0195	0.23
S800K2	0.0202	0.0013	0.0977	0.0275	0.0091	0.0192	0.29
S800K3	0.0231	0.0005	0.1111	0.0066	0.0112	0.0255	0.31
S800K4	0.0367	0.0078	0.2191	0.0191	0.0181	0.0328	0.57
S800K5	0.0428	0.0034	0.1128	0.1352	0.0107	0.0258	0.49
A800K2	0.0393	0.0014	0.0337	0.1201	0.0011	0.0174	1.72
P800K2	0.0380	0.1316	0.0255	0.0246	0.0036	0.0240	1.76

The potassium content in the potassium hydroxide activated Starbons® after the washing processes is also unremarkable (0.01~0.04%), showing that the potassium hydroxide used for the activation process had been effectively removed from the activated Starbons®.

A800K2 had a lower potassium content (0.04%) than A800 and P800K2 had the same potassium content (0.04%) as P800. For both A800K2 and P800K2, the total trace element composition was much lower than that of A800 and P800, showing that the aqueous washes were effective in removing not only potassium residues but also other trace elements present.

2.2.2.5 CHN analysis

The elemental compositions of the obtained samples were also characterised by CHN analysis as presented in **Table 2.9**. Comparison of S300 and S800 shows that as the temperature at which the Starbon® material is prepared increases from 300 to 800 °C, the carbon content increases whilst the hydrogen and other content decrease due to the degradation of the polysaccharide in the carbonisation process (oxygen containing groups in the polysaccharide turning into polycyclic aromatic rings). S800 has significantly higher carbon content than either A800 or P800, partly due to the presence of significant amounts of metallic elements in A800 (8.1% in total and includes 5.4% calcium) and P800 (6.7% in total and includes 5.0% sodium) as determined by ICP-OES (**Table 2.8**). Subtraction of the ICP-OES total percentage from the combustion analysis rest percentage, suggests oxygen contents of 7.5, 11.0 and 20.1% for S800, A800 and P800 respectively. Therefore, A800 and P800 contain more oxygen than S800 due to the presence of carboxylic acid and/or methyl ester groups in precursors of alginic acid and pectin although most of them are thought to be removed during the carbonisation step.

Converting S300 into activated Starbons® S800K1–K5 gives materials which contain about 10% less carbon than non-activated S800 and conversely about 10% more other content. A800K2 and P800K2 also showed a reduction in their carbon content compared to A800 and P800 respectively, though in the case of P800K2 this reduction was only 3.5%. The decrease of carbon content and increase of other content are partly due to removal of carbon

atoms (as carbon monoxide and carbon dioxide) during the activation process with potassium hydroxide and partly due to the introduction of additional oxygen atoms during the activation.[309]

Table 2.9 Combustion analysis of nonactivated S800, A800, P800 and KOH activated Starbons®, Algibons and Pecbons.

Material	% C	% H	% Rest
S300	70.6	3.3	26.1
S800	91.6	0.2	8.2
S600K4	57.9	2.5	39.6
S1000K4	70.9	0.6	28.5
S800K1	80.3	0.6	19.1
S800K2	83.8	0.1	16.1
S800K3	74.2	0.5	25.4
S800K4	78.3	0	21.7
S800K5	83.5	0.3	16.3
A800	80.9	0	19.1
A800K2	70.0	0	30.0
P800	72.1	1.1	26.8
P800K2	68.6	0.5	30.9

2.2.2.6 XPS analysis

The chemical composition of S800, A800, P800 and potassium hydroxide activated S800K2, A800K2 and P800K2 were further analysed by XPS. The deconvolution of the high-resolution XPS spectra of C1s and O1s for the samples was conducted as shown in **Figure 2.13**, the deconvolution results and assignments are listed in **Table 7.5** and **Table 7.6**

in **Appendix 7.1**.

The C1s spectra were composed of seven components, which include carbon atoms in: polyaromatic structures ($C(sp^2)$); aliphatic structures ($C(sp^3)$); phenolic, alcohol or ether groups (C–O); carbonyl or quinone groups (C=O); carboxyl, lactone, or ester groups (O–C=O) and satellite peaks derived from **π**-**π*** transitions in aromatic rings. Three oxygen-containing functionalities can be identified by the deconvolution of the O1s spectra. The binding energies of ~531 eV, ~532eV and ~534 eV correspond to carbonyl groups; ether, phenol or hydroxyl groups; and carboxylic acid groups respectively.[310]

For S800K2 and A800K2, the XPS data in **Table 7.5** and **Table 7.6** in **Appendix 7.1** shows an increase in the total amount of surface oxygen present compared to the corresponding non-activated X800 material (5.2 to 13.5% for S800 to S800K2 and 9.3 to 14.4% for A800 to A800K2) with a corresponding reduction in surface carbon composition (94.8 to 86.3% for S800 to S800K2 and 87.4 to 84.8% for A800 to A800K2), but P800K2 contains less surface oxygen than P800 (8.8% versus 14.4%). The increase of the surface oxygen content of S800K2 and A800K2 is due to the potassium hydroxide activation and is consistent with the combustion analysis. Whereas, the lower surface oxygen content of P800K2 can be attributed to decarboxylation of acid and ester groups under the strongly basic and high temperature conditions as shown by the O-C=O component of the carbon 1s peak (3.3% in P800 versus 2.6% in P800K2). For all the samples, the oxygen content of the surface as determined by XPS was found to be lower than the bulk oxygen content determined by combustion analysis (the rest content minus the total trace element content), indicating that the interior of the materials is more oxygenated than the surface.

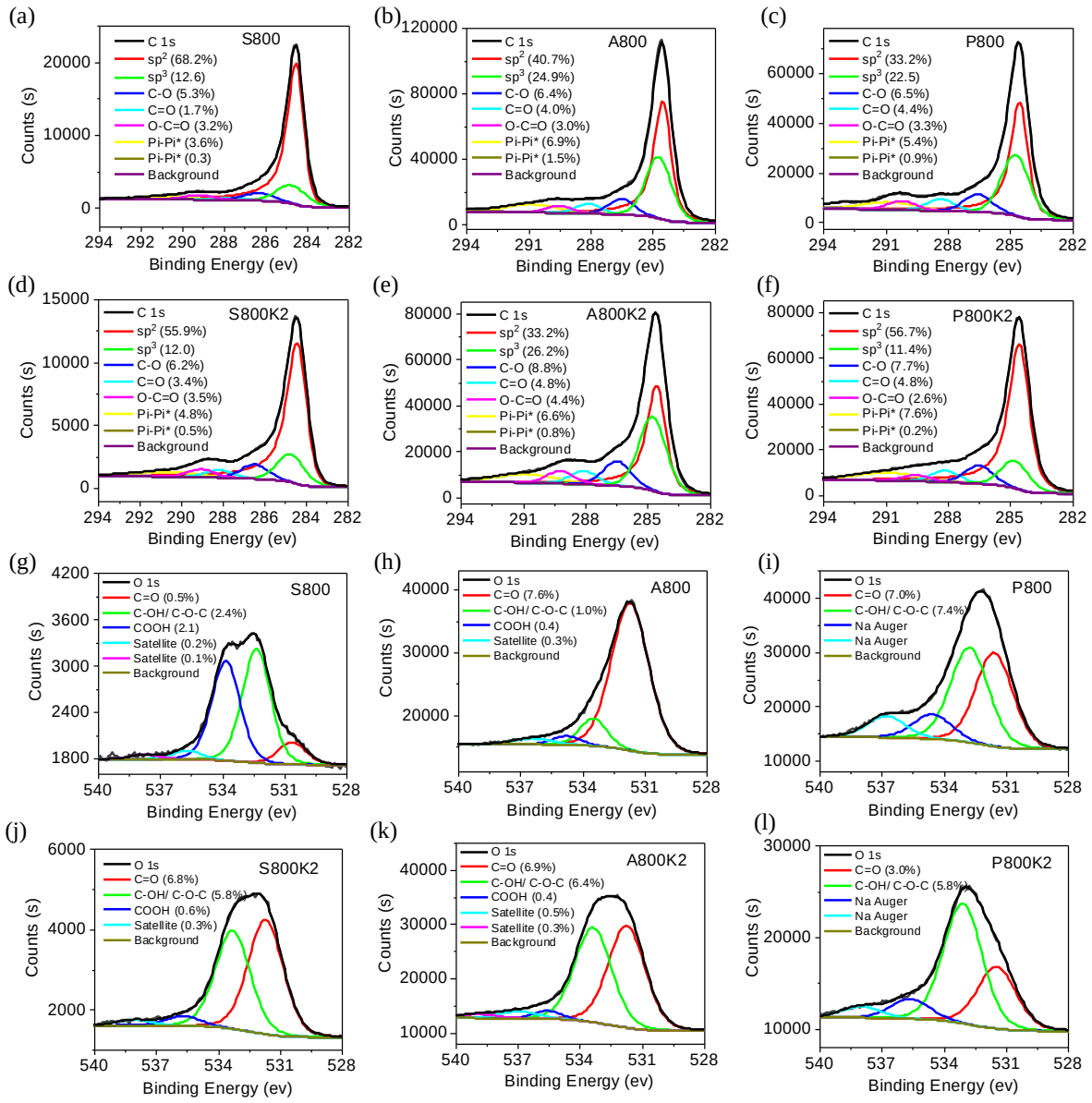

Figure 2.13 XPS spectra of C1s of (a-c) S800, A800 and P800 and (d-f) S800K2, A800K2 and P800K2; O1s of (g-i) S800, A800 and P800 and (j-l) S800K2, A800K2 and P800K2.

2.2.3 Summary

Potassium hydroxide activation has been demonstrated to be an effective and scalable method to synthesise and tailor microstructure within mesoporous Starbons®, Algibons and Pecbons, giving ultrahigh surface areas and high percentages of ultramicropores and micropores.

As the temperature at which the potassium hydroxide activation is conducted increases, the textural properties of the resultant material increase and then decrease, with the 800 °C carbonised material possessing the highest surface area, total pore volume and also the largest percentage of micropores. Use of less activator (precursor:potassium hydroxide=1:1) has been demonstrated to be capable of producing hierarchical materials by conserving the mesoporous structure whilst also increasing the ultramicro- and microporosity. Use of intermediate amounts of potassium hydroxide (precursor:potassium hydroxide=1:2 or 1:3) most extensively tunes the ultramicroporosity and gives rise to high surface areas. Use of more potassium hydroxide (precursor:potassium hydroxide=1:5) results in a typical microporous material with overwhelming microporosity and the highest surface area.

2.3 Preparation and Characterisation of CO_2 Activated Starbons®

2.3.1 Introduction

Chemical activation has some disadvantages such as requiring washing processes to remove the chemical agents and corrosion phenomenon cannot be avoided due to the utilisation of chemical agents. Compared to using potassium hydroxide for chemical activation, physical activation using carbon dioxide is a potentially cleaner process, producing activated materials containing no residuals which may affect the subsequent performance of the activated material in applications. It also has the ability to produce activated carbon with a high surface area, a broadened microporosity and a desirable degree of mesoporosity.

Carbon dioxide activation is commonly carried out in a two-step process consisting of pyrolysing the carbonaceous precursor at 400~900 °C under an inert atmosphere, followed by a further heat treatment at 700~1200 °C with controlled gasification in a stream of oxidising carbon dioxide. It is reported that the intrinsic porous structure of the precursors has a major impact on the reaction of carbon and carbon dioxide, by providing active sites for reaction and influencing the diffusion routes for the reactants and the generated volatile matter.[311] In addition, carbon dioxide gasification primarily takes place on the surface of mesopores because the density of active sites on the surface of mesopores is higher than that on the surface of micropores.[312]

Therefore, in this section, preformed non-activated S800, A800 and P800 which have stable mesoporous structures were activated by subjecting them to a flow of carbon dioxide in

a fixed bed reactor (within a thermogravimetric instrument) at 750~1000 °C within two hours to obtain activated samples. The reaction was monitored by measuring the concentration of carbon monoxide produced during activation using a FTIR gas cell. The effects of temperature and time of the activation on the porous structure of activated Starbons® were investigated, allowing activated Starbons® to be prepared with a high diversity of textural properties.

The samples prepared by carbon dioxide activation are denoted as SxCy, AxCy or PxCy, where C indicates carbon dioxide activation; x represents the activation temperature (750~1000 °C) and y represents the activation time (15~120 minutes). For example, S900C15 indicates that S800 was activated at 900 °C and the temperature was maintained at 900 °C for 15minutes. Yields of products in this section were obtained by dividing the mass of the product by the mass of the precursor (e.g. S800, A800 or P800).

2.3.2 Results and Discussion

2.3.2.1 CO_2 activated Starbons®

2.3.2.1.1 CO_2 activated Starbons® prepared at different temperature

Samples of S800 were separately heated from room temperature to 800, 850, 900, 950 and 1000 °C, with a heating rate of 10 °C min^{-1} and a carbon dioxide flow rate of 50 cm^3 min^{-1}. Then the temperature was kept constant for 15 minutes, followed by cooling down under nitrogen to study the effect of activation temperature. The yields of all the samples are presented in **Table 2.10.**

As shown in **Figure 2.14a**, by increasing the temperature from 800 °C to 1000 °C, the total burn-off weight% of the process increases from 15% to 66%. The change of mass can be divided into two stages: a slight and gradual decrease of weight (~10%) at temperatures

below 150 °C is attributed to the desorption of carbon dioxide and evaporation of water from the precursor. The consumption of carbon atoms by reaction with carbon dioxide occurs above 600 °C and is coupled with the expulsion of volatiles, giving rise to a significant mass loss. The rate of reaction with carbon dioxide and hence the release of volatile materials increased as the temperature increased. Therefore, there is an increase in the burn-off rate with an increase in temperature.

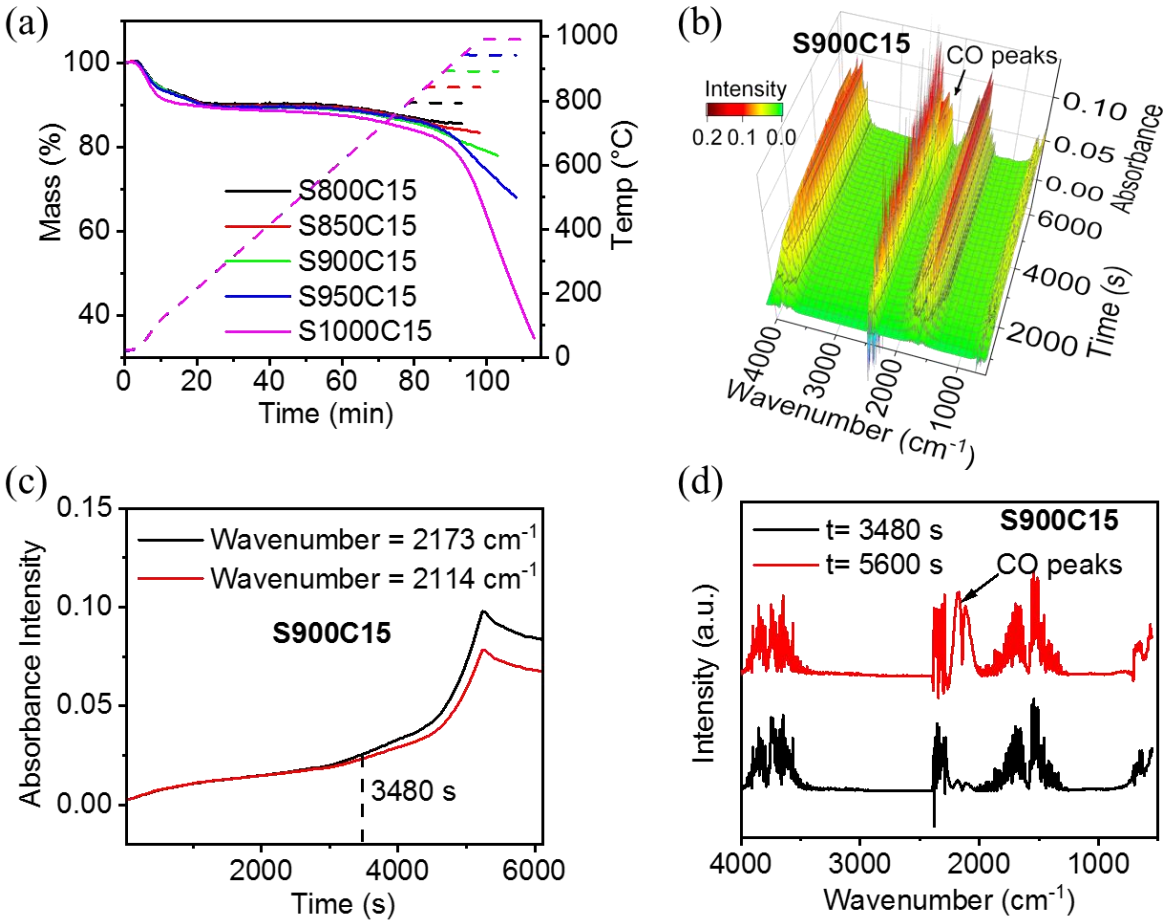

Figure 2.14 (a) TGA curves of activation time versus temperature and burn-off wt% for CO_2 activation of S800 as the temperature rises from 20 °C, (b) real-time FTIR spectra of the off-gases from the TGA experiment of preparing S900C15, (c) change of absorbance with time of FTIR spectra of CO and (d) specific FTIR spectra at 3480 s (black) and 5600s (red).

Real-time FTIR spectra during the synthesis of S900C15 were acquired to understand the carbon dioxide activation process as shown in **Figure 2.14b-d**. The peaks of carbon dioxide at 2350 cm^{-1} and 667 cm^{-1} can be seen during the entire experiment due to the utilisation of carbon dioxide. The peaks of water located in the range of 1500-1800 cm^{-1} and 3300-3800 cm^{-1} appear from 600 s (corresponding to 100 °C), because of the evaporation of water and dehydration of Starbon®. The double peak of carbon monoxide, which occurs at 2114 cm^{-1} and 2173 cm^{-1}, appears from around 3480 s (close to 600 °C), demonstrating that the reaction between the carbon material and carbon dioxide occurs once the temperature reaches 600 °C, which agrees well with the TGA curves**,** in which raising temperatures to 600 °C resulted in dramatic mass loss.

Table 2.10 Textural properties of S800 and the CO_2 activated Starbons® with different heat treatment temperatures.

Material	S_{BET} (m^2g^{-1})	V_{micro} ($V_{ultramicro}$) (cm^3g^{-1}) HK	V_{meso} (cm^3g^{-1}) BJH	V_{total} (cm^3g^{-1}) P/P_0=0.99	Percentage of micro (ultramicro) (%)	Yield (%)
S800	507	0.20 (0.14)	0.36	0.55	36.4 (25.5)	100
S800C15	529	0.21 (0.17)	0.37	0.58	36.2 (29.3)	85.3
S850C15	637	0.26 (0.20)	0.31	0.60	43.3 (33.3)	83.4
S900C15	983	0.39 (0.31)	0.38	0.77	50.6 (40.3)	77.5
S950C15	930	0.38 (0.28)	0.35	0.73	52.1 (38.4)	67.6
S1000C15	1535	0.62 (0.42)	0.52	1.16	53.4 (36.2)	34.1

The textural properties of the carbon dioxide activated Starbons® produced at different heat treatment temperatures were determined by measuring nitrogen adsorption-desorption isotherms at 77 K. The pore size distributions in the micro, meso and whole range were calculated using HK, BJH and DFT models from the adsorption branch of the isotherms. The textural properties of the materials are shown in **Table 2.10, Figure 2.15** and **Table 7.1-7.3** and **Figure 7.1-7.3** in **Appendix 7.1**. As shown in **Table 2.10**, after carbon dioxide activation, a hierarchical structure was developed by conserving the mesoporous structure whilst

extensively enhancing the ultramicro- and microporosity in the activated materials. The appearance of the isotherms as a combination of type I and type IV in **Figure 2.15a** and the distinct enhanced distribution in both micro- and mesopore regions in **Figure 2.15b,c** are indicative of the well-developed hierarchical structure of the carbon dioxide activated materials. Due to the existence of intrinsic pores in S800, carbon atoms can be removed from the interior of the material and the diffusion resistance of gas through the particles is small compared to the gasification resistance. These factors result in the creation of micropores, opening up of closed micropores and enlargement of micropores and mesopores.

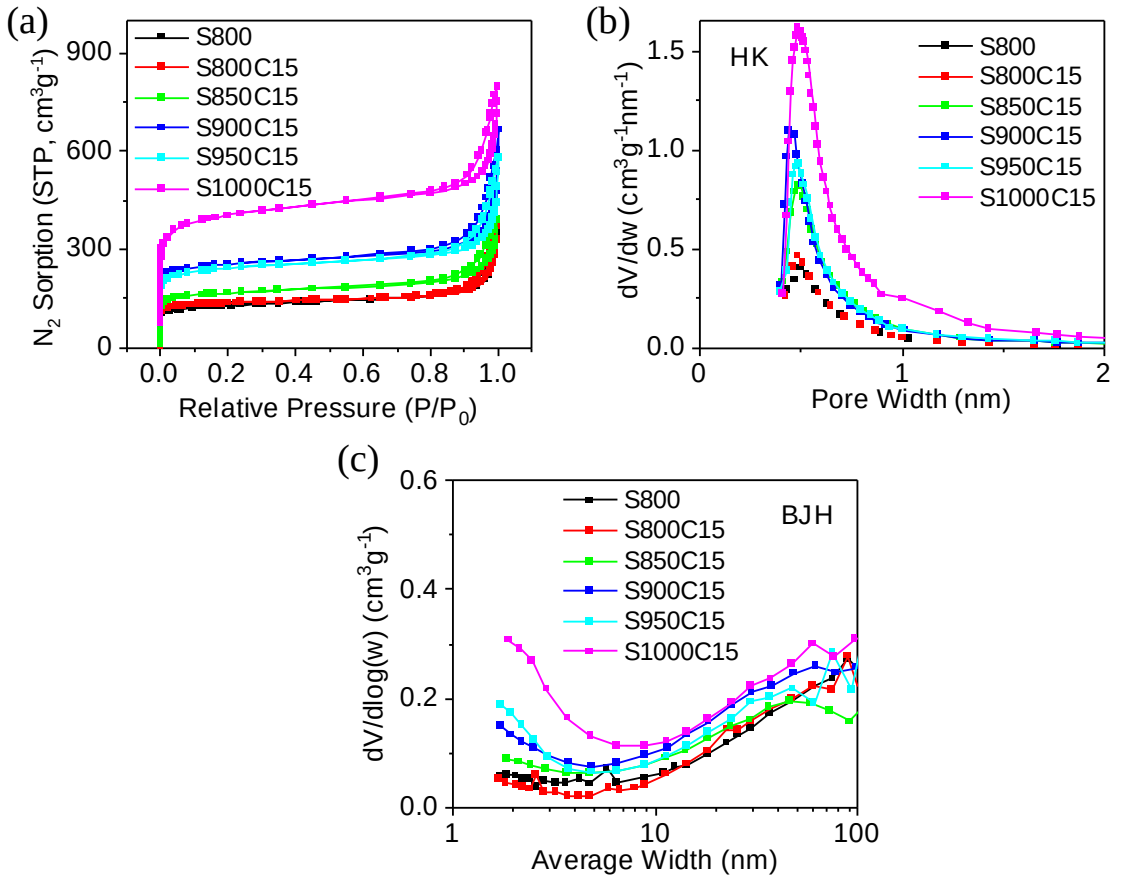

Figure 2.15 (a) N_2 adsorption isotherms at 77 K; (b,c) pore size distributions in (b) the micropore region determined by the HK method and (c) the mesopore region determined by the BJH method of S800 and CO_2 activated Starbons®.

In addition, the ultramicro, micro and total pore volumes and surface areas of carbon

dioxide activated Starbons® show an increasing trend with increasing heat treatment temperature. Conversely correlated to the development of porosity, the yield of product decreases due to the continuous burn off of carbon as the activation temperature increases. Specifically, activation of S800 at 800 °C to give S800C15 only results in a slight development of ultramicropores compared to S800. When higher temperatures were applied, both ultramicropores and supermicropores were developed in S850C15, S900C15 and S950C15. Both additional micropores and mesopores (2~10 nm) were extensively developed when the activation was conducted at 1000 °C, which may be attributed to the intense creation and enlargement of micropores at 1000 °C, causing the partial destruction of adjacent micropore walls and the creation of mesopores.

2.3.2.1.2 CO_2 activated Starbons® prepared at 900 or 950 °C with different activation holding times

According to the above results, activation of S800 at 900 or 950 °C is capable of both conserving the mesoporous structure and extensively enhancing the ultramicro- and microporosity, whilst resulting in only a moderate mass loss of 22~32% (the yields of samples are shown in **Table 7.4** in **Appendix** 7.1). Therefore, the effect of activation time was investigated by activating S800 to 900 or 950 °C with a heating rate of 10 °C min^{-1} and a carbon dioxide flow rate of 50 cm^3 min^{-1}, whilst changing the hold time at the final temperature from 15 to 30, 60, 90 and 120 minutes.

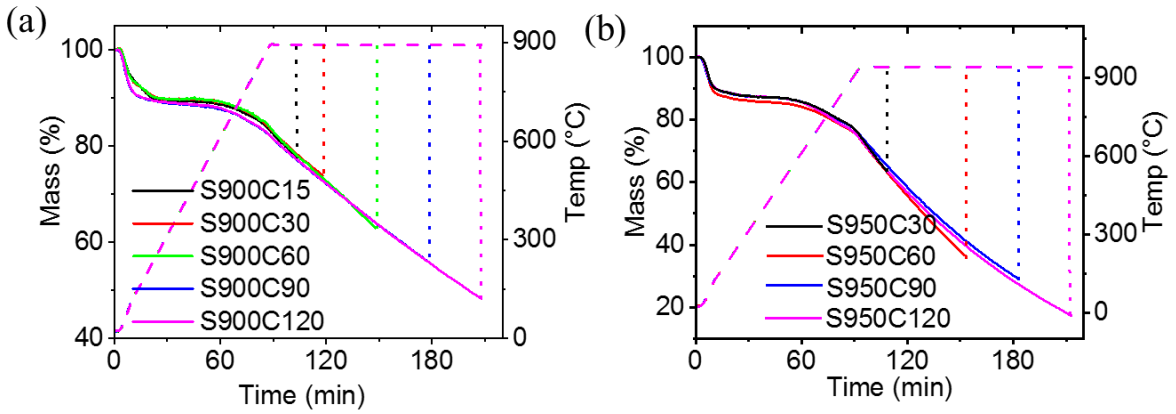

Figure 2.16 TGA curves of activation time versus burn-off wt% for CO_2 activation of S800 with temperature rising from 20 °C up to (a) 900 °C and (b) 950 °C with different holding time (15, 30, 60, 90 and 120 minutes).

All the activation processes shown in **Figure 2.16** exhibit obvious weight loss of 10~12% at temperatures below 150 °C due to desorption of carbon dioxide as well as dehydration of the material. Once the temperature reaches above 600 °C, the consumption of carbon atoms and removal of volatiles results in another dramatic mass loss. The total burn-off value increases gradually from 22% to 52% as the activation time increases from 15 to 120 min at 900 °C and from 36% to 83% at 950 °C (as shown in **Table 7.4** in **Appendix** 7.1).

The textural properties of the carbon dioxide activated Starbons® resulting from heat treatment with different holding times were determined by various models as shown in **Table 2.11, Figure 2.17** and **Table 7.1-7.3** and **Figure 7.1-7.3** in **Appendix 7.1**. Increasing the activation holding time leads to the creation of ultramicro-, micro- and mesopores in the hierarchically porous activated materials, which exhibit combined isotherms of type I and type IV as shown in **Figure 2.17a**. The broadened pore size distribution and the increased intensity in both micro- and mesopore regions in **Figure 2.17b,c** indicate the development of the hierarchical structure.

Table 2.11 Textural properties of starting material S800 and the CO_2 activated Starbons® with different heat treatment times.

Material	S_{BET} (m^2g^{-1})	V_{micro} ($V_{ultramicro}$) (cm^3g^{-1}) HK	V_{meso} (cm^3g^{-1}) BJH	V_{total} (cm^3g^{-1}) P/P_0=0.99	Percentage of micro (ultramicro) (%)	Yield (%)
S800	507	0.20 (0.14)	0.36	0.55	36.4 (25.5)	100
S900C15	983	0.39 (0.31)	0.38	0.77	50.6 (40.3)	77.5
S900C30	1119	0.45 (0.34)	0.50	0.98	45.9 (34.7)	74.0
S900C60	1097	0.44 (0.33)	0.40	0.89	49.4 (37.1)	63.0
S900C90	1475	0.59 (0.43)	0.45	1.05	56.2 (41.0)	55.8
S900C120	1914	0.77 (0.52)	0.71	1.49	51.7 (34.9)	48.5
S800	722	0.28 (0.23)	0.22	0.51	54.9 (45.1)	100
S950C30	1618	0.64 (0.46)	0.27	0.94	68.1 (48.9)	63.9
S950C60	2180	0.89 (0.53)	0.41	1.32	67.4 (40.2)	36.0
S950C90	2457	1.04 (0.56)	0.59	1.64	63.4 (34.1)	29.4
S950C120	2733	1.16 (0.56)	0.96	2.09	55.5 (26.8)	17.5

A trade off between the developed porosity and the yield of product is observed as both activation temperature and activation time increase. When the activation was conducted at 950 °C, the enhancement of the micro- and mesoporosities was more significant than at 900 °C. As a result of the super developed porosity, this material has the lowest yield of 18%, but the surface area, micropore volume and mesopore volume of S950C120 are four times higher than those of the precursor S800 (**Table 2.11**). The increase of mesopore volume occurs later than the increase in micropore volume. On extending the activation time, the number of larger micro- and mesopores increases more than the number of smaller pores (e.g. super-micropores *vs* ultra-micropores and mesopores *vs* micropores) which results in first an increase and then a decrease of ultramicro- and microporosities. Therefore, the high degree of activation leads to the creation of limited numbers of ultramicropores which are continuously developed into wider pores.

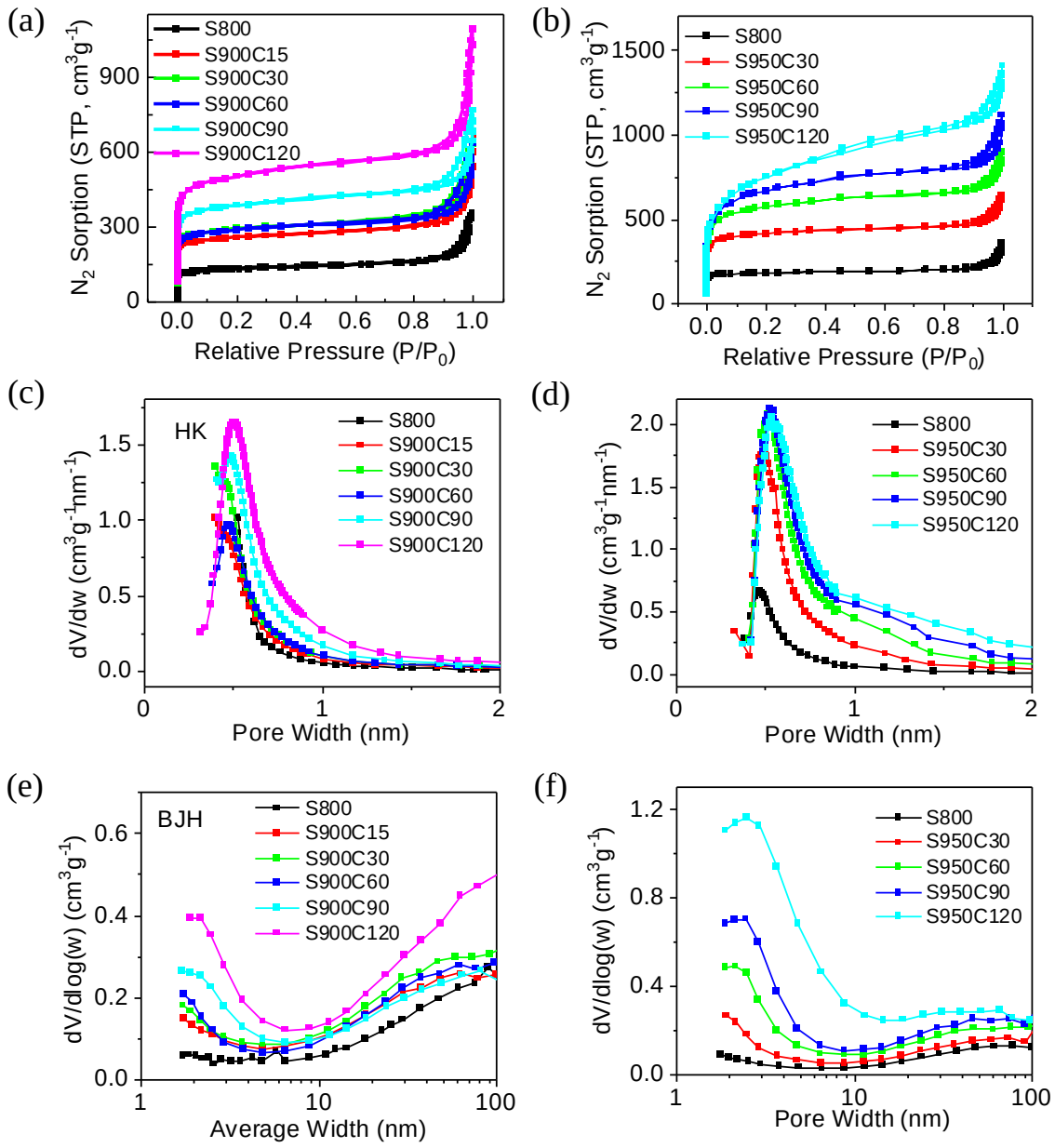

Figure 2.17 (a,b) N_2 adsorption isotherms at 77 K; (c~f) pore size distributions of materials in (c,d) the micropore region determined by the HK method and (e,f) the mesopore region determined by the BJH method of S800 and CO_2 activated Starbons®.

2.3.2.1.3 CO_2 activated Starbons® prepared at 900 °C with different CO_2 flow rates

Samples of S800 were heated from room temperature to 900 °C with a heating rate of 10 °C min^{-1}, followed by a 15 minutes hold time. The carbon dioxide flow rate was changed

from 50 cm^3 min^{-1} to 25 and 100 cm^3 min^{-1} to study the effects of carbon dioxide flow rate on activation process. Three overlapping TGA curves can be observed in **Figure 2.18** although the carbon dioxide flow rates were changed, which indicated that the burn-off wt% is not sensitive to the carbon dioxide flow rate in the range investigated.

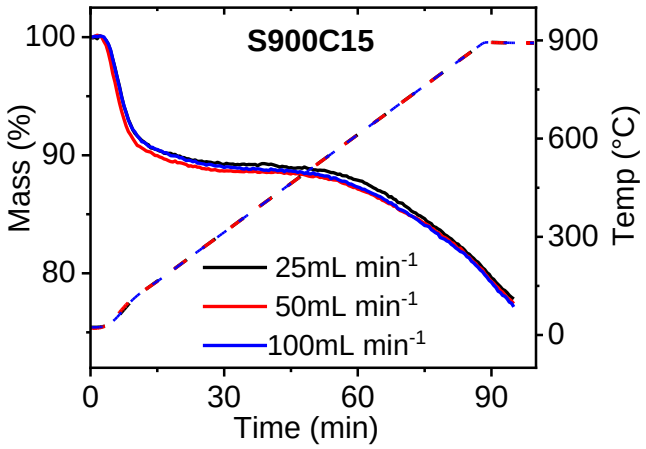

Figure 2.18 TGA curves of activation time versus burn-off% for CO_2 activation of S800 with temperature rising from 20 °C up to 900 °C, followed by 15 minutes hold time with different CO_2 flow rates.

The textural properties and yields shown in **Table 2.12, Figure 2.19** and **Table 7.1-7.3** and **Figure 7.1-7.3** in **Appendix 7.1** indicate that a high carbon dioxide flow rate leads to a slightly lower yield of product and is favourable for developing more micro- and mesopores in the materials. There is a larger increase in the number of large micropores and mesopores than in the number of ultramicropores. Overall, the highest ultramicro- and microporosities were introduced when a carbon dioxide flow rate of 50 cm^3 min^{-1} was applied. A slight enhancement of the isotherms and pore size distribution can be observed amongst the materials as a result of increasing the carbon dioxide flow rate.

Table 2.12 Textural properties of S900C15 prepared by using different CO_2 flow rates.

Material	S_{BET} (m^2g^{-1})	V_{micro} ($V_{ultramicro}$) (cm^3g^{-1}) HK	V_{meso} (cm^3g^{-1}) BJH	V_{total} (cm^3g^{-1}) P/P_0=0.99	Percentage of micro (ultramicro) (%)	Yield (%)
25 cm^3 min^{-1}	873	0.35 (0.27)	0.35	0.70	50.0 (38.6)	77.8
50 cm^3 min^{-1}	983	0.39 (0.31)	0.38	0.77	50.6 (40.3)	77.5
100 cm^3 min^{-1}	1020	0.41 (0.31)	0.52	0.94	43.6 (33.0)	77.1

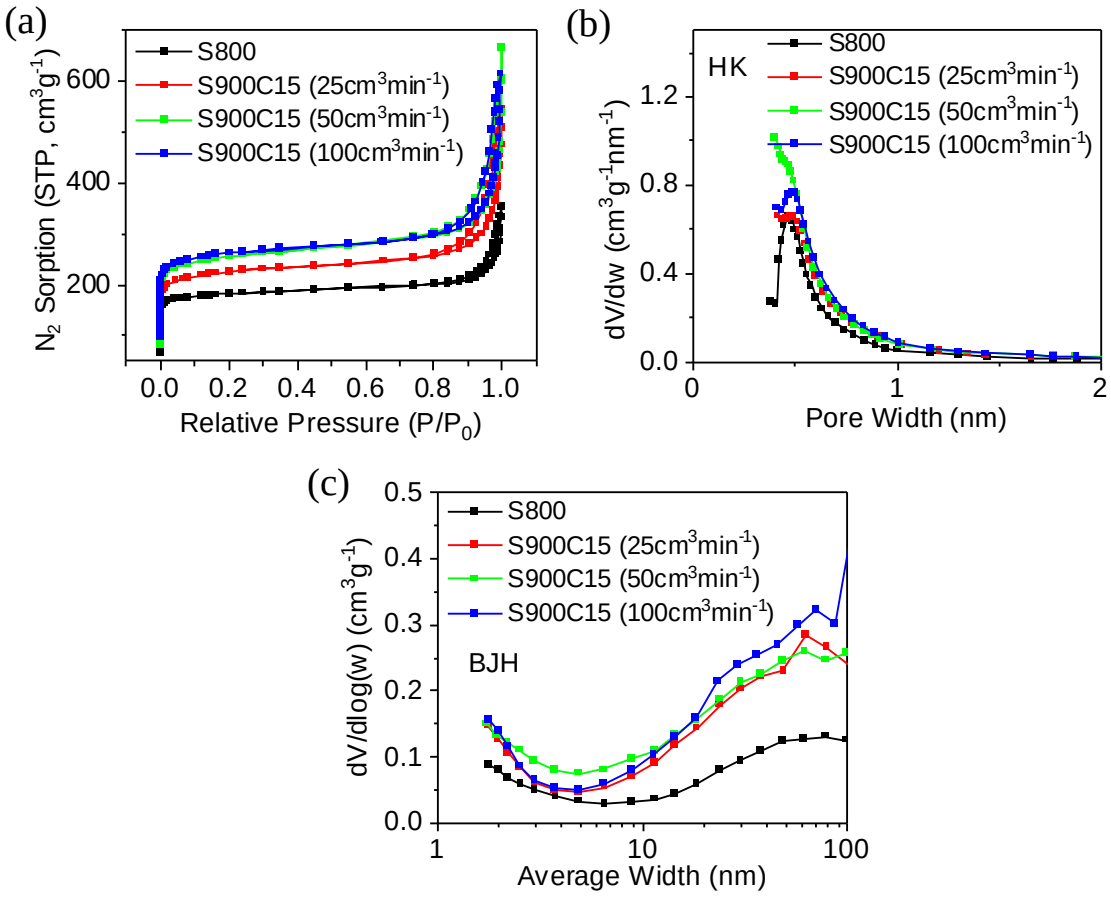

Figure 2.19 (a) N_2 adsorption isotherms at 77 K; (b,c) pore size distributions in (b) the micropore region determined by the HK method and (c) the mesopore region determined by the BJH method of S900C15 prepared by using different CO_2 flow rates.

2.3.2.2 CO_2 activated Algibons and Pecbons

Activation of S800 by carbon dioxide at 900 °C has been shown to be capable of developing both micropores and mesopores. The difference between flow rates of 50-100 mL

min^{-1} was negligible, so for activation of Algibons and Pecbons, the flow rate was fixed at 50 mL min^{-1}. Samples of A800 were heated from room temperature to 900 °C with a heating rate of 10 °C min^{-1}, then the temperature was kept constant for 0~30 minutes to study the effect of activation time on Algibons. Mass losses of 36%, 68% and 98% were observed in the TGA curves shown in **Figure 2.20a** and **Table 2.13** at holding times of 0, 10 and 30 minutes, respectively. P800 underwent a mass loss of 73% when activated at 900 °C even with no hold time. Therefore, P800 is more reactive to carbon dioxide than A800, and S800 is the least reactive. Therefore, in order to activate A800 and P800 to a similar extent as S800, lower temperatures of 750 °C and 700 °C were used for activating A800 and P800.

For activation of both A800 and P800, the dramatic mass loss above 600 °C in the TGA curves in **Figure 2.20a-c** as well as the double peaks of carbon monoxide appearing from around 3600 seconds in the real-time FTIR spectra in **Figure 2.20d-f**, demonstrate that the reaction of carbon in both A800 and P800 with carbon dioxide starts at 600 °C.

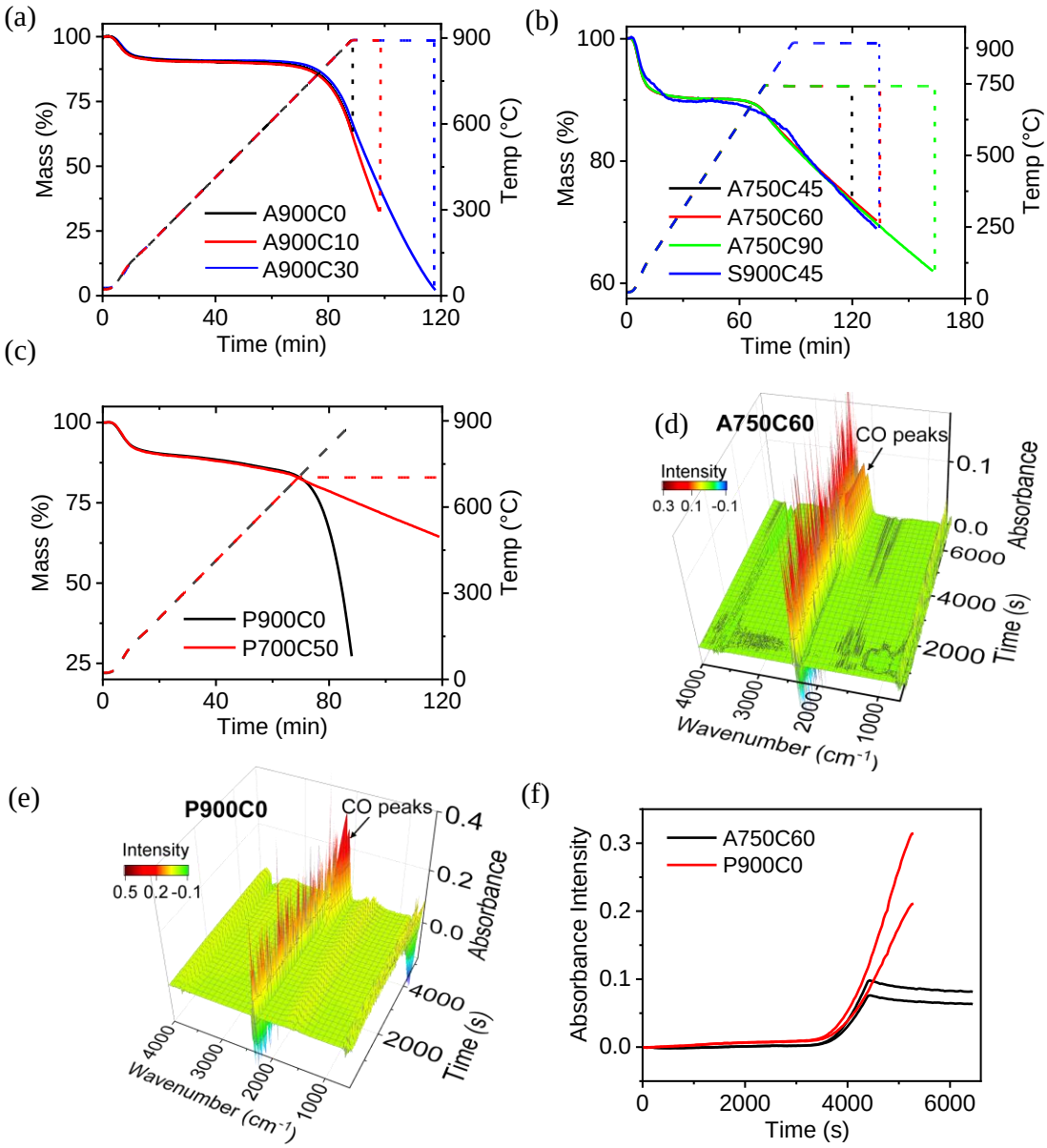

Figure 2.20 TGA curves of activation time versus temperature and burn-off wt% for CO_2 activation of (a,b) A800 and (c) P800; real-time FTIR spectrum of the off-gases from the TGA experiment of preparing (d) A750C60 and (e) P900C0; and (f) the change of absorbance with time of the FTIR spectra of CO.

The textural properties in **Table 2.13**, **Table 7.1-7.3** and **Figure 7.1-7.3** in **Appendix 7.1** and nitrogen adsorption isotherms and pore size distributions shown in **Figure 2.21** reveal that both micropores and mesopores were developed in the hierarchical structure of the

carbon dioxide activated Algibons and Pecbons. The development of porosity in activated Algibons and Pecbons was associated with a decrease of product yield. Algibons with ultramicro and micropore volumes of up to 0.21 $cm^3 g^{-1}$and 0.32 $cm^3 g^{-1}$ and surface areas of up to 762 $m^2 g^{-1}$ were obtained at a relatively low activation temperature of 750 °C. The development of mesopores at 750 °C was not obvious but the simultaneous enhancement of both micro- and mesoporosity becomes significant when the activation was conducted at a higher temperature of 900 °C compared to a longer activation time at a lower temperature. Likewise, a higher activation temperature leads to a greater increase of surface area and total porosity for Pecbons. However, since A800 and P800 contain more oxygen containing functional groups than S800 as determined by CHN and XPS analysis, their reactivity with carbon dioxide is higher than that of S800 during the same activation process. The high reactivity results in lower yields of products under the same activation conditions. Therefore, the activation of A800 and P800 at 900 °C has to be conducted with a very short hold time. As a result, the increase in porosity is not comparable to that of activated Starbon® prepared at the same activation temperature but a longer activation time.

Table 2.13 Textural properties of starting material A800, P800 and CO_2 activated Algibons and Pecbons.

Material	S_{BET} (m^2g^{-1})	V_{micro} ($V_{ultramicro}$) (cm^3g^{-1}) HK	V_{meso} (cm^3g^{-1}) BJH	V_{total} (cm^3g^{-1}) P/P_0=0.99	Percentage of micro (ultramicro) (%)	Yield (%)
A800	322	0.13 (0.08)	0.71	0.81	16.0 (9.9)	100
A750C45	738	0.31 (0.21)	0.68	0.99	31.3 (21.2)	73.8
A750C60	756	0.32 (0.21)	0.76	1.09	29.4 (19.3)	70.0
A750C90	762	0.32 (0.21)	0.74	1.05	30.5 (20.0)	61.8
A900C0	822	0.35 (0.22)	0.86	1.18	29.7 (18.6)	63.8
A900C10	868	0.38 (0.21)	0.98	1.33	28.6 (15.8)	31.7
P800	262	0.11 (0.07)	0.43	0.54	20.4 (13.0)	100
P700C50	734	0.31 (0.21)	0.47	0.78	39.7 (26.9)	64.5
P900C0	946	0.40 (0.22)	0.54	0.93	43.0 (23.7)	27.1

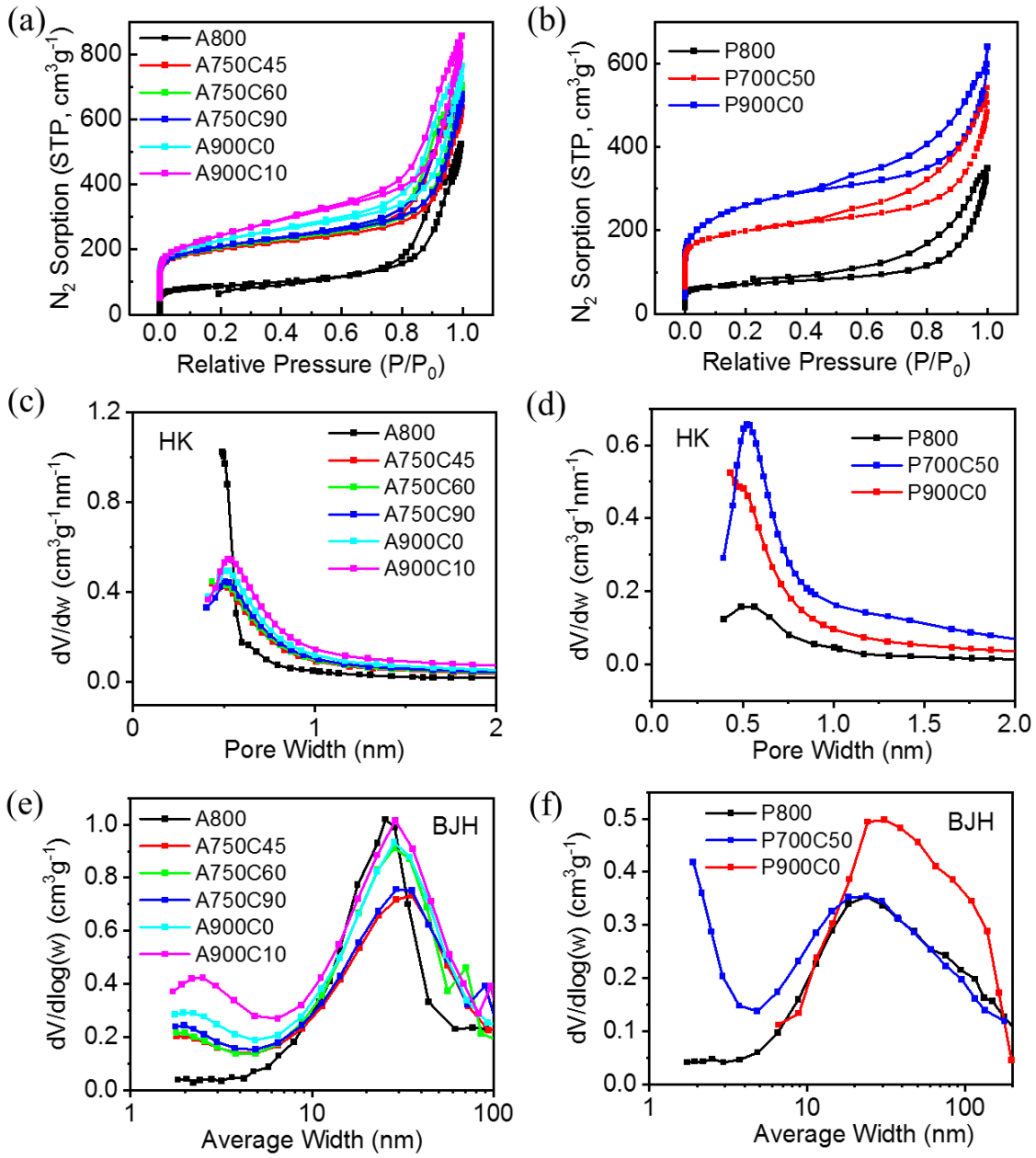

Figure 2.21 (a,b) N_2 adsorption isotherms at 77 K; (c-f) pore size distributions in (c,d) the micropore region determined by the HK method and (e,f) the mesopore region determined by the BJH method of A800, P800 and CO_2 activated Algibons and Pecbons.

2.3.2.3 SEM and TEM characterisation

The development of surface morphology and porous structure of the carbon dioxide activated carbons were studied by SEM and TEM.

2.3.2.3.1 Starbons®

The SEM images and particle size distributions in **Figure 2.22** reveal that carbon dioxide activation leads to particle sizes of 10-18 µm for carbon dioxide activated samples compared to 14 µm for S800. The carbon framework was further developed by carbon dioxide activation, showing additional mesopores, macropores and channels in the carbon skeleton of carbon dioxide activated Starbons®, which differ from the smooth surface morphology of potassium hydroxide activated Starbons® (see **Figure 2.9**). In addition, the higher degree of activation associated with a higher activation temperature or a longer activation time results in a higher developed porosity in these hierarchically activated Starbons®.

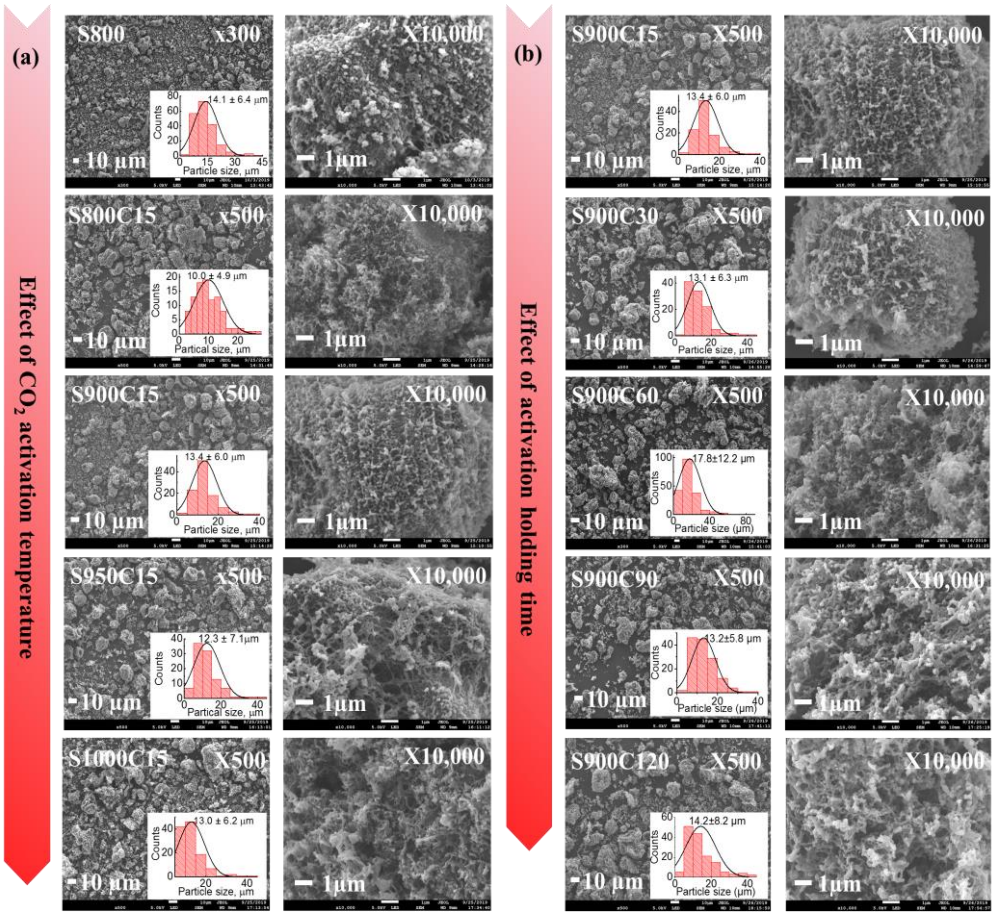

Figure 2.22 SEM images of S800 and CO_2 activated Starbons® with different activation (a) temperature and (b) holding time.

The morphology and structure evolution were further revealed by TEM images shown in **Figure 2.23**. The porous structure of S800 and S950C90 consists of randomly distributed micropores and mesopores. Moreover, numerous additional micropores and mesopores are observed in the carbon framework of S950C90 as a result of the carbon dioxide activation.

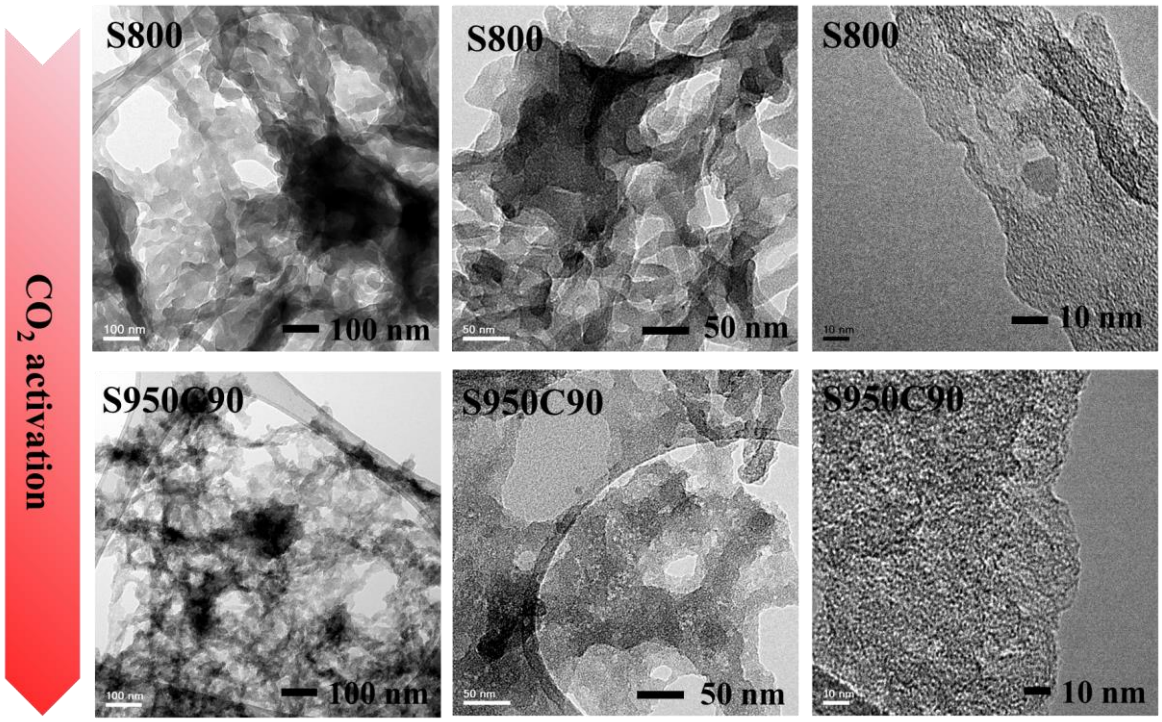

Figure 2.23 TEM images of S800 and S950C90 at different magnifications.

2.3.2.3.2 Algibons and Pecbons

The SEM images and particle size distributions shown in **Figure 2.24** reveal that the particle sizes of Algibons after carbon dioxide activation were also retained (40-47 µm) compared to A800 (51 µm), whereas the average particle size of carbon dioxide activated Pecbons increased significantly (51 µm) compared to P800 (16 µm). The gasification of carbon in platelet P800 with carbon dioxide during the activation results in significant consumption of carbon, leading to the disappearance of some small particles.

Similarly to the carbon dioxide activation of Starbons®, more cracks and caves of larger size were created on activated Algibons and Pecbons by activating A800 and P800. The

carbon skeleton framework indicates the development of mesopores and macropores in the hierarchically porous structure of the carbon dioxide activated Algibons and Pecbons.

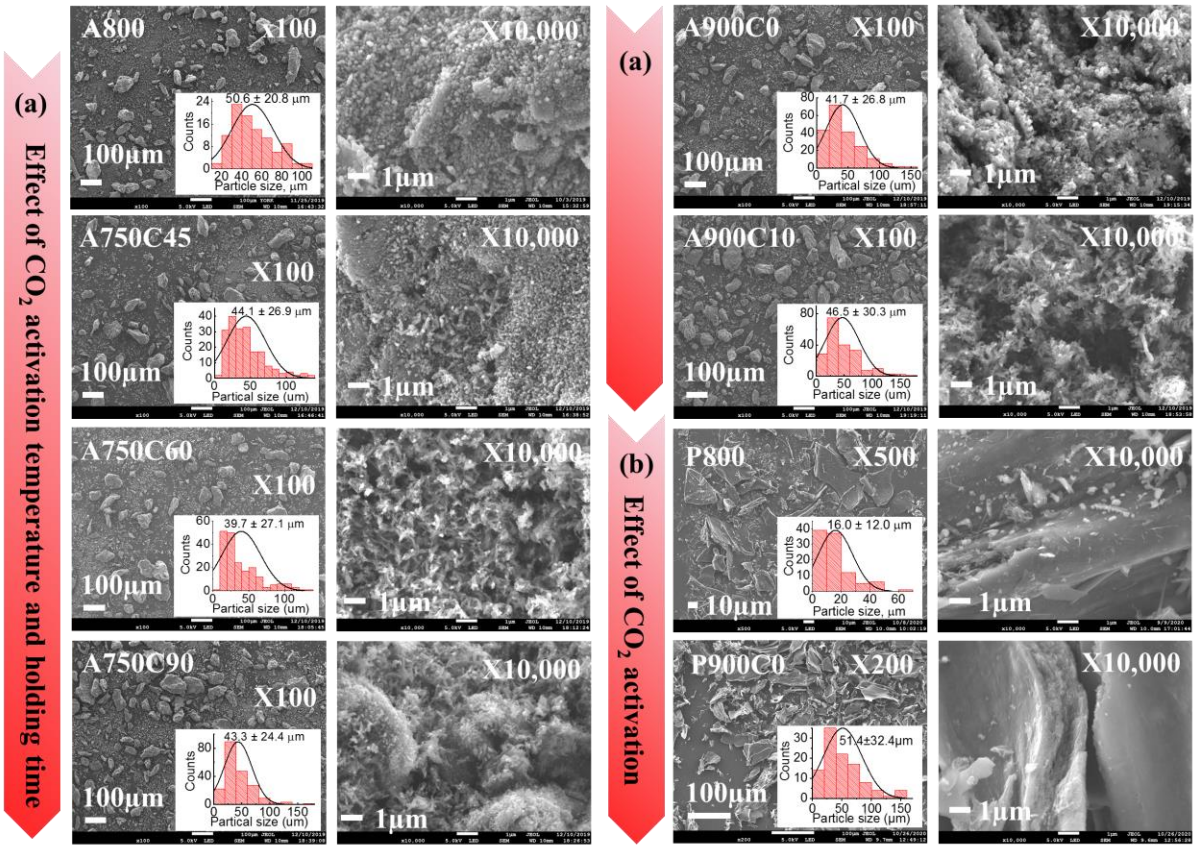

Figure 2.24 SEM images of (a) A800 and CO_2 activated Algibons and (b) P800 and CO_2 activated Pecbons.

2.3.2.4 CHN analysis

The elemental compositions of the carbon dioxide activated materials were characterised by CHN analysis and the data are presented in **Table 2.14**. Due to the gasification of carbon by reaction with the oxidising carbon dioxide during the activation process, the carbon content in the activated Starbons®, Algibons and Pecbons all decreased after carbon dioxide activation. In addition, the decline of the carbon content became more significant as the activation time increased. As the activation time increases, the carbon content decreases consistent with the material becoming more oxygenated due to loss of carbon as carbon

monoxide.

Table 2.14 Combustion analysis of non-activated S800, A800, P800 and CO_2 activated Starbons®, Algibons and Pecbons.

Material	% C	% H	% Rest
S800	91.6	0.2	8.2
S950C15	92.6	0	7.4
S950C30	90.1	0	9.9
S950C60	88.1	0	10.4
S950C90	88.7	0	11.3
S950C120	78.0	0	22.0
A800	80.9	0	19.1
A750C60	74.7	0	25.3
P800	72.1	1.1	26.8
P700C50	62.7	0.8	36.4

2.3.2.5 XPS analysis

The surface chemical composition of the carbon dioxide activated materials: S950C90, A750C60 and P700C50 were analysed by XPS. Deconvolutions of the high-resolution XPS spectra of C1s and O1s for the samples are shown in **Figure 2.25** and **Table 7.5,7.6** in **Appendix 7.1**. Carbon dioxide activation (at 700–950 ^{o}C) resulted in an increase in surface carbon content (94.8 to 98.5% for S800 to S950C90; 87.4 to 90.9% for A800 to A750C60 and 76.2 to 77.2% for P800 to P700C50) and decrease in surface oxygen content (5.2 to 1.3% for S800 to S950C90; 9.3 to 6.8% for A800 to A750C60 and 14.4 to 13.8% for P800 to P700C50)**.** Since the combustion (CHN) analysis indicates that the oxygen content increases

after carbon dioxide activation, therefore, the interior of the materials is more oxygenated than the surface.

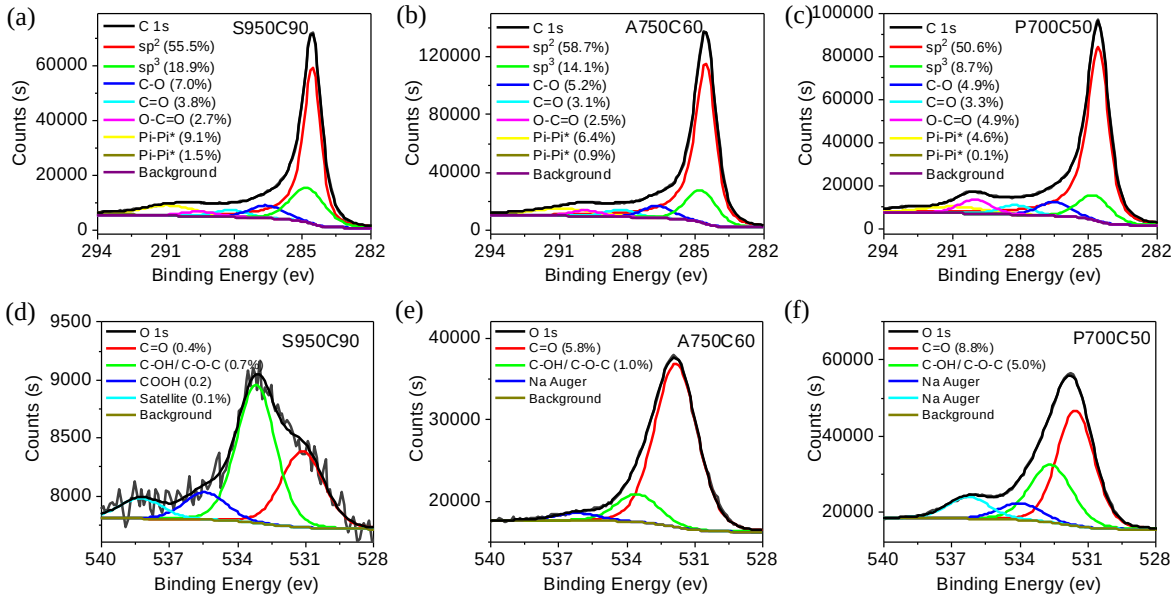

Figure 2.25 XPS spectra of C1s of (a) S950C90, (b) A750C60, (c) P700C50; O1s of (d) S950C90, (e) A750C60, (f) P700C50.

2.3.3 Summary

In contrast to the potassium hydroxide activated materials which had high microporosity, both micropores and mesopores were well developed by carbon dioxide activation, resulting in high surface areas and high porosities in the hierarchically activated materials. Again, in contrast to the smooth surface morphology and the identification of micropores in potassium hydroxide activated materials, a more amorphous porous framework with additional micropores and mesopores can be observed in the carbon dioxide activated materials.

The surface area and pore size distribution of carbon dioxide activated materials can be tailored by selecting appropriate activating conditions of temperature, heat treatment duration time and carbon dioxide flow rate. Material with a higher surface area and porosity can be

obtained when the precursor is activated under more severe conditions. However, only larger pores (meso- and macropores) can be developed extensively and the creation of small sized pores (ultramicro and supermicropores) is limited even after a high degree of activation. In addition, the activation of the precursors, especially Algibons and Pecbons, must be conducted at an appropriate temperature to prevent excessive burn-off of material and reduction of yield.

2.4 Preparation and Characterisation of O_2 Activated Starbons®

2.4.1 Introduction

As another green physical activation process, oxygen activation can be used to produce activated carbons with controllable micro- and mesoporosity. Similarly to carbon dioxide activation, oxygen activation is generally accomplished by pyrolysing a carbonaceous precursor in an inert atmosphere and subsequent oxidising the material in a gasification stream (air or oxygen). However, to restrain the over burn-off, the oxygen activation step is generally carried out under relatively mild conditions (e.g. lower temperature, short time or reduced oxygen partial pressure).

Therefore, in this section, preformed non-activated S800, A800 and P800 were activated by subjecting them to a flow of diluted air (a mixed flow of 200 cm^3 min^{-1} nitrogen and 20 cm^3/min air to give an oxygen concentration of 2%) in a thermogravimetric instrument at temperatures of 700~800 °C with a heating rate of 10 °C $minute^{-1}$ and a hold time of up to one hour to give activated samples. The effects of temperature and time of the activation on the activated materials were investigated by monitoring the concentration of carbon dioxide and carbon monoxide produced during activation using a FTIR gas cell. Oxygen activated samples are denoted as SxOy, AxOy or PxOy, where O represents oxygen activation, x represents the activation temperature and y represents the activation time. Yield of product in this section was obtained by dividing the mass of the product by the mass of the precursor (e.g. S800, A800 or P800).

2.4.2 Results and Discussion

2.4.2.1 O_2 activated Starbons®

The effect of activation temperature on the physical characteristics of Starbons® was investigated by activating S800 from room temperature to 700, 750 and 800 °C. S800 was also heated from room temperature to 750 °C followed by three hold times (0, 40 and 56 minutes) to study the effects of hold time on the activation of Starbons®. For comparison, a blank experiment was carried out by treating S800 at 750 °C under a pure nitrogen atmosphere instead of diluted air to give a material denoted as S750N0. The yields of all the samples are presented in **Table 2.15**.

As shown in **Figure 2.26a**, when preparing S750N0, although the majority of the non-carbon atoms of S800 had been removed during its previous carbonisation process, its heat treatment to 750 °C under a nitrogen atmosphere still led to a total mass loss of 6%. The mass loss is ascribed to the evaporation of water at temperatures above ~100 °C and the partial degradation at high temperature. As a result, peaks of water (1500~1800 cm^{-1} and 3300~3800 cm^{-1}) and carbon dioxide (2350 cm^{-1} and 667 cm^{-1}) appear in the real-time FTIR spectra from ~600 seconds (**Figure 2.26c**). However, for the oxygen activation of S800 to 750 °C using a 2% atmosphere of oxygen, a mass loss of 25% was observed when preparing S750O0. In addition to the evaporation of water above ~100 °C, there was a dramatic mass decrease once the temperature reached 400 °C (at 2280 s), due to the carbon atoms reacting with oxygen and the removal of volatiles. Consistently, the carbon dioxide peaks in the real-time FTIR spectra of S750O0 increased sharply in intensity from ~2280 s (**Figure 2.27d-f**).

For activation conducted at different temperatures and duration times (**Figure 2.26a,b**), the same slope of the mass loss in the TGA curves demonstrated that the reaction rate was independent of the variation of temperature or hold time. However, an obvious increase of the

total burn-off wt% is observed as the temperature increases from 700 °C to 800 °C (18% to 29%) or the hold time increases from 0 to 56 min at 750 °C (25% to 60%) as shown in Table 2.15. Therefore, the activation can be controlled by altering the activation temperature or time.

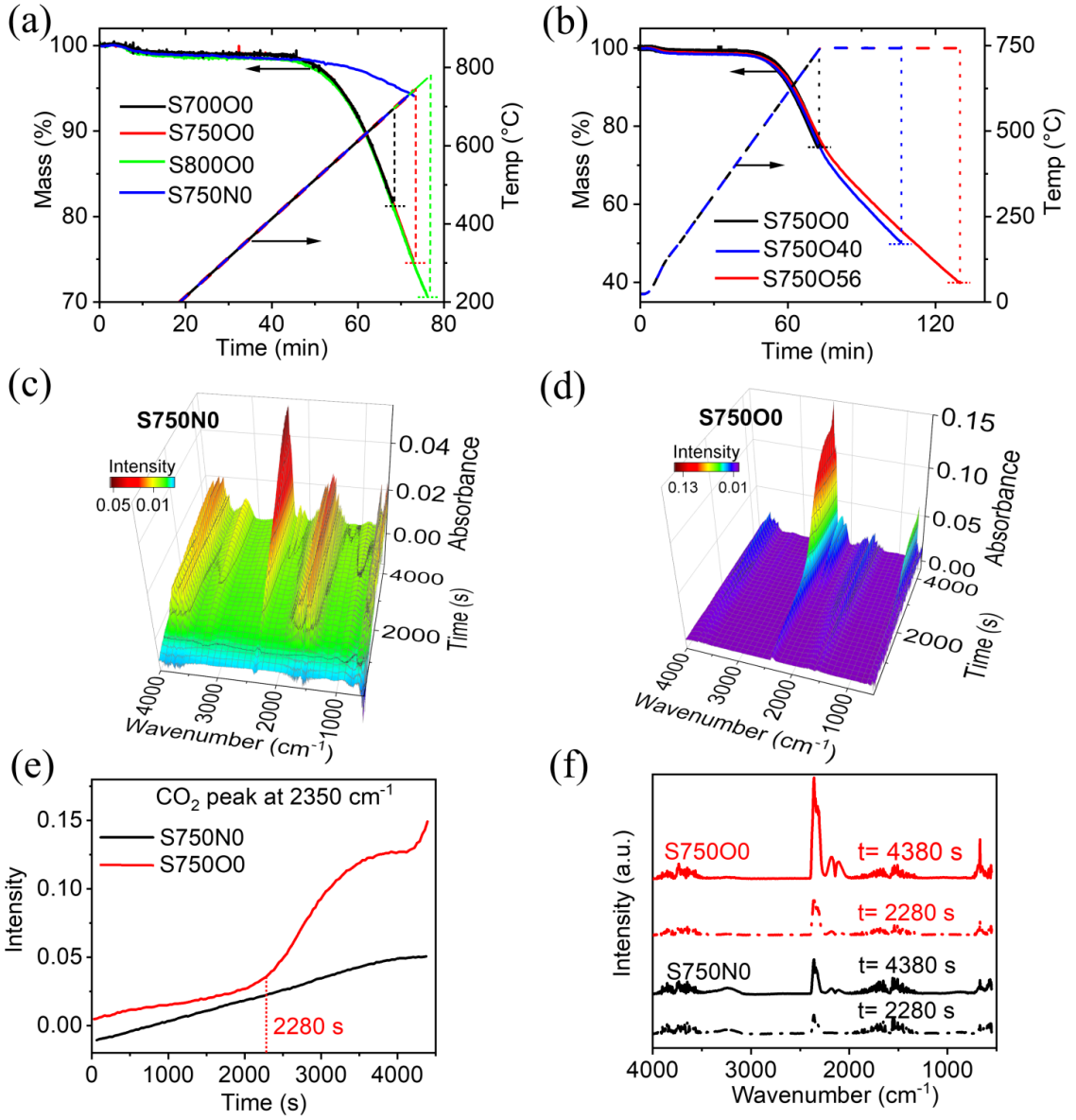

Figure 2.26 (a) TGA curves of O_2 activation of S800 at different temperatures; (b) TGA curves of O_2 activation of S800 at 750 °C with different hold times; (c, d) real-time FTIR spectra of the off-gases from the TGA experiments of preparing (c) S750N0 and (d) S750O; (e) the change of absorbance with time of the FTIR spectra of CO_2 and (f) FTIR spectra at 2280 s (400 °C) and 4380 s (750 °C).

Table 2.15 Textural properties of S800 and O_2 activated Starbons®.

Material	S_{BET} (m^2g^{-1})	V_{micro} ($V_{ultramicro}$) (cm^3g^{-1}) HK	V_{meso} (cm^3g^{-1}) BJH	V_{total} (cm^3g^{-1}) P/P_0=0.99	Percentage of micro (ultramicro) (%)	Yield (%)
S800	402	0.16 (0.11)	0.40	0.54	29.6 (20.4)	100
S700O0	897	0.35 (0.27)	0.14	0.50	70.0 (54.0)	81.6
S750O0	1100	0.43 (0.33)	0.14	0.58	74.1 (56.9)	74.5
S800O0	935	0.37 (0.28)	0.20	0.57	64.9 (49.1)	70.6
S750O40	889	0.35 (0.27)	0.09	0.45	77.8 (60.0)	49.9
S750O56	777	0.31 (0.23)	0.15	0.46	67.4 (50.0)	39.9

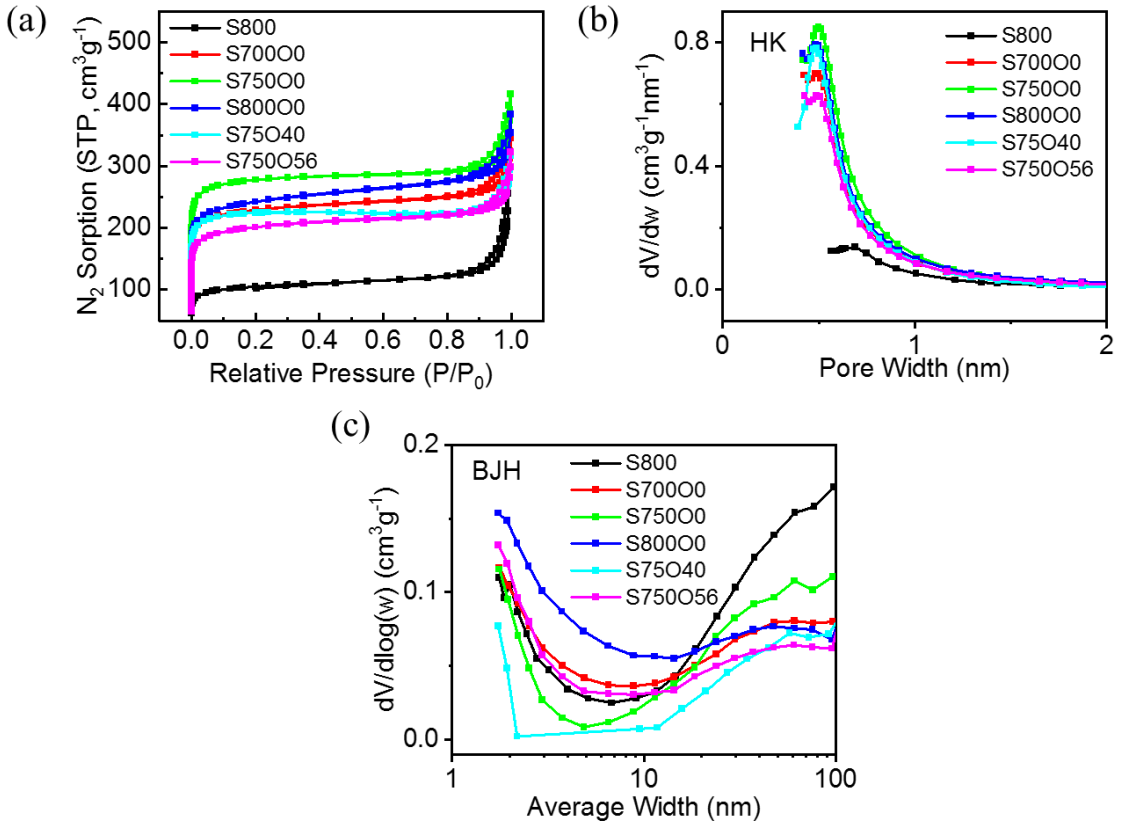

Figure 2.27 (a) N_2 adsorption isotherms at 77 K; (b,c) pore size distributions in (b) the micropore region determined by the HK method and (c) the mesopore region determined by the BJH method of S800 and O_2 activated Starbons®.

The effect of oxygen activation conditions on the porous structure of activated Starbons® was evaluated by measuring nitrogen adsorption-desorption isotherms at 77 K. The textural

properties determined by the HK and BJH models are summarised in **Table 2.15** and **Figure 2.27**. The amount of each pore size calculated by the DFT method has been included in **Table 7.1-7.3** and **Figure 7.1-7.3** in **Appendix 7.1** for comparison.

As shown in **Table 2.15**, the surface areas of oxygen activated Starbons® are all higher than that of the S800 precursor. This is attributed to an increase in the micropore volume. The reaction of carbon with oxygen coupled with the expulsion of steam contributes to the creation of ultramicropores and micropores. However, due to the high reactivity of oxygen, some mesopores were destroyed after oxygen activation. Severe activation conditions lead to greater mass loss but no further development of porosity. The surface area, ultramicropore volume and micropore volume are highest when S800 was activated at 750 °C, resulting in the largest adsorption of nitrogen and an enhancement of the micropore size distribution of S750O0 (**Figure 2.27**). Further burn-off of carbon at a higher temperature (800 °C) or after a longer time (750 °C, 40 and 56 minutes) causes a partial destruction of porosity.

Oxygen activation is less competent in developing porosity compared to carbon dioxide activation even when the mass loss is the same. In particular, under the mild activation conditions used to prepare S900C30 and S750O0, when the yields of products are similar (~74%), the ability to develop micropores is same for both activation methods, but oxygen activation destroys mesopores in S750O0 and carbon dioxide activation further develops mesopores in S900C30. When preparing S900C120 and S750O40 with product yields around 50% under more drastic conditions, the development of micropores and mesopores is more intensified by carbon dioxide activation but on the contrary, further oxygen activation leads to the destruction of porosity.

2.4.2.2 O_2 activated Algibons and Pecbons

To allow a direct comparison, A800 and P800 were activated with oxygen at 750 °C under the same conditions (2% oxygen) used for S800. Since a lower temperature circumvents the excessive reaction of oxygen with carbon, oxygen activated Algibons and Pecbons were also prepared by activation of A800 and P800 at 400 or 500 °C.

The effect of the oxygen activation conditions on the mass loss profile of A800 and P800 are shown in **Figure 2.28** and **Table 2.16.** As expected, for a specified activation temperature, increasing the hold time leads to a higher mass loss. Two main steps can be observed in the curves, including the loss of moisture above 100 °C and the oxidation of carbon at high temperature. However, the oxidation of A800 and P800 occurs earlier and is more drastic than seen for S800. They show a distinct mass loss around 1500 seconds (270 °C, in the TGA curves) and a higher carbon dioxide absorbance intensity in the FTIR spectra. As seen for carbon dioxide activation, oxygen activation of P800 occurs most drastically amongst the precursors as it undergoes the biggest mass loss under the same activation conditions.

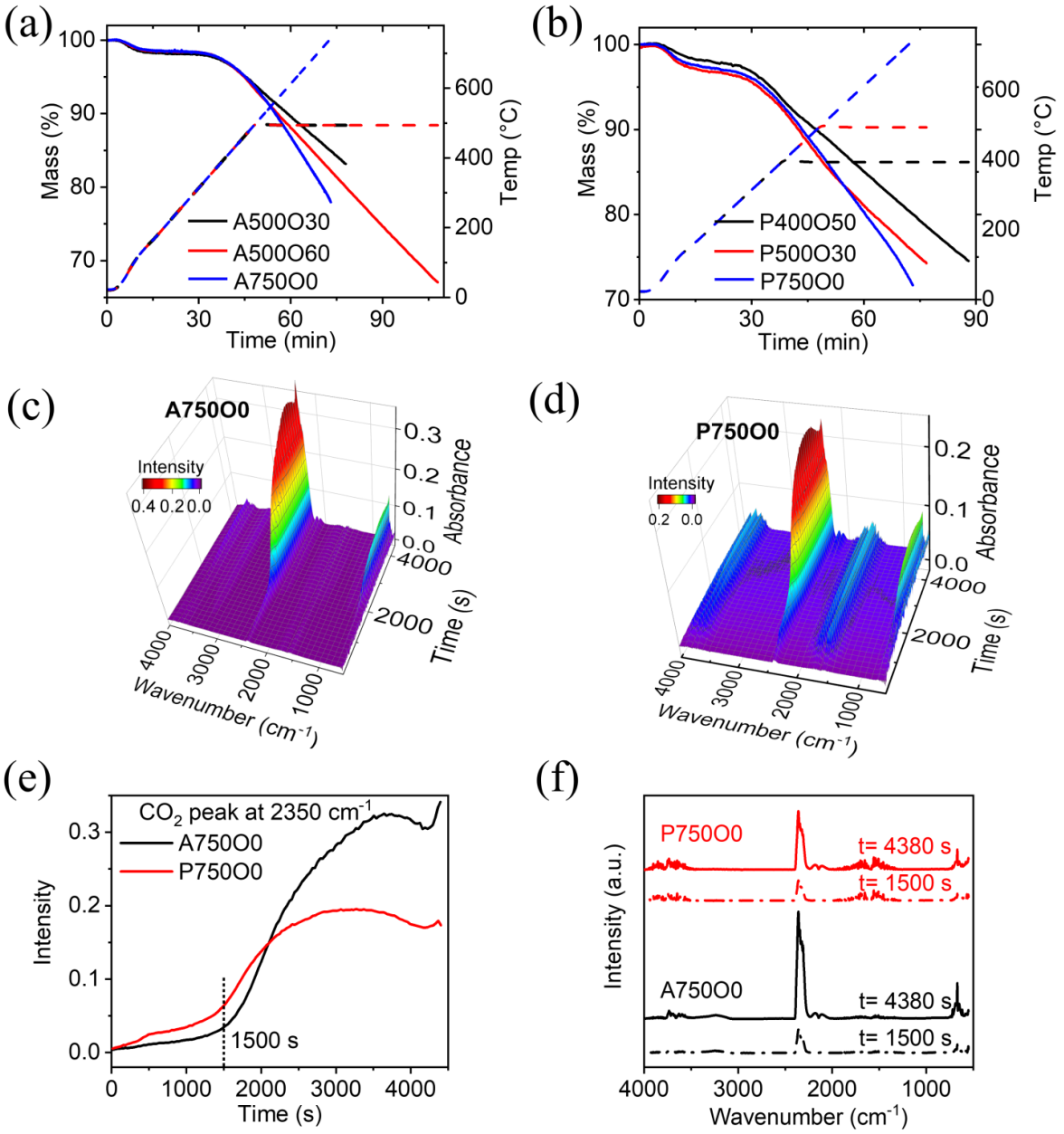

Figure 2.28 (a) TGA curves of O_2 activation of A800; (b) TGA curves of O_2 activation of P800; (c) and (d) real-time FTIR spectra of the off-gases from the TGA experiments preparing (c) A750O0 and (d) P750O0; (e) the change of absorbance with time of the FTIR spectra of CO_2 and (f) FTIR spectra at 1500 s and 4380 s.

Table 2.16 Textural properties of starting materials A800 and P800 and the O_2 activated Algibons and Pecbons.

Material	S_{BET} (m^2g^{-1})	V_{micro} ($V_{ultramicro}$) (cm^3g^{-1}) HK	V_{meso} (cm^3g^{-1}) BJH	V_{total} (cm^3g^{-1}) P/P_0=0.99	Percentage of micro (ultramicro) (%)	Yield (%)
A800	322	0.13 (0.08)	0.71	0.81	16.0 (9.9)	100
A500O30	640	0.27 (0.18)	0.70	0.97	27.8 (18.6)	83.1
A500O60	647	0.27 (0.19)	0.66	0.96	28.1 (19.8)	66.9
A750O0	629	0.26 (0.17)	0.67	0.94	27.7 (18.1)	77.9
P800	262	0.11 (0.07)	0.43	0.54	20.4 (13.0)	100
P400O50	385	0.16 (0.11)	0.44	0.60	26.7 (18.3)	74.5
P500O30	361	0.15 (0.10)	0.32	0.49	30.6 (20.4)	74.3
P750O0	550	0.23 (0.16)	0.47	0.71	32.4 (22.5)	71.7

Tables 2.16, **Figure 2.29** and **Table 7.1-7.3** and **Figure 7.1-7.3** in **Appendix 7.1** summarise the textural characterisation of the oxygen activated Algibons and Pecbons. Although inferior to those of oxygen activated S800, the surface areas and micropore volumes of the activated Algibons and Pecbons is doubled due to the partial gasification of carbon by oxygen. In addition, some of the mesopores were preserved after activation.

For the oxygen activation of Algibons and Pecbons, the textural properties were not significantly affected by altering the activation conditions. For example, at the same reaction temperature, an increase in hold time led to a rise in mass loss but not to any additional gain in textural properties. This can be attributed to the fact that the oxidation rate is very high even at low temperature compared to the diffusion rate. As a result, reaction occurs in the larger pores or on the external surface of the particles, resulting in the consumption of carbon but not the development of micro and mesopores. Further increasing the time may result in further decrease of the yield and degradation of the porosity.

At the same mass loss, the development of porosity by oxygen activation of Algibons and Pecbons is also inferior to that of carbon dioxide activation. For example, when preparing

A750C60 and A500O60 with a yield of about 70%, both the micropore and mesopore volume in A750C60 is higher than that of A500O60.

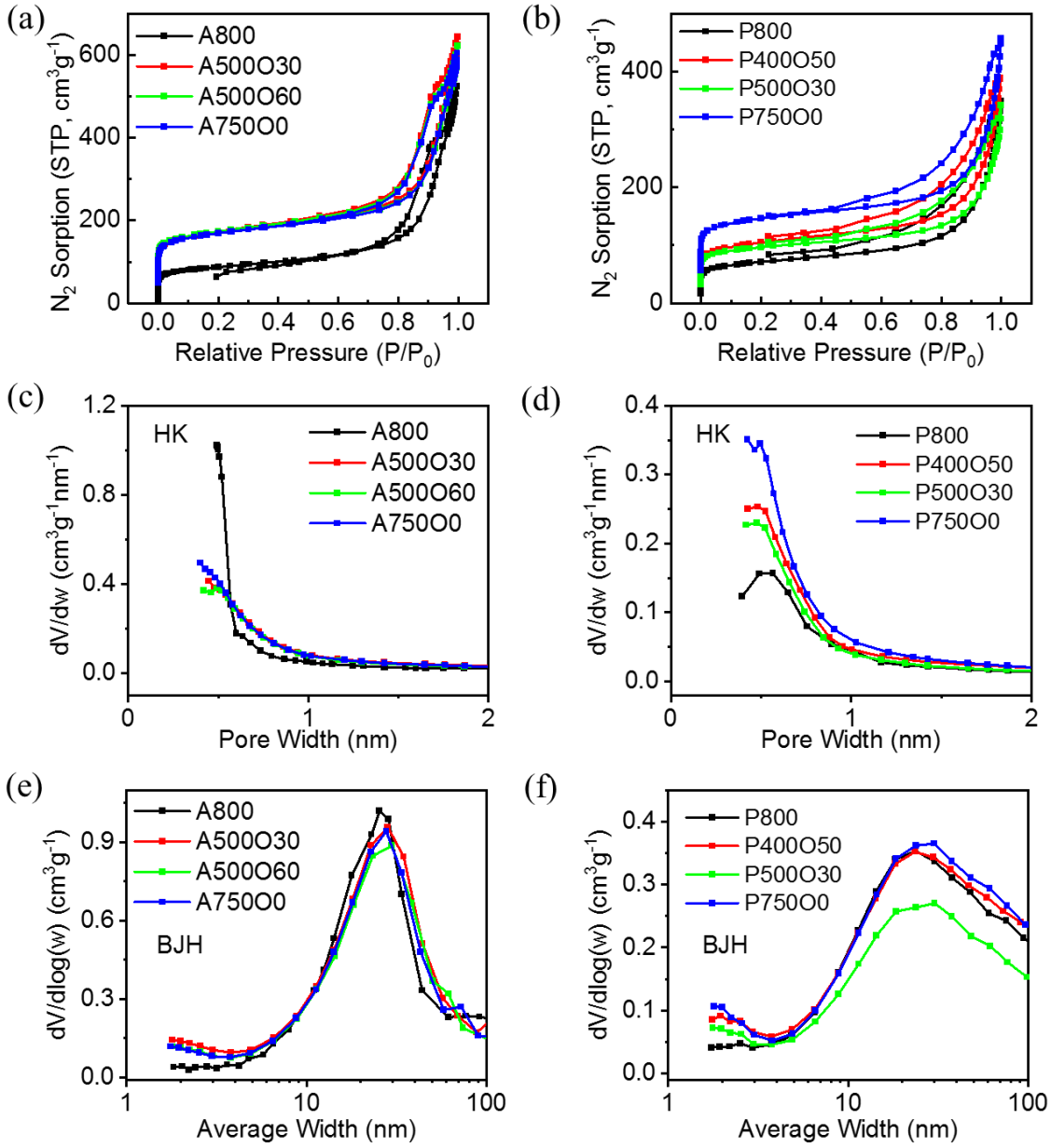

Figure 2.29 (a,b) N_2 adsorption isotherms at 77 K; (c-f) pore size distributions in (c,d) the micropore region determined by the HK method and (e,f) the mesopore region determined by the BJH method of A800, P800 and O_2 activated Algibons and Pecbons.

2.4.2.3 SEM and TEM characterisation

The morphology of S800, A800, P800 and oxygen activated Starbons®, Algibons and Pecbons were studied by SEM and images are shown in **Figure 2.30.** As seen for carbon dioxide activation, activation of S800 and A800 by oxygen results in no change in the average particle size. However, oxygen activation of P800 results in a significant increase in the average particle size (78 μm for P400O50 compared to 16 μm for P800) suggesting that oxygen selectively destroys the smaller particles of P800. More irregular and rougher surface morphology is observed in the images of oxygen activated materials, compared to the precursors.

It is worth noting that the changes in particle width between the samples prepared by different activation methods are all relatively small: less than one order of magnitude. Thus, all of the starch derived samples analysed had average particle widths of 10–40 μm; the alginic acid derived materials analysed had average particle widths of 12–99 μm; and the pectin derived samples had average particle widths of 15–78 μm.

The oxygen activation of S800 results in a partial collapse of the spherical network, whilst the particle sizes remain unchanged. The burning of carbon with oxygen occurs not only on the exterior particles surface but also in the internal pore structures and thus leads to a great loss of the meso- and macroporous framework. Similar to the oxygen activation of S800, the consumption of carbon in A800 and P800 results in the formation of cracks, caves and grains of various sizes on the surfaces of activated Algibons and Pecbons. No obvious structural collapse or change of particle sizes occurs during the activation of A800 and P800. The retention of the skeleton framework in the oxygen activated Algibons and Pecbons is due to the conservation of their meso- and macroporous network. However, an increase of the particle size can be observed in the oxygen activated Pecbons. This can be explained on the

basis that the super high oxidation rate of oxygen with carbon leads to the rapid consumption of smaller particles of P800.

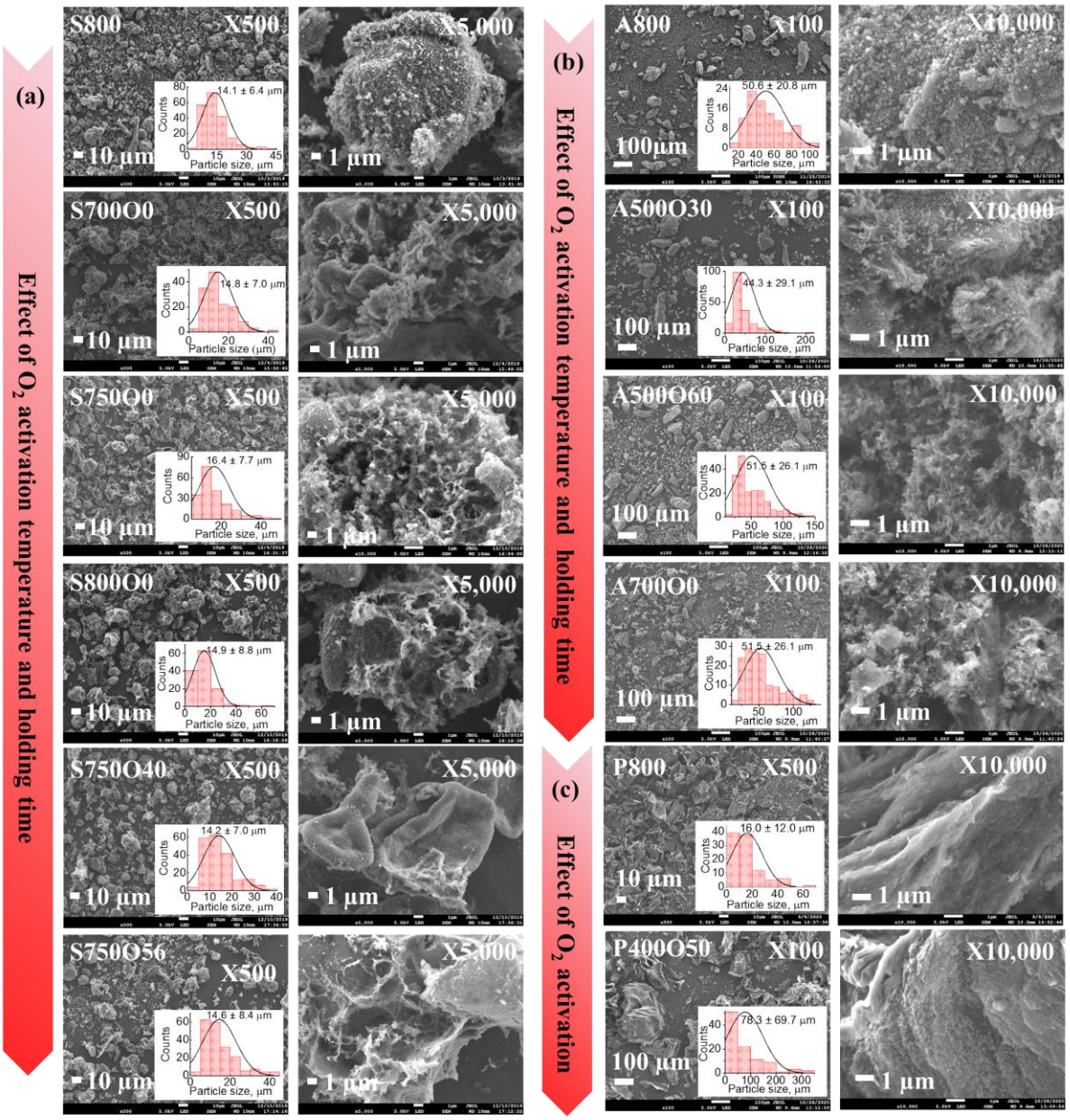

Figure 2.30 SEM images of S800, A800, P800 and oxygen activated Starbons®, Algibons and Pecbons.

2.4.2.4 CHN analysis

Table 2.17 Combustion analysis of nonactivated S800, A800, P800 and O_2 activated Starbons®, Algibons and Pecbons.

Material	% C	% H	% Rest
S800	87.8	0.5	11.7
S700O0	80.4	0	19.6
S750O0	84.6	0	15.4
S800O0	84.9	0	15.1
S750O56	81.9	0	18.1
A800	80.9	0	19.1
A750O0	78.3	0.9	20.8
P800	72.1	1.1	26.8
P400O50	66.8	0.2	33.0

The CHN data presented in **Table 2.17** reveals that the carbon content in the oxygen activated Starbons®, Algibons and Pecbons all decreased after their oxidation with oxygen, which is similar to the results obtained by carbon dioxide activation. The continued consumption of carbon during a long hold time also leads to a decrease of the carbon content.

2.4.2.5 XPS analysis

The chemical composition of oxygen activated materials S750O0, A750O0 and P400O50 were analysed by XPS. The deconvolution of the high-resolution XPS spectra of C1s and O1s are shown in **Figure 2.31** and **Tables 7.5,7.6** in **Appendix 7.1**. The proportion of surface oxygen-containing functionalities of activated Starbon® and Algibon as determined by XPS decreased after oxygen activation, whereas the combustion analysis indicates that the oxygen content increases after activation, therefore the surface of the materials is less

oxygenated than the interior. However, P400O50 shows a higher proportion of oxygen-containing functionalities compared to P800. This can be explained by the lower activation temperature (400 °C) used in the case of P400O50, since oxygen activation at 400 °C is known to result in predominant oxygenation of the surface whereas at higher temperatures, removal of carbon (as carbon monoxide and carbon dioxide) is the dominant process.[310]

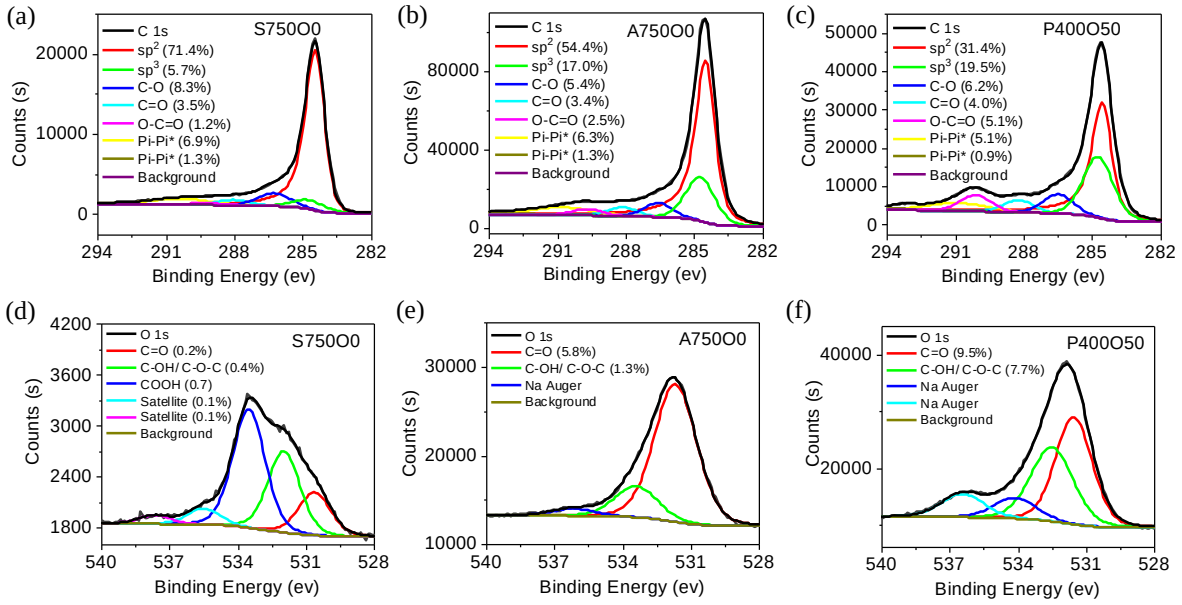

Figure 2.31 XPS spectra of (a-c) C1s of (a) S750O0, (b) A750O0, (c) P400O50 and (d-f) O1s of (d) S750O0, (e) A750O0 and (f) P400O50.

2.4.2.6 ICP-OES analysis

Six carbon dioxide and oxygen activated samples were analysed by ICP-OES as listed in **Table 2.18**. In all cases, both the potassium and total trace elemental contents of these samples were higher than those of the potassium hydroxide activated samples. The metal content of P700C50 was particularly high with values for sodium and potassium of 9.2 and 1.6% respectively. This is consistent with the presence of carboxylic acid groups in this pectin derived material.

Table 2.18 Main metallic element and total trace element composition of carbon dioxide and oxygen activated Starbons®, Algibons and Pecbons.

Element (%)	K	Al	Ca	Fe	Mg	Na	Total
S950C90	0.1218	0.0973	0.2076	0.7654	0.0408	0.1739	4.12
S750O0	0.0535	0.0284	0.0850	0.0752	0.0308	0.1567	9.18
A750C60	0.1895	0.0531	3.3755	0.0749	0.0879	0.3663	4.44
A750O0	0.0815	0.0442	2.7425	0.0613	0.0722	0.3245	4.17
P700C50	1.5862	0.0809	0.5526	0.0562	0.1559	9.2554	12.02
P400O50	0.8087	0.0129	0.2037	0.0131	0.0602	3.8084	4.93

2.4.3 Summary

Similar effects were observed in both oxygen activation and carbon dioxide activation of Starbons®. An increase of the activation temperature or isothermal hold time results in increasing burning off of the material, which influences the textural properties of the activated Starbon®. There is a limited increase of ultramicro- and micropores, which occurs at the start of activation or under mild activation conditions. After a certain level of conversion, mesopores start to develop whereas the micropores degrade. In addition, due to the high reactivity of oxygen towards carbon on both the interior and outer surfaces, destruction of the pore network occurs and results in the collapse of the structure after oxygen activation.

Pore structure development was also observed by oxygen activation of Algibon and Pecbon. However, due to the high reactivity of oxygen with carbon in Algibons and Pecbons, the activation has to be carried out under milder conditions. As a result, the change of the textural properties was not significant within the range of variation of activation conditions investigated.

2.5 Conclusion

Our study has demonstrated that it is possible to prepare activated Starbons®, Algibons and Pecbons with tailored properties in terms of micro-, mesoporous texture and surface area. The characteristics of the resulting materials depend on the nature of the starting material, the activation agent, the degree of activation and the activation conditions used.

Potassium hydroxide activation is an efficient and scalable method to engineer the microstructure of mesoporous Starbons®, Algibons and Pecbons, giving rise to high surface areas of up to 2452 m^2 g^{-1} and a high percentage of microporosity of up to 95%. Hierarchically activated materials with enhanced micropores and partly preserved mesopores can be produced when mild activation conditions are used, for example using a relatively low activation temperature or a small amount of potassium hydroxide. Carbon dioxide and oxygen activations are green and energy saving processes. The precursors and the activation conditions both have significant effects on the burn-off values and as a result on the surface area and pore size configuration of the activated materials. Both micropores and mesopores were well developed by carbon dioxide activation, resulting in ultrahigh surface areas of up to 2733 m^2 g^{-1} and high porosities with total pore volumes up to 2.1 cm^3g^{-1} in the hierarchically activated materials. Materials with relatively high surface areas and porosities can be prepared when the precursor was activated under severe conditions. Oxygen (diluted air) activation presents high energy savings compared to activation with potassium hydroxide or carbon dioxide. It shows the advantage of rapidly developing micropores but the disadvantage of destroying part of mesopores. For all these three activation strategies, the increase of small sized pores (ultramicro- and micropores) was limited when high degrees of activation were employed.

Chapter 3: Application of Hierarchically Porous Starbon® Materials to CO_2 Capture

3.1 Introduction

Mesoporous Starbons® have been shown to be good recyclable carbon dioxide adsorbents.[86] An adsorbent with a hierarchical pore structure would favour carbon dioxide adsorption and separation, as ultramicro- and micropores are efficient in selectively "sieving" large gas components and mesopores contribute to fast diffusion kinetics.

Therefore, in this chapter, the hierarchically activated Starbons®, which possess tailored micro and mesoporosities, were applied to carbon dioxide adsorption. The effect of different activating agents (potassium hydroxide, carbon dioxide and oxygen) and activation conditions on the textural properties and thus carbon dioxide uptake of the relevant materials was investigated through use of a simultaneous thermal analyser (STA) at 308 K and atmospheric pressure. Simultaneously, efforts were made to correlate the changes in the carbon dioxide adsorption capacity of Starbons® with their textural properties.

It should be noted that the percentage mass changes obtained experimentally were converted to moles per gram by assuming that the mass changes which occurred on switching the flow gas from nitrogen to carbon dioxide were all ascribed to carbon dioxide adsorption and that the effect of nitrogen desorption and buoyancy were negligible[313]. Volumetric nitrogen adsorption analysis confirmed that nitrogen adsorption by the activated Starbons® is negligible (as discussed in Section 3.2.9). S. Jribi et al. compared adsorption data obtained from thermogravimetric analysis before and after buoyancy correction at 30 °C and pressures up to 7 MPa. They concluded that a buoyancy correction is needed at higher pressures due to the increase of carbon dioxide density as the pressure increases. However, at low pressures (1 bar and below), no buoyancy correction is needed.[313]

The evaluation of the performance of a carbon dioxide adsorbent includes not only its adsorption capacity, but also the adsorption kinetics, cycle stability, ease of regeneration,

heats of adsorption, selectivity of adsorption, which are as important as the carbon dioxide adsorption capacity.[314] Therefore, in addition to the adsorption capacity, the regenerability of the materials over multiple adsorption-desorption cycles was investigated. The enthalpy of adsorption was calculated based on the experimental data of the changes in heat flow during carbon dioxide uptake. The adsorption kinetics of the samples at 308 K were determined using two commonly used kinetic models (Pseudo-first order and Pseudo-second order).

To obtain the static adsorption performance, the adsorption isotherms of pure carbon dioxide and nitrogen for S800 and some potassium hydroxide activated Starbons® were measured volumetrically in the range of 0-10 bar at 273, 298 and 323 K by collaborators at Fudan University, using a Quantachrome Isorb HP2 instrument. To acquire insight into the adsorption mechanism, the experimental pure carbon dioxide adsorption data was fitted to three standard isotherm models (Langmuir, Freundlich and Temkin). Based on the isotherm models, thermodynamic parameters (Gibbs free energy, enthalpy and entropy) were obtained by numerical analysis. The measurement of the adsorption isotherms at different temperatures allowed determination of the isosteric enthalpy of adsorption (Q_{st}), which indicates the strength of interaction between the adsorbent surface and adsorbate molecule. The selective adsorption of carbon dioxide over nitrogen in binary mixtures was evaluated based on the pure carbon dioxide and nitrogen isotherms according to the ideal adsorbed solution theory (IAST) method.

3.2 Results and Discussion

3.2.1 CO_2 Adsorption Capacity

The carbon dioxide adsorption of all the samples was investigated following the previously reported procedure[198] by using a simultaneous thermal analyser (STA) to measure

mass and heat flow changes during adsorption and desorption phenomena when the sample was alternately exposed to a steady flow of 60 ml min^{-1} of pure nitrogen or carbon dioxide.

The carbon dioxide adsorption was determined by measuring the change of the sample mass at atmospheric pressure and 308 K. Multiple adsorption and desorption cycles were run to determine the regenerability of the samples. The textural properties (ultramicropore surface area, t-plot micropore surface area, t-plot external surface area, BET surface area) and volume of pores in all sizes ranges) and corresponding carbon dioxide capture capacities (in both % and mmol g^{-1}) of all materials determined by STA are summarised in **Table 7.7** in **Appendix 7.2**.

3.2.1.1 CO_2 capture capacity of Starbons® prepared at different carbonisation temperatures

As shown in **Figure 3.1**, mass increases and positive heat flows coincide with the gas flow being changed from 100% nitrogen to 100% carbon dioxide until saturation adsorption is reached. Mass decreases and negative heat flows coincide with the gas flow being changed back to 100% nitrogen so that the sample was regenerated. Identical to the previously reported behaviour of Starbons® produced by the solvent exchange method,[198] Starbons® obtained by the freeze drying method showed completely reversible and extremely rapid carbon dioxide adsorption and desorption under constant temperature and pressure and gas-composition swing conditions. There is no visible carbon dioxide uptake decay after several cycles, indicating that the material is readily regenerated and easily reused in the next adsorption cycle. In addition, the freeze-drying method derived Starbons® show better carbon dioxide adsorption capacity compared to the solvent exchange method derived Starbons®. Specifically, the carbon dioxide uptake of S600 and S800 produced by freeze drying are (4.7±0.2)% ((1.07±0.05) mmol g^{-1}) and (7.0±0.1)% ((1.59±0.02) mmol g^{-1}), whereas S650

and S800 obtained by the solvent exchange method were reported to be 4.0 and 4.5%, respectively[198].

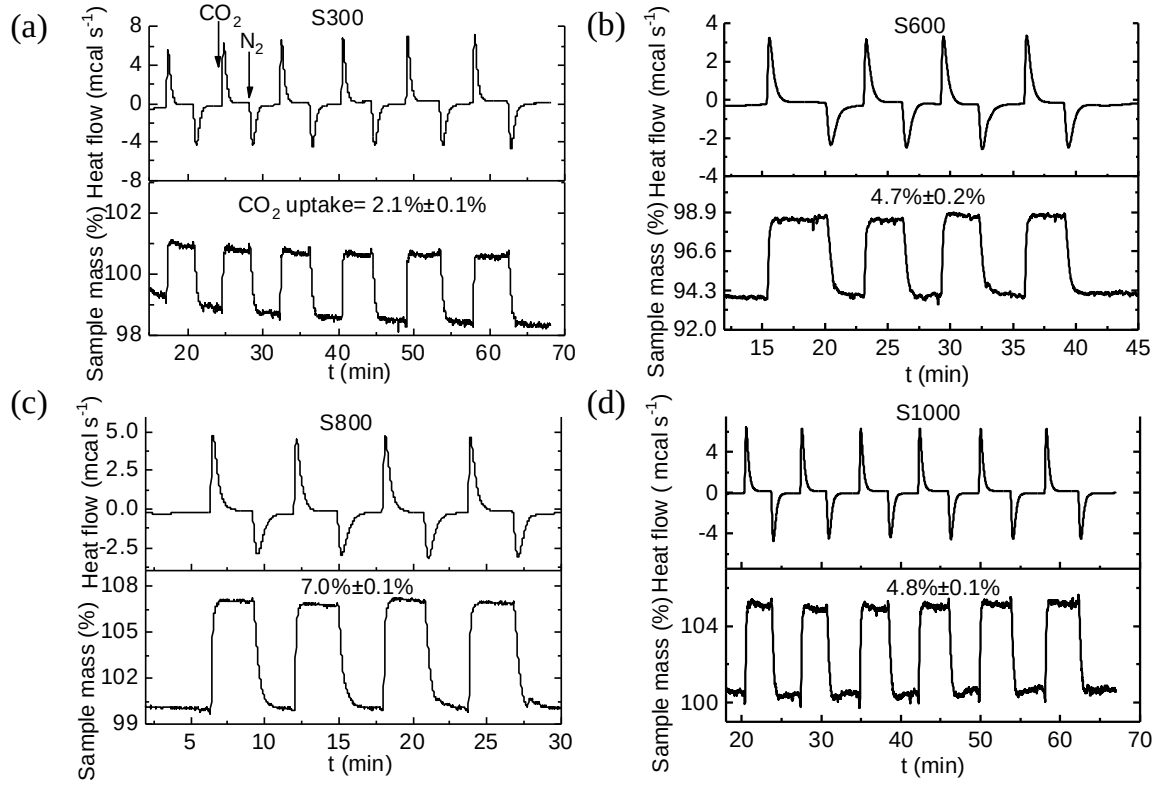

Figure 3.1 STA plots of mass and heat flow change over multiple cycles of CO_2 adsorption and desorption onto (a) S300, (b) S600, (c) S800 and (d) S1000 at 308 K.

To have a better understanding of the factors that determine the carbon dioxide capture capacity, the dependence of carbon dioxide adsorption capacity on surface areas (including t-plot micropore surface area and external surface area) and pore volume (in all size ranges) of Starbons® prepared at different carbonisation temperatures were investigated as shown in **Figure 3.2**. By comparison of the carbon dioxide uptake capacities and textural properties of Starbons®, it can be concluded that it is a combination of factors including the presence of ultramicropores (<0.7 nm) and micropore surface area that contribute to the high carbon dioxide uptake capacity.

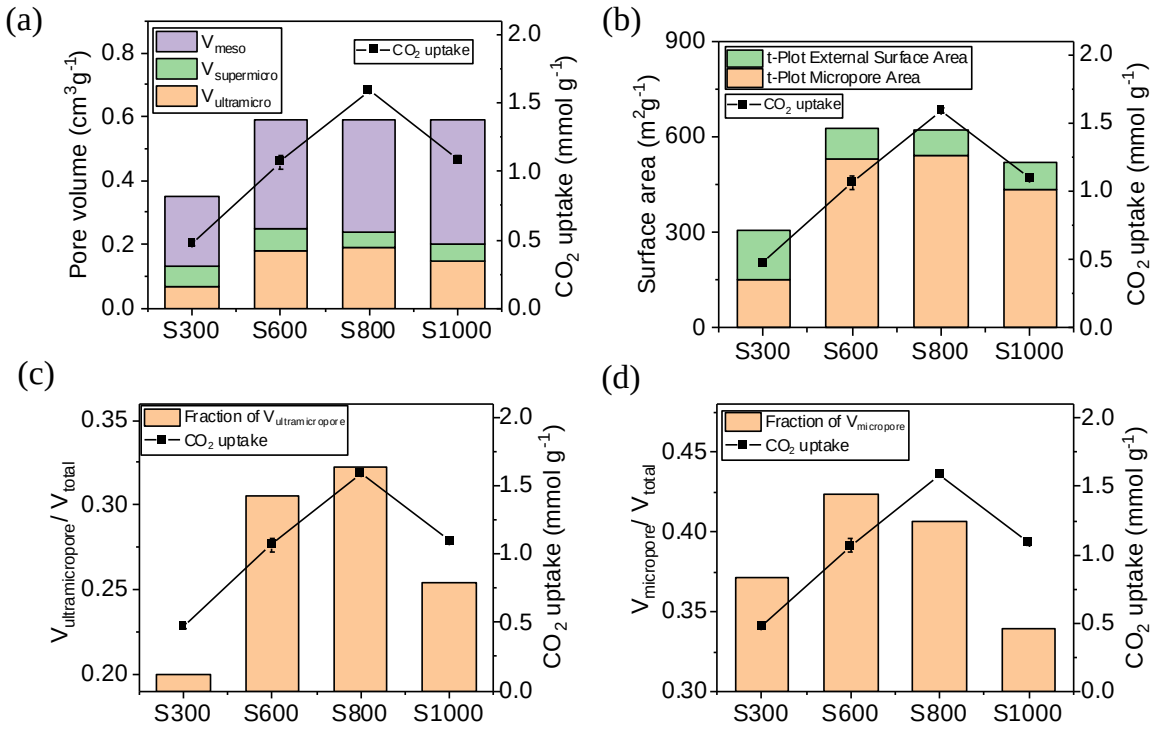

Figure 3.2 Correlation between CO_2 uptake (308 K, 1 bar) and (a) pore volume, (b) surface area (micropore area and external surface area were calculated by the t-plot method), (c) ultramicroporosity and (d) microporosity of Starbons® prepared at different carbonisation temperatures.

Ultramicropores are known to be favourable for the adsorption of carbon dioxide at low-pressure compared to supermicropores or mesopores. Due to the influence of Van de Waals forces and short-range interactions (attractive and repulsive forces), the adsorption potential in narrow pores is stronger which make the pore-filling processes more facile. A mesoporous structure is also believed to be beneficial in carbon dioxide adsorption as mesopores serve as passages for the adsorbate molecules to reach micropores.[315] However, the mesopore volume and the external surface area seems not to be directly associated with the change in carbon dioxide adsorption capacity. S800 exhibits the optimal carbon dioxide adsorption, corresponding to it possessing the highest micropore surface area, ultramicropore volume and percentage of ultramicropores.

3.2.1.2 CO_2 capture capacity of KOH activated Starbons®

All of the potassium hydroxide activated Starbons® also show completely reversible and extremely rapid carbon dioxide adsorption and desorption under the same gas-composition swing conditions (**Figure 3.3**). In addition, they all exhibit enhanced carbon dioxide adsorption capacity compared with the non-activated Starbon® carbonised at the same temperature. The potassium hydroxide activated Starbons® exhibit a gradual increase and then decrease of adsorption capacity as the mass ratio of S300 to potassium hydroxide increases from 1:1 to 1:5. Amongst them, S800K2 exhibits double and seven times the carbon dioxide adsorption capacity (13.7±0.2)% ((3.11±0.05) mmol g^{-1}) compared to S800 (7.0%) and reported Norit activated carbon (~2%)[198], revealing the potential of activated Starbons® in carbon dioxide adsorption.

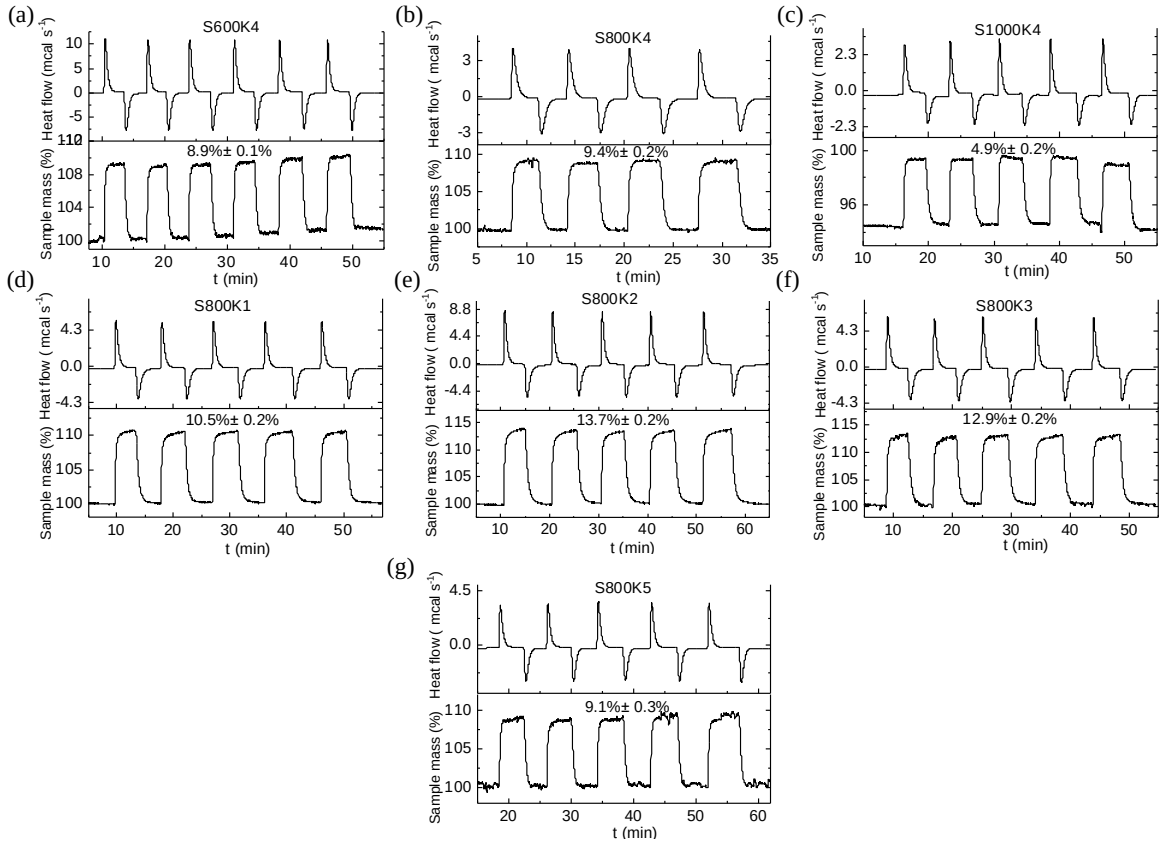

Figure 3.3 STA plots of mass and heat flow changes over multiple cycles of CO_2 adsorption and desorption onto KOH activated Starbons®.

The dependence of carbon dioxide adsorption capacity on the porosities of the potassium hydroxide activated Starbons® were investigated as shown in **Figure 3.4**. In agreement with the above discussion, **Figure 3.4** shows that S600K4 and S800K4 exhibit higher carbon dioxide capture capacities than S1000K4, attributed to the effect of their higher micropore surface areas, ultramicropore volumes and ultramicroporosities. For the comparison of S800K(1-5), it is of interest that S800K2 exhibits an extremely high carbon dioxide capacity, whilst it has only a moderate surface area and porosity (S_{BET}= 1294 m^2 g^{-1}, S_{micro}= 1177 m^2 g^{-1}, V_{total}= 0.59 cm^3 g^{-1}, V_{micro}= 0.49 cm^3 g^{-1}, $V_{ultramicro}$= 0.39 cm^3 g^{-1}) compared to the other highly activated samples (S800K3–5). This is because S800K2 possesses an extraordinarily high content of ultramicropores (66%) as well as a high micropore surface area, which both play crucial roles in efficient carbon dioxide capture. For enhancement of the carbon dioxide adsorption capacity at a relative low pressure, micropore filling is the predominant adsorption process and requires a fine porous structure with substantial amounts of ultramicropores and a high micropore surface area.

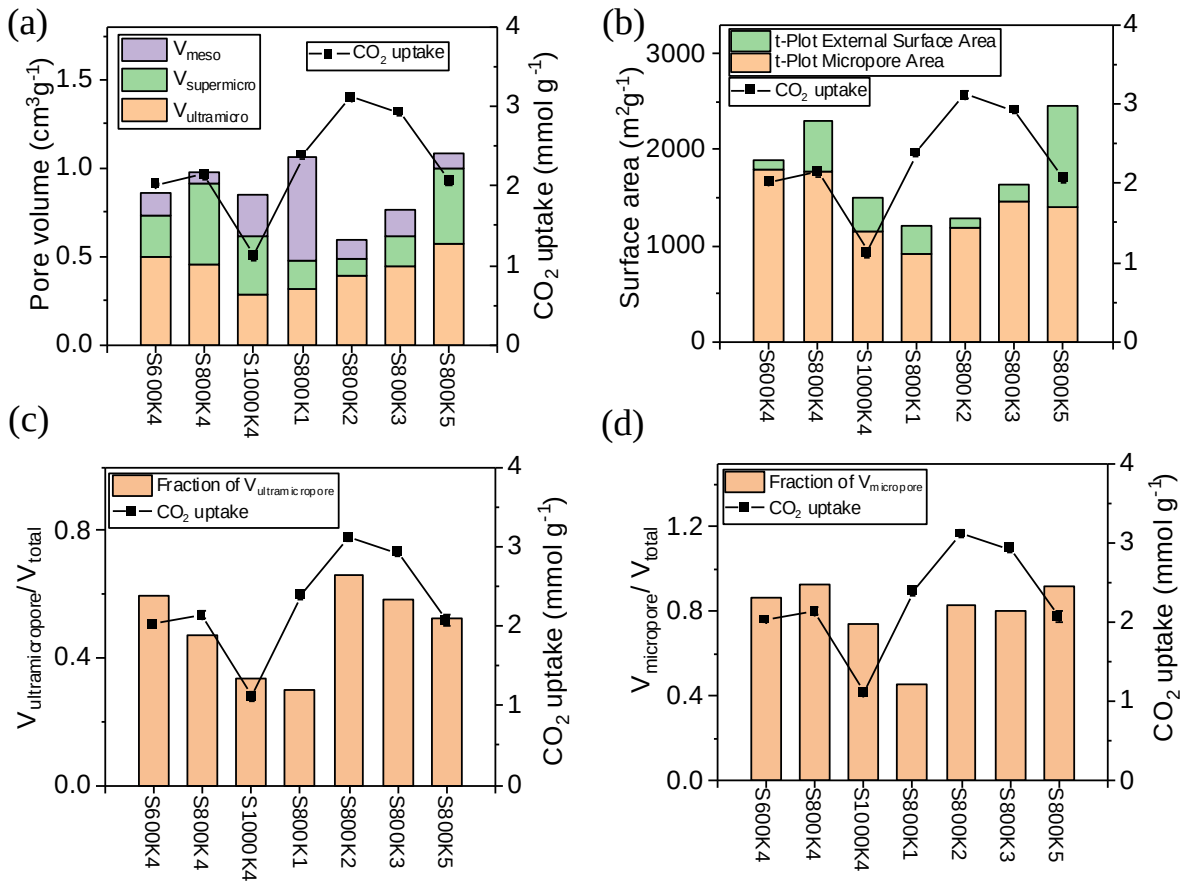

Figure 3.4 Correlation between CO_2 uptake (308 K, 1 bar) and (a) pore volume, (b) surface area, (c) ultramicroporosity and (d) microporosity of KOH activated Starbons®.

3.2.1.3 CO_2 capture capacity of KOH activated Algibons and Pecbons

The carbon dioxide capture capacities of A800, P800 and potassium hydroxide activated Algibons and Pecbons are shown in **Figure 3.5**. A800 and P800 show inferior carbon dioxide adsorption capacities of (6.0±0.1)% ((1.36±0.02) mmol g^{-1}) and (4.7±0.1)% ((1.07±0.02) mmol g^{-1}) compared to S800 (7.0%). However, similarly to Starbons®, the potassium hydroxide activated Algibons and Pecbons had enhanced carbon dioxide capture capacity compared to the non-activated materials.

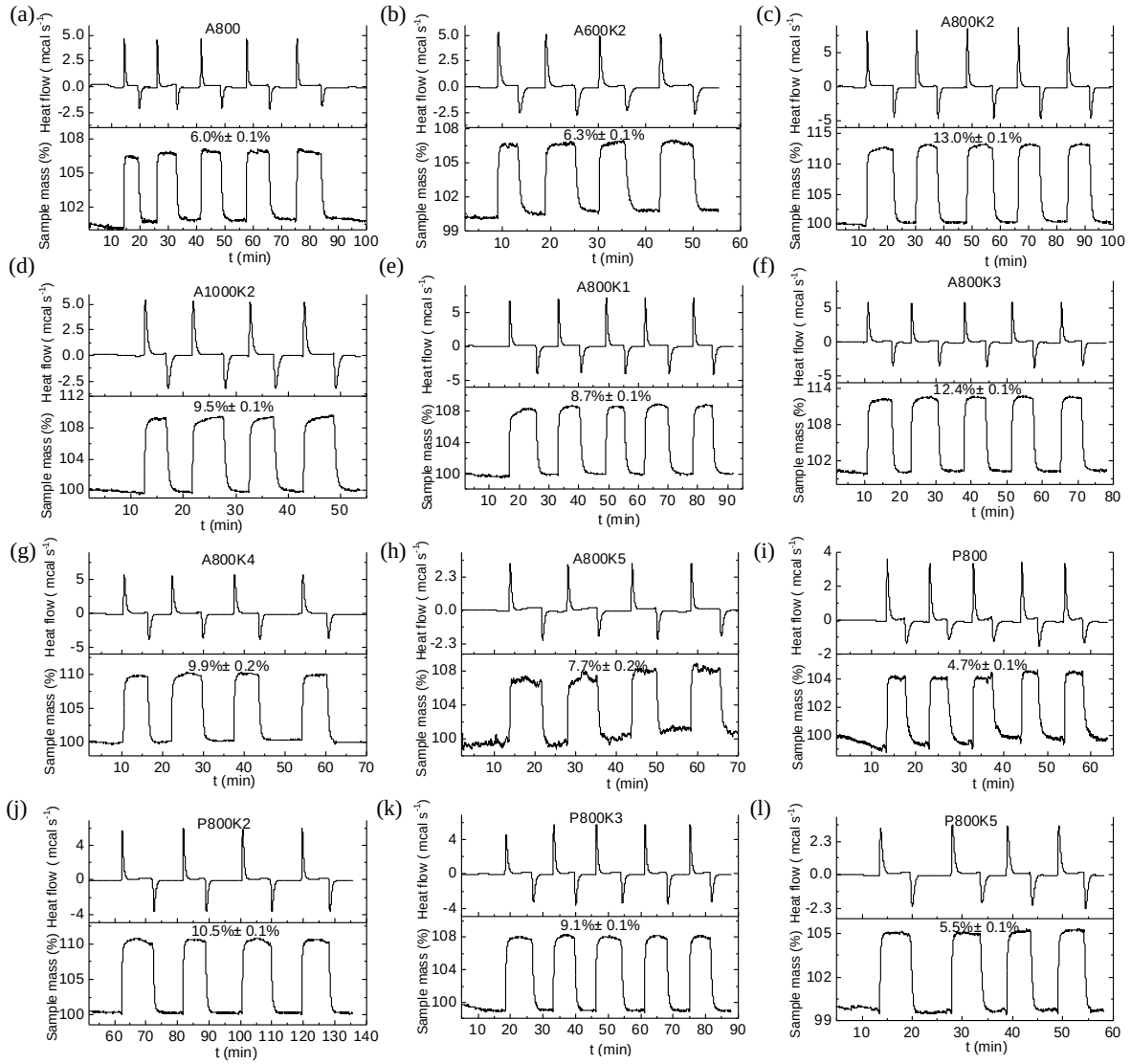

Figure 3.5 STA plots of mass and heat flow changes over multiple cycles of CO_2 adsorption and desorption onto (a) A800, (b-h) KOH activated Algibons, (i) P800 and (j-l) KOH activated Pecbons at 308 K.

For Algibons, 800 °C is the optimal activation temperature and A800K2 exhibits the optimal carbon dioxide adsorption of (13.0±0.1)% ((2.95±0.02) mmol g^{-1}). When the activation was conducted at 800 °C whilst varying the mass ratio of A300 and potassium hydroxide from 1:1 to 1:5, the adsorption capacity also shows first an increase and then decrease with A800K2 (mass ratio of 1:2) having the highest carbon dioxide adsorption capacity. For Pecbons, the same mass ratio of 1:2 also makes P800K2 exhibit the most prominent adsorption in the series of activated Pecbons. Interestingly, all the materials

activated by potassium hydroxide with a mass ratio of 1:2 (precursor: potassium hydroxide) exhibit about double the carbon dioxide uptake of the corresponding non-activated materials.

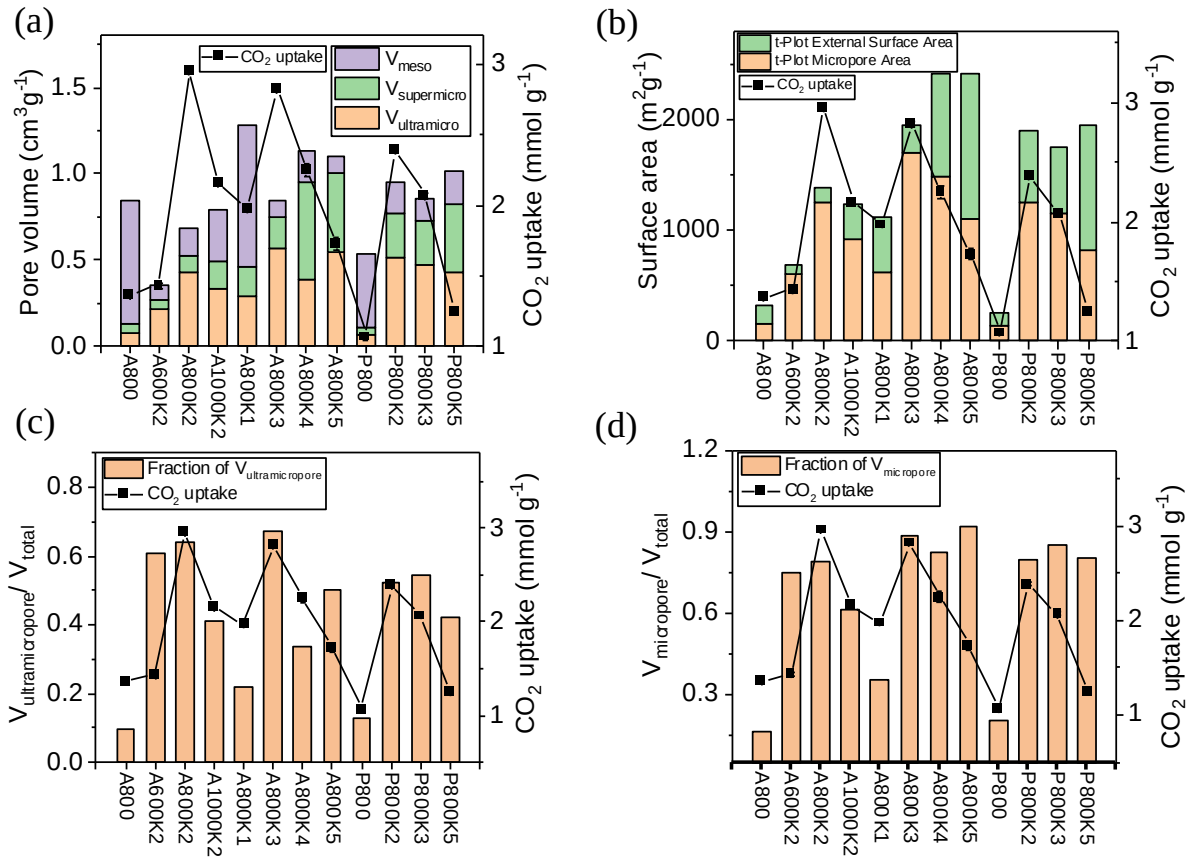

Figure 3.6 Correlation between CO_2 uptake (308 K, 1 bar) and (a) pore volume, (b) surface area, (c) ultramicroporosity and (d) microporosity of KOH activated Algibons and Pecbons.

The dependence of carbon dioxide adsorption capacity on the textural properties of the potassium hydroxide activated Algibons and Pecbons is shown in **Figure 3.6**. Compared to non-activated A800 and activated A600K2 and A1000K2, A800K2 exhibits the highest carbon dioxide capture capacity due to it having the highest ultramicropore volume and micropore surface area; whereas the effect of larger pores and the external surface area are negligible. When comparing potassium hydroxide activated Algibons and Pecbons with different mass ratios of precursor and potassium hydroxide: the presence of ultramicropores

and the micropore surface area also appear to be playing predominant roles. Larger pores with pore sizes above 0.7 nm becomes less important in determining the carbon dioxide capture capacity.

3.2.1.4 CO_2 capture capacity of CO_2 activated Starbons®

Compared to non-activated S800, most of the carbon dioxide activated Starbons® have higher carbon dioxide capacities (**Figure 3.7**), demonstrating the effectiveness of carbon dioxide activation. The adsorption capacity of the activated Starbon® improved as the activation temperature increased from 800 to 900 °C, followed by a decrease with further increasing the temperature to 950 or 1000 °C. As a result, Starbon® activated at 900 °C achieved the highest carbon dioxide adsorption capacity of (8.7±0.2)% ((1.98±0.05) mmol g^{-1}), which outperformed the non-activated S800 (1.59±0.02) mmol g^{-1} by 24%. However, excessive activation times lead to degradation of the adsorption capacity of the sample, especially under the combined effect of high temperature and long activation time (e.g., 950 °C and 90 min or 950 °C and 120 minutes).

The correlation of the carbon dioxide uptake and the textural properties of the carbon dioxide activated Starbons® are shown in **Figure 3.8**. The change of the carbon dioxide capture capacity amongst the materials is mostly consistent with the changes in their ultramicroporosity (**Figure 3.8c**) and to some extent of their micropore surface area. Moderate activation conditions lead to the creation of ultramicro-, micro- and mesopores. However, over burn-off of carbon under extreme conditions leads to greater development of meso- and macropores. As a result, the ultramicroporosity is amongst the highest when the samples were activated at 900 °C for only 15 minutes, corresponding to the highest carbon dioxide uptake of (1.98±0.05) mmol g^{-1} for S900C15. However, due to its limited ability to increase the ultramicroporosity (to at most 42%) and micropore surface area (to at best 745

m^2g^{-1}), carbon dioxide activation is inferior to potassium hydroxide activation which achieves 66% ultramicroporosity and a micropore surface area of 1,177 m^2g^{-1} for S800K2.

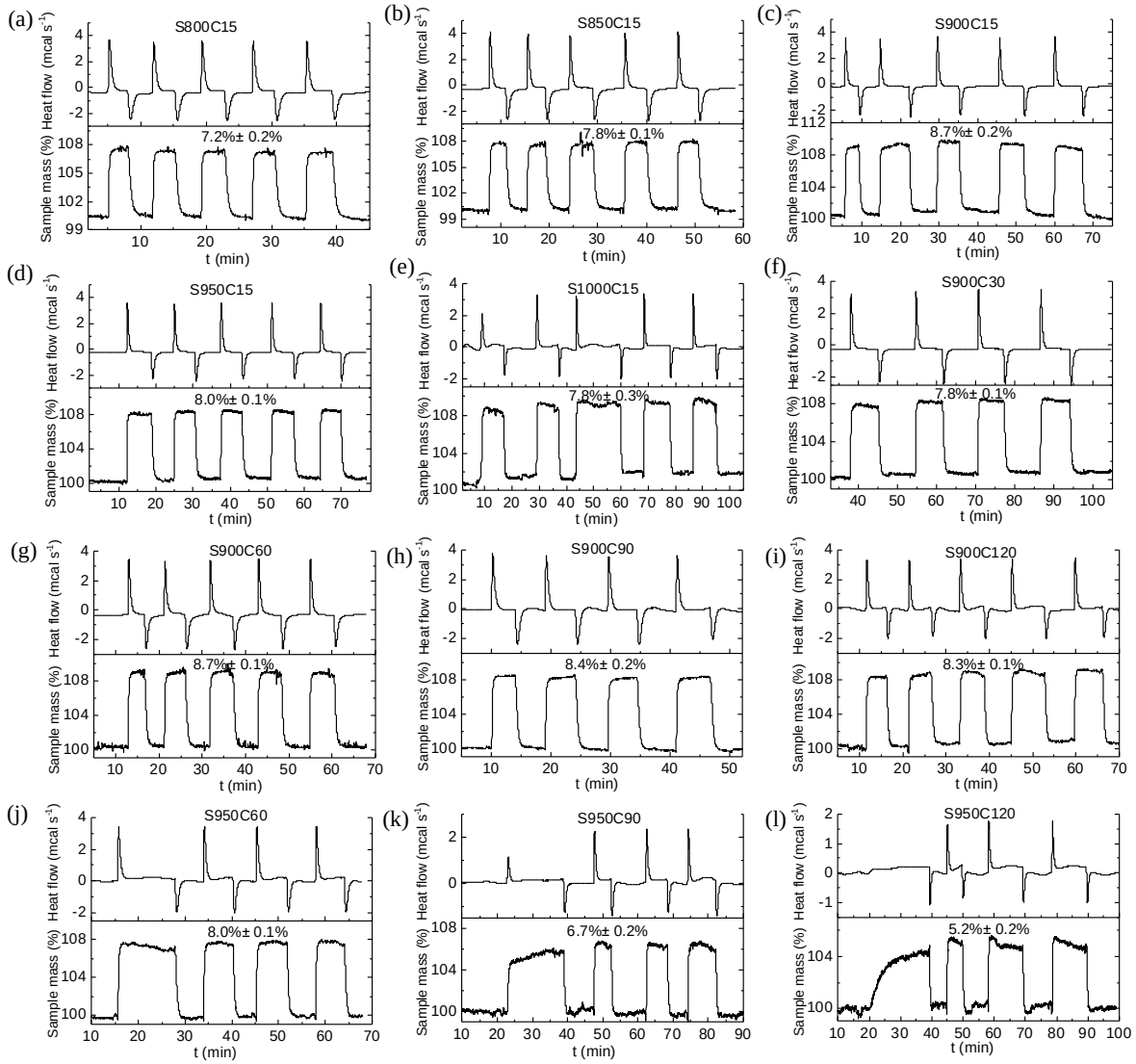

Figure 3.7 STA plots of mass and heat flow changes over multiple cycles of CO_2 adsorption and desorption at 308 K onto CO_2 activated Starbons®.

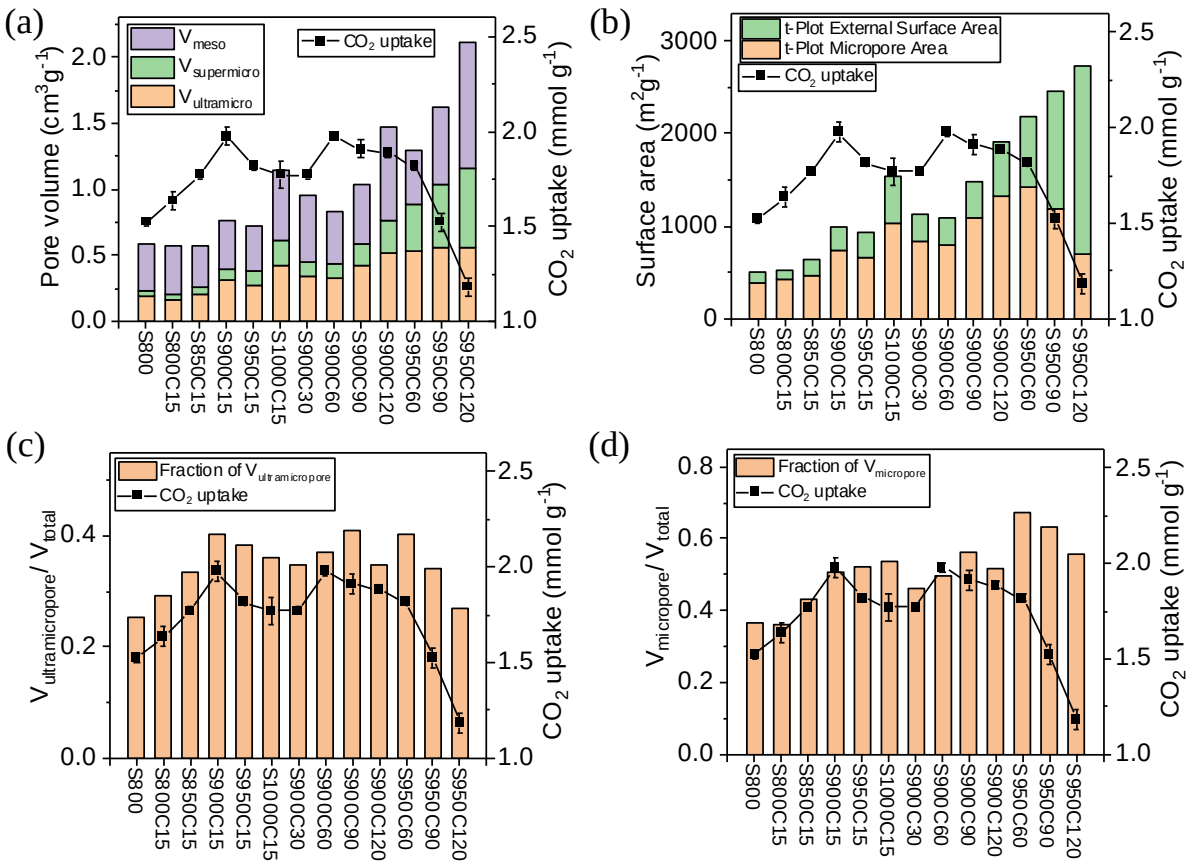

Figure 3.8 Correlation between CO_2 uptake (308 K, 1 bar) and (a) pore volume, (b) surface area, (c) ultramicroporosity and (d) microporosity of CO_2 activated Starbons®.

3.2.1.5 CO_2 capture capacity of CO_2 activated Algibons and Pecbons

Similarly to Starbons®, the carbon dioxide capture capacity of Algibons and Pecbons activated by carbon dioxide is not enhanced as much as by potassium hydroxide activation. As shown in **Figure 3.9**, the carbon dioxide capture capacity increased slightly when A800 was activated using carbon dioxide at 750 °C and P800 was activated at 700 °C and 900 °C. However, the over burn-off of the A800 under severe conditions (e.g. 900 °C for 10 minutes) results in a decline in the adsorption capacity of the resultant materials (A900C10).

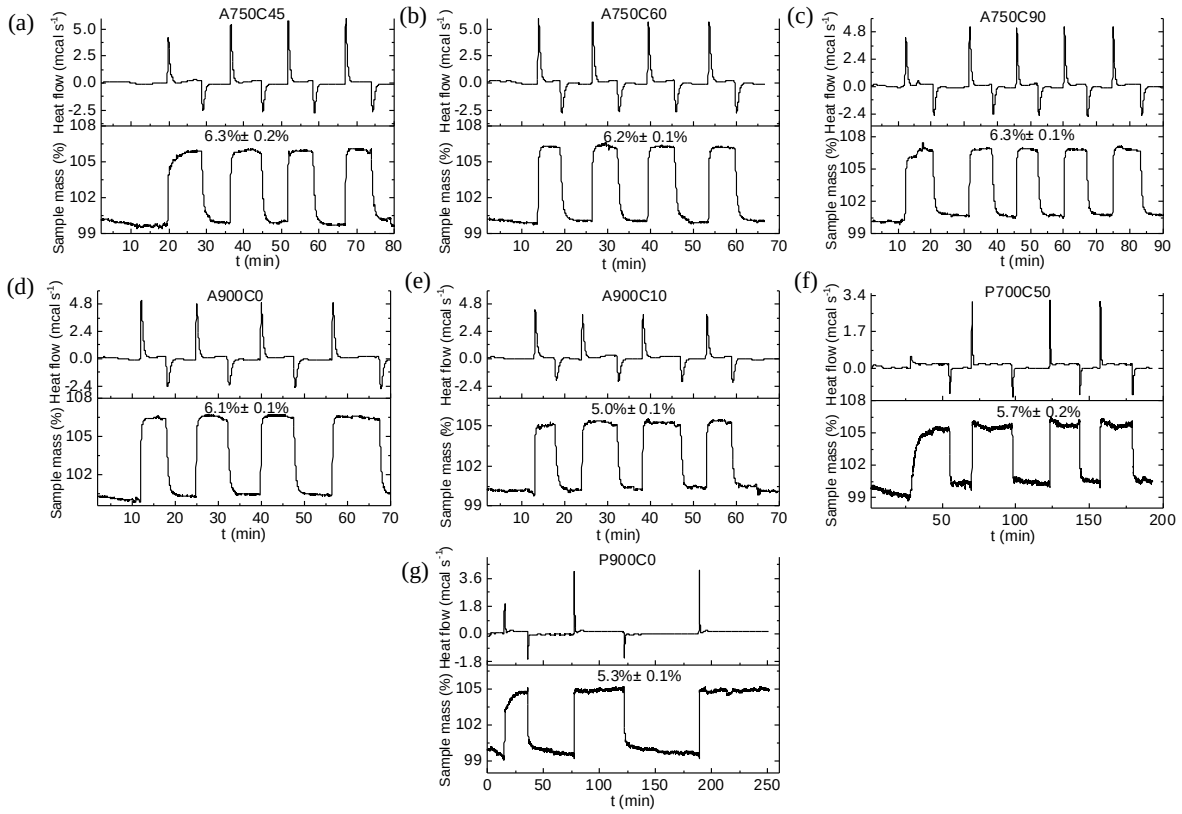

Figure 3.9 STA plots of mass and heat flow change over multiple cycles of CO_2 adsorption and desorption at 308 K onto CO_2 activated Algibons and Pecbons.

Figure 3.10 shows that the variation of carbon dioxide uptake of the materials is consistent with the change in their ultramicroporosity and micropore surface area. The number of ultramicropores in the activated Algibons and Pecbons created by carbon dioxide activation were essentially unchanged, whilst larger pores with pore size larger than 0.7 nm were increasingly developed under progressively more severe conditions. The greater degree of growth of the larger pores results in a decline of the ultramicroporosity in A900C10 and P900C0, corresponding to lower carbon dioxide uptakes. Likewise, a higher activation temperature and a longer activation time leads to a greater increase of total surface area, but there is less increase of the micropore surface area.

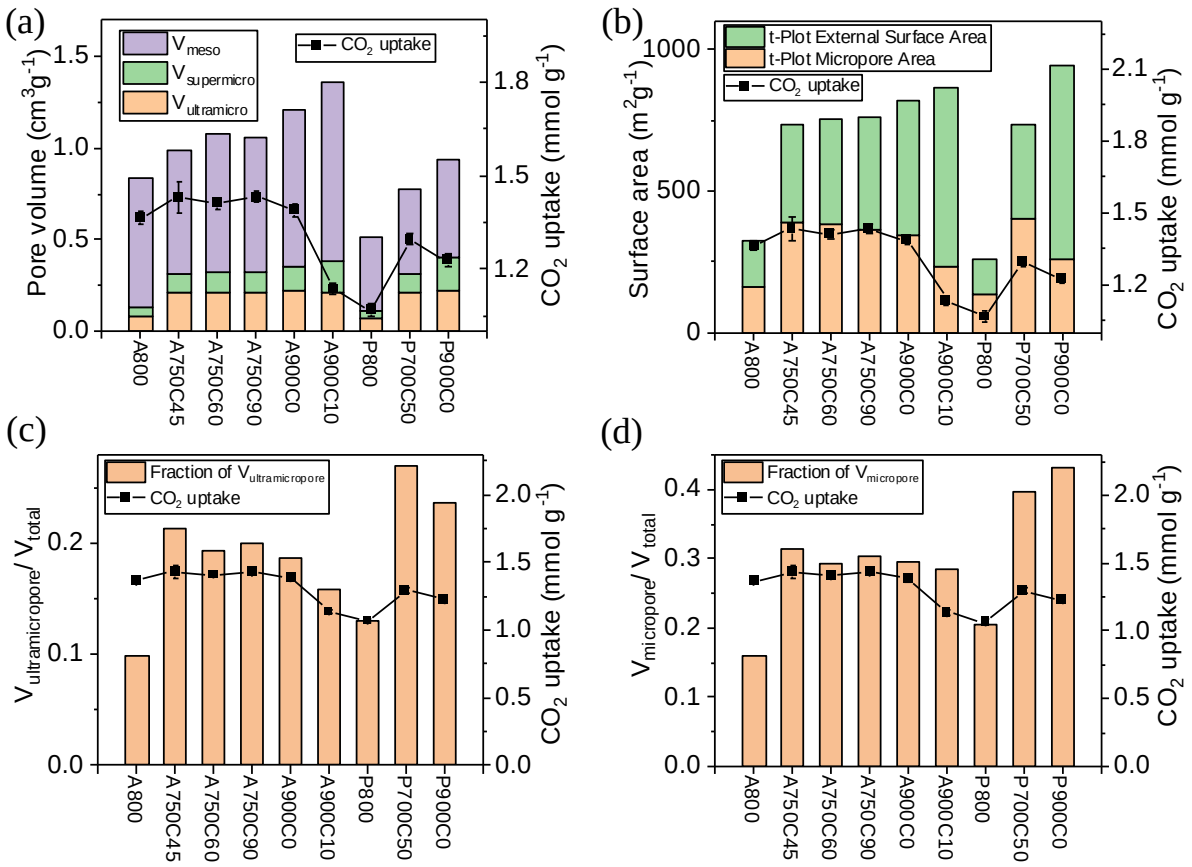

Figure 3.10 Correlation between CO_2 uptake (308 K, 1 bar) and (a) pore volume, (b) surface area, (c) ultramicroporosity and (d) microporosity of CO_2 activated Algibons and Pecbons.

3.2.1.6 CO_2 capture capacity of O_2 activated Starbons®, Algibons and Pecbons

The influence of oxygen activation on the adsorption capacity of Starbons® is similar to that of carbon dioxide activation, with the carbon dioxide adsorption capacity fluctuating in the same range of (8-9)% ((1.82-2.05) mmol g^{-1}). Mild activation conditions are more conducive to improve the carbon dioxide uptake of Starbons®. Amongst these materials, **Figure 3.11** shows that S750O0 has the highest adsorption capacity of (8.9±0.1)% ((2.02±0.02) mmol g^{-1}), which is 27% higher than that of non-activated sample S800. In

contrast, for both Algibons and Pecbons, similar carbon dioxide adsorption capacities are observed between the non-activated and activated materials. Therefore, the influence of oxygen activation on the carbon dioxide uptake of Algibons and Pecbons is not significant within the range of conditions studied.

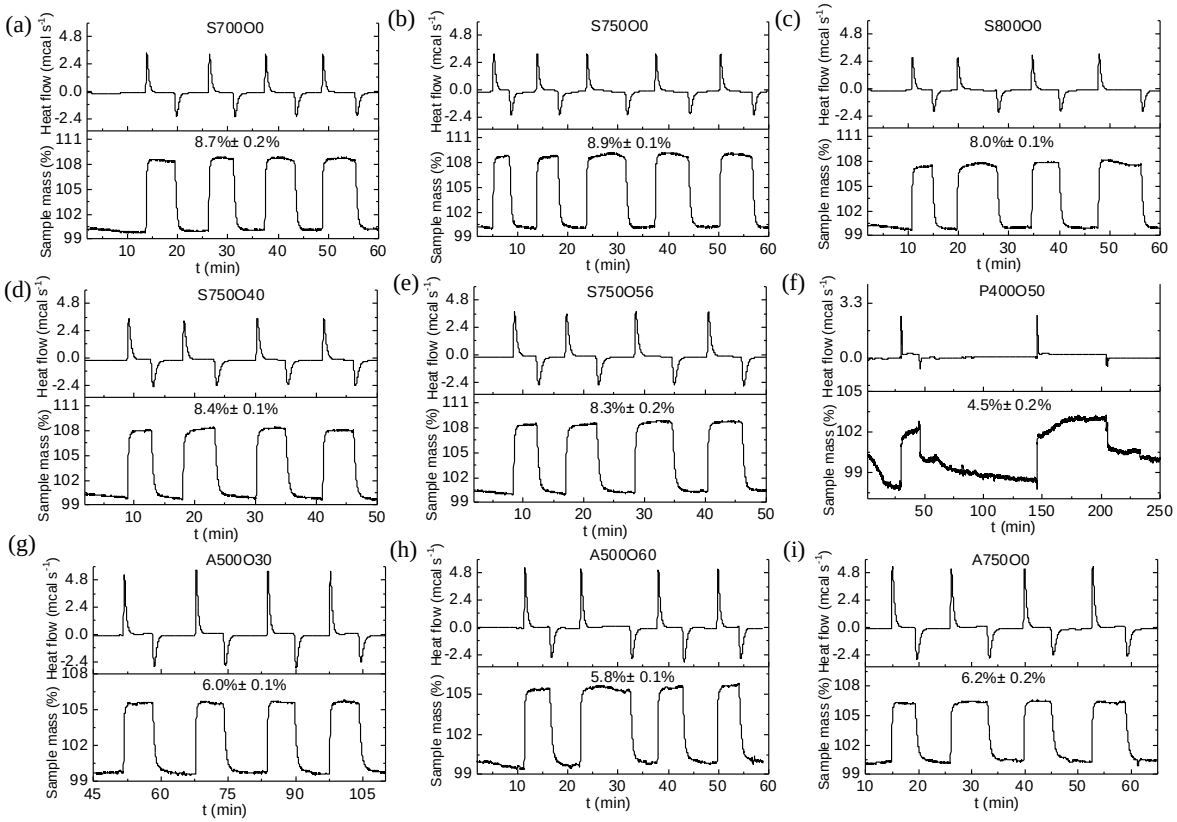

Figure 3.11 STA plots of mass and heat flow change over multiple cycles of CO_2 adsorption and desorption at 308 K onto O_2 activated Starbons®, Algibons and Pecbons.

The change of carbon dioxide adsorption capacities of the Starbons® shows the same trend as the ultramicro and microporosity and the micropore surface area as shown in **Figure 3.12**. Although the mesoporous structures were well developed for Algibons and Pecbons, their poor ultramicro- and microporous structure led to their poor adsorption performance compared to Starbons®. The slow and irreversible desorption of carbon dioxide in P400O50 is attributed to the high magnitude of its enthalpy of adsorption as discussed in **Section 3.2.3**.

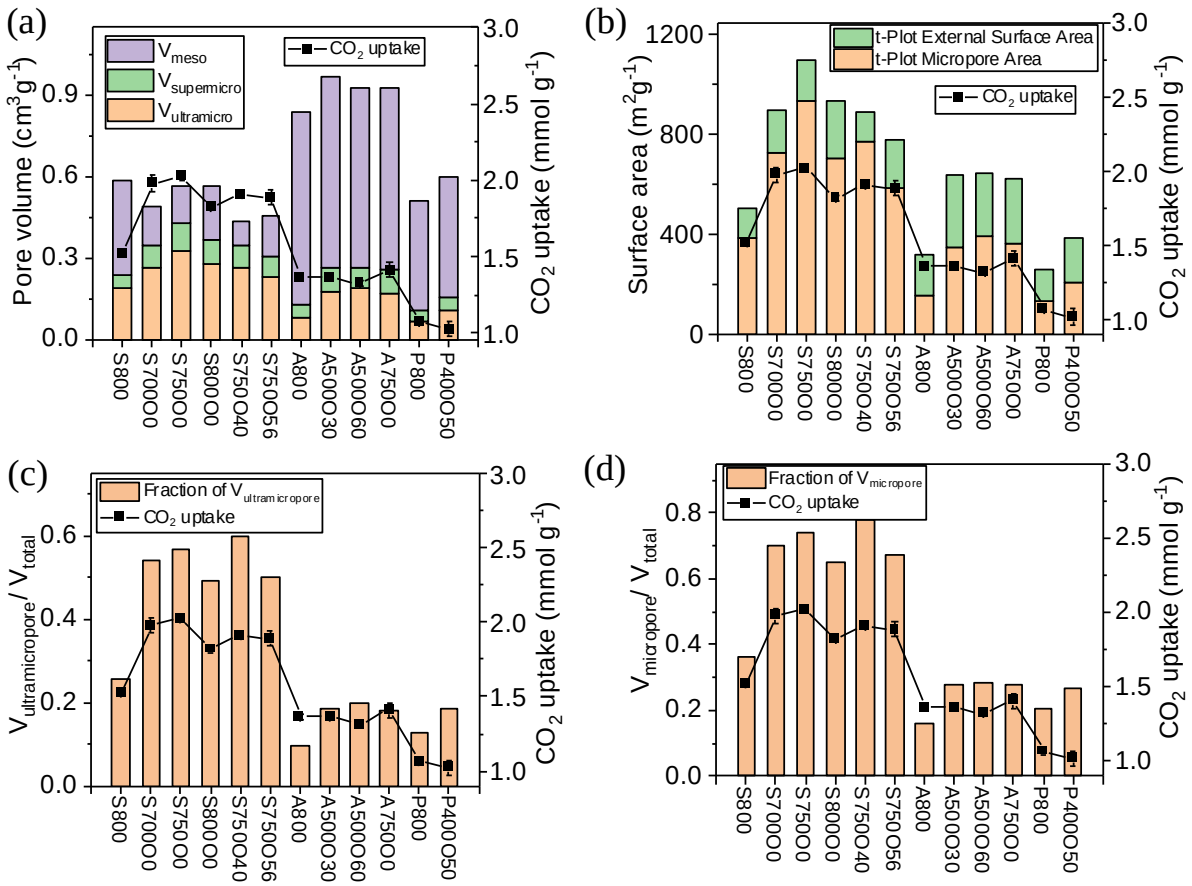

Figure 3.12 Correlation between CO_2 uptake (308 K, 1 bar) and (a) pore volume, (b) surface area, (c) ultramicroporosity and (d) microporosity of O_2 activated Algibons and Pecbons.

3.2.2 Correlation between CO_2 Capture Capacities and Textural Properties of Adsorbents

To better understand the carbon dioxide adsorption behaviors of the Starbon® materials, the correlation of their carbon dioxide adsorption capacities with their surface areas and hierarchical porosities in more detail were further investigated (**Figure 3.13** and **Figure 7.4** in **Appendix 7.2).** The detailed porosity and carbon dioxide adsorption values are presented in **Table 7.7** in **Appendix 7.2**. Plots of the carbon dioxide uptake capacities against the porosity characteristics of the materials showed that the carbon dioxide uptake of the samples

is not determined by meso- or total pore volume or BET total surface area (**Figure 7.4**), but is correlated to the ultramicroporosity (0.4-0.7 nm) and micropore surface area (**Figure 3.13 a,e)**. Since no single parameter gave a strong correlation with the carbon dioxide adsorption capacity, correlations involving combinations of two parameters were investigated. The product of the ultramicropore surface area and the ratio of volume of pores with 0.4-0.7 nm diameter to total pore volume was found to give a best linear correlation with the carbon dioxide capacity for all the materials (**Figure 3.13f**).

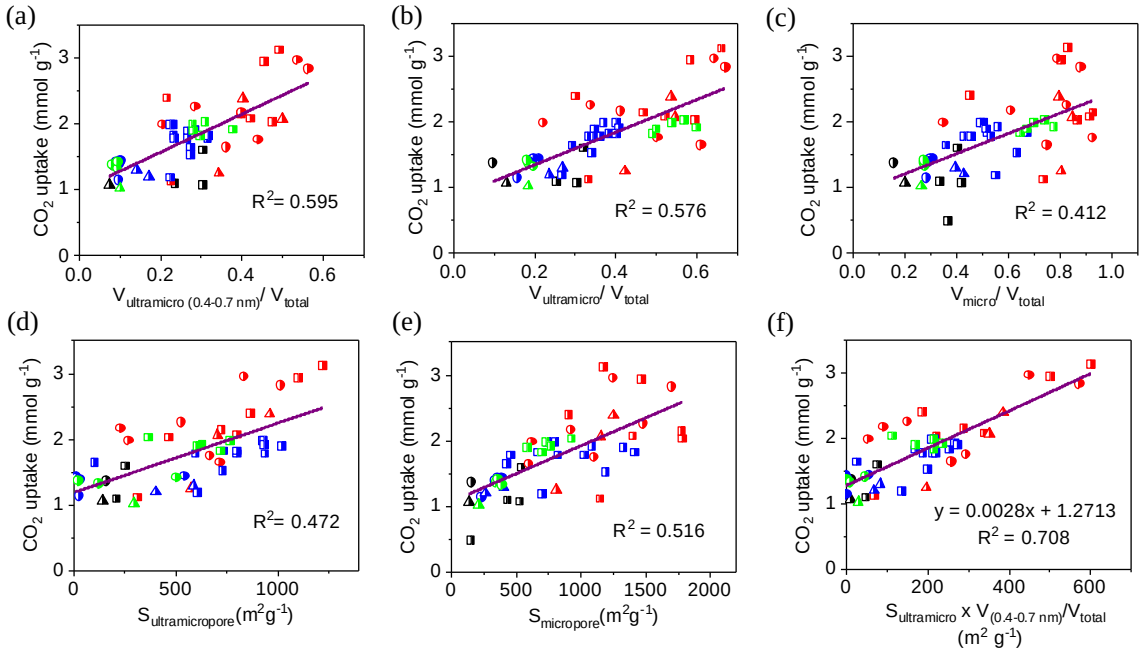

Figure 3.13 CO_2 uptake (1 bar, 308 K) versus (a) ultramicropore (0.4-0.7 nm) ratio, (b) ultramicropore (<0.7 nm) ratio, (c) micropore (<2 nm) ratio, (d) ultramicropore surface area, (e) micropore surface area and (f) ultramicropore surface area x ultramicropore (0.4-0.7 nm) ratio of all materials studied in this work. Stars, squares, circles and triangles represent commercial AC, Starbons®, Algibons and Pecbons, respectively; colours in black, red, blue and green represent non-activated, KOH activated, CO_2 activated and O_2 activated materials, respectively.

This correlation suggests that for efficient carbon dioxide adsorption at ambient

temperature and pressure, the pore size of an adsorbent must be large enough to accommodate more than one layer of gas molecules (0.4-0.7 nm), considering that the kinetic diameter of carbon dioxide molecules is 0.33 nm.[190] However, an excessive width of slit pores would lead to a decrease of the loading of gas molecules due to the decreased overlapping of potentials from neighbouring walls and carbon dioxide and wall atoms in the pores.

In addition, the adsorption of carbon dioxide by the Starbon® materials only partially fills their ultramicropores, giving a dependence on ultramicropore volume (corresponding to filled pores) and ultramicropore surface area (corresponding to partially filled pores). This leaves space available in the ultramicropores and larger micropores to accommodate more carbon dioxide at higher pressures. The role of large micropores (0.7-2 nm) and even mesopores (2-50 nm) in carbon dioxide capture at increased pressure were investigated in section 3.2.5.

3.2.3 Enthalpy of CO_2 Adsorption Calculated Based on Calorimetric Data

The isosteric enthalpy of adsorption, ΔH_{ads} or Q_{st} ($\Delta H_{ads} = -Q_{st}$) is also an important parameter for evaluating an adsorbent in carbon dioxide capture applications. It provides deeper insights into the interaction of the adsorbent and gas molecules.[316] The isosteric enthalpy of adsorption is defined as the heat released or required when an adsorptive molecule adsorbs or desorbs from an adsorbent surface. ΔH_{ads} can be used to determine the regeneration energy for the desorption of the adsorbate. For physisorption, the enthalpy of desorption (ΔH_{des}) is the reverse of the enthalpy of adsorption ($\Delta H_{des} = -\Delta H_{ads}$).

There are two approaches to determine the ΔH_{ads}: calculation based on experimental

data and molecular simulation. For the former method, the ΔH_{ads} can be calculated directly from the released heat using a calorimetric-thermogravimetric system and it represents the average heat of adsorption. For the latter method, the ΔH_{ads} as a function of adsorption amount is generally determined either via the Clausius-Clapeyron approach or by virial analysis using adsorption isotherms, which provide the isosteric heat of adsorption as a function of surface coverage.

The enthalpy of carbon dioxide adsorption was investigated by both methods in this research. Firstly, the change of heat flow during the carbon dioxide adsorption process determined by differential scanning calorimetry (DSC) in the STA instrument was used to calculate the enthalpy of adsorption. The enthalpy of adsorption of each material can be calculated by integration of the peak of the heat flow change in the differential scanning calorimetry measurement, in conjunction with the change of mass measured by thermogravimetric analysis. The percentage mass changes obtained experimentally were converted to moles per gram by assuming that the mass changes which occurred on switching the flow gas from nitrogen to carbon dioxide were only due to carbon dioxide adsorption. Therefore, the carbon dioxide molar adsorption values calculated and used in the enthalpy calculations may be slightly lower than the true values, which may lead to a slight overestimation of the enthalpies. The enthalpy values of carbon dioxide adsorption on Starbons®, Algibons and Pecbons are shown in **Figure 3.14** and **Table 7.7**.

A high magnitude for the enthalpy of adsorption is indicative of a strong interaction between the pore surface and carbon dioxide molecules. The enthalpy of carbon dioxide adsorption on Starbons® and Algibons have magnitudes in the range of 25-54 KJ mol^{-1}, indicating the moderately strong interactions of carbon dioxide with the adsorbents and the fully reversible physisorption of carbon dioxide: with in the optimal range of physisorption of 30-60 KJ mol^{-1}.[317] The corresponding magnitudes for adsorption onto the carbon dioxide and

oxygen activated Pecbons are higher (69 KJ mol^{-1} for P700C50 and 74 KJ mol^{-1} for P400O50). The high magnitude enthalpy can be attributed by the electrostatic interactions of metallic ions in the samples with carbon dioxide (12.0 and 4.9% of metallic ions in P700C50 and P400O50, respectively, as shown in **Table 2.18** and most of which are sodium and potassium).

Obvious variations of the enthalpies of adsorption between materials activated by different methods are observed. Potassium hydroxide activated materials exhibit the highest carbon dioxide capture capacities but have enthalpies of adsorption of smaller magnitude than the non-activated, carbon dioxide and oxygen activated materials. In contrast, carbon dioxide activated materials have the highest magnitude enthalpies of adsorption even though they exhibit relatively low carbon dioxide capture capacities. This can be explained on the basis that the carbon dioxide activated materials physisorb relatively little carbon dioxide which can be adsorbed predominantly as a monolayer resulting in strong favourable interactions between the pore walls and the carbon dioxide molecules. Potassium hydroxide activated materials physisorb more carbon dioxide which requires multilayer binding of carbon dioxide within the pores. Therefore, the further adsorbed carbon dioxide molecules experience weaker favourable interactions with the cell walls resulting in a decrease of the magnitude of the average enthalpy of adsorption.

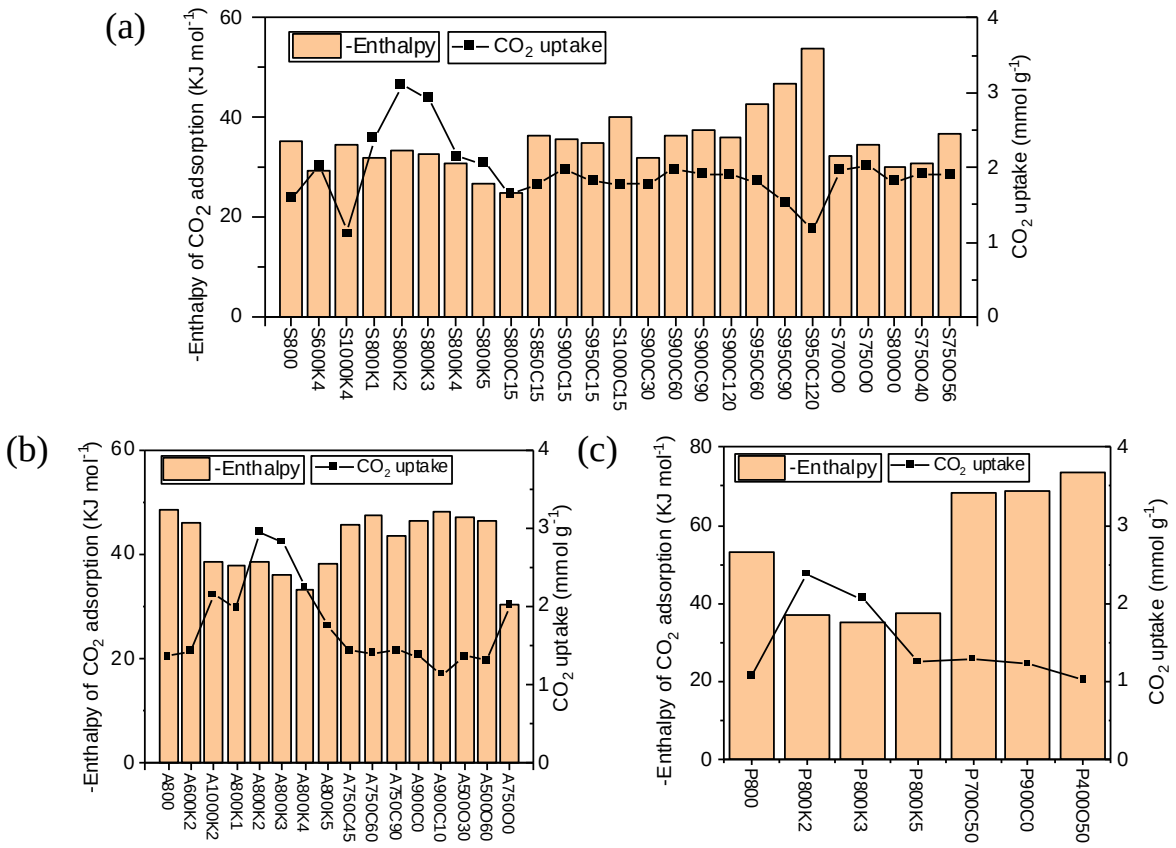

Figure 3.14 Enthalpy of CO_2 adsorption determined by heat flow change during STA measurement at 308K of (a) Starbons®, (b) Algibons and (c) Pecbons.

3.2.4 CO_2 Adsorption Kinetics

The adsorption kinetics provide additional important parameters to describe the adsorption behaviour of the adsorbent in carbon dioxide adsorption. They indicate the adsorption efficiency of an adsorbent towards carbon dioxide and gives information for predicting adsorption rates. Therefore, in order to determine the adsorption kinetics, the widely used pseudo-first order and pseudo-second order models (as shown in **Table 1.3**)[318] were applied to fit the experimental data obtained under a pure carbon dioxide flow as a function of time at 308 K (determined by STA). The experimental and predicted carbon dioxide uptakes and fitted kinetic parameters for the best performing material S800K2 and the

non-activated material S800 for carbon dioxide adsorption are shown in **Figure 3.15** and **Table 3.**1. The results for the other samples (except P400O0 for which the carbon dioxide adsorption was too low to allow accurate modelling of the kinetics) are shown in **Figure 7.5** and **Table 7.8** in **Appendix 7.2**.

As shown in **Figure 3.15** and **Figure 7.5**, the mass of all the samples increased rapidly (within 1 minute) once the samples were exposed to carbon dioxide. **Table 3.1 and Table 7.8** show that the pseudo-first order model provides a better fit for all samples compared to the pseudo-second order model, as evidenced by its higher value of R^2 and lower value of sum square error (SSE) as determined according to **Eq. (1.12)**. The better fitting of the pseudo-first order method indicates that the adsorption is controlled by the diffusion step, which is proportional to the concentration of carbon dioxide molecules and relates to the porous structure of the adsorbents. The pseudo-first order rate constants (k_1) of the samples are higher than the other reported materials,[318,321,322] especially for S800, P800 and some carbon dioxide activated Starbons®, demonstrating their higher adsorption rate. This can be ascribed to the presence of both micropores and mesopores in the samples, the presence of mesopores reduces the diffusion resistance and facilitates the transportation of carbon dioxide to the adsorption sites.[319] However, in contrast to the carbon dioxide adsorption capacity, no correlation could be found between the rates of carbon dioxide adsorption and the textural properties of samples. This is probably due to the diffusion mechanism of gas molecules is much more complicated than what the pseudo-first order predicted, which relates to the synthetic effects of external diffusion, pore diffusion and surface adhesion.

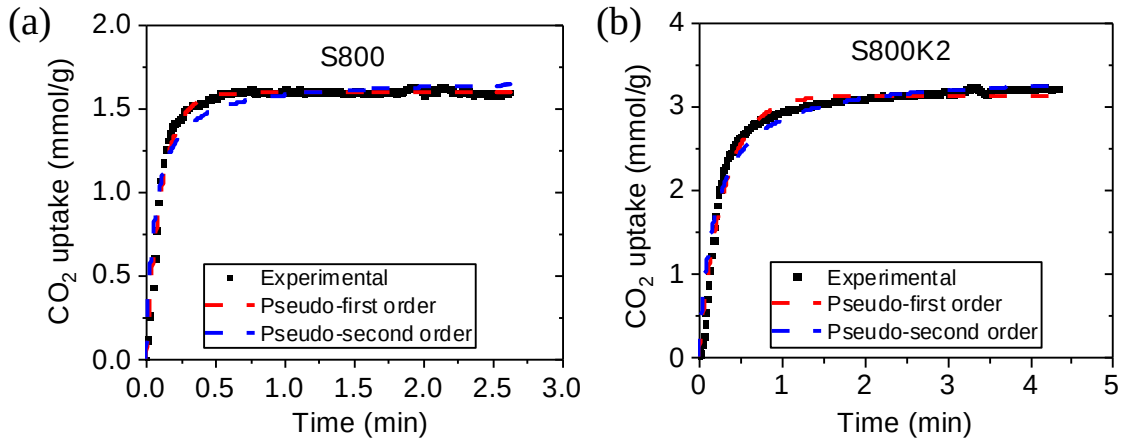

Figure 3.15 Experimental and predicted CO_2 uptake of S800 (a) and S800K2 (b) at 308 K and 1 bar.

Table 3.1 Experimental and kinetic parameters for CO_2 uptake on samples.

Sample		Pseudo-first-order model				Pseudo-second-order model			
	$q_{e-(exp)}$[a]	k_1[b]	q_e[a]	R^2	SSE	k_2[c]	q_e[a]	R^2	SSE
S800	1.62	8.847	1.592	0.988	0.118	9.500	1.674	0.929	0.715
S800K2	3.22	3.296	3.127	0.977	2.049	1.481	3.398	0.959	3.710

a) Units: mmol g^{-1}; b) Units: min^{-1}; c) Units: g min^{-1} $mmol^{-1}$

3.2.5 CO_2 Adsorption Isotherms

The carbon dioxide adsorption capacities of the most representative materials: S800 and S800K2 were further evaluated over a pressure range of 0-10 bar at three different temperatures: 273, 298 and 323 K as shown in **Figure 3.16** and **Table 7.9** in **Appendix 7.2**. The carbon dioxide adsorption capacities of S800K3 and S800K5 were also recorded at 273 K and 0-10 bar to allow comparison of the data with S800 and S800K2. This experimental work was carried out by collaborators at the University of Fudan.

A reduction of the carbon dioxide adsorption capacity is observed on increasing the adsorption temperature, since the higher molecular kinetic energy of carbon dioxide molecules at a higher temperature enables carbon dioxide to escape from the pore surface of

adsorbents more easily. The high adsorption at low temperature demonstrates that the carbon dioxide adsorption of all the materials is an exothermic process.[13,309] S800K2 exhibited outstanding carbon dioxide adsorption capacities of 6.2, 4.0 and 2.7 mmol g^{-1} at 1 bar and temperatures of 273, 298 and 323 K, respectively, compared to non-activated S800 which had carbon dioxide adsorption capacities of 3.4, 2.4 and 1.8 mmol g^{-1} at the same temperatures. An increase of the carbon dioxide pressure from 0-10 bar leads to an increase of the carbon dioxide adsorption capacity for all the samples at all temperatures. As a result, the carbon dioxide adsorption capacity of S800K2 at 10 bar reaches 12.7, 9.8 and 8.0 mmol g^{-1} at temperatures of 273, 298 and 323 K, respectively. Non-activated S800 had adsorption capacities of 9.6, 6.2 and 4.9 mmol g^{-1} at the same temperatures and pressure. Due to their similar ultramicroporosity and micropore surface, the carbon dioxide adsorption capacities of S800K3 and S800K2 are very similar at all pressures investigated as shown in **Figure 3.16e,f**. The 1 bar results agree with the STA results. In addition, S800K5 (with highest surface area, largest total pore volume and microporosity) shows extraordinary carbon dioxide storage capacities of 20.3 mmol g^{-1} at 273 K and 10 bar pressure, although its carbon dioxide capacities at 1 bar are lower (5.9 mmol g^{-1} at 273 K) than those of S800K2 and S800K3. In contrast to the crucial role of ultramicroporosity in carbon dioxide adsorption at low pressure, the supermicro-, meso- and even macropores become non-negligible at a higher pressure, by providing more space for carbon dioxide storage as well as promoting efficient diffusion of carbon dioxide. Therefore, in contrast to the trend of the STA results at 1 bar pressure, the carbon dioxide adsorption capacity at 10 bar increased as the amount of potassium hydroxide activating agent was increased, corresponding to the higher total surface area and total pore volume in the highly activated materials.

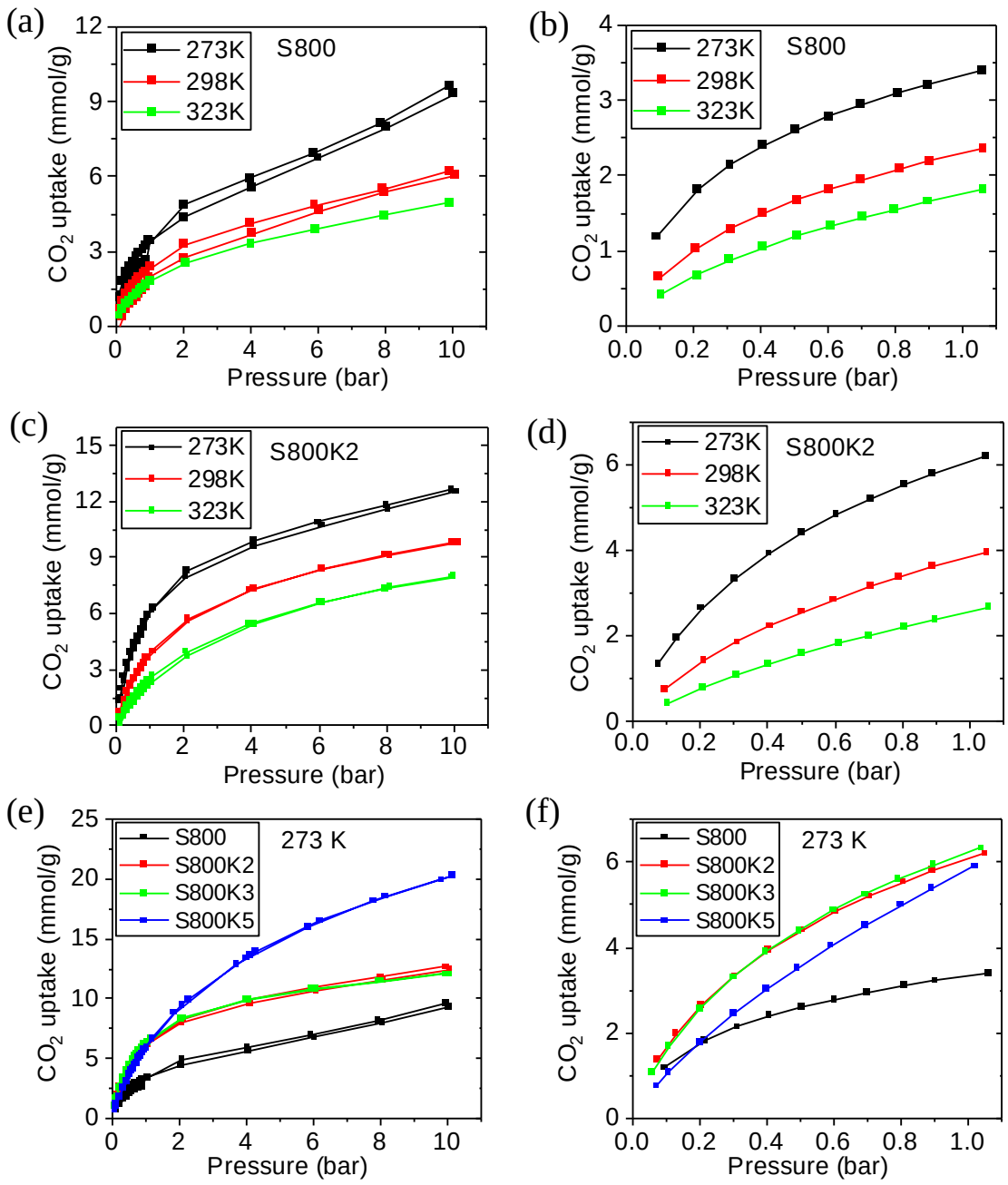

Figure 3.16 (a,c) CO_2 adsorption and desorption isotherms measured at 273, 298 and 323 K of (a) S800 and (c) S800K2; (e) CO_2 adsorption and desorption isotherms of S800, S800K2, S800K3, S800K5 at 273 K; (b,d, and f) the corresponding adsorption branches of the relevant isotherms that ends at 1 bar.

The negligible hysteresis shown in the isotherms suggests that the materials will be recyclable in carbon dioxide adsorption. To further investigate the adsorption mechanism,

three isotherm models: Langmuir, Freundlich and Temkin (equations are given in **Table 1.4**) were fitted to the carbon dioxide adsorption isotherms.[320,321] The fitting results are shown in **Figure 3.17** and **Table 3.2**.

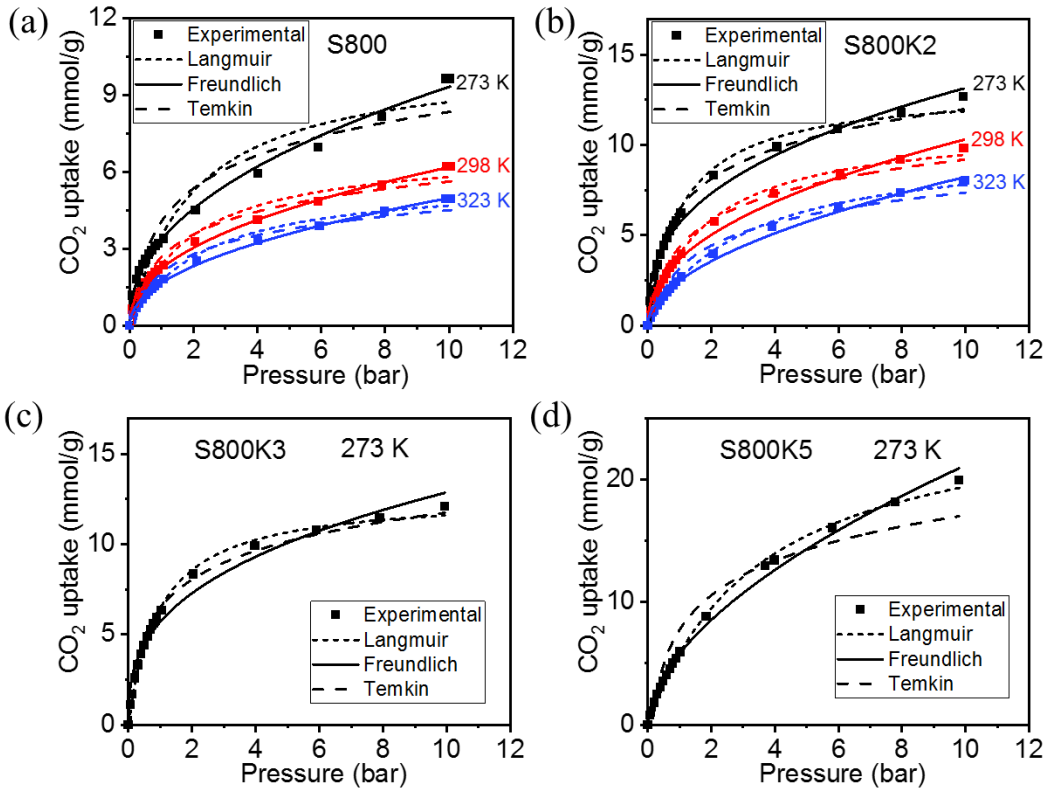

Figure 3.17 Isotherm models fitted to the experimental adsorption data of (a) S800, (b) S800K2, (c) S800K3 and (d) S800K5.

For S800, the Freundlich model has the best fit with the experimental data with a R^2 value of above 0.995, indicating multilayer adsorptions occurred on the heterogeneous surface of S800. For the potassium hydroxide activated materials (S800K2, S800K3 and S800K5), both Langmuir and Freundlich isotherms fit the experimental data well by showing high R^2 (above 0.985), indicating that both monolayer and multilayer adsorptions occurred on these materials. The increasing accuracy of the Langmuir model in fitting the experimental data of S800K2, S800K3 and S800K5 demonstrates a predominance of micropore filling in the potassium hydroxide activated materials. In addition, the decrease of the adsorption

coefficients of K_L and K_F with increasing adsorption temperature indicates the exothermic nature of the adsorption and 1/n is less than one which suggests that the adsorption is favourable.

Table 3.2 Isotherm parameters via Langmuir, Freundlich and Temkin fits.

Sample	T (K)	Langmuir			Freundlich			Temkin		
		q_m[a]	K_L[b]	R^2	K_F[c]	1/n	R^2	B[d]	K_T[e]	R^2
S800	273	10.4	0.507	0.950	3.364	0.442	0.995	1.851	9.057	0.930
	298	6.9	0.529	0.978	2.248	0.440	0.998	1.275	8.235	0.961
	323	5.8	0.440	0.986	1.680	0.472	0.998	1.066	6.895	0.962
S800K2	273	13.1	0.953	0.989	5.684	0.365	0.985	2.406	14.635	0.985
	298	11.2	0.548	0.996	3.678	0.448	0.989	2.102	7.944	0.968
	323	10.1	0.336	0.997	2.447	0.522	0.993	1.823	5.662	0.956
S800K3	273	12.7	1.033	0.995	5.705	0.354	0.988	2.304	16.451	0.986
S800K5	273	26.2	0.284	0.997	5.775	0.564	0.993	4.055	6.739	0.917

a) Units: mmol g^{-1}; b) Units: atm^{-1}; c) Units: mmol g^{-1} $atm^{-1/n}$; d) Units: KJ mol^{-1}; e) Units: atm^{-1}

3.2.6 Thermodynamic Study

Thermodynamic parameters including Gibbs free energy (ΔG°), adsorption enthalpy (ΔH°) and adsorption entropy (ΔS°) of carbon dioxide adsorption can be used to estimate the effect of temperature on carbon dioxide adsorption and provide further insight into the adsorption mechanism. Therefore, following the modelling of the carbon dioxide adsorption isotherms, the Freundlich equilibrium constants obtained at 273, 298 and 323 K for S800 and S800K2 were used in **Eq. (1.13, 1.14 and 1.15)**[321,322] to estimate the thermodynamic constants as shown in **Table 3.3**. Van't Hoff plots of ln(K_F) versus 1/T are shown in **Figure 3.18**. ΔS and ΔH were calculated from the intercept and slope of a linear plot of ln K_F vs 1/T.

Table 3.3 Thermodynamic parameters of CO_2 adsorption onto S800 and S800K2.

	T (K)	ΔG° (KJ mol^{-1})	ΔH° (KJ mol^{-1})	ΔS° (J mol^{-1} K^{-1})	R^2
	273	-2.754	-10.21	-27.37	0.998
	298	-2.007			
S800	323	-1.393			
	273	-3.940	-12.17	-30.09	0.999
	298	-3.227			
S800K2	323	-2.436			

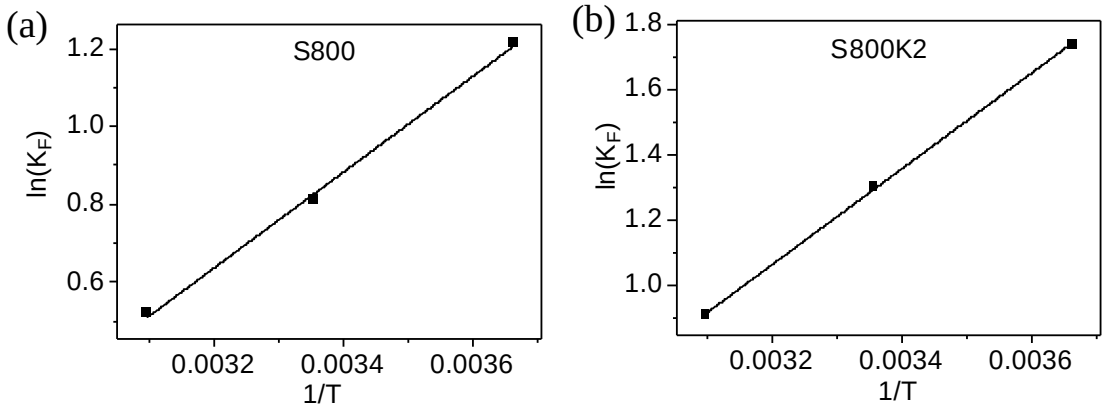

Figure 3.18 Van't Hoff plot of ln(K_F) versus 1/T of (a) S800 and (b) S800K2.

The negative values of ΔG° at various temperatures reveals that the adsorption process proceeds spontaneously. In addition, both samples exhibit higher values of ΔG° at lower temperatures, indicating that carbon dioxide adsorption on both samples is exothermic and so more favourable at a lower temperature. The exothermic and physisorption nature of the adsorption on both samples is also confirmed by negative ΔH° values of -10.21 and -12.17 KJ mol^{-1} (<20 KJ mol^{-1}).[321] The negative value of ΔS° indicates an increase in order after adsorption of carbon dioxide onto the surface of S800 and S800K2.[323] In addition, the temperatures at which carbon dioxide adsorption ceases to be favourable (ΔG° = 0) are 373K for S800 and 404K for S800K2, indicating that S800K2 can adsorb carbon dioxide up to a higher temperature than S800.

3.2.7 Isosteric Enthalpy of Adsorption Based on Isotherm Simulations

As mentioned above, instead of directly measuring the enthalpy of adsorption by using calorimetric-thermogravimetric data, the enthalpy can also be calculated according to molecular simulations by either the Clausius-Clapeyron approach or virial analysis using adsorption isotherms.[324] To further examine the strength of interactions between carbon dioxide and the samples at a specific loading of carbon dioxide, the isosteric enthalpy of adsorption was evaluated from the Clausius-Clapeyron equation (**Eq. 3.1**) based on the Freundlich model fitted carbon dioxide adsorption isotherms obtained at 273, 298 and 323 K.

$$Q_{st} = -R\left[\frac{\partial lnP}{\partial\left(\frac{1}{T}\right)}\right]_{q_e} \qquad (3.1)$$

Q_{st} (at a given q_e) is the isosteric enthalpy of carbon dioxide adsorption, which can be calculated through slopes of plots of lnP versus 1/T. q_e is the adsorption amount at equilibrium, R is the universal gas constant (8.314 J mol^{-1} K^{-1}), T represents the temperature at which an isotherm is measured, and P represents a pressure at which a specific q_e is reached at a temperature of T**.**

The Q_{st} of S800 and S800K2 were found to be in the range of 20-25 and 19-42 KJ mol^{-1}, respectively (**Figure 3.19**), consistent with physisorption of carbon dioxide onto the carbon based materials. A higher Q_{st} means a stronger interaction between carbon dioxide and the adsorbent surface. The moderate values of Q_{st} determined for S800 and S800K2 indicate the physisorption nature of the adsorption, which suggests an easy regeneration of the adsorbent requiring only low energy input. The high Q_{st} at the initial adsorption stage (low carbon dioxide loading) of S800K2 indicates a high potential of adsorption, which benefits from its prominent microporosity, especially the ultramicroporosity. The Q_{st} drops gradually as the

occupation of adsorption sites increases as the carbon dioxide uptake increases. The decreasing proportion of carbon dioxide adsorbed in ultramicropores is accompanied by lowering of van der Waals forces and short-range interactions (attractive and repulsive forces) in larger micropores, leading to a weakening interaction between the adsorbent surface and carbon dioxide molecules.[325] As a result, S800K2 exhibits a low Q_{st} of 19 KJ mol^{-1} at high carbon dioxide saturation. The results indicate that the adsorption first occurs in the narrow pores followed by in larger pores. The declining value of Q_{st} also indicate the role of surface heterogeneity in initial carbon dioxide capture.

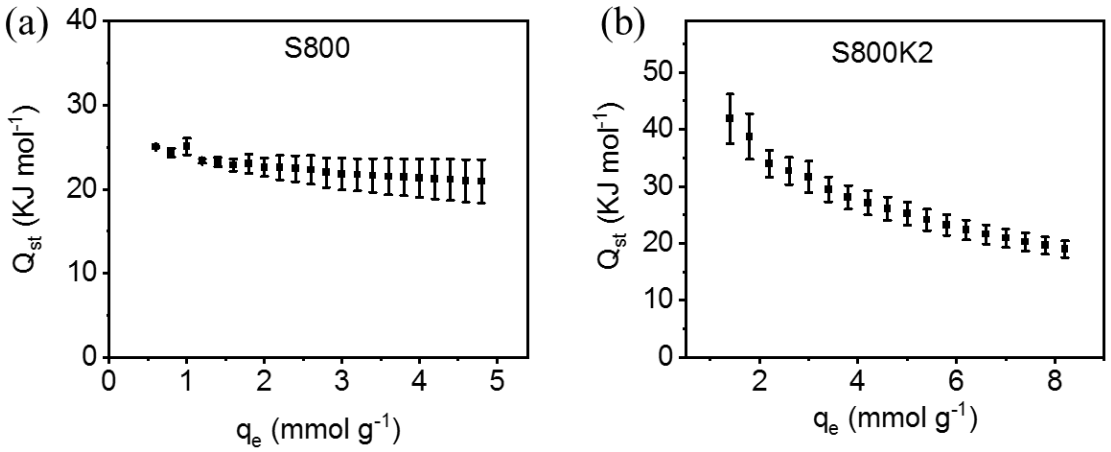

Figure 3.19 Isosteric enthalpy of CO_2 adsorption of (a) S800 and (b) S800K2 obtained at 273, 298 and 323 K.

3.2.8 Binary Component Adsorption Measurement

Post-combustion flue gas mainly contains a binary mixture of carbon dioxide (12-15%) and nitrogen (73-77%) since other minor impurities including water (5-7%), oxygen (3-4%), sulphur oxides (<800 ppm) and nitrogen oxides (500 ppm) are removed during the pre-treatment processes.[172] Therefore, to assess the potential of the samples in practical post-combustion applications, the effect of gas composition on the adsorption capacities of S800

and S800K2 at 308K was further investigated by varying the concentration of carbon dioxide in a mixture of carbon dioxide and nitrogen (the range of partial pressures of carbon dioxide is shown in **Table 3.4**). In addition, several adsorption and desorption cycles were performed to study the recyclability of the samples (**Figure 3.20**).

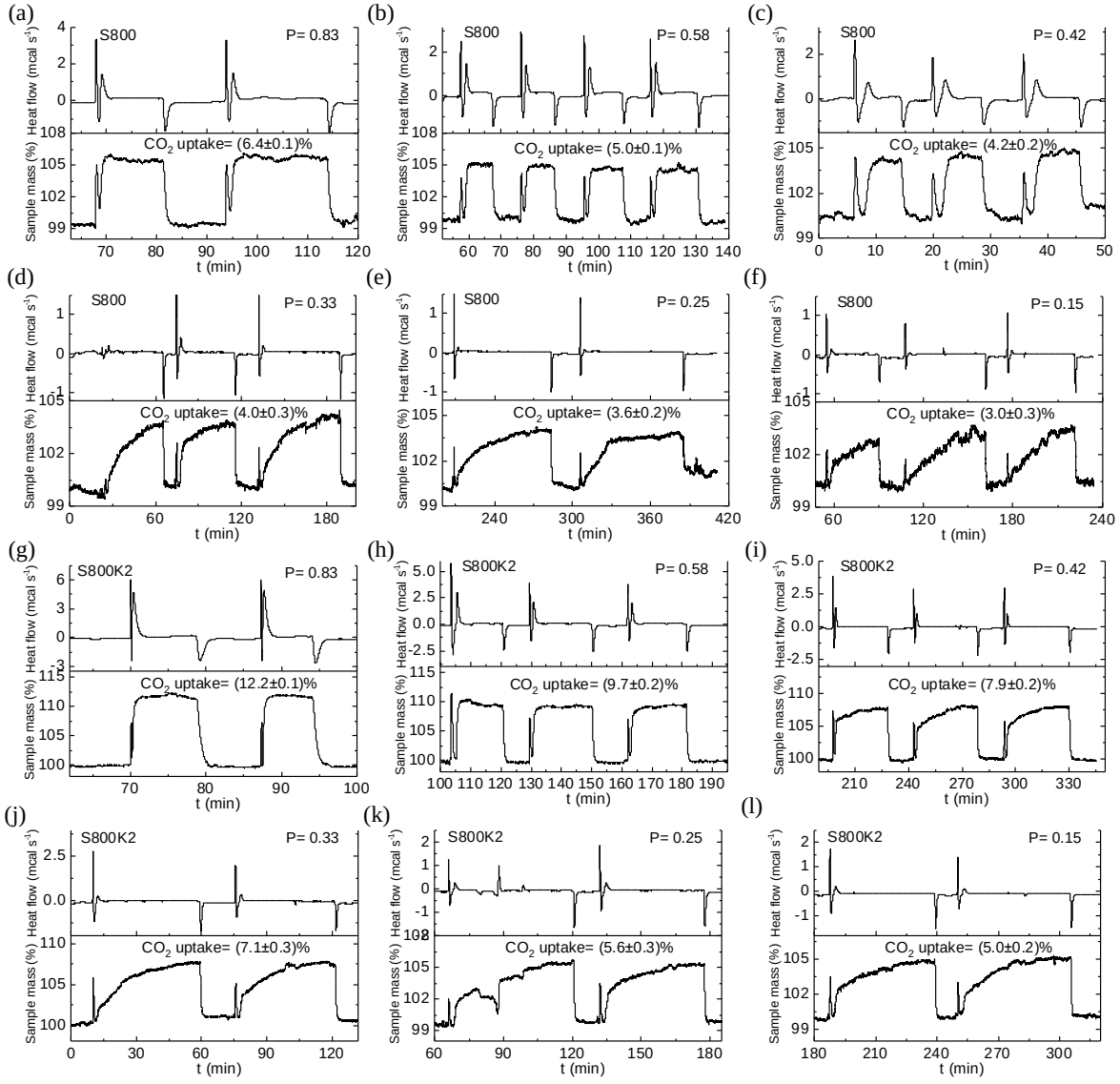

Figure 3.20 STA plots of mass and heat flow changes over multiple cycles of CO_2 adsorption and desorption using mixtures of carbon dioxide and nitrogen with different CO_2 partial pressures onto (a-f) S800 and (g-l) S800K2 at 308 K.

Table 3.4 and Figure 3.20 show that the carbon dioxide uptake for S800 and S800K2 decreases as the carbon dioxide content (pressure) in the gas mixture decreases. Thus, at

308K the carbon dioxide adsorption capacities of S800 and S800K2 decreased from 1.50 to 0.68 and from 3.11 to 1.14 mmol g^{-1} respectively as the carbon dioxide partial pressure was reduced from 1.00 to 0.15 bar (the partial pressure of carbon dioxide in a typical post combustion flue gas is 0.15 bar). In addition, although the adsorption of carbon dioxide became slower as the carbon dioxide content was reduced, desorption remained rapid for both samples when the gas flow was switched back to pure nitrogen. Both samples were nearly fully regenerated after desorption, as no decrease of the adsorption capacity or adsorption rate was observed in the next adsorption cycle. These results further verify the applicability of Starbons® in post-combustion carbon dioxide capture applications.

Table 3.4 CO_2 adsorption capacities of S800 and S800K2 under different CO_2 partial pressures measured at 308 K by STA.

CO_2 content (%)	CO_2 partial pressure (bar)	CO_2 uptake			
		S800		S800K2	
		%	mmol/g	%	mmol/g
100	1	6.7±0.1	1.50±0.02	13.7±0.2	3.11±0.05
83	0.83	6.4±0.1	1.45±0.02	12.2±0.1	2.77±0.02
58	0.58	5.0±0.1	1.14±0.02	9.7±0.2	2.20±0.05
42	0.42	4.2±0.2	0.95±0.05	7.9±0.2	1.80±0.05
33	0.33	4.0±0.3	0.91±0.07	7.1±0.3	1.61±0.07
25	0.25	3.6±0.2	0.82±0.05	5.6±0.3	1.27±0.07
15	0.15	3.0±0.3	0.68±0.07	5.0±0.2	1.14±0.05

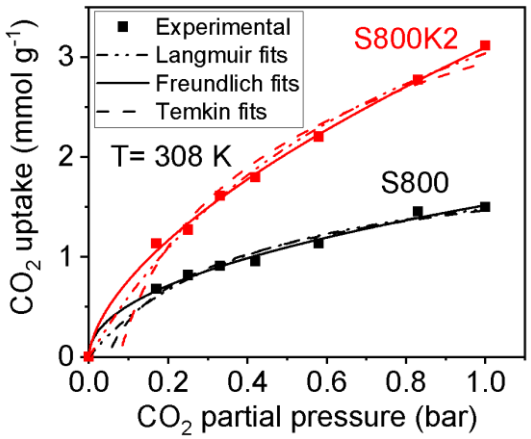

Figure 3.21 Experimental and fitting isotherms of CO_2 adsorption onto S800 and S800K2 measured at 308 K and 1 bar by STA.

The adsorption capacities of S800 and S800K2 at 0.15 bar are consistent with the static carbon dioxide adsorption values listed in **Table 7.9** in **Appendix 7.2**. At 0.15 bar, S800K2 with well-developed ultramicroporosity shows slightly higher carbon dioxide adsorption capacity compared to most commercial carbons (typically <1 mmol g^{-1}).[326] Its carbon dioxide adsorption capacity at low partial pressure is however not competitive with those of heteroatom-functionalised carbons which potentially have enhanced surface basicity and hence enhanced adsorption affinity.[327] For example, benzimidazole derived ultra-microporous carbon with a nitrogen content of 17.6 wt% and polyisocyanurate derived carbon foam with a potassium content of 6.5 wt% show exceptionally high adsorption capacities of up to 2.1 and 2.3 mmol g^{-1}, respectively, at 0.15 bar and 298 K.[328,329] Their strongly polarised surfaces results in their high capture capacities at low partial pressure. However, the strong affinity of these materials for carbon dioxide could also lead to energy intensive and hence costly regeneration of the sorbent.[330]

The plots shown in **Figure 3.21** and the fitting parameters listed in **Table 3.5** indicate that the adsorption of carbon dioxide onto S800 and S800K2 from a carbon dioxide and nitrogen gas mixture at 308 K can be well described by the Freundlich model (R^2 close to 1). The adsorption constants K_F determined from the STA results at 308 K (1.8 mmol g^{-1} $bar^{-1/n}$ for S800 and 3.1 mmol g^{-1} $bar^{-1/n}$ for S800K2) are consistent with the value obtained by static adsorption measurement using pure carbon dioxide at 298 and 323K (2.2 and 1.7 mmol g^{-1} $bar^{-1/n}$ for S800; 3.7 and 2.5 mmol g^{-1} $bar^{-1/n}$ for S800K2). Gibbs free energies ($\Delta G°$, -1.4 KJ mol^{-1} for S800 and -2.9 KJ mol^{-1} for S800K2) calculated based on the adsorption constant K_F at 308 K are also consistent with the values obtained by the static adsorption results determined using pure carbon dioxide at 298 K and 323K (-2.0 and -1.4 KJ mol^{-1} for S800; -3.2 and -2.4 KJ mol^{-1} for S800K2). Such results further demonstrate the exothermic nature of the adsorption.

Table 3.5 Isotherm parameters via Langmuir, Freundlich and Temkin fits.

Model	Parameters	S800	S800K2
Langmuir	q_m (mmol g^{-1})	2.1	5.5
	K_L (bar^{-1})	2.347	1.240
	R^2	0.983	0.992
Freundlich	K_F (mmol g^{-1} $bar^{-1/n}$)	1.757	3.097
	1/n	0.468	0.606
	R^2	0.994	0.998
Temkin	B (KJ mol^{-1})	0.495	1.182
	K_T (bar^{-1})	21.37	13.14
	R^2	0.983	0.981

3.2.9 CO_2 Adsorption Selectivity

In addition to a high carbon dioxide adsorption capacity, the selective adsorption of carbon dioxide over nitrogen is also a very important criterion for evaluating adsorbents for carbon dioxide capture. Selective adsorption of carbon dioxide over nitrogen can be estimated by calculating the initial slope ratio of the single-component gas (carbon dioxide and nitrogen) adsorption isotherms.[331] Other than initial slope calculations, the selectivity of adsorption of a binary mixture is usually predicted based on the single component adsorption isotherms by applying Ideal Adsorbed Solutions Theory (IAST), which assumes that an ideal solution is formed from the adsorbed phase. The adsorption selectivity for a binary mixture is calculated as follows:[332,333]

$$S = \frac{q_1 p_2}{q_2 p_1}$$

where q_1 (mmol g^{-1}) and q_2 (mmol g^{-1}) are the carbon dioxide amount adsorbed at the equilibrium partial pressure of p_1 (bar) and p_2 (bar), respectively. The typical composition of a post-combustion flue gas is around 15% carbon dioxide and 85% nitrogen in volume percentage. Therefore, the equilibrium partial pressures of nitrogen and carbon dioxide in the bulk phase are deemed to be 0.85 bar and 0.15 bar.[334]

S800K2 exhibits the highest carbon dioxide adsorption capacity at 1 bar pressure, therefore, its selective adsorption of carbon dioxide over nitrogen at 273 and 298 K were investigated. Due to the S800K5 exhibits the highest carbon dioxide adsorption capacity at 10 bar pressure at 273 K, its selective adsorption of carbon dioxide over nitrogen at 273 K were also investigated. The experimental data of nitrogen adsorption of samples was fitted to Langmuir, Freundlich and Temkin models as shown in **Figure 7.6** and **Table 7.10** in **Appendix 7.2.** The fitting results indicate that the adsorption behaviours of carbon dioxide and nitrogen onto S800, S800K2 and S800K5 can be well described by both the Langmuir and Freundlich models as both showed a high correlation coefficient (R^2) of over 0.99. Due to the greater polarisability (29.11×10^{-25} cm^{-3}) and enhanced quadrupole moment (4.30×10^{-26} esu^{-1} cm^{-1}) of carbon dioxide as compared to nitrogen (17.40×10^{-25} cm^{-3} and 1.52×10^{-26} esu^{-1} cm^{-1}, respectively),[315] as well as the coexistence of micropores and mesopores, all samples exhibited a preferential adsorption of carbon dioxide over nitrogen, indicative of high carbon dioxide versus nitrogen selectivities.

Based on the Freundlich fitted single-component adsorption isotherms, the selectivities for adsorption of carbon dioxide over nitrogen (in a 0.15: 0.85, v:v gas mixture) by S800 and S800K2 at 298 K; S800K2 and S800K5 at 273 K were calculated by applying the ideal adsorbed solution theory (IAST). The results are shown in **Figure 3.22e,f** and **Table 3.6**. The selectivity of S800K2 was calculated to be 59.9 at 1 bar and 36.6 at 10 bar at 298 K, which are double the values for S800 (29.1 at 1 bar 15.7 at 10 bar). The superior selectivity of S800K2 can be ascribed to its high content of ultramicro- and micropores (66% and 83% of its total pore volume),[328] wherein the molecular sieving effect is optimised and the affinity between the carbon dioxide molecules and the walls of the micropores is strengthened.[335] The stronger adsorption affinity of S800K2 with carbon dioxide as compared to S800 is evidenced by its higher isosteric enthalpy as shown in **Figure 3.19**. In contrast, for the

mesoporous sample S800, both carbon dioxide and nitrogen molecules can better access and be accommodated in mesopores, which reduces the carbon dioxide binding affinity and makes the material less effective in gas separation.[336,337]

Reducing the adsorption temperature to 273 K slightly increases the selectivity of S800K2 to 64.5 and 40.5 at 1 and 10 bar, respectively. Compared to S800K2, the lower carbon dioxide adsorption capacity of S800K5 at low pressures (below 6.2 bar) at 273 K results in its lower selective adsorption of carbon dioxide over nitrogen, however, the adsorption selectivity of S800K5 was slightly higher than that of S800K2 at higher pressures (above 6.2 bar) attributed by its higher carbon dioxide adsorption capacities at higher pressures. The IAST selectivity of S800K2 is amongst the highest reported for carbon materials under the same conditions, indicating its excellent potential as a carbon dioxide capture adsorbent for a flue gas stream.[338]

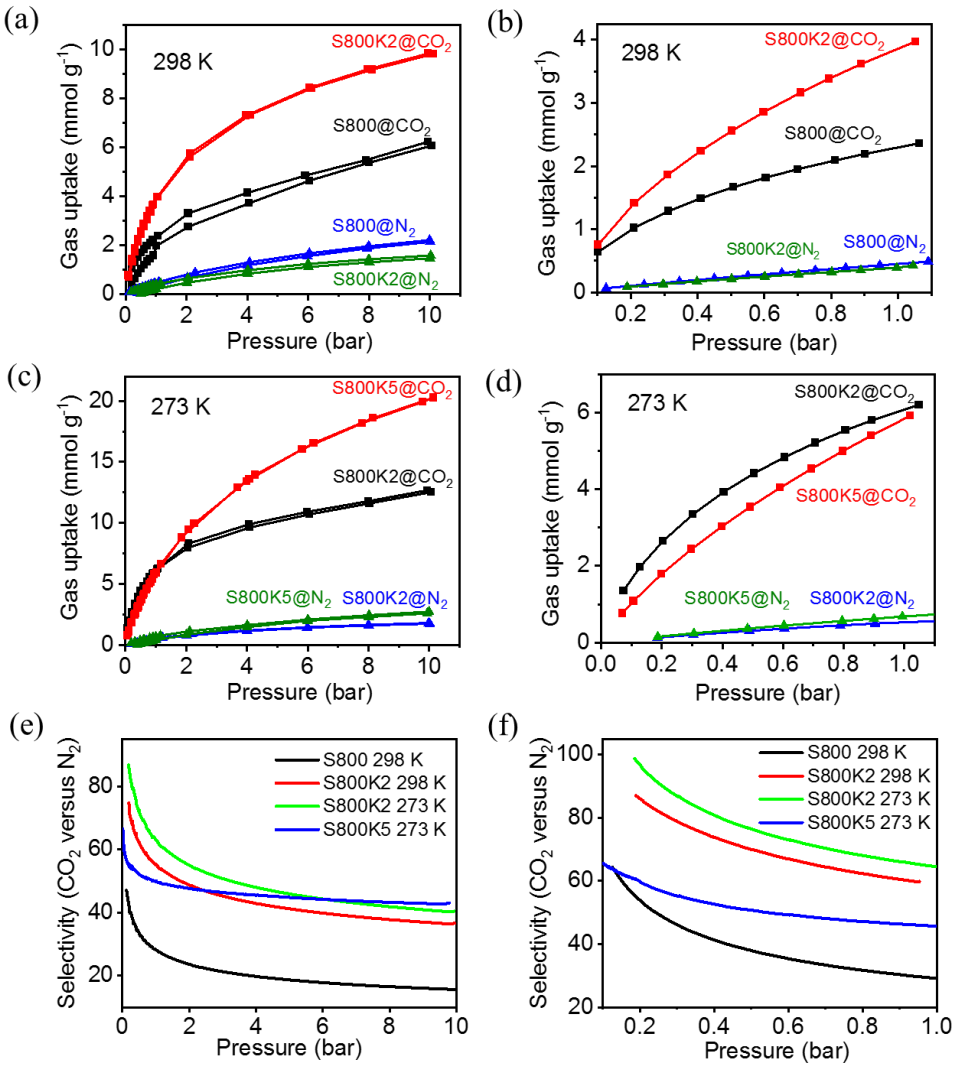

Figure 3.22 (a-d) comparison of CO_2 and N_2 sorption isotherms of (a, b) S800 and S800K2 at 298 K at (a) 0-10 bar and (b) 0-1 bar; (c, d) S800K2 and S800K5 at 273 K at (c) 0-10 bar and (d) 0-1 bar; (e, f) adsorption selectivity of CO_2 versus N_2 of S800, S800K2 at (e) 0-10 bar and (f) 0-1 bar (calculated using only 0-1 bar adsorption isotherm).

Table 3.6 Selectivity of CO_2 versus N_2.

Sample	Temperature (K)	Selectivity at 1 bar	Selectivity at 10 bar
S800	298	29.1	15.7
S800K2	298	59.9	36.6
S800K2	273	64.5	40.5
S800K5	273	45.6	43.1

3.2.10. Comparison of CO_2 adsorption capacity and selectivity to literature data

Table 3.7 summarizes the carbon dioxide capacities and selectivities of recently reported biomass-based carbon materials. It has previously been reported that once the carbon dioxide adsorption capacity reaches 3 mmol g^{-1}, selectivity is more important than capacity from a cost of capture perspective.[339] It shows that most adsorbents cannot have both high adsorption capacity and selectivity. The best sample prepared in this work (S800K2) is amongst the best adsorbents in terms of capacity at 0 and 25 °C ambient pressure and its selectivity for adsorption of carbon dioxide versus nitrogen is higher than the other non-nitrogen doped carbons under the same conditions.

Table 3.7 Comparison of CO_2 capture capacity and selectivity of biomass derived porous carbon materials.

			CO_2 uptake (mmol g^{-1})		**CO_2/N_2 Selecivity[a]**	
Material (Biomass precursor)	**Preparation method**	**N content (wt%)**	**0 °C, 1 bar**	**25 °C, 1 bar**	**25 °C, 1 bar**	**Ref.**
a-CL (Celtuce leaves)	KOH activation	0.6	6	4.4	N.A.	340
AS-2-600 (Sawdust)	KOH activation	N.A.	6.1	4.8	5.4[b]	341
WDC-03 (Packaging waste)	KOH activation	N.A.	5.3	4.2	16[c]	342
AcA5 (Glucose)	KOH and acrylic acid activation	0	5.9	3.8	N.A.	343
M1273-150 (Starch)	CO_2 activation	N.A.	4.3	3.2	N.A.	344
PP (Pomegranate peel)	KOH activation	N.A.	6	4.1	15.1	345
CA-HC300 (Glucose)	KOH activation	0	5.9	4.3	N.A.	13
KLB2 (Arundo donax)	KOH activation	0.9	6.3	3.6	N.A.	114
p-2-973-1.5 (Pine nutshell)	KOH activation	0.01	7.7	5	8.4[b]	346
MCC-K3 (Wheat flour)	KOH activation	N.A.	5.7	3.5	15	347
CLC–AC–CO_2 (Cross-linked cellulose)	CO_2 activation	2.2	5.0	N.A.	32.9	348
MPC3 (Casein)	KOH activation	0.2	4.1	2.3	N.A.	309

TAC-0.5-700 (Biomass tar)	KOH activation	3	6	4.1	24	349
AC-Air (Bamboo)	Air activation	0.5	4.1	2.3	N.A.	350
HAC-850-KOH (Walnut shell and urea)	KOH activation	0.9	5.1	3.1	10.3[c]	331
R-HAC20 (Starch)	H_2O_2/steam activation	0	5.8	3.9	18	351
CF-850-act (Cellulose fibers)	Steam activation	N.A.	4.4	3	39.2[d]	352
S800SE (Starch)	Carbonisation		N.A.	2.8@5bar	14.0[e]	86
S800 (Starch)	Carbonisation	0	3.4	2.4	29.1	This work
S800K2 (Starch)	Carbonisation and KOH activation	0	6.2	4.0	59.9	This work

N.A. means not available; SE means the sample was prepared by the solvent exchange drying method; a) selectivity determined by the IAST method; b) selectivity determined from the ratio of the amount of CO_2 and N_2 adsorbed; c) selectivity determined by the initial slope method; d) selectivity determined by the Henry's law method and e) selectivity determined by Langmuir model ($(K_Lq_m)_{CO2}/(K_Lq_m)_{N2}$, K_L is Langmuir constant and q_m is adsorption amount at equilibrium).

3.3 Conclusions

Enhancement in carbon dioxide adsorption capacity and selectivity can be achieved by fine tailoring of the ultramicroporosity of Starbon® materials. Amongst the materials studied, S800K2 shows the best carbon dioxide capacities of 6.2, 4.0 and 2.7 mmol g^{-1} at 1 bar and temperatures of 273, 298 and 323 K respectively as measured by the adsorption isotherms and 3.1 mmol g^{-1} as measured by STA at 1 bar and 308 K. Due to the high abundance of ultramicro- and micropores in S800K2, its selectivity for adsorption of carbon dioxide over nitrogen was calculated to be 59.9 at 1 bar and 36.6 at 10 bar. These values are double those obtained for non-activated S800 under the same conditions. Moreover, all the samples showed a complete regenerability over multiple sorption cycles.

It was found that a higher ultramicropore surface area and a higher degree of ultramicroporosity (0.4-0.7 nm) are the predominant factors that determine the carbon dioxide adsorption capacity at ambient pressure. Therefore, although the porous structures were well developed in Starbons® activated by carbon dioxide and oxygen activation, the carbon dioxide adsorption capacities of the relevant samples are moderate due to their predominant mesoporosity. Comparison of carbon dioxide uptake at higher pressures by the potassium hydroxide activated Starbons® shows that the combined influence of high surface area and large pore volume leads to a high carbon dioxide storage capacity at high pressure. As a result, S800K5 exhibits the highest 10 bar pressure carbon dioxide adsorption capacity of 20.3 mmol g^{-1} at 273 K due to it having the highest total surface area and pore volume.

The better fitting of a pseudo-first order kinetic model with the experimental data indicates that the carbon dioxide adsorption rate is proportional to the concentration of gas molecules and relates to the porous structure of the adsorbents. Heterogeneity of adsorption on the sample surface was confirmed both from the Langmuir and Freundlich isotherm fits and from the decreasing value of the enthalpy of adsorption with increasing carbon dioxide adsorption. That the adsorption was physisorption, exothermic and spontaneous were confirmed from both thermodynamic parameters and the low values of the enthalpy of adsorption.

Chapter 4: Application of Hierarchically Porous Starbon® Materials to Methylene Blue Adsorption

4.1 Introduction

It has previously been demonstrated that there is good promise for mesoporous Starbons® to act as methylene blue (MB) and acid blue 92 (AB) adsorbents for potential water purification.[64] The preparation and utilisation of Starbons® with adjustable surface chemistry, functionality and porosity enabled clarification of the importance of pore texture (large pore volumes and diameters) and surface functionality (low hydroxyl and high aromatic functionality) in dye adsorption. However, the extensive use of Starbons® as adsorbents has been limited by their relatively low degree of porosity, low surface area (265-535 m^2 g^{-1}) and electrostatic repulsion between the porous surface and the dye.

Therefore, in this chapter, hierarchically activated Starbons®, which possess high specific surface areas and well-developed micro- and mesoporosities, were applied to methylene blue adsorption. Compared to solely microporous or mesoporous structures, the hierarchical porous structure is conducive to achieving an exceptional adsorption performance, wherein, both micropores and mesopores provide adsorption sites and the mesopores facilitate mass transfer by creating free diffusion paths for the adsorbate into the interior surface.[232]

In addition to improving the adsorption performance of Starbons®, the relationship between pore textual properties and adsorption ability was established in order to obtain further insight into the mechanism of methylene blue adsorption. To achieve the desired rate of adsorption and maximum efficiency of methylene blue removal, the effect of adsorption conditions including contact time between the adsorbate and the adsorbent, pH, temperature and initial concentration of the methylene blue solution on the adsorption rate, efficiency and capacity were studied systematically.

4.2 Results and Discussion

The adsorption kinetics were investigated at various methylene blue concentrations at 298 K. The absorbance of a sample of the methylene blue solution that was taken at each time interval (t) was measured by using UV–Vis spectrophotometry at a wavelength of 665 nm. The concentration of the solution after adsorption time t (C_t, mg L^{-1}) was calculated based on the absorbance value using external standard calibration. The quantity of methylene blue adsorbed at time t (q_t, mg g^{-1}); at equilibrium (q_e, mg g^{-1}); and the percentage removal at equilibrium (R_e, %) can be calculated according to **Eq. (4.1-4.3)**:

$$q_t = (C_0 - C_t)\ V/m \quad (4.1)$$

$$q_e = (C_0 - C_e)\ V/m \quad (4.2)$$

$$R = 100\ (C_0 - C_t) / C_0 \quad (4.3)$$

where, C_0 (mg L^{-1}), C_t (mg L^{-1}) and C_e (mg L^{-1}) represent the initial, at time t, and equilibrium concentrations of methylene blue respectively; V (L) is the volume of solution (adsorbate); and m (g) is the mass of adsorbent.

For adsorption isotherm studies, the adsorbents were mixed with various concentrations of methylene blue solution, all the adsorptions were ensured to reach equilibrium (4 h). The effect of temperature on adsorption was studied by varying the adsorption temperature within the range of (298-318) K. For the study of the effect of pH on the adsorption of methylene blue onto S950C90 at 298 K, the initial methylene blue concentration was 500 mg L^{-1}. The solution pH was adjusted using 0.1 M sodium hydroxide or 0.1 M hydrochloric acid to the range of 3.0–11.0. For all the experiments, the ratio of adsorbent to methylene blue solution was 10 mg: 20 mL (adsorbent concentration of 0.5 mg mL^{-1}). Except for the study of pH influence, all the experiments were conducted without adjusting the solution pH as this is more preferred in the practical potential application of purifying wastewater.

4.2.1 Effect of Contact Time and Adsorption Kinetics

The effect of contact time on the ability of potassium hydroxide, carbon dioxide and oxygen activated Starbons® to adsorb methylene blue at different initial concentrations at 298 K was investigated. As comparisons, the adsorption of methylene blue onto non-activated Starbon® (S800) and commercial activated carbon (AC) were also studied. To quantify the rate of adsorption, the adsorption kinetics were studied by fitting the experimental adsorption data to pseudo-second order and Elovich models (detailed information of these models is provided in **Table 1.3**). The experimental adsorption data, kinetic fitting plots and the kinetics parameters are shown in **Figure 4.1** and **Table 4.1.**

The results in **Figure 4.1** reveal that the adsorption rates of all the samples were initially very fast and then became slower and finally the adsorption equilibrium were reached within a maximum of three hours. Due to the relatively low surface coverage in the early stage, the methylene blue molecules could occupy vacant adsorption sites rapidly. However, as the adsorption process progressed and approached equilibrium, the available adsorption positions were reduced and the methylene blue molecules already on the surface of the adsorbent caused steric hindrance and electrostatic repulsion for other approaching methylene blue molecules.[233,353] Compared to the non-activated Starbon® (S800, **Figure 4.1a**), the potassium hydroxide, carbon dioxide and oxygen activated Starbons® and commercial activated carbon (**Figure 4.1b-k**) exhibited a more rapid adsorption process. Most of the methylene blue was adsorbed in the first thirty minutes and for S800K4 (**Figure 4.1e**) and S950C90 (**Figure 4.1i**), the adsorption equilibrium times were as short as five minutes.

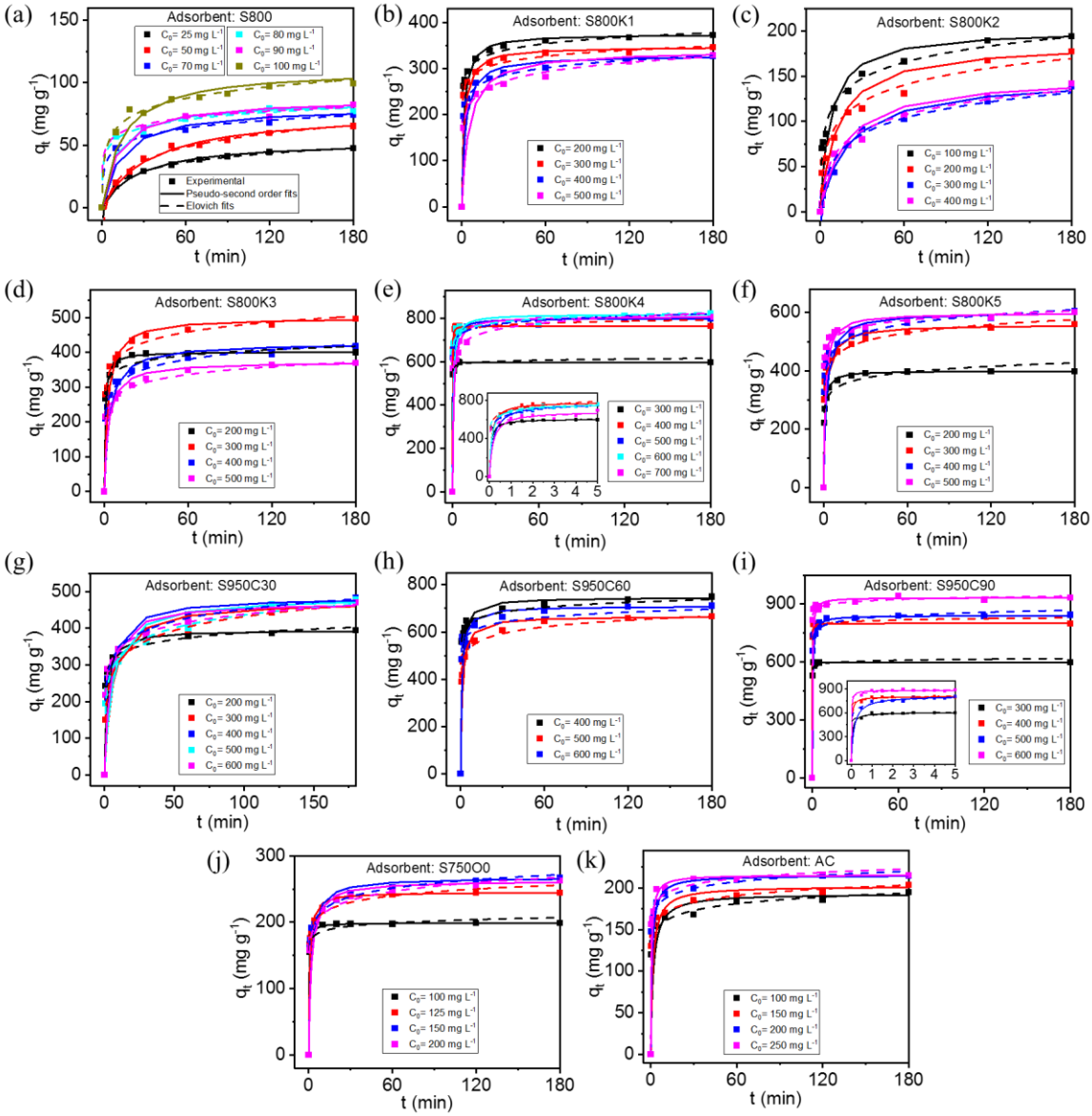

Figure 4.1 Effects of contact time on adsorption of methylene blue onto (a-j) Starbons® and (k) commercial activated carbon at different initial methylene blue concentrations at an adsorption temperature of 298 K.

Table 4.1 Kinetic parameters via pseudo-second order and Elovich fits.

Sample			Pseudo-second order				Elovich		
	C_0[a]	$q_{e\text{-}exp}$[b]	k_2[c]	$q_{e\text{-}cal}$[b]	R^2	h[d]	α[d]	β[e]	R^2
	25	49.4	0.0007	54.4	0.9985	2.083	5.831	0.0972	0.9986
	50	70.0	0.0004	78.1	0.9961	2.303	5.621	0.0632	0.9939
	70	78.0	0.0009	80.7	0.9954	5.956	155.5	0.1089	0.9970
	80	83.7	0.0012	84.8	0.9964	8.439	467.6	0.1148	0.9925
	90	85.2	0.001	87.0	0.9941	7.755	1217	0.1271	0.9912
S800	100	109.9	0.0006	111.5	0.9936	7.851	138.3	0.0733	0.9905
	200	373.0	0.0018	374.5	0.9999	248.8	6.047×10^{6}	0.0471	0.9960
	300	346.0	0.0017	347.2	0.9998	202.0	5.971×10^{6}	0.0512	0.9969
	400	324.3	0.0013	327.9	0.9997	135.5	1.342×10^{5}	0.0423	0.9967
S800K1	500	338.4	0.0006	339.0	0.9979	66.98	8.792×10^{3}	0.0334	0.9973
	100	197.8	0.0007	201.6	0.9985	28.70	269.1	0.0390	0.9921
	200	180.5	0.0004	186.9	0.9938	15.42	83.89	0.0374	0.9815
	300	137.3	0.0003	148.8	0.9971	7.427	24.24	0.0390	0.9861
S800K2	400	140.5	0.0004	150.4	0.9955	8.615	30.30	0.0401	0.9923
	200	400.0	0.0041	401.6	1	657.9	9.656×10^{6}	0.0435	0.9692
	300	497.3	0.0008	500.0	0.9997	195.7	5.175×10^{4}	0.0245	0.9906
	400	428.1	0.0006	427.4	0.9988	113.5	1.240×10^{4}	0.0260	0.9949
S800K3	500	367.6	0.0009	373.1	0.9998	129.0	1.875×10^{4}	0.0311	0.9928
	300	597.5	0.0267	606.1	0.9999	9804	4.570×10^{10}	0.0377	0.9988
	400	765.3	0.0132	781.3	0.9993	8065	1.230×10^{7}	0.0176	0.9935
	500	799.2	0.0029	800.0	0.9999	1832	6.370×10^{12}	0.0384	0.9873
	600	822.3	0.002	819.7	0.9998	1309	2.400×10^{13}	0.0398	0.9922
S800K4	700	809.6	0.0014	813.0	0.9999	900.9	1.160×10^{8}	0.0246	0.9910
	200	397.8	0.0041	400.0	0.9999	662.3	4.788×10^{5}	0.0349	0.9696
	300	560.0	0.0011	558.7	0.9996	340.1	2.936×10^{5}	0.0245	0.9638
	400	604.3	0.0008	602.4	0.9991	295.9	2.816×10^{5}	0.0229	0.9822
S800K5	500	601.1	0.0013	598.8	0.9995	478.5	2.450×10^{8}	0.0349	0.9943
	200	394.6	0.0016	395.3	0.9997	247.5	7.443×10^{5}	0.0384	0.9970
	300	473.5	0.0004	473.9	0.9956	86.21	1.530×10^{3}	0.0184	0.9970
	400	483.8	0.0005	485.4	0.9984	124.4	6.925×10^{3}	0.0212	0.9963
	500	478.9	0.0004	485.4	0.9961	88.03	2.761×10^{3}	0.0197	0.9883
S950C30	600	470.3	0.0006	471.7	0.9979	123.6	1.509×10^{4}	0.0239	0.9967
	400	748.7	0.0014	746.3	0.9998	800.0	8.240×10^{9}	0.0334	0.9935
	500	664.9	0.0013	666.7	0.9998	574.7	2.748×10^{6}	0.0245	0.9818
S950C60	600	710.3	0.0016	709.2	0.9999	806.5	1.340×10^{9}	0.0327	0.9764
	300	597.9	0.0359	603.4	0.9998	1.307×10^{4}	5.30×10^{11}	0.0419	0.9946
	400	798.1	0.0543	799.9	0.9999	3.477×10^{4}	1.15×10^{16}	0.0438	0.9964
	500	843.9	0.0039	840.3	0.9999	2765	1.88×10^{14}	0.0403	0.9863
S950C90	600	934.0	0.0051	933.0	0.9999	4475	4.96×10^{25}	0.0656	0.9963
	100	198.7	0.0241	198.8	1	952.4	1.60×10^{11}	0.1403	0.9842
	125	244.3	0.0058	245.1	0.9999	346.0	3.423×10^{6}	0.0686	0.9906
	150	267.0	0.0021	267.4	0.9996	152.2	2.293×10^{5}	0.0538	0.9983
S750O0	200	262.7	0.0021	262.5	0.9995	145.8	1.151×10^{5}	0.0519	0.9945
	100	194.9	0.003	193.1	0.9988	110.1	1.116×10^{6}	0.0860	0.9773
	150	203.5	0.0033	202.0	0.9992	135.0	3.244×10^{5}	0.0872	0.9808
	200	214.3	0.0051	215.1	0.9999	234.2	1.66×10^{7}	0.0882	0.9733
AC	250	214.9	0.0085	215.5	0.9999	396.8	1.20×10^{8}	0.0963	0.8918

a) Units: mg L^{-1}; b) Units: mg g^{-1}; c) Units: g mg^{-1} min^{-1}; d) Units: mg g^{-1} min^{-1} e) Units: g mg^{-1}

The experimental data fitted well with the pseudo-second order and Elovich kinetics models, as judged by the high correlation coefficient (R^2) values (**Table 4.1**). A good fit of

the Elovich model with the experimental data indicates that the adsorption of methylene blue onto these samples is an integrative heterogeneous diffusion process which is controlled by the reaction rate and diffusion.[256] However, the higher values of R^2 (close to unity) and the fact that the values calculated from the pseudo-second order model ($q_{e\text{-}cal}$) were consistent with the experimental data ($q_{e\text{-}exp}$) indicate the pseudo-second order model is more applicable. This indicates that the adsorption process includes diffusion of the external liquid film, surface adsorption and intra-particle diffusion processes, and that the adsorption rate is determined by the number of unoccupied adsorption vacancies on the adsorbent surface.[233]

The rate of adsorption can be further quantified by the h value (mg g^{-1} min^{-1}) as shown in **Table 4.1**. The h value indicates the initial adsorption rate (**Eq. (1.11)**). S800K4 and S950C90 exhibit exceptionally high h values of (901-9804) and (2765-34770) mg g^{-1} min^{-1}, respectively which greatly exceed the values for S800 (2.1-8.4 mg g^{-1} min^{-1}) and commercial activated carbon of (110-397 mg g^{-1} min^{-1}). Especially for S950C90, the micropores provide effective sites for the adsorption of methylene blue molecules and the extensive network of mesopores and macropores in the porous structure enhance the diffusion of methylene blue molecules to the inner surface of the adsorbent. As a result, a fast overall adsorption rate is attained by S950C90.

4.2.2 Effect of Initial Concentration of Methylene Blue on Adsorption

The equilibrium capacities of the adsorbents at different initial methylene blue concentrations were determined in triplicate and the average values are presented in **Figure 4.2** and **Table 7.11** in **Appendix 7.3**. For most of the adsorbents, the adsorption capacities (q_e, mg g^{-1}) improved as the methylene blue concentration was increased due to the increasing

driving force from the concentration gradient. The increase of the adsorption capacities with the increase of the methylene blue concentration also indicates that there were sufficient adsorption binding sites on the adsorbents for methylene blue molecules at low concentration ranges. Then, the maximum adsorption capacities were obtained when saturation was reached at high concentrations. All the Starbons® exhibit excellent removal efficiencies (R_e, %) towards methylene blue at low initial concentrations (close to 100%). With the increase of the concentrations of methylene blue solutions, the removal efficiencies decrease dramatically as the absorbents reach their maximum adsorption capacities and all sites were occupied by methylene blue molecules at high concentrations.

Compared to the nonactivated S800 and commercial activated carbon, the adsorption capacities of potassium hydroxide, carbon dioxide and oxygen activated Starbons® at adsorption equilibrium have been greatly improved. S950C90 has the largest capacity of (891 ± 43) mg g^{-1} and removal efficiency of (74 ± 4)% at a methylene blue concentration of 600 mg L^{-1}. The adsorption capacity is almost nine times higher than that of S800 (106 ± 8) mg g^{-1} and four times higher than that of commercial activated carbon ((231 ±6) mg g^{-1}). The high adsorption capacity, as well as the high removal efficiency of activated Starbons® reveal the high potential of the activated Starbons® in practical applications where complete decolouration of wastewater with a high adsorption capacity is needed.

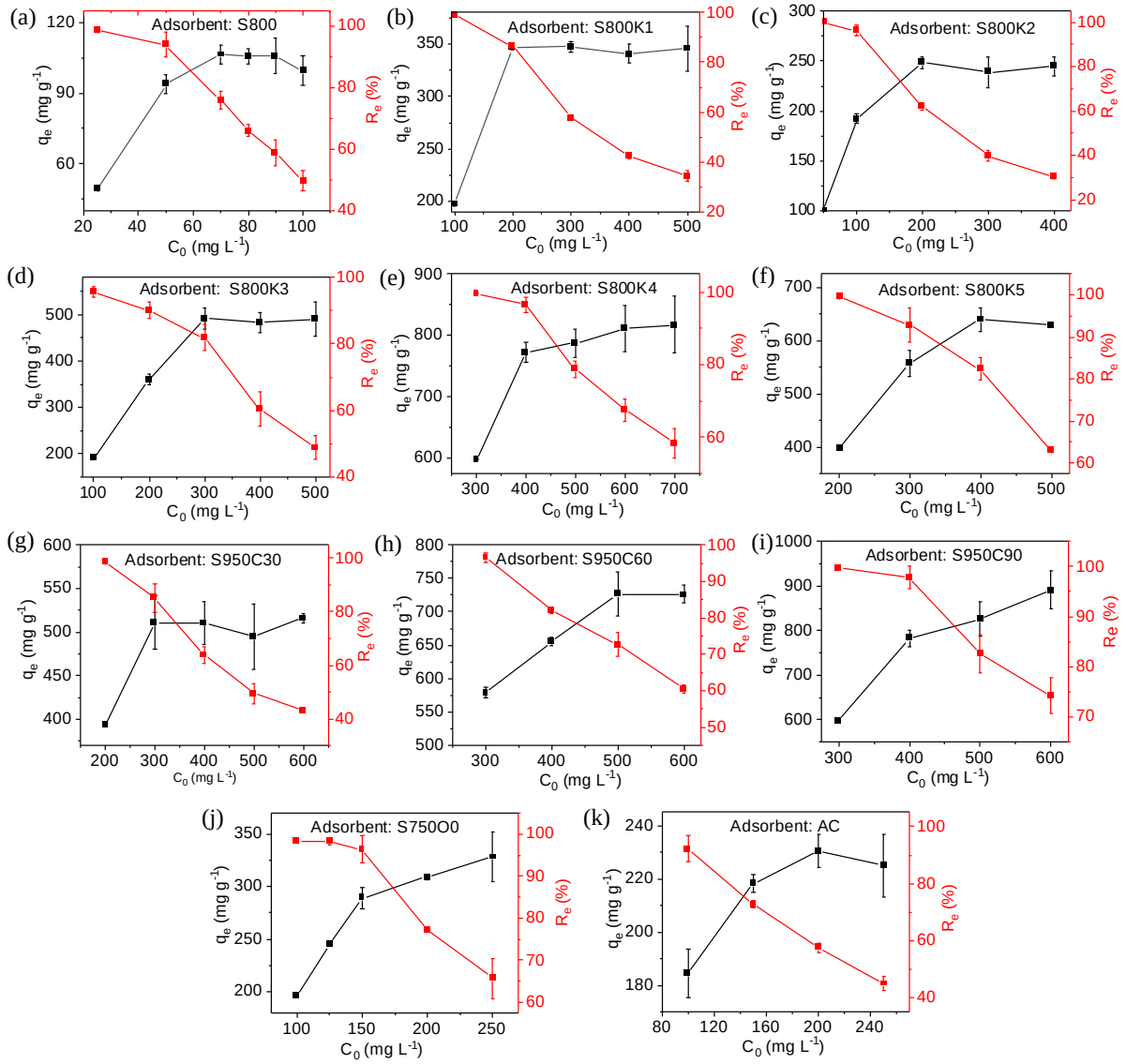

Figure 4.2 Effect of initial concentration of methylene blue on equilibrium adsorption capacities and remove efficiencies for methylene blue of materials at 298 K. Error bars represent standard deviations.

4.2.3 Effect of Temperature on Adsorption

The effect of temperature on equilibrium capacities and removal efficiencies of the best performing materials: S800K4 and S950C90 at different methylene blue concentrations were studied in triplicate at the range of 298-318 K and the results are presented in **Figure 4.3 and Table 4.2**. As the initial concentration of methylene blue increased, the maximum adsorption

capacities increased at all temperatures. However, at a given initial concentration, no obvious change of adsorption capacity is observed on increasing the temperature in the range of 298-318 K.

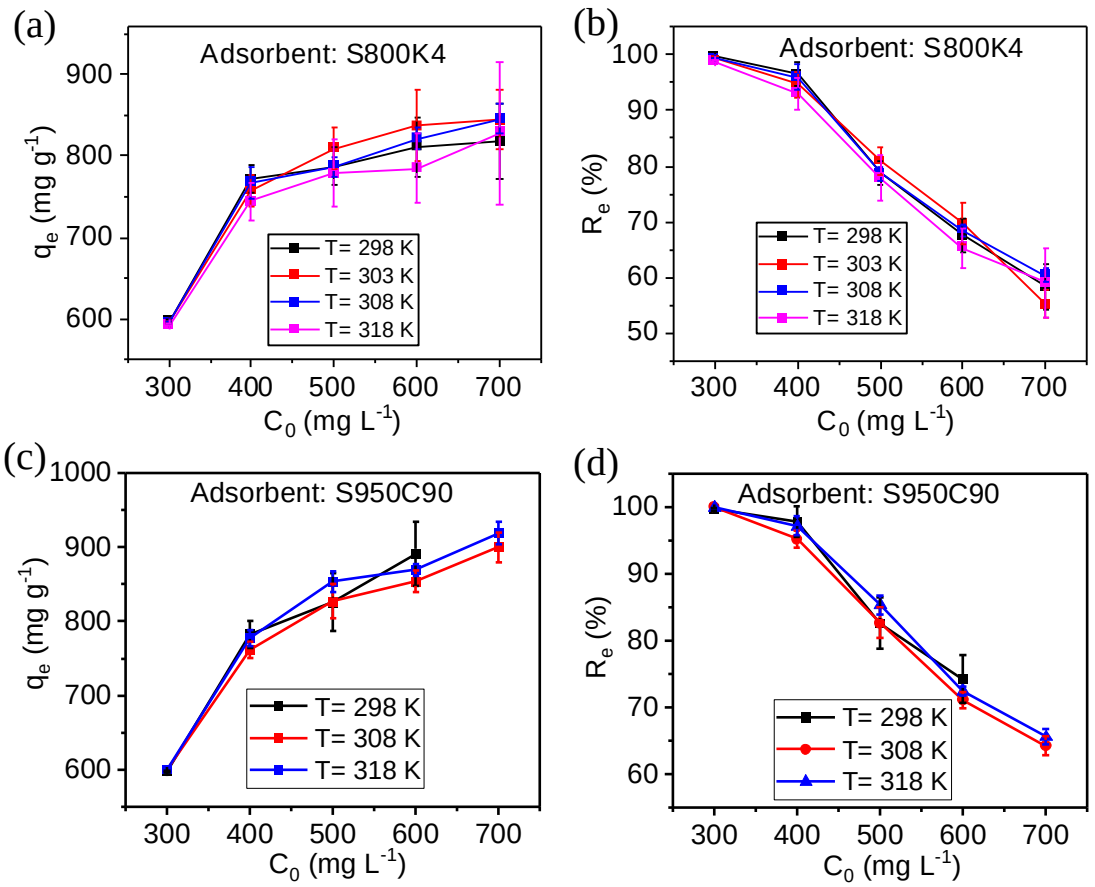

Figure 4.3 Effect of temperature on the equilibrium adsorption capacities and removal efficiencies of methylene blue onto (a,b) S800K4 and (c,d) S950C90 at different initial concentrations of methylene blue. Error bars represent standard deviations.

In addition, more than 95% removal efficiency of methylene blue could be achieved by both samples at methylene blue concentrations of 300 and 400 mg L^{-1} throughout the range of temperatures investigated, indicating the high efficiency of the adsorbents for methylene blue adsorption at relatively high concentrations (compared to the other samples). The additional adsorption sites accessible in these adsorbents contribute to the higher adsorption capacities at higher concentrations. The adsorption capacities and removal efficiencies of S950C90

were all higher than those of S800K4 at higher concentrations of 500-700 mg L^{-1}. A highest capacity of (919 ± 15) mg g^{-1} for S950C90 was attained at a methylene blue concentration of 700 mg L^{-1} at 318 K.

Table 4.2 Equilibrium adsorption capacities and removal efficiencies of methylene blue onto S800K4 and S950C90 at different initial concentrations and temperatures.

Sample	T (K)	C_0 (mg L^{-1})	Q_e (mg g^{-1})	R_e (%)
		300	597.9±0.7	99.7±0.1
		400	771.8±16.5	96.5±2.1
		500	787.2±22.7	78.7±2.3
		600	811.0±36.9	67.6±3.1
	298	700	817.0±46.0	58.4±4.0
		300	597.2±1.0	99.53±0.2
		400	757.3±18.4	94.66±2.3
		500	809.3±25.6	80.93±2.6
		600	836.6±43.5	69.71±3.6
	303	700	844.1±36.8	55.29±2.6
		300	597.5±0.3	99.59±0.1
		400	767.2±18.5	95.90±2.3
		500	787.2±12.0	78.72±1.2
		600	821.6±13.8	68.47±1.2
	308	700	845.4±18.4	60.39±1.3
		300	597.1±1.1	99.52±0.2
		400	744.7±23.0	93.09±2.9
		500	778.4±41.8	77.84±4.2
		600	784.7±43.0	65.39±3.6
S800K4	318	700	828.4±87.4	59.17±6.2
		300	597.9±1.4	99.65±0.2
		400	782.5±18.4	97.81±2.3
		500	825.9±38.7	82.59±3.9
	298	600	891.0±43.1	74.25±3.6
		300	597.6±0.7	99.59±0.1
		400	761.6±10.6	95.20±1.3
		500	826.8±23.2	82.68±2.3
		600	853.7±14.8	71.14±1.2
	308	700	899.8±20.3	64.27±1.5
		300	598.7±1.1	99.83±0.1
		400	777.6±11.3	97.20±1.4
		500	853.8±14.1	85.38±1.4
		600	869.2±7.6	72.43±0.6
S950C90	318	700	918.9±15.1	65.64±1.1

4.2.4 Adsorption Isotherms

In order to understand the characteristics and mechanism of adsorption at equilibrium, the obtained equilibrium adsorption data was fitted to the Langmuir, Freundlich and Temkin isotherm models. The nonlinear forms of the isotherm models are described in **Table 1.4**. The fitting plots and corresponding parameters are shown in **Table 4.3** and **Figure 4.4**.

Table 4.3 Equilibrium adsorption capacity and remove efficiency of methylene blue onto materials at different initial concentrations and temperatures.

		Langmuir			Freundlich				Temkin		
Sample	T (K)	q_m[a]	K_L[b]	R^2	K_F[c]	1/n	R^2	ΔG_{ads}[d]	K_T[e]	B	R^2
	298	819.7	1.525	0.708	628.9	0.049	0.889	-31.4	2.320×10^7	36.71	0.868
	303	847.5	2.492	0.549	591.8	0.066	0.966	-31.2	1.173×10^5	50.34	0.948
	308	847.5	3.119	0.326	601.0	0.061	0.912	-31.9	3.844×10^5	47.35	0.895
S800K4	318	826.5	3.868	0.186	566.4	0.067	0.938	-32.6	8.584×10^4	51.64	0.923
	298	887.1	1.863	0.870	627.9	0.069	0.920	-30.7	1.302×10^5	52.66	0.902
	308	912.1	2.657	0.637	632.3	0.061	0.956	-32.0	2.115×10^5	51.45	0.962
S950C90	318	896.2	3.651	0.157	687.5	0.050	0.943	-33.7	1.100×10^7	44.42	0.946
S800	298	107.2	0.342	0.983	70.79	0.115	0.831	-23.7	7.562×10^2	10.50	0.772
S800K1	298	344.8	0.096	0.606	234.6	0.076	0.856	-28.1	2.262×10^4	22.93	0.810
S800K2	298	243.9	0.468	0.407	150.9	0.095	0.949	-26.3	4.007×10^3	18.39	0.902
S800K3	298	500.0	5.625	0.501	199.6	0.177	0.863	-24.2	5.002×10^3	74.28	0.788
S800K5	298	632.9	1.139	0.686	421.4	0.088	0.927	-29.1	6.342×10^3	47.38	0.905
S950C30	298	510.2	1.082	0.953	392.7	0.049	0.803	-30.2	1.270×10^7	23.57	0.780
S950C60	298	740.7	5.082	0.279	482.1	0.077	0.946	-29.8	9.878×10^3	49.95	0.948
S750O0	298	325.7	1.300	0.912	219.8	0.093	0.813	-27.3	3.227×10^3	26.52	0.792
AC	298	229.4	1.493	0.393	162.0	0.074	0.909	-27.2	2.041×10^4	15.66	0.893

a) Units: mg g^{-1}; b) Units: L mg^{-1}; c) Units mg $g^{-1}(L\ mg^{-1})^{1/n}$); d) KJ mol^{-1}; e) Units: L mg^{-1}

It is observed that the Langmuir model is not applicable for all the materials, and the correlation coefficients (R^2) of the Freundlich isotherm model are higher than those of the Langmuir and Temkin isotherm models for most adsorbents (**Table 4.3 and Figure 4.4**). The best fit of the Freundlich model with the experimental data indicates that the adsorption process is multilayer and non-ideal adsorption with adsorption sites distributed non-uniformly on the heterogeneous surface with different heats of adsorption and affinities.[254] In addition, the adsorption driving force and the surface heterogeneity can be evaluated in the Freundlich

model, by the 1/n value which represents the adsorption affinity or the degree of the surface heterogeneity.[237] The values of 1/n were all less than 0.5, indicating that the adsorption of methylene blue onto these materials occurred easily. The larger values of K_F for methylene blue adsorption onto S950C90 at higher temperature than that of lower temperature indicates that the adsorption is favourable at higher operating temperatures.

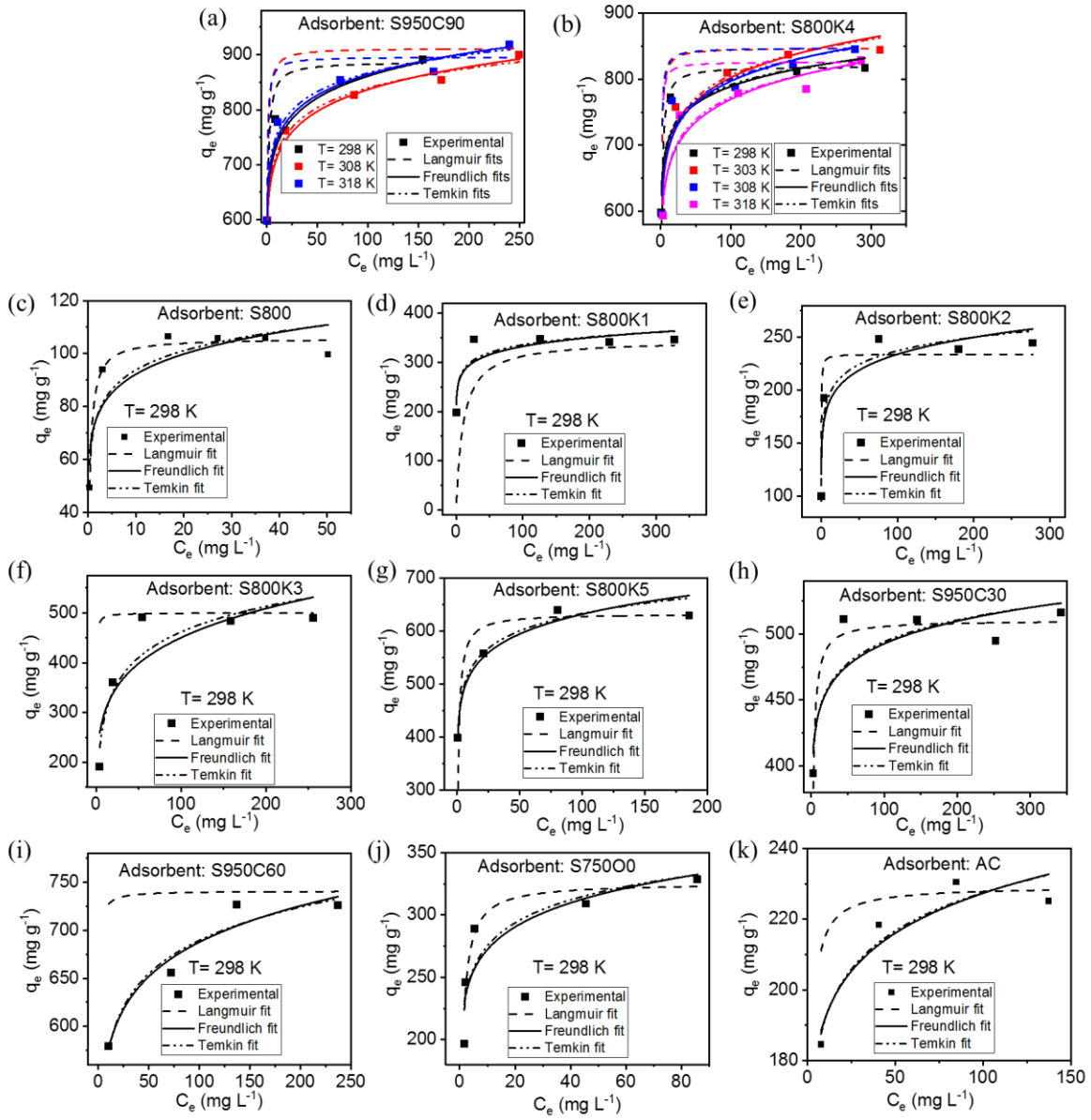

Figure 4.4 Adsorption isotherms of methylene blue onto (a-j) Starbons® and (k) commercial activated carbon at different initial methylene blue concentrations.

Based on the Freundlich isotherm constant (K_F), the thermodynamic equilibrium constant K_{eq} can be calculated according to **Eq. (4.4)**.[232] Then the Gibbs free energy ($\Delta G°$) as listed in **Table 4.3** was calculated based on K_{eq} using equation **Eq. (1.13)** to estimate the effect of temperature on methylene blue adsorption.

$$K_{eq} = \frac{K_F p}{1000}\left(\frac{10^6}{p}\right)^{1-\frac{1}{n}} \quad (4.4)$$

where p is the density of pure water (assumed as 1.0 g mL^{-1}).

As shown in **Table 4.3**, at 298 K, all the samples show negative Gibbs energy change values for the adsorption of methylene blue between -23.7 and -31.4 kJ mol^{-1}, confirming the spontaneous nature of the adsorption process. The least negative value (-23.7 kJ mol^{-1}), corresponding to adsorption of methylene blue being least favourable, was obtained for the mesoporous S800. The two most negative values at 298 K (-30.7 and -31.4 kJ mol^{-1}), corresponding to adsorption of methylene blue being most favourable, were obtained for S950C90 and S800K4 respectively, which have the highest adsorption capacities. At higher temperatures, the Gibbs free energies of adsorption became more negative, decreasing to -32.6 kJ mol^{-1} at 318 K for S800K4 and to -33.7 kJ mol^{-1} at 318 K for S950C90.[354]

4.2.5. Effect of pH

Methylene blue is a cationic macromolecular dye, but its state can be altered by the pH of the solution. In addition, the surface charge of the adsorbent can also be affected by the pH, which as a result affects its adsorption performance. pH_{zpc} can be used to analyse the surface charge between the adsorbent and adsorbate. It refers to the pH value of the solution when the charge (Zeta potential) on the surface of the adsorbent is zero.[232] Therefore, the effect of different pH values of the methylene blue solution on the best performing sample, S950C90, was investigated.

The pH_{zpc} of S950C90 was determined as 5 as shown in **Figure 4.6a** (the Zeta potential at pH 5 was zero). The surface charges of S950C90 were positive at pH values below 5 and became negative when the solution pH was above 5. **Figure 4.6b** shows that the pH is an important factor that determines the methylene blue adsorption of S950C90. The adsorption capacity and removal efficiency increased from (819 ± 36) mg g^{-1} and (82 ± 4)% at pH 4 to (937 ± 20) mg g^{-1} and (94 ± 2)% at pH 9 and then the adsorption capacity tended to be stable as the pH continued to rise. The results can be ascribed to the fact that the adsorbent has a more negative potential on its surface when the pH is higher, which can be demonstrated by the results shown in **Figure 4.6a**. Therefore, the decrease in adsorption capacity and removal efficiency at lower solution pH ($pH < pH_{zpc}$) can be ascribed to the enhanced electrostatic repulsion between the increasingly positively charged adsorbent surface and the methylene blue cations. In addition, competition of the excess protons with methylene blue cations for adsorption sites also results in lower adsorption capacities at lower pH values. In contrast, the favourable adsorption of methylene blue on S950C90 at higher pH ($pH > pH_{zpc}$) is due to the enhanced electrostatic attraction between the negative charged adsorbent and positive charged methylene blue molecules.

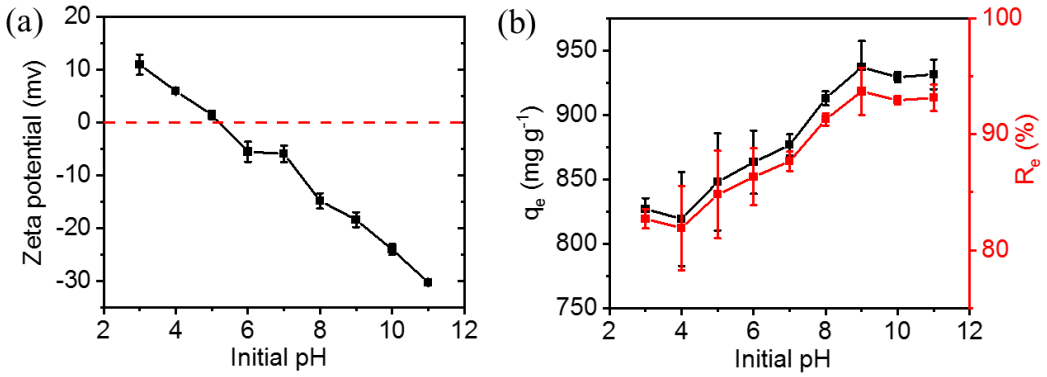

Figure 4.5 Zeta potential (a) and adsorption capacities and removal efficiencies (b) of S950C90 at different pH values of methylene blue solution.

4.2.6 Correlation between Methylene Blue Adsorption Capacities and Textural Properties of the Adsorbents

In addition to the surface charge and functional groups which could affect the adsorption performance of the adsorbent by affecting its interaction with methylene blue molecules, porosity is another important factor that determines the adsorption behaviour. Therefore, to obtain insight into the effect of textural property on methylene blue adsorption performance, the correlation between the adsorption capacities (at adsorption equilibrium at 298 K) and the textural properties of adsorbents was further studied, and the data is presented in **Table 4.5**.

Table 4.4 Textural properties of Starbons® and commercial AC and their corresponding methylene blue adsorption capacities at 298 K.

Material	S_{BET} (m^2 g^{-1})	$S_{Micropore}$ (m^2 g^{-1})	$S_{External}$ (m^2 g^{-1})	$V_{pore\ size<0.7\ nm}$ (cm^3 g^{-1})	$V_{pore\ size<0.8\ nm}$ (cm^3 g^{-1})	$V_{pore\ size<0.9\ nm}$ (cm^3 g^{-1})	$V_{pore\ size<1\ nm}$ (cm^3 g^{-1})	$V_{pore\ size<2\ nm}$ (cm^3 g^{-1})	V_{total} (cm^3 g^{-1})	methylene blue adsorption capacity (mg g^{-1})
AC	812	421	391	0.21	0.24	0.25	0.27	0.34	0.74	230.5±6.3
S800	619	543	76	0.19	0.2	0.21	0.22	0.24	0.59	105.9±7.7
S800K1	1214	908	306	0.32	0.35	0.38	0.4	0.48	1.06	347.3±5.0
S800K2	1294	1177	117	0.39	0.42	0.44	0.45	0.49	0.59	248.3±6.0
S800K3	1633	1468	165	0.45	0.5	0.53	0.55	0.62	0.77	491.1±23.7
S800K4	2299	1781	518	0.46	0.56	0.62	0.66	0.91	0.98	817.0±46.0
S800K5	2452	1404	1048	0.57	0.64	0.7	0.76	1	1.09	638.9±21.4
S950C30	1618	395	1223	0.46	0.5	0.53	0.56	0.64	0.94	515.9±5.3
S950C60	2180	1418	761	0.53	0.6	0.66	0.71	0.89	1.32	726.1±33.1
S950C90	2457	1193	1264	0.56	0.64	0.71	0.77	1.04	1.64	891.0±43.1
S750O0	1100	933	168	0.33	0.36	0.38	0.39	0.43	0.58	328.4±24.1

The exceptionally high adsorption capacity of S950C90 ((891 ± 43) mg g^{-1}) can be attributed to its well-developed hierarchical porous structure (highest surface area and micro- and mesopore volumes), wherein, micropores provide effective adsorption sites for

methylene blue molecules; whilst the abundant meso- and macropores provide spaces to reduce the hindrance effect and facilitate the diffusion of methylene blue molecules into the adsorbent. The correlation of the methylene blue adsorption capacities with the volumes of pores with diameter less than 0.7 nm (ultramicropores), 0.8 nm, 0.9 nm, 1 nm and 2 nm (micropores); total volumes; total (BET) surface areas; micropore surface areas and external surface areas of the samples is shown in **Figure 4.7**. The correlation of the methylene blue adsorption capacities with the volumes of pores with diameter between 2-50 nm, larger than 2 nm; fraction of the volume of pores in different sizes; fraction of micropore surface area and external surface area of the samples is shown in **Figure 7.7** and **Table 7.12** in **Appendix 7.3**.

The methylene blue adsorption capacity of an adsorbent is greatly determined by the size of the methylene blue molecule (0.72 nm in width and 1.43 nm in length as shown in **Figure 1.7**). Therefore, methylene blue molecules can be inhibited to access to ultramicropores (pore size less than 0.7 nm). As a result, the correlation of the adsorption capacities with the volumes of ultramicropores is relatively low (**Figure 4.7a**). A better linear relationship was acquired between the adsorption performance and the pore volumes as the pore size increased to 2 nm (**Figure 4.7b-e**). In contrast, the correlation between the adsorption capacity and pore volumes becomes worse when the pore size is larger than 2 nm (**Figure 7.7a,b** and **Table 7.12** in **Appendix 7.3**). The relatively low resistance facilitates the diffusion of methylene blue molecules into the larger pores but also makes it easier for the dye to get out of them.[353] Therefore, the volumes of micropores (pore size less than 2 nm) shown in **Figure 4.7e** exhibited the best correlation to the methylene blue adsorption capacities. In addition, **Figure 4.7g-i** shows that micropore surface area and external surface area contribute to the adsorption capacity as a synergetic effect, therefore, the adsorption capacity is also best correlated to the total (BET) surface area. These results indicate that the

adsorption capacity of the adsorbent depends on the coefficient effects of the volume of micropores and the total surface area.

A comparison of S800K4 and S800K5 (**Table 4.5**) appears not to be consistent with the above conclusion. S800K5 exhibited a lower adsorption capacity compared to S800K4, although its surface area and micropore volume are slightly higher. This is because the extra surface area and micropore volume of S800K5 is attributed to its higher ultramicropore volume, whereas the pore volume with pore size of 0.7-2.0 nm is slightly lower.

In addition, there is a combination effect of the micropores and mesopores that contributes to a high adsorption capacity, which can be seen by comparison of S800K1 and S800K2 or of S800K5 and S950C90 (**Table 4.5**). Due to its mesopores, the adsorption capacity of S800K1 is higher than that of S800K2, although its surface area and micropore volume are slightly lower. Similarly, the surface area and micropore volume of S800K5 and S950C90 are very similar, whereas, due to its additional mesoporous structure, the adsorption capacity of S950C90 is particularly high. The non-negligible contribution of mesopores is evidenced by the poor correlation of the fraction of pore volumes with pore size smaller than 0.7, 0.8, 0.9, 1 and 2 nm (**Figure 7.7c-g** in **Appendix 7.3**) with the adsorption capacities.

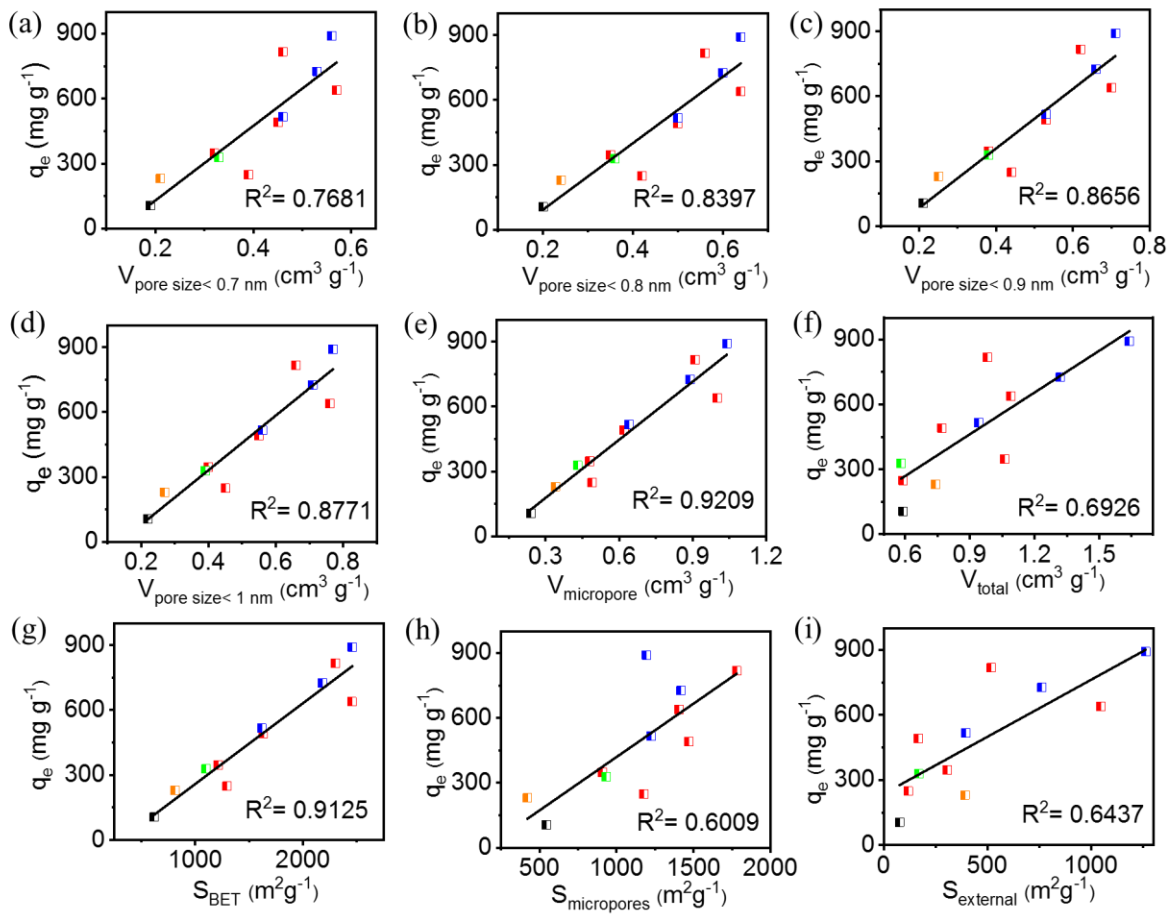

Figure 4.6 methylene blue adsorption capacity at 298 K versus (a-e) the volume of pores with diameters less than (a) 0.7 nm, (b) 0.8 nm, (c) 0.9 nm, (d) 1 nm, (e) 2 nm; (f) total pore volume; (g) BET (total) surface area; (h) micropore surface area and (i) external surface area of Starbons® and commercial activated carbon. Colours in black, red, blue, green and orange represent non-activated S800, KOH activated, CO_2 activated, O_2 activated Starbons® and commercial activated carbon, respectively.

4.2.7. Recyclability

Desorption and recyclability are also important in evaluating an adsorbent in a practical dye adsorption application. Therefore, the recyclability of S950C90 towards adsorption of methylene blue (500 mg L^{-1}) at 298 K was studied. The desorption was conducted by mixing

the adsorbed sample with solution of ethanol and acetic acid (v/v:20/1) and ultrasonicating the suspension.

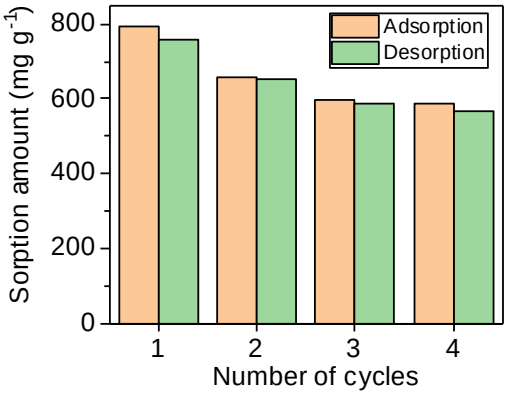

Figure 4.7 Recyclability of S950C90 at 298K.

The recyclability of S950C90 is shown in **Figure 4.8**. The first cycle adsorption capacity of S950C90 at the initial concentration of 500 mg L^{-1} at 298K was 793 mg g^{-1}, which is consistent with the previous results. The removal of methylene blue was efficient, as the first desorption removed 756 mg g^{-1} or 95% of the adsorbed methylene blue. The adsorption and desorption capacities of the second, third and fourth cycles were found to be 660 and 654 mg g^{-1}; 597 and 587 mg g^{-1}; 586 and 568 mg g^{-1}, respectively. The high desorption percentages of 99%, 98% and 97% for the last three cycles demonstrate the high desorption efficiency of the adsorbent.

After each adsorption or desorption, the absorbance of the remaining solution was tested to allow us the calculation of the methylene blue mass that was adsorbed or desorbed. The sorption amount (mg g^{-1}) in **Figure 4.8** was calculated based on the methylene blue mass that was adsorbed or desorbed divided by the predetermined initial mass of the adsorbent. Therefore, the partial loss of the adsorbent during the multiple washing and transferring processes, inevitably leads to a decrease of the sorption capacity during the subsequent cycles. However, in spite of the partial loss of the sample, 74% of adsorption capacity was still

preserved after three cycles of adsorption and desorption, suggesting the high recyclability of the adsorbent for methylene blue removal.

4.2.8. TG-FTIR Analysis

In order to further understand the adsorption behaviour, the best performing adsorbent S950C90 was pyrolysed from 20 to 625 °C using a thermogravimetric analyser coupled to a Fourier transform infrared spectrometer (TG-FTIR) under nitrogen with a heating rate of 10 °C min^{-1} and hold temperature at 625 °C for 1 hour, both before and after methylene blue adsorption (adsorption capacity is (826 ± 39) mg g^{-1} at 298 K and initial concentration of methylene blue is 500 mg L^{-1}). Methylene blue was also pyrolysed under the same conditions as a comparison.

Due to the evaporation of water, a mass loss of 16%, 16% and 2% is observed in the TGA curves of methylene blue, S950C90, and S950C90 after adsorption (**Figure 4.9a**), corresponding to the temperature below 100 °C (DTG curves in **Figure 4.9b**). Then, the S950C90 underwent a low mass loss of 10% due to slight dehydration and decomposition (the peaks of produced water located in the range of 1500-1800 cm^{-1} and 3300-3800 cm^{-1} show persistently during the heat treatment; the peaks of produced carbon dioxide at 2350 cm^{-1} and 667 cm^{-1} enhanced gradually from 600 s and 100 °C as shown in **Figure 4.9c**).

However, the significant extend of decomposition of methylene blue results in a large mass loss of 46%. Due to the coexistence of methylene blue in the porous structure of S950C90, the mass loss of S950C90 after adsorption reached to 30%. This result is supported by the appearance of ammonia (800-1200 cm^{-1}) and methane (2800-3100 cm^{-1}) in the FTIR spectra at 1200-4000 seconds (corresponding to 220-650 °C) as shown in **Figure 4.9d-f** for S950C90 after adsorption.

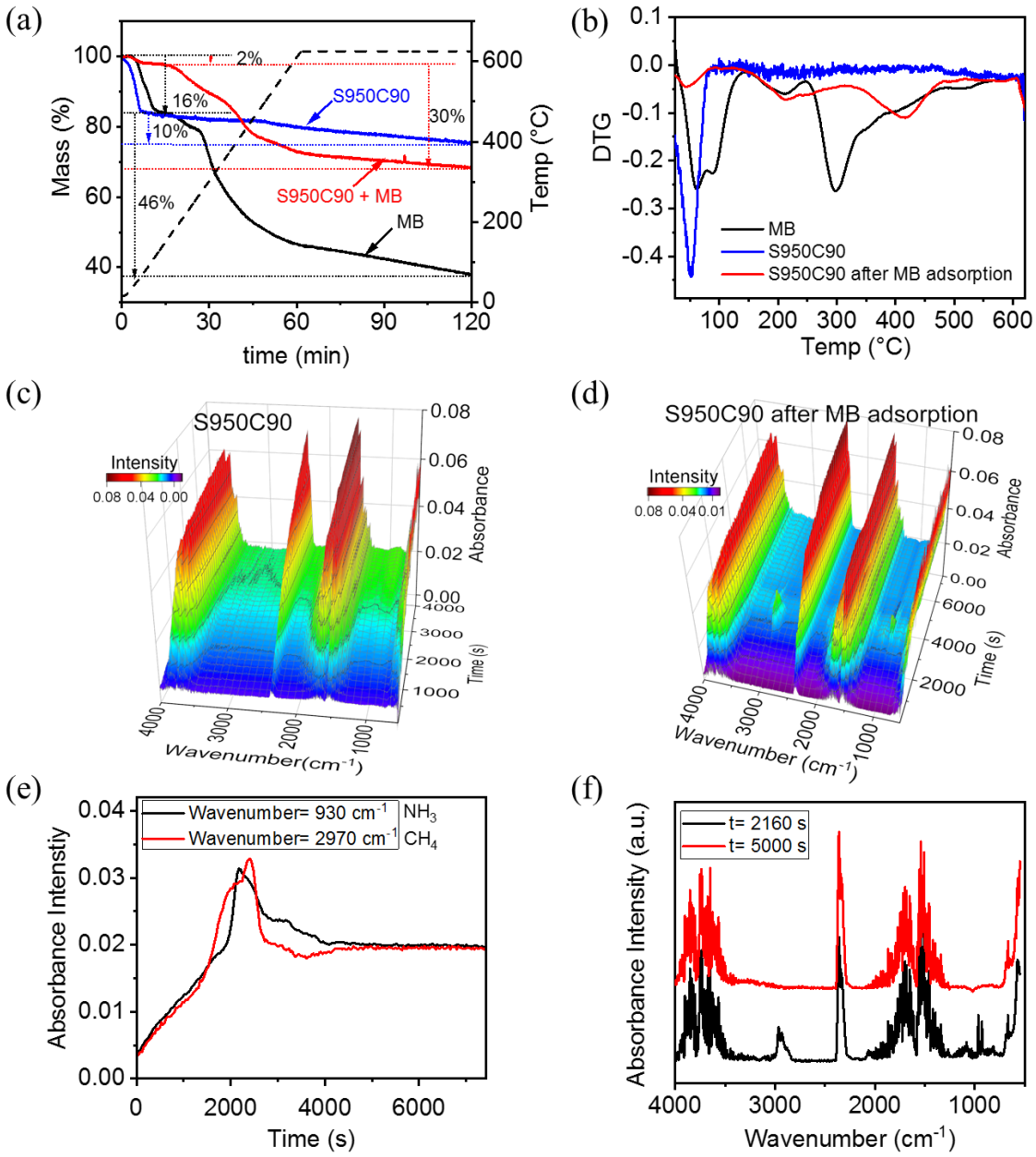

Figure 4.8 (a) TGA and (b) DTG curves from pyrolysing methylene blue and S950C90 before and after methylene blue adsorption under nitrogen; (c,d) real-time FTIR spectra of the off-gases from the TGA experiment of pyrolysing S950C90 (c) before and (d) after methylene blue adsorption; (e) change of absorbance with time of FTIR spectra of NH_3 and H_2S and (f) specific FTIR spectra at 2160 s (black) and 5000 s (red) during the pyrolysis of S950C90 after methylene blue adsorption.

The hydrogen and nitrogen come from the adsorbed methylene blue. In addition, due to the effect of additional hydrogen bonding and electrostatic attraction between the surface of

S950C90 and methylene blue molecules, the decomposition temperatures of S950C90 after adsorption (216 and 418 °C) were higher than those of methylene blue (214 and 297 °C). Based on the decomposition fraction of methylene blue, S950C90 and S950C90 after adsorption (46%/ (100%–16%), 10%/ (100%–16%), and 30%/ (100%–2%), respectively), the adsorption capacity of S950C90 was calculated as 851 mg g^{-1} which compares well with the predetermined value of (826 ± 39) mg g^{-1}.

4.2.9. CHN and XPS Analysis

The adsorption capacities of S950C90 and S800K4 were (826 ± 39) and (787 ± 23) mg g^{-1}, respectively at 298 K with an initial concentration of methylene blue of 500 mg L^{-1}. Based on the experimental results, the contents of nitrogen and sulphur introduced into the S950C90 and S800K4 after adsorption were calculated to be 5.9% and 4.5% for S950C90 and 5.8% and 4.4% for S800K4. Therefore, to further verify the adsorption capacities of the adsorbents, the elemental compositions of S950C90, S800K4 and the corresponding samples after methylene blue adsorption were determined by CHN and S analysis and the data are presented in **Table 4.6**. The increase in content of nitrogen and sulphur within S950C90 and S800K4 after methylene blue adsorption were 4.3% and 3.1%; and 4.9% and 2.3%, respectively, which are close to the calculated values.

Table 4.5 Combustion and XPS analysis of S950C90 and S800K4 before and after methylene blue (MB) adsorption.

Material	CHN analysis					XPS analysis			
	% C	% H	% N	% S	% Rest	% C	%O	%N	%S
S950C90	88.7	0	0	1.2	10.1	98.5	1.3	0	0.1
S950C90+MB	77.1	3.4	4.3	4.3	10.9	91.3	3.1	3.5	1.7
S800K4	78.3	0	0	1.7	20.0	88.2	10.6	0.4	0.2
S800K4+MB	74.2	3.3	4.9	4.0	13.7	78.1	11.9	5.4	2.7

To better understand the surface chemistry of Starbons® after methylene blue adsorption, XPS was used to analyse the elemental surface composition of S950C90 and S800K4, before and after methylene blue adsorption. The wide scan spectra of S950C90 before and after methylene blue adsorption and high-resolution spectra of C1s, O1s and N1s of S950C90 after methylene blue adsorption are shown in **Figure 4.10**. The corresponding spectra of S800K4 before and after methylene blue adsorption are shown in **Figure 7.8** in **Appendix 7.3**. The elemental composition obtained by integrating the peaks of C1s, O1s and N1s are listed in **Table 4.7**.

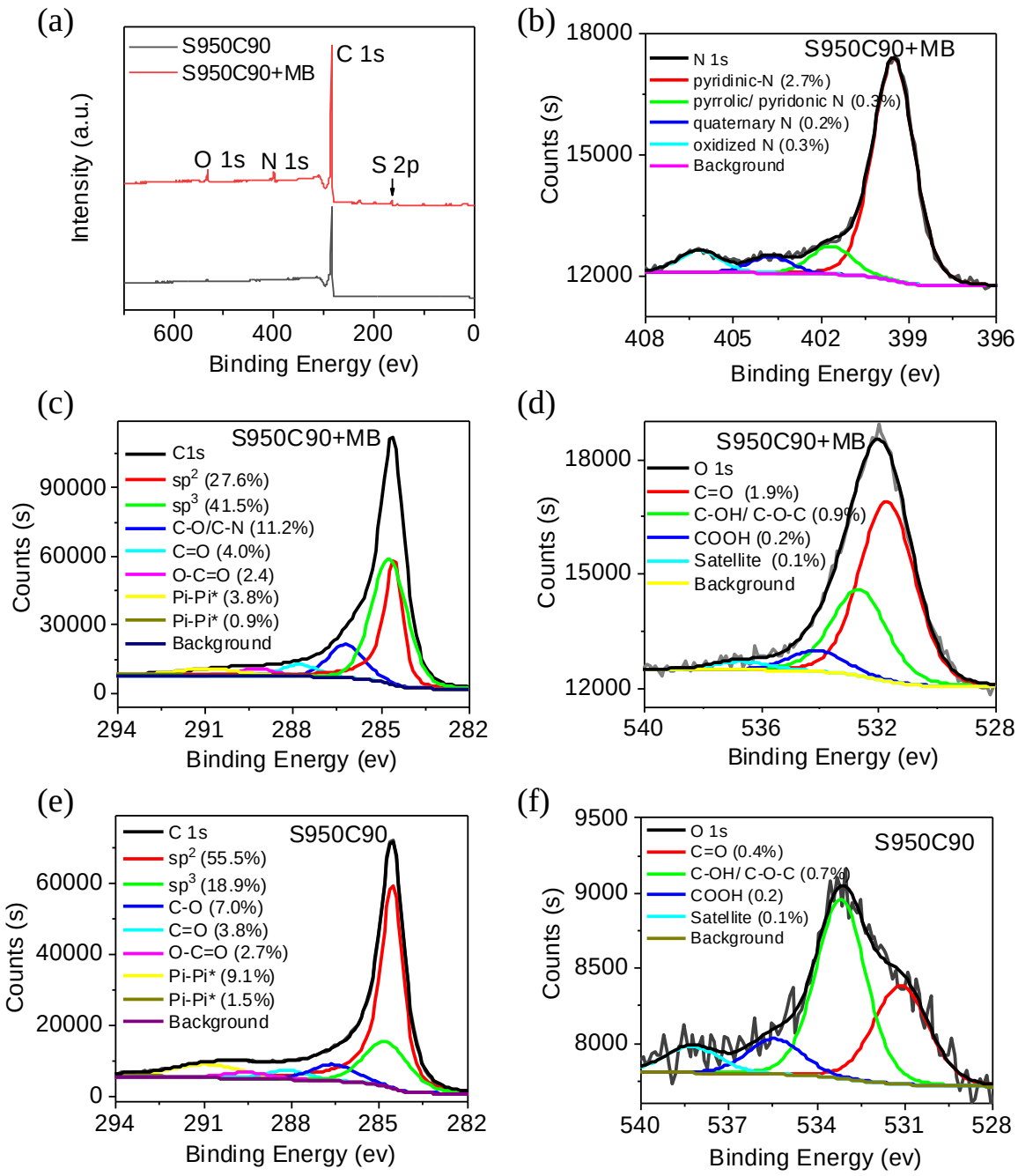

Figure 4.9 (a) Wide scan XPS spectra of S950C90 before and after MB adsorption; (b–d) high resolution spectra of S950C90 after MB adsorption in (b) N1s, (c) C1s and (d) O1s regions; (e–f) high resolution spectra of S950C90 in (e) C1s and (f) O1s regions.

The presence of peaks corresponding to N1s and S2p in the spectra of S950C90 and S800K4 after methylene blue adsorption (**Figure 4.10a** and **Figure 7.8a**) indicates the presence of methylene blue on the surface of S950C90 and S800K4.

Table 4.6 Assignments and quantification of the XPS spectra of S950C90 before and after MB adsorption.

		C1s							
Sample		**C sp^2**	**C sp^3**	**C-O/N**	**C=O**	**O-C=O**	**π-π***	**π-π***	**Total C%**
S950C90	Peak (eV)	284.5	284.7	286.5	288.1	289.5	290.9	294.0	
	Atomic (%)	55.5	18.9	7.0	3.8	2.7	9.1	1.5	98.5
S950C90 +MB	Peak (eV)	284.5	284.7	286.2	287.8	289.2	290.9	294.0	
	Atomic (%)	27.6	41.5	11.2	4.0	2.4	3.8	0.9	91.3
S800K4	Peak (eV)	284.5	284.8	286.7	288.4	290.0	290.9	294.0	88.2
	Atomic (%)	42.5	21.2	8.7	5.9	2.7	5.8	1.3	
S800K4 +MB	Peak (eV)	284.4	284.7	286.1	287.8	289.2	290.8	293.9	78.1
	Atomic (%)	22.0	28.9	15.8	5.2	2.4	3.0	0.7	

		O 1s				
Sample		**C=O**	**C-OH/C-O-C**	**COOH**	**C=O in O-C=O**	**Total O%**
S950C90	Peak (eV)	531.1	533.2	535.4	538.3	
	Atomic (%)	0.4	0.7	0.2	0.1	1.3
S950C90 +MB	Peak (eV)	531.7	532.6	534.1	536.7	
	Atomic (%)	1.9	0.9	0.2	0.1	3.1
S800K4	Peak (eV)	531.7	533.2	535.4	537.1&538.9	10.6
	Atomic (%)	3.8	5.5	0.7	0.6	
S800K4 +MB	Peak (eV)	531.6	532.8	534.6	537.0	11.9
	Atomic (%)	5.6	5.4	0.6	0.3	

The C1s peaks at 286.5, 288.1 and 289.5 eV were assigned to the carbon signals of phenol, alcohol, ether, amine or amide groups (C–O/C-N); carbonyl or quinone groups (C=O); and carboxylic acid, lactone, or ester groups (O–C=O), respectively. The shifting of these peaks after methylene blue adsorption suggests an electrostatic attraction between the negative charged oxygen containing groups on S950C90 and the positive charged dimethyliminium ($=N^{+}Me_2$) groups on methylene blue.[355] The O1s peaks of S950C90 at 533.2, 535.4 and 538.3 eV were assigned to ether, phenol or alcohol groups (C-OH/C-O-C); carboxylic acid groups (COOH); and carbonyls in C=O and COO, respectively. The shift of these O1s peaks to 532.6, 534.1 and 536.7 eV after methylene blue adsorption also suggests the interaction of oxygen containing groups to methylene blue. The same shifting and intensity changes of these C1s and O1s peaks are observed for S800K4 after methylene blue adsorption.

In addition, due to the adsorption of methylene blue onto S950C90 and S800K4, the concentrations of amine or amide groups (C-N) were significantly increased. The concentrations of the shake-up peaks at 290.9 and 294.0 eV resulting from the π-π* transitions of aromatic rings on S950C90 and S800K4 decreased after methylene blue adsorption, suggesting π-π interactions between the aromatic rings of S950C90 and conjugated system of methylene blue.[356] As a result, the adsorption of cationic methylene blue onto S950C90 and S800K4 depends on both electrostatic and π-π interactions.

4.2.10. Textural Property Comparison

To further verify the incorporation of methylene blue molecules into the porous structure of the adsorbent, the textural properties of S800K4 and the corresponding sample after methylene blue adsorption were investigated by measuring nitrogen adsorption-desorption isotherms at 77 K. **Figure 4.11** shows that the typical microporous material S800K4 was completely converted to a non-porous material as both the micropores and mesopores were occupied by methylene blue molecules after methylene blue adsorption.

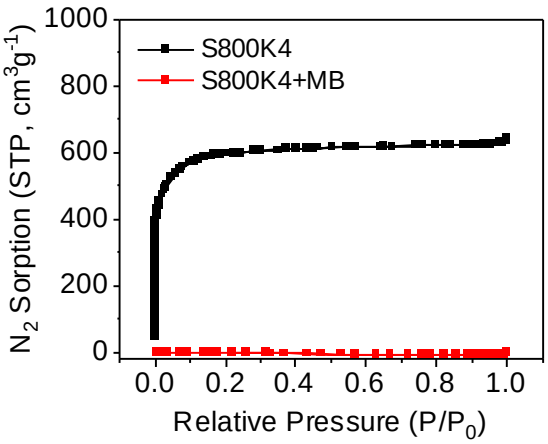

Figure 4.10 N_2 sorption isotherms of S800K4 and the corresponding sample after MB adsorption at 77 K.

4.2.11. SEM and EDS

The surface morphology and element composition of S950C90 before and after methylene blue adsorption were revealed by SEM and EDS images as shown in **Figure 4.12**. The lower magnification images are shown in **Figure 7.9** in **Appendix 7.3**. In order to increase the electrical conductivity, both specimens were coated with carbon before the analysis, therefore carbon mapping is not shown.

Figure 4.12 shows that there are fewer mesopores, macropores and carbon channels of S950C90 after methylene blue adsorption compared to S950C90, indicative of the incorporation of methylene blue molecules within the porous structure of S950C90. The main elemental composition of S950C90 shown by the EDS mapping results are oxygen and sulphur (carbon is not shown). The elemental composition of methylene blue is carbon, oxygen, nitrogen, sulphur and chlorine (as shown in Figure 1.10). As a result, after methylene blue adsorption, a large quantity of nitrogen, sulphur and chlorine were detected on the surface of S950C90 according to the EDS analysis.

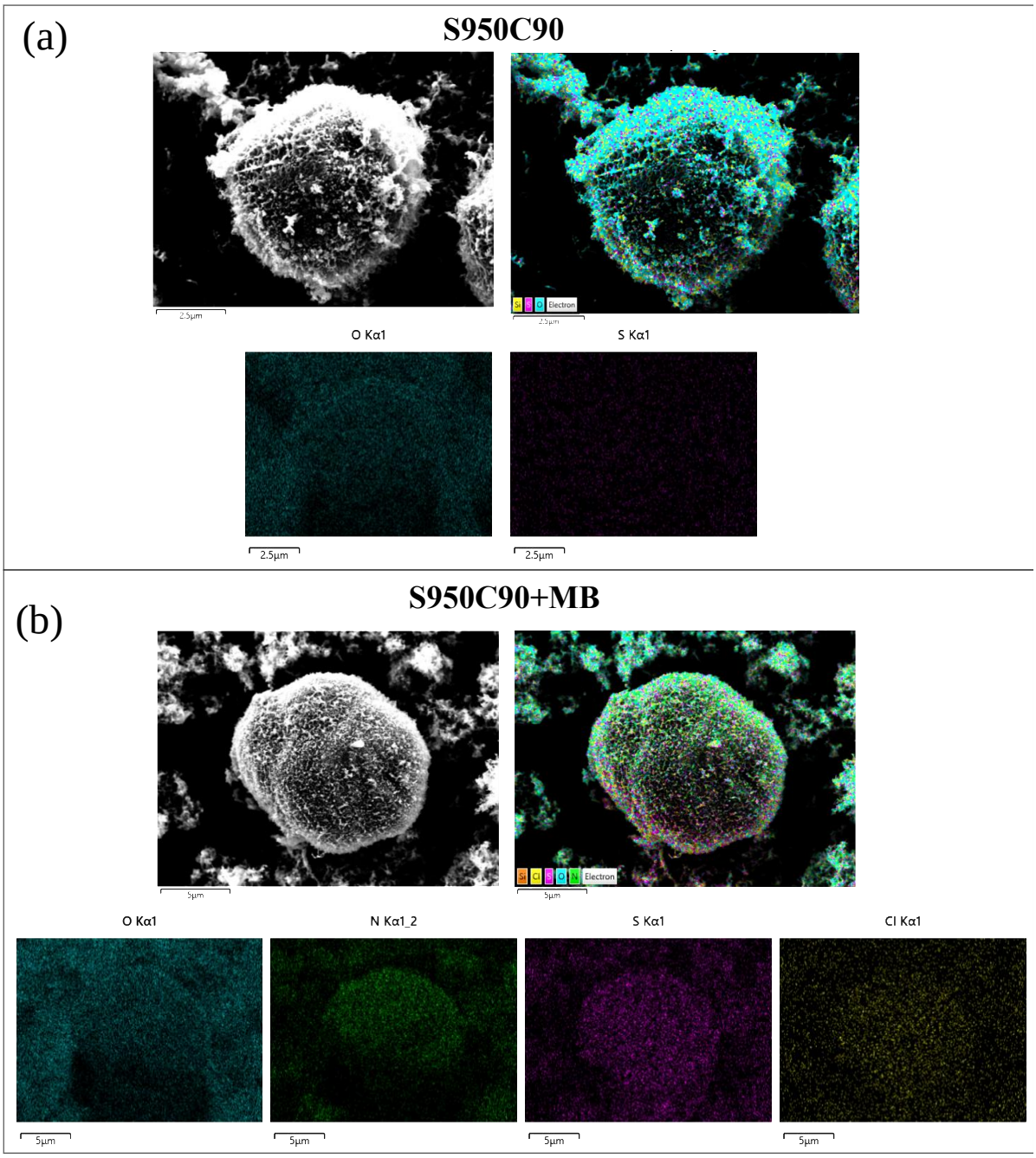

Figure 4.11 SEM-EDS images of (a) S950C90 and (b) S950C90 after methylene blue adsorption at high magnifications.

4.2.12. Comparison of MB adsorption capacity to literature data

Table 4.8 provides data to allow comparison of the adsorption capacities of various biomass derived adsorbents towards methylene blue. The methylene blue adsorption capacities of S950C90 in this work are amongst the highest values reported by adsorbents derived from biomass. In addition, the preparation of S950C90 by carbon dioxide activation is greener than the other adsorbents which are prepared by chemical activation.

Table 4.7 Comparison of MB maximum capacity onto biomass derived carbon materials.

Sample (Biomass precursor)	Preparation method	S_{BET} ($m^2\ g^{-1}$)	Adsorption temperature (^oC)	q_m ($mg\ g^{-1}$)	Ref.
PAC2 (Bituminous coal)	Steam activation	857	20	580[a]	357
AGS-BC (Sludge)	$ZnCl_2$ activation	741	25	90.9	358
HH-KT (Hazelnut shells)	HTC and KOH activation	1700	20	524	359
CN500 (Cashew nutshell)	$ZnCl_2$ activation	1871	25	476	228
MBAC (Sewage sludge and coconut shell)	HTC and KOH activation	874	30/40	589[b]/623[b]	360
AMH1 (Acacia mangium wood)	H_3PO_4 activation	1161	27	159.89	361
OSHTC3 (Coconut shell)	HTC and NaOH activation	876	30	200	362
AC-3 (Coconut shell)	NaOH activation	2825	25	916	363
a-HPTC (Wood)	Carbonization, oxidation and KOH activation	2925	25	838	231
ZHTP-[2] (Coconut shells)	HTC-$ZnCl_2$ and CO_2 activation	1652	25	526	364
S-350-7 (Spruce-pine-fir)	Carbonisation and air activation	725	25	269	365
A300 (Alginic acid)	Carbonisation	280	/	186	64

ALiC (Lignin and chitosan)	Carbonisation	/	20	36.3	233
Fruli (D-Fructose)	HTC with eutectic salt mixture	431	20	83	366
S800K4 (Starch)	Carbonisation and KOH activation	2299	25/35	817/845	This work
S950C90 (Starch)	Carbonisation and CO_2 activation	2457	25/45	891 (937[b])/919	This work

HTC: hydrothermal carbonization; a) adsorption at a pH value of 11; b) adsorption at a pH value of 9.

4.3 Conclusions

The hierarchically activated Starbons® were applied to methylene blue adsorption. The adsorption rate, efficiency and capacity were affected by the adsorption conditions. Compared to S800 and commercial activated carbon, S950C90 exhibits an exceptionally high initial rate of adsorption of (2765-34769) mg g^{-1} min^{-1} at 298 K and adsorption capacities of (891 ± 43) mg g^{-1} at 298 K and (919 ± 15) mg g^{-1} at 318 K without adjusting the pH value of the methylene blue solution. By further adjusting the pH value of the methylene blue solution to 9 at 298 K, the adsorption capacity of S950C90 reached 937 ± 20 mg g^{-1}. The high adsorption capacity of S950C90 at 298 K was also evidenced by TG-FTIR, CHN, porosimetry and SEM-EDS analysis. The adsorption capacity of the adsorbent depends predominantly on the volume of micropores and surface area and also on the combination effect of mesopores, wherein, the micropores provide effective sites for the adsorption of methylene blue molecules and the mesopores and macropores in the porous structure enhance the diffusion of methylene blue molecules to the inner surface of the adsorbent.

The good fit of adsorption data with the pseudo-second order kinetics model indicates that the adsorption rate is determined by the number of unoccupied adsorption vacancies on the adsorbent surface. The good fit of the experimental data with the Freundlich isotherm model also indicates that the adsorption is a multilayer and heterogeneous adsorption. The values of the Freundlich constant as well as the higher value of the Gibbs energy change at higher temperature than that at lower temperature indicate the favourability of the adsorption at higher operating temperatures. The negative Gibbs energy change values confirm the spontaneous nature of the adsorption process. The adsorption enthalpy values of 13.62 KJ mol^{-1} suggest that the adsorption is a physisorption process and that the adsorption process is endothermic. The positive values of adsorption entropy suggest an increase in randomness at

the interface of solid and solution during the adsorption. A good recyclability is also observed for the best performing sample S950C90, which still preserved 74% of its adsorption capacity after three cycles of adsorption and desorption.

Chapter 5: Overall Conclusions and Future Work

5.1 Conclusions

Starch, alginic acid and pectin derived mesoporous Starbons® were prepared by a freeze-drying method combined with pyrolysis carbonisation. Hierarchical Starbons® with diverse pore sizes, pore shapes and a wide range of micro- and mesopore volumes were further produced by potassium hydroxide, carbon dioxide and oxygen activation. The characteristics of the resulting materials can be tailored by choice of appropriate starting material, activation agent and activation conditions. The textual properties of the activated Starbons® endow them with high adsorption ability towards carbon dioxide and methylene blue.

Potassium hydroxide activation is most efficient in engineering the microstructure. At an activation temperature of 800 °C, the resultant material possesses the largest percentage of micropores and the highest surface area. A hierarchical structure with an enhanced micropore volume and preserved mesopore volume can be achieved by use of a low amount of potassium hydroxide (precursor:potassium hydroxide=1:1). Use of intermediate amounts of potassium hydroxide (precursor: potassium hydroxide=1:2 or 1:3) most extensively tunes the ultramicroporosity (around 65%). Use of more potassium hydroxide (precursor: potassium hydroxide=1:5) results in a typical microporous material with a vast majority of microporosity of above 92% and an ultrahigh surface area of above 2400 $m^2 g^{-1}$ (S800K5 and A800K5).

In contrast to potassium hydroxide activation, both micropores and mesopores were well developed by carbon dioxide and oxygen activation. The increase of ultramicro- and micropores is limited and mainly occurs at the start of activation or under mild activation conditions. However, meso- and macropores can be developed extensively under more severe conditions. A hierarchical Starbon® (S950C120) with an ultrahigh surface area of 2733 $m^2 g^{-1}$

and total pore volume of ~2.1 $cm^3 g^{-1}$ (micropore volume of ~1.2 $cm^3 g^{-1}$ and mesopore volume of ~1.0 $cm^3 g^{-1}$) was obtained by carbon dioxide activation. In addition, the rate of reaction of carbon dioxide and oxygen with the precursors is affected by the nature of the polysaccharide used. P800 was found to be the most reactive towards carbon dioxide and oxygen, followed by A800, and S800 was the least reactive precursor. Therefore, the activations of A800 and P800 were conducted at lower activation temperatures, especially for the oxygen activation to prevent excessive burn-off of material.

Enhancement in carbon dioxide adsorption capacity and selectivity can be achieved by fine tailoring of the ultramicroporosity of Starbon® materials. Amongst the materials studied, S800K2 shows the best carbon dioxide capacities of 6.2, 4.0 and 2.7 mmol g^{-1} at 1 bar and temperatures of 273, 298 and 323 K respectively as measured by the adsorption isotherms and 3.1 mmol g^{-1} as measured by STA at 1 bar and 308 K. Due to the high abundance of ultramicro- and micropores in S800K2, its selectivity for adsorption of carbon dioxide over nitrogen was predicted to be 55.3 at 1 bar and 36.6 at 10 bar. These values are double those obtained for non-activated S800 under the same conditions. In addition, S800K5 exhibits the highest 10 bar pressure carbon dioxide adsorption capacity of 20.3 mmol g^{-1} at 273 K and 10.8 mmol g^{-1} at 323 K. We conclude that a higher micropore surface area and a higher degree of ultramicroporosity are the predominant factors that determine the carbon dioxide adsorption capacity at ambient pressure, whereas the combined effects of high surface area and total pore volume lead to a high carbon dioxide storage capacity at high pressure. The fit of the experimental data with both the Langmuir and Freundlich isotherm models indicates that both monolayer and multilayer adsorptions occurred on the heterogeneous surface of samples. The exothermic, spontaneous and physisorption nature of the adsorption process were confirmed from both thermodynamic parameters and the low values of the enthalpy of adsorption.

The hierarchical Starbon® S950C90 exhibits an exceptionally high methylene blue adsorption rate and adsorption capacity of (891 ± 43) mg g^{-1} at 298 K and (919 ± 15) mg g^{-1} at 318 K. The adsorption capacity of S950C90 reached (937 ± 20) mg g^{-1} by further adjusting the pH value of the methylene blue solution to 9 at 298 K due to the enhanced electrostatic attraction between the positive charged methylene blue molecules and negative charged adsorbent. S950C90 also showed a good desorption ability and recyclability, whereby, 74% of its adsorption capacity were preserved after three cycles of adsorption and desorption. The adsorption capacity of the adsorbent depends predominantly on the volume of micropores and surface area and to some extent also on the combination effect of mesopores. The micropores provide effective sites for the adsorption of methylene blue molecules and the meso- and macropores enhance the diffusion of methylene blue molecules to the inner surface of the adsorbent. The good fit of the experimental data with the Freundlich isotherm model indicates that the adsorption is a multilayer and heterogeneous adsorption. The adsorption enthalpy values of 13.62 KJ mol^{-1} indicate that the adsorption is a physisorption process and that the adsorption process is endothermic. The spontaneous nature of the adsorption process is confirmed by the negative Gibbs energy change values.

5.2 Future Work

Enhancement of CO_2 capture by incorporation of nitrogen into hierarchically porous Starbon® materials

In addition to the porous structure of adsorbent, the carbon dioxide capture capacity and selectivity also depend on the affinity between the adsorbate and adsorbent, which may be enhanced by doping the adsorbent with heteroatoms including nitrogen[93], oxygen,[367] sulphur[94] and phosphorus.[368] Amongst these, doping porous carbons with nitrogen-containing

groups has been widely reported to enhance the carbon dioxide capture based on mechanisms including acid–base interactions,[369] electrostatic (quadrupole) interactions[370] and hydrogen-bonding interactions.[371] In our group, a series of nitrogen doped Starbon® materials with nitrile functionality and preserved mesoporosity was previously prepared.[307] The nitrile functionality was introduced by combining chitosan with polysaccharide (alginic acid) in the gelatisation step or by injecting ammonia into the polysaccharide aerogel or the final Starbon product. However, the porosity of the resultant Starbons® (surface area of 250-520 cm^2 g^{-1} and pore volume of 0.32~0.75 cm^3 g^{-1}) remain moderate.

Therefore, based on the pore engineering of Starbon® materials in this work, hierarchically, nitrogen doped Starbon® materials could be prepared by selecting an optimal activation strategy together with nitrogen doping methodology. Apart from the reported used of chitosan and ammonia, other nitrogen sources (e.g. urea, melamine and amino acid lysine etc.) may also be able to be incorporated into a nitrogen free polysaccharide (e.g. starch or alginic acid) prior to expansion or into an intermediate product (e.g. S300) after initial carbonisation. A synergistic effect resulting from the well-developed porous structure and a modified surface functionality that enhances the affinity between the adsorbate and adsorbents may be achieved to further enhance the carbon dioxide capture capacity and selectivity of the materials.

Possible applications of hierarchically activated Starbons®

Mesoporous Starbons® have demonstrated great promise in various applications.[64,80,86,88,89] Hierarchically porous materials with diverse micro-, meso- and macroporosities have shown their superiority in applications of catalysis,[372,373] adsorption and separation,[284,232,315] and energy conversion and storage[122,161]. High contact surface areas can provide sufficient adsorption sites, micro- and mesopores can provide size and shape selectivities for guest

molecules and macroporous networks can provide ready mass transport. Therefore, the newly developed hierarchically structured Starbons® may offer advantages over mesoporous Starbons® in a wide range of applications.

For example, in addition to carbon dioxide adsorption, the hierarchically porous Starbons® may be used for separation and storage of methane from biogas and coalbed gas; and may show better performance on adsorption of other acidic gases (e.g. hydrogen sulfide and sulphur dioxide) from flue gases. Apart from the adsorption of methylene blue in solution, the removal of other pollutants from wastewater such as other dyes (e.g. acid blue), organic acids, halogenated and phenolic compounds and toxic heavy metals (e.g. Au^{3+}, Pt^{2+} and Pd^{2+}) by using the hierarchically activated Starbons® can also be further investigated.

Scaling up hierarchically activated Starbons® and applying them in adsorption and separation on a large-scale

To industrialize separation technology, a carbon-based adsorbent should have a high adsorption capacity, exhibit rapid adsorption and desorption kinetics which are reproducible over multiple cycles and have a low enthalpy of adsorption to minimise the energetic cost of regeneration.[374] In addition, the adsorbent should be reliably producible on a large scale, since industrial adsorption columns will require thousands of kilograms of adsorbent.[375] In addition, the preparation and adsorption operational costs must be minimized to make industrial deployment economically viable.

The non-activated Starbon® precursors are commercially available and are being produced on a 10s-100s Kg scale.[376] The activated Starbons® reported in this work have been shown to fulfil the above requirements of performance in carbon dioxide and methylene blue adsorption with the additional advantage of being sustainably sourced from waste biomass. However, the activated Starbons® presented in this work were prepared only at laboratory

scale. Pilot scale production of other active carbons without loss of their textural properties has already been realised[377,378] and they are widely used in greenhouse gas adsorption and fuel gas storage.[379,380] As the processes are similar, modifications can be made to existing equipment to adapt it to scaling up the production of activated Starbons®. Further research will be required to optimise the production parameters with the aim being to reproducibly produce batches of products with consistent parameters including particle size, morphology, surface chemistry and porous structure. This will enable the industrial application of the materials prepared in this work.

Chapter 6: Experimental

6.1 Chemicals

All materials were used as received without further purification. Starch (Hylon VII) was purchased from National Starch & Chemical Ltd (UK). Alginic acid (from brown algae), pectin (from citrus fruit peel; >74% galacturonic acid), activated carbon, analytical grade potassium hydroxide and sodium hydroxide were purchased from Sigma-Aldrich (UK). t-butanol (TBA, ≥99% purity) was purchased from Fluka Analytical. Ethanol, acetic acid (≥99%) and hydrochloric acid solution (37%, wt) was purchased from Fisher Scientific (UK). p-Toluenesulfonic acid (PTSA, 98% purity) and methylene blue (MB, high purity, biological stain) were supplied by Alfa Aesar. Deionized water was used in this work.

6.2 Main Instruments used

Synthesis of Starbons®

CEM MARS™ 6 microwave; Lablyo freeze dryer; Barnstead Thermolyne 6000 Muffle Furnace; Fistreem vacuum oven; Rotary evaporator; HORIBA Scientific tube furnace; Centrifuge and NETZSCH STA409 coupled with a Bruker Equinox 55 FTIR; VWR ultrasonic cleaner.

Characterisation

Micromeritics ASAP 2020 volumetric adsorption analyser; Agilent 7700 series inductively coupled plasma-optical emission spectrometry (ICP-OES); CE-440 CHN analyser; Thermo K-Alpha+ XPS; JEOL 7800F SEM; JEOL 2011 TEM; STA 625 thermal analyser; Quantachrome Isorb HP2; Julabo SW22 incubator shaker; Thermo Genesys 180 UV-visible spectrometer and Malvern Zetasizer Nano ZS90.

6.3 Synthesis of Starbons®

6.3.1 Synthesis of Starbons® by Using the Freeze Drying Method Combined with Pyrolysis Carbonisation

As previously reported, the synthesis of Starbons® includes expansion, freeze drying and then carbonisation.[74] For starch derived Starbons®, starch was gelatinised in deionized water [1 g: 10 mL (w/v ratio)] by microwave heating using a CEM MARS™ 6 microwave. The microwave was programmed to heat the mixture from room temperature to 140 °C with a heating rate of 10 °C min^{-1} and hold the temperature at 140°C for 10 minutes. Then the mixture was cooled to 5 °C for 24 hours to facilitate retrogradation to produce a porous gel. Then t-butanol (30 wt% relative to the weight of distilled water) and p-Toluenesulfonic acid (5 wt% relative to the weight of starch) were added to the porous gel, followed by stirring for 2 hours at room temperature. Then the obtained gel was freeze dried on a Lablyo freeze dryer with vacuum of 100 mTorr and condenser temperature of -103.9 °C for at least 24 hours until a dry expanded-starch powder was obtained.

For alginic acid derived Starbons®, the porous gel was prepared by mixing the alginic acid with water [1 g: 10 mL (w/v ratio)], stirring at 90 °C for 2 hours and subsequently cooled to 5 °C for 24 hours to facilitate retrogradation. t-butanol (30 wt% relative to the weight of distilled water) was added to the porous gel, followed by stirring for 2 hours at room temperature and freeze drying on the Lablyo freeze dryer at the same conditions for at least 24 hours until a dry expanded-alginic powder was obtained.

For pectin derived Starbons®, the porous pectin gel was prepared by dissolving pectin powder into a 3:1 weight ratio mixture of water and t-butanol [1 g: 10 mL (w/v ratio)]. Then the mixture was sonicated for several hours at 40 °C until the pectin was fully dissolved. The

subsequent freeze drying and carbonization steps were as described for the synthesis of alginic acid derived Starbons®. For both preparing alginic acid and pectin derived Starbons®, no p-Toluenesulfonic acid was added. The resulting starch, alginic acid or pectin derived aerogel was finally carbonised in a Barnstead Thermolyne 6000 Muffle vacuum Furnace to specified temperatures (300, 600, 800 and 1000 °C) using the heating program as listed in **Table 6.1**.

Table 6.1. Temperature controlling program for generating X300 from the porous gel and X600/800/1000 from X300.

Starting material	Temperature (°C)	Ramp rate (°C /min)	Isothermal time (h)	Product
Porous aerogel	25	-	-	-
	100	5.0	1	-
	210	0.3	1	-
	300	0.3	-	X300
Starting material	**Temperature (°C)**	**Ramp rate (°C /min)**	**Isothermal time (h)**	**Product**
X300	300	10.0	-	-
	400	0.3	-	X400
	600	1.0	-	X600
	800	3.0	-	X800
	1000	3.0	-	X1000

6.3.2 Synthesis of KOH Activated Starbons®

Activation of Starbons® was carried out according to previously reported typical procedures[105,342]. X300 was used as the starting material for the activation process. X300 (1 g) was impregnated with KOH (KOH:X300, 1:1~5:1, w:w) using a solution of KOH (100 mL) in ethanol:water (95:5, v:v) and stirring overnight at room temperature. Followed by removing the solvent via evaporating the mixture at 60 °C under vacuum using a rotary evaporator, the resulting mixture was dried in a Fistreem vacuum oven at 80 °C for 24 hours.

The carbonisation process was carried out by heating the mixture powder in a HORIBA Scientific tube furnace with a heating rate of 2 °C min^{-1} to the final temperature of 600, 800, 1000 °C for 1 hour under pure nitrogen (100 cm^3 min^{-1}). Afterwards, the residue was washed with 2 mol L^{-1} hydrochloric acid and then distilled water to remove excess potassium hydroxide and potassium salts until the pH of the filtrate was approximately 7.0. The final samples were obtained after remove the solvent by centrifugation and drying the powders at 80 °C for 24 hours.

6.3.3 Synthesis of CO_2 Activated Starbons®

Carbon dioxide activation was carried out in a NETZSCH STA409 coupled to a Bruker Equinox 55 FTIR. Preformed Starbons® (X800) were used as the starting materials. The burn-off wt% of the X800 was monitored by the thermogravimetric instrument and the composition of the gases from the reaction of carbon with carbon dioxide were analysed in real time using FTIR during the activation process.

X800 (100 mg) was placed in a ceramic cup and heated from room temperature to the required temperature (700~1000 °C) with a heating rate of 10 °C min^{-1} under a flow of pure carbon dioxide (flow rate 50 cm^3 min^{-1}). The maximum temperature was maintained for a specified period of time (0~1 hour). At the end of the activation period, the sample was cooled under a flow of pure nitrogen (flow rate 50 cm^3 min^{-1}).

6.3.4 Synthesis of O_2 Activated Starbons®

Oxygen activation was also carried out in a NETZSCH STA409 coupled with a Bruker Equinox 55 FTIR. Preformed Starbons® X800 were used as the starting material. The burn-off wt% of the X800 was monitored by the thermogravimetric instrument and the composition of the resultant gases from the reaction of carbon with oxygen was analysed in

real time using FTIR during the activation process.

X800 (100 mg) was placed in a ceramic cup and subjected to a flow of 200 cm^3 min^{-1} nitrogen and 20 cm^3 min^{-1} air (overall O_2=2%) and heated from room temperature to a specified temperature (400~800 °C) with a heating rate of 10 °C min^{-1}. The maximum temperature was maintained for a specified period of time (0~1 hour). At the end of the activation period, the sample was cooled under a flow of pure nitrogen (flow rate 50 cm^3 min^{-1}).

6.4 Characterisation

6.4.1 Physisorption Measurements

The textural properties of all samples were investigated by measuring nitrogen adsorption-desorption isotherms on a Micromeritics ASAP 2020 volumetric adsorption analyser at 77 K. Before the analyses, the powdered samples (~0.1g) were degassed at 200 °C for 8 hours to remove moisture and other contaminants.

The BET model was applied for the determination of surface area; the total pore volume (V_{total}) was estimated at a relative pressure of 0.99; the Barrett-Joyner-Halenda (BJH) method was used for determination of mesopore volume and mesopore size distribution. The HK method for carbon materials with slit-shaped pores was applied for the determination of micropore volume (V_{micro}), ultramicropore volume ($V_{ultramicro}$) and micropore size distribution. The DFT method assuming a slit pore model and a non-local DFT method (NLDFT) assuming non-homogeneous fluid at a solid interface in a slit pore model were also applied for the characterisation of the pore volume in all sizes in the activated Starbons®.

6.4.2 ICP-OES Analysis

An Agilent 7700 series inductively coupled plasma-optical emission spectrometry (ICP-OES) was used to determine the composition of elements in samples. The analysis was carried out by the Biorenewables Development Centre. Samples (~50 mg) were digested by a solution of nitric acid and hydrogen peroxide (10 mL, 4:1, v:v). The mixtures were then microwave heated to 200 °C for over 30 minutes, and the temperature was held at 200 °C for 15 minutes. After cooling down, the mixtures were emptied into 100 mL conical flasks and diluted to up to the mark with distilled water and then analysed. The results for each element were fitted onto a calibration curve. The results recorded were then multiplied by the dilution factor, to produce the concentration for each element in the samples.

6.4.3 CHN and S Analysis

The quantity of carbon, hydrogen, nitrogen and sulfur in samples were determined by using an Exeter Analytical Inc. CE-440 analyser by Dr Graeme McAllister (University of York) based on a high temperature combustion method. The sample was burnt at 975 °C under high purity oxygen in a nickel sleeve in a high temperature furnace. The organic matter is converted into stable oxidised forms: water, carbon dioxide, nitrogen and sulfur dioxide. By passing the gas mixture through specialised reagents, the concentration of the resulting combustion products can be acquired. The concentration of water, carbon dioxide and sulfur dioxide produced is proportional to the amount of hydrogen, carbon, and sulfur. The difference between pure helium and a gas mixture containing nitrogen corresponds to the amount of nitrogen in the sample.

6.4.4 XPS Analysis

To investigate the surface chemical compositions of samples, XPS analysis was performed using a Thermo K-Alpha+ XPS fitted with a monochromated Al kα X-ray source by Dr David Morgan at the University of Cardiff. Data were collected at a pass energy of 2150 eV for survey spectra and 40 eV for high-resolution scans. The spectra were collected at a pressure below 10^{-7} Torr and a room temperature of 294 K. Peaks were fit with a Shirley background prior to component analysis. Data was analysed using CasaXPS (v2.3.34) after subtraction of the background and using modified sensitivity factors as supplied.

6.4.5 Scanning Electron Microscopy (SEM)

The morphology of samples was observed using a scanning electron microscopy (SEM, JEOL 7800F) at an accelerating voltage of 5 kV, working distance of 10 mm with a LED detector. Energy dispersive X-ray spectrometer (EDS) analysis was performed by setting the accelerating voltage at 15 kV. The sample was mounted on an aluminium plate and coated with carbon to increase the conductivity prior to analysis.

6.4.6 Transmission Electron Microscopy (TEM)

The morphology of samples was also observed using transmission electron microscopy (JEOL 2011 TEM) at an accelerating voltage of 100 kV. Samples were prepared by sonicating the material in ethanol and depositing it on a holey carbon support film (300 mesh cupper grid).

6.4.7 CO_2 Adsorption Studies

6.4.7.1 CO_2 adsorption studies using STA in CO_2 and N_2 composition swing conditions

The carbon dioxide adsorption of all the samples was investigated using a STA 625 thermal analyser with a gas composition swing method.[86] Before each measurement, sample (~ 10.0 mg) was heated at 373 K for 1 hour under a flow of nitrogen (60 ml min^{-1}) to ensure the removal of residual water and impurities. After cooling to room temperature under nitrogen, the sample was heated to 308 K at 1 °C min^{-1} under nitrogen (60 ml min^{-1}) and then the temperature was kept at 308 K during remainder of the analysis. A three-way valve was employed to switch the gas flow between pure carbon dioxide (60 ml min^{-1}) and pure nitrogen (60 ml min^{-1}) for carbon dioxide adsorption and desorption, respectively. The changes of mass and heat flow were recorded by the TGA and DSC capabilities of the STA 625. Multiple adsorption and desorption cycles were run to determine the regenerability of the samples.

6.4.7.2 CO_2 adsorption studies using STA in CO_2 and N_2 gas mixtures

The adsorption of S800 and S800K2 under a binary gas mixture of carbon dioxide and nitrogen at 308 K was studied by feeding a mixed gas flow (60 mL min^{-1}) into the analyser instead of a pure carbon dioxide.[86] Sample (~ 10.0 mg) was first heated at 373 K for 1 hour under a flow of nitrogen to ensure the removal of residual water and impurities. After cooing to room temperature under nitrogen, the sample was heated to 308 K at 1 °C min^{-1} under nitrogen and then the temperature was kept at 308 K during remainder of the analysis.

The content of carbon dioxide in the gas mixture was adjusted to 15%, 25%, 33%, 42%, 58%, 83% and 100%, respectively. Adsorption occurred when the sample was exposed to the

gas mixture and after reaching equilibrium, the sample was regenerated by switching the gas mixture back to pure nitrogen. Multiple adsorption and desorption cycles were run at each carbon dioxide concentration to determine the regenerability of the samples.

6.4.7.3 CO_2 and N_2 adsorption isotherm studies

The adsorption isotherms of pure carbon dioxide and nitrogen for S800 and some potassium hydroxide activated Starbons® were measured volumetrically by Mr. Cheng Li at Fudan University, using a Quantachrome Isorb HP2 instrument. Before measurement, all samples were degassed under vacuum at 473 K for 8 hours. The carbon dioxide and nitrogen adsorptions were performed under the same conditions in the range of 0~10 bar at 273, 298 and 323 K.

6.4.8 Methylene Blue Adsorption Studies

A stock methylene blue solution at a concentration of 1000 mg L^{-1} was prepared by dissolving an appropriate amount of methylene blue in deionised water. Then the stock solution was diluted to various concentrations (25-700) mg L^{-1} as required for the study of methylene blue adsorption. The ratio of adsorbent to methylene blue solution was 10 mg: 20 mL (adsorbent concentration of 0.5 mg mL^{-1}). The experiment was conducted by shaking the mixture in a Julabo SW22 incubator shaker at a controlled temperature (298, 308 or 318 K) and agitation rate (100 rpm). At appropriate time intervals, samples of the methylene blue solution (1 mL) were withdrawn and filtered through a 0.45 μm membrane filter. The absorbance of the sample was measured by using UV–Vis spectrophotometry at a wavelength of 665 nm. The concentration of methylene blue remaining in the supernatant solution was calculated based on the absorbance value using external standard calibration. Except for the

study of adsorption kinetics, all experiments were carried out in triplicate and the results presented are the calculated average values.

6.4.8.1 UV–Vis Spectrophotometer Analysis

UV-visible spectral analysis was carried out using a Thermo Genesys 180 UV-visible spectrometer between 200 and 800 nm. Distilled water was used as reference. Standard methylene blue solutions of known concentrations (1~10 mg L^{-1}) were prepared and analysed to get a calibration curve as shown in **Figure 6.1**. The concentration of methylene blue left in solutions was calculated according to the standard curve at maximum wavelength of 665 nm.

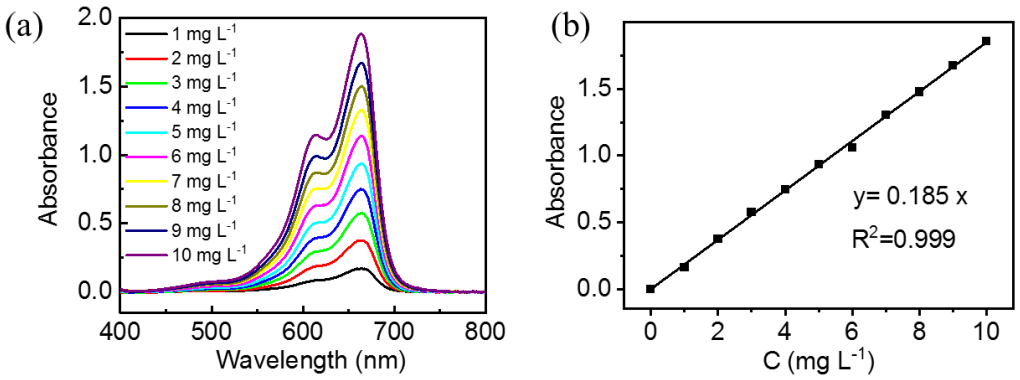

Figure 6.1 (a) UV-vis spectra of methylene blue solutions at various concentrations and (b) standard calibration curve of methylene blue.

6.4.8.2 Zeta Potential Analysis

The Zeta potential of samples was determined by using a Malvern Zetasizer Nano ZS90. Sample (1 mg) was added to distilled water (20 mL) and the pH of the mixture was adjusted to 3~11 by adding 0.1 mol L^{-1} hydrochloric acid or sodium hydroxide solution dropwise. A pH meter was used to test the pH values of the solutions. Then the solution was sonicated for five minutes before testing.

6.4.8.3 Recyclability Studies

The recyclability of S950C90 towards adsorption of methylene blue was studied over four cycles. Firstly, the adsorption of a methylene blue solution (20 mL, 500 mg L^{-1}) onto S950C90 (10 mg) was conducted at 298 K without adjusting the pH value of the solution. After reaching adsorption equilibrium (4 hours), the adsorbent was separated by centrifugation. Then, desorption was conducted by mixing the adsorbed sample with ethanol and acetic acid (150 mL, 20:1, v:v) and ultrasonicating the suspension for 5 minutes. The washing process was repeated three times, then the solid was collected by centrifugation, the solvent was collected together and its absorbance was tested. The solid was then used for another adsorption and desorption cycle.

Chapter 7: Appendix

7.1 Appendix 1: Data for Chapter 2

Table 7.1 Comparison of micropore volumes determined by various models.

Material	t-plot	HK	DFT	NLDFT
S800	0.15	0.20	0.14	0.18
S600K4	0.70	0.73	0.64	0.70
S800K4	0.69	0.91	0.78	0.87
S1000K4	0.52	0.62	0.45	0.53
S800K1	0.35	0.48	0.39	0.44
S800K2	0.44	0.49	0.43	0.49
S800K3	0.55	0.62	0.54	0.60
S800K5	0.75	1.00	0.82	0.93
A800	0.06	0.13	0.06	0.08
A600K2	0.23	0.27	0.23	0.26
A800K2	0.47	0.53	0.44	0.49
A1000K2	0.36	0.49	0.40	0.45
A800K1	0.25	0.46	0.33	0.37
A800K3	0.64	0.75	0.64	0.72
A800K4	0.57	0.95	0.76	0.89
A800K5	0.43	1.01	0.77	0.90
P800	0.05	0.11	0.07	0.08
P800K2	0.49	0.77	0.63	0.72
P800K3	0.47	0.73	0.58	0.66
P800K5	0.32	0.82	0.61	0.71
S800C15	0.17	0.21	0.16	0.17
S850C15	0.18	0.26	0.20	0.23
S900C15 ($25cm^3 min^{-1}$)	0.26	0.35	0.29	0.32
S900C15 ($50cm^3 min^{-1}$)	0.29	0.39	0.32	0.36
S900C15 ($100cm^3 min^{-1}$)	0.30	0.41	0.33	0.38
S950C15	0.26	0.38	0.29	0.35
S1000C15	0.41	0.62	0.49	0.55
S900C30	0.32	0.45	0.35	0.40
S900C60	0.31	0.44	0.36	0.41
S900C90	0.43	0.59	0.48	0.54
S900C120	0.52	0.77	0.61	0.68
S950C30	0.47	0.64	0.53	0.58
S950C60	0.55	0.89	0.70	0.79
S950C90	0.49	1.04	0.78	0.84
S950C120	0.28	1.16	0.74	0.91
A750C45	0.16	0.31	0.20	0.25
A750C60	0.16	0.32	0.20	0.25

A750C90	0.15	0.32	0.20	0.26
A900C0	0.14	0.35	0.21	0.27
A900C10	0.10	0.38	0.20	0.26
P700C50	0.16	0.31	0.22	0.26
P900C0	0.10	0.40	0.26	0.32
S700O0	0.28	0.35	0.30	0.34
S750O0	0.36	0.43	0.36	0.42
S800O0	0.27	0.37	0.31	0.35
S750O40	0.30	0.35	0.28	0.32
S750O56	0.23	0.31	0.26	0.29
A500O30	0.14	0.27	0.17	0.22
A500O60	0.16	0.27	0.18	0.22
A750O0	0.15	0.26	0.17	0.21
P400O50	0.09	0.16	0.11	0.13
P500O30	0.09	0.15	0.10	0.12
P750O0	0.14	0.23	0.17	0.19

Figure 7.1 Comparison of micropore volumes determined by various models.

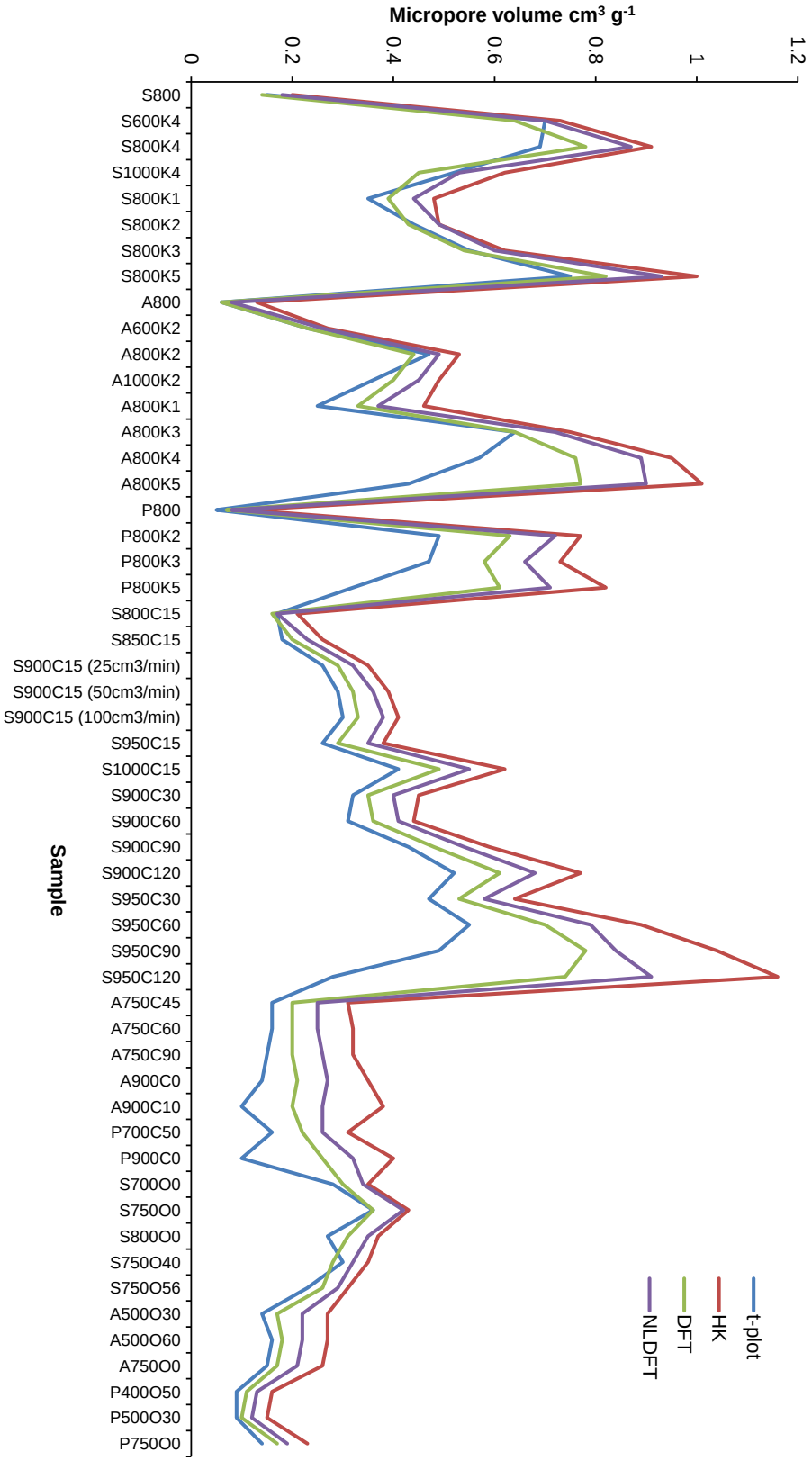

Table 7.2 Comparison of mesopore volumes determined by various models.

Material	BJH	DFT	NLDFT
S800	0.36	0.22	0.26
S600K4	0.13	0.01	0.04
S800K4	0.04	0.04	0.01
S1000K4	0.23	0.28	0.21
S800K1	0.58	0.54	0.41
S800K2	0.10	0.06	0.04
S800K3	0.14	0.09	0.08
S800K5	0.11	0.11	0.06
A800	0.71	0.62	0.65
A600K2	0.08	0.06	0.05
A800K2	0.15	0.10	0.09
A1000K2	0.30	0.23	0.22
A800K1	0.82	0.75	0.76
A800K3	0.09	0.07	0.04
A800K4	0.18	0.21	0.07
A800K5	0.10	0.16	0.09
P800	0.43	0.43	0.38
P800K2	0.18	0.20	0.12
P800K3	0.13	0.13	0.08
P800K5	0.20	0.27	0.18
S800C15	0.37	0.31	0.24
S850C15	0.31	0.36	0.24
S900C15 (25cm^3/min)	0.35	0.41	0.30
S900C15 (50cm^3/min)	0.38	0.43	0.33
S900C15 (100cm^3/min)	0.52	0.41	0.35
S950C15	0.34	0.43	0.29
S1000C15	0.52	0.64	0.41
S900C30	0.50	0.55	0.38
S900C60	0.40	0.53	0.33
S900C90	0.45	0.42	0.34
S900C120	0.71	0.85	0.58
S950C30	0.27	0.32	0.21
S950C60	0.41	0.53	0.35
S950C90	0.59	0.71	0.76
S950C120	0.96	1.07	0.87
A750C45	0.68	0.71	0.64
A750C60	0.76	0.79	0.72
A750C90	0.74	0.74	0.68
A900C0	0.86	0.87	0.79
A900C10	0.98	1.04	0.92

P700C50	0.47	0.47	0.42
P900C0	0.54	0.57	0.49
S700O0	0.14	0.16	0.10
S750O0	0.14	0.18	0.10
S800O0	0.20	0.17	0.13
S750O40	0.09	0.13	0.06
S750O56	0.15	0.13	0.09
A500O30	0.70	0.73	0.65
A500O60	0.66	0.71	0.61
A750O0	0.67	0.72	0.62
P400O50	0.44	0.47	0.40
P500O30	0.32	0.35	0.30
P750O0	0.47	0.46	0.41

Figure 7.2 Comparison of mesopore volumes determined by various models.

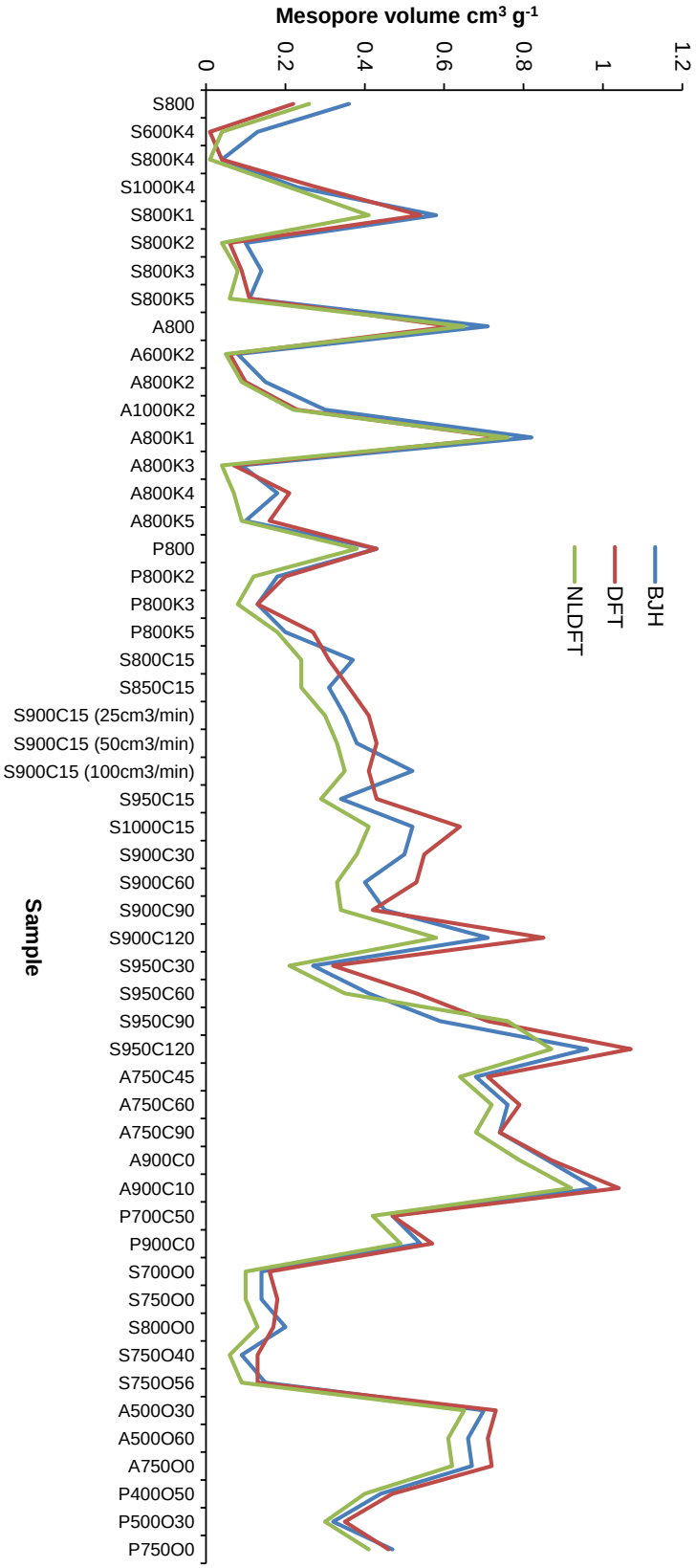

Table 7.3 Comparison of total pore volumes determined by various models.

Material	P/P_0=0.99	DFT	NLDFT
S800	0.55	0.36	0.44
S600K4	0.81	0.65	0.74
S800K4	0.95	0.78	0.82
S1000K4	0.84	0.73	0.74
S800K1	1.06	0.93	0.85
S800K2	0.59	0.49	0.53
S800K3	0.77	0.63	0.68
S800K5	1.09	0.93	0.99
A800	0.81	0.68	0.73
A600K2	0.36	0.29	0.31
A800K2	0.67	0.54	0.58
A1000K2	0.80	0.63	0.67
A800K1	1.31	1.08	1.13
A800K3	0.85	0.71	0.76
A800K4	1.15	0.97	0.96
A800K5	1.09	0.93	0.99
P800	0.54	0.50	0.46
P800K2	0.97	0.83	0.84
P800K3	0.86	0.71	0.74
P800K5	1.02	0.88	0.89
S800C15	0.58	0.47	0.41
S850C15	0.60	0.56	0.47
S900C15 (25cm^3/min)	0.70	0.70	0.62
S900C15 (50cm^3/min)	0.77	0.75	0.69
S900C15 (100cm^3/min)	0.94	0.74	0.73
S950C15	0.73	0.72	0.64
S1000C15	1.16	1.13	0.95
S900C30	0.98	0.90	0.78
S900C60	0.89	0.89	0.74
S900C90	1.05	0.90	0.88
S900C120	1.49	1.46	1.26
S950C30	0.94	0.85	0.79
S950C60	1.32	1.23	1.14
S950C90	1.64	1.49	1.60
S950C120	2.09	1.81	1.78
A750C45	0.99	0.91	0.89
A750C60	1.09	0.99	0.97
A750C90	1.05	0.94	0.94
A900C0	1.18	1.08	1.06
A900C10	1.33	1.24	1.18

P700C50	0.78	0.69	0.68
P900C0	0.93	0.83	0.81
S700O0	0.50	0.46	0.44
S750O0	0.58	0.54	0.52
S800O0	0.57	0.48	0.48
S750O40	0.45	0.41	0.38
S750O56	0.46	0.39	0.38
A500O30	0.97	0.90	0.87
A500O60	0.96	0.89	0.83
A750O0	0.94	0.89	0.83
P400O50	0.60	0.58	0.53
P500O30	0.49	0.45	0.42
P750O0	0.71	0.63	0.60

Figure 7.3 Comparison of total pore volumes determined by various models.

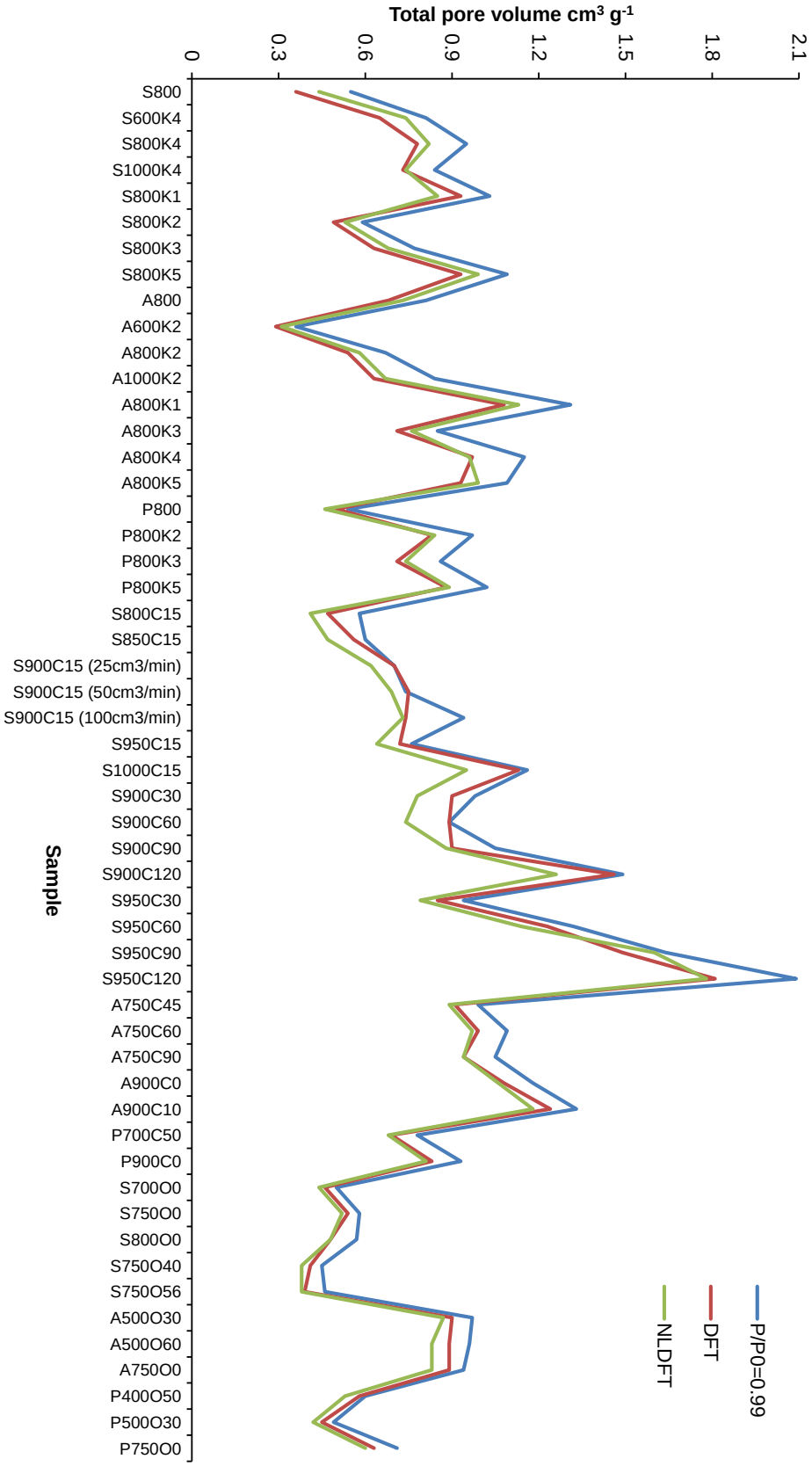

Table 7.4 Sample and yield.

Sample	Yield (%)		Sample	Yield (%)		Sample	Yield (%)
S800K1	26.5		A800K1	27.0		P800K2	34.4
S800K2	43.2		A800K2	37.2		P800K3	22.7
S800K3	49.8		A800K3	32.5		P800K5	11.9
S800K4	28.4		A800K4	26.2			
S800K5	25.2		A800K5	14.4			
S600K4	39.0		A600K2	37.9			
S1000K4	17.1		A1000K2	31.9			
Sample	**Yield (%)**		**Sample**	**Yield (%)**		**Sample**	**Yield (%)**
S800C15	85.3		S900C90	55.8		A750C45	73.8
S850C15	83.4		S900C120	48.5		A750C60	70.0
S900C15	77.5		S950C30	63.9		A750C90	61.8
S950C15	67.6		S950C60	36.0		A900C0	63.8
S1000C15	34.1		S950C90	29.4		A900C10	31.7
S900C30	74.0		S950C120	17.5		P700C50	64.5
S900C60	63.0					P900C0	27.1
Sample	**Yield (%)**		**Sample**	**Yield (%)**		**Sample**	**Yield (%)**
S700O0	81.6		A500O30	83.1		P400O50	74.5
S750O0	74.5		A500O60	66.9		P500O30	74.3
S800O0	70.6		A750O0	77.9		P750O0	71.7
S750O40	49.9						
S750O56	39.9						

Table 7.5 Deconvolution results and assignments of the XPS C1s spectra for the materials.

		C1s							
Sample		**C Sp^2**	**C sp^3**	**C-O**	**C=O**	**O-C=O**	**π-π***	**π-π***	**Total C (%)**
S800	Peak (eV)	284.5	284.7	286.3	287.5	289.2	290.8	293.9	94.8
	Atomic (%)	68.2	12.6	5.3	1.7	3.2	3.6	0.3	
A800	Peak (eV)	284.5	284.7	286.5	288.1	289.5	290.9	293.9	87.4
	Atomic (%)	40.7	24.9	6.4	4.0	3.0	6.9	1.5	
P800	Peak (eV)	284.5	284.7	286.6	288.3	290.2	290.9	294.0	76.2
	Atomic (%)	33.2	22.5	6.5	4.4	3.3	5.4	0.9	
S800K2	Peak (eV)	284.3	284.7	286.5	288.2	289.0	290.7	293.8	86.3
	Atomic (%)	55.9	12.0	6.2	3.4	3.5	4.8	0.5	
A800K2	Peak (eV)	284.5	284.7	286.5	288.1	289.2	290.9	294.0	84.8
	Atomic (%)	33.2	26.2	8.8	4.8	4.4	6.6	0.8	
P800K2	Peak (eV)	284.5	284.8	286.5	288.1	289.5	290.9	294.0	91
	Atomic (%)	56.7	11.4	7.7	4.8	2.6	7.6	0.21	
S950C90	Peak (eV)	284.5	284.7	286.5	288.1	289.5	290.9	294.0	98.5
	Atomic (%)	55.5	18.9	7.0	3.8	2.7	9.1	1.5	
A750C60	Peak (eV)	284.5	284.7	286.6	288.3	289.8	290.9	294.0	90.9
	Atomic (%)	58.7	14.1	5.2	3.1	2.5	6.4	0.9	
P700C50	Peak (eV)	284.5	284.7	286.5	288.2	290.0	290.9	294.0	77.2
	Atomic (%)	50.6	8.7	4.9	3.3	4.9	4.6	0.1	
S750O0	Peak (eV)	284.4	284.7	286.2	288.0	289.2	290.4	293.9	98.2
	Atomic (%)	71.4	5.7	8.3	3.5	1.2	6.9	1.3	
A750O0	Peak (eV)	284.4	284.7	286.6	288.2	289.7	290.8	293.9	90.4
	Atomic (%)	54.4	17.0	5.4	3.4	2.5	6.3	1.3	
P400O50	Peak (eV)	284.5	284.7	286.5	288.2	290.1	290.9	294.0	72.1
	Atomic (%)	31.4	19.5	6.2	4.0	5.1	5.1	0.9	

Table 7.6 Deconvolution results and assignments of the XPS O1s spectra for the materials.

		O1s					
Sample		**C=O**	**C-O**	**O-C=O**	**C=O in O-C=O**		**Total O (%)**
S800	Peak (eV)	530.6	532.4	533.8	535.7	537.8	5.2
	Atomic (%)	0.5	2.4	2.1	0.2	0.1	
A800	Peak (eV)	531.7	533.5	534.8	536.4		9.3
	Atomic (%)	7.6	1.0	0.4	0.3		
P800	Peak (eV)	531.6	532.8				14.4
	Atomic (%)	7.0	7.4				
S800K2	Peak (eV)	531.7	533.3	535.7	538.1		13.6
	Atomic (%)	6.8	5.8	0.6	0.3		
A800K2	Peak (eV)	531.7	533.4	535.6	536.9	538.9	14.4
	Atomic (%)	6.9	6.4	0.4	0.5	0.3	
P800K2	Peak (eV)	531.4	533.1				8.8
	Atomic (%)	3	5.8				
S950C90	Peak (eV)	531.1	533.2	535.4	538.3		1.3
	Atomic (%)	0.4	0.7	0.2	0.1		
A750C60	Peak (eV)	531.8	533.5				6.8
	Atomic (%)	5.8	1				
P700C50	Peak (eV)	531.5	532.6				13.8
	Atomic (%)	8.8	5.0				
S750O0	Peak (eV)	530.6	532.0	533.5	535.5	537.6	1.5
	Atomic (%)	0.2	0.4	0.7	0.1	0.1	
A750O0	Peak (eV)	531.7	533.4				7.1
	Atomic (%)	5.8	1.3				
P400O50	Peak (eV)	531.5	532.5				17.2
	Atomic (%)	9.5	7.7				

7.2 Appendix 2: Data for Chapter 3

Table 7.7 Textural properties, CO_2 capture capacities, enthalpies and rate constants (determined by STA) of materials.

Material	S_{micro} (m^2g^{-1})	$S_{external}$ (m^2g^{-1})	S_{BET} (m^2g^{-1})	$V_{ultramicro}$ 0.4-0.7 nm ($cm^3\,g^{-1}$)	$V_{ultramicro}$ <0.7 nm ($cm^3\,g^{-1}$)	$V_{supermicro}$ 0.7-2 nm ($cm^3\,g^{-1}$)	V_{micro} <2 nm ($cm^3\,g^{-1}$)	V_{meso} ($cm^3\,g^{-1}$)
S300	154	151	305			0.13	0.13	0.22
S600	533	94	627	0.18	0.18	0.07	0.25	0.34
S800	543	76	619	0.18	0.19	0.05	0.24	0.35
S1000	437	83	520	0.14	0.15	0.05	0.2	0.39
A800	160	163	322	0.07	0.08	0.05	0.13	0.71
P800	135	127	262	0.04	0.07	0.04	0.11	0.43
S600K4	1784	106	1890	0.4	0.5	0.23	0.73	0.13
S1000K4	1151	353	1503	0.19	0.28	0.34	0.62	0.23
S800K1	908	306	1214	0.23	0.32	0.16	0.48	0.58
S800K2	1177	117	1294	0.29	0.39	0.1	0.49	0.1
S800K3	1468	165	1633	0.35	0.45	0.17	0.62	0.14
S800K4	1781	518	2299	0.39	0.46	0.45	0.91	0.07
S800K5	1404	1048	2452	0.46	0.57	0.43	1	0.09
A600K2	598	89	687	0.13	0.22	0.05	0.27	0.08
A800K2	1249	143	1392	0.36	0.43	0.1	0.53	0.15
A1000K2	923	311	1233	0.32	0.33	0.16	0.49	0.3
A800K1	626	491	1117	0.27	0.29	0.17	0.46	0.82
A800K3	1699	253	1952	0.48	0.57	0.18	0.75	0.09
A800K4	1482	937	2419	0.33	0.39	0.56	0.95	0.18
A800K5	1102	1311	2414	0.48	0.55	0.46	1.01	0.1
P800K2	1251	644	1895	0.39	0.52	0.25	0.77	0.18
P800K3	1152	594	1747	0.43	0.47	0.26	0.73	0.13
P800K5	812	1142	1954	0.35	0.43	0.39	0.82	0.2
S800C15	430	99	529	0.16	0.17	0.04	0.21	0.37
S850C15	462	175	637	0.19	0.2	0.06	0.26	0.31
S900C15	745	238	983	0.18	0.31	0.08	0.39	0.38
S950C15	668	261	930	0.17	0.28	0.1	0.38	0.35
S1000C15	1033	502	1535	0.31	0.42	0.2	0.62	0.52
S900C30	827	292	1119	0.23	0.34	0.11	0.45	0.5
S900C60	805	292	1097	0.2	0.33	0.11	0.44	0.4
S900C90	1089	386	1475	0.3	0.43	0.16	0.59	0.45
S900C120	1331	583	1914	0.4	0.52	0.25	0.77	0.71
S950C60	1418	761	2180	0.42	0.53	0.36	0.89	0.41
S950C90	1193	1264	2457	0.45	0.56	0.48	1.04	0.59
S950C120	703	2030	2733	0.47	0.56	0.6	1.16	0.96

A750C45	393	344	738	0.1	0.21	0.1	0.31	0.68
A750C60	385	371	756	0.1	0.21	0.11	0.32	0.76
A750C90	363	399	762	0.11	0.21	0.11	0.32	0.74
A900C0	343	479	822	0.12	0.22	0.13	0.35	0.86
A900C10	237	631	868	0.13	0.21	0.17	0.38	0.98
P700C50	404	330	734	0.11	0.21	0.1	0.31	0.47
P900C0	260	686	946	0.16	0.22	0.18	0.4	0.54
S700O0	732	165	897	0.14	0.27	0.08	0.35	0.14
S750O0	933	168	1100	0.18	0.33	0.1	0.43	0.14
S800O0	704	230	935	0.17	0.28	0.09	0.37	0.2
S750O40	772	118	889	0.17	0.27	0.08	0.35	0.09
S750O56	590	188	777	0.13	0.23	0.08	0.31	0.15
A500O30	354	286	640	0.08	0.18	0.09	0.27	0.7
A500O60	396	251	647	0.09	0.19	0.08	0.27	0.66
A750O0	364	265	629	0.09	0.17	0.09	0.26	0.67
P400O50	209	177	385	0.06	0.11	0.05	0.16	0.44

Material	**V_{total} ($cm^3 g^{-1}$)**	**$V_{0.4-0.7\ nm}/V_{total}$**	**$V_{<0.7\ nm}/V_{total}$**	**$V_{micropore}/V_{total}$**	**$V_{mesopore}/V_{total}$**	**CO_2 uptake (mmol g^{-1})**	**CO_2 adsorption enthalpy (-KJ mol^{-1})**	**k_1 for CO_2 adsorption (min^{-1})**
S300	0.35	-	-	0.37	0.63	0.48	40.2	6.81
S600	0.59	0.31	0.31	0.42	0.58	1.07	42.4	6.55
S800	0.59	0.31	0.32	0.41	0.59	1.59	35.3	8.85
S1000	0.59	0.24	0.25	0.34	0.66	1.09	38.3	8.32
A800	0.81	0.09	0.1	0.16	0.88	1.36	48.6	5.16
P800	0.54	0.07	0.13	0.2	0.80	1.07	52.9	7.33
S600K4	0.84	0.48	0.6	0.87	0.15	2.02	29.1	5.51
S1000K4	0.84	0.23	0.33	0.74	0.27	1.11	34.5	4.74
S800K1	1.06	0.22	0.3	0.45	0.55	2.39	31.7	4.36
S800K2	0.59	0.49	0.66	0.83	0.17	3.11	33.6	3.3
S800K3	0.77	0.45	0.58	0.81	0.18	2.93	32.7	4.05
S800K4	0.98	0.40	0.47	0.93	0.07	2.14	30.9	5.25
S800K5	1.09	0.42	0.52	0.92	0.08	2.07	26.7	4.38
A600K2	0.36	0.36	0.61	0.75	0.22	1.64	46	4.52
A800K2	0.67	0.54	0.64	0.79	0.22	2.95	38.5	3.6
A1000K2	0.8	0.40	0.41	0.61	0.38	2.16	38	4.22
A800K1	1.31	0.21	0.22	0.35	0.63	1.98	38.6	2.92
A800K3	0.85	0.56	0.67	0.88	0.11	2.82	36.1	3.06
A800K4	1.15	0.29	0.34	0.83	0.16	2.25	33.3	3.55
A800K5	1.09	0.44	0.51	0.93	0.09	1.75	38.2	5.68
P800K2	0.97	0.40	0.54	0.79	0.19	2.39	36.9	3.79
P800K3	0.86	0.50	0.55	0.85	0.15	2.07	35.1	2.46
P800K5	1.02	0.34	0.42	0.8	0.20	1.25	37.6	5.57
S800C15	0.58	0.28	0.29	0.36	0.64	1.64	25	3.74

S850C15	0.6	0.32	0.33	0.43	0.52	1.77	36.3	4.85
S900C15	0.77	0.23	0.4	0.51	0.49	1.98	35.8	4.93
S950C15	0.73	0.23	0.38	0.52	0.48	1.82	34.9	5.59
S1000C15	1.16	0.27	0.36	0.53	0.45	1.77	40.2	5.58
S900C30	0.98	0.23	0.35	0.46	0.51	1.77	31.9	6.29
S900C60	0.89	0.22	0.37	0.49	0.45	1.98	36.4	5.08
S900C90	1.05	0.29	0.41	0.56	0.43	1.91	37.4	6.9
S900C120	1.49	0.27	0.35	0.52	0.48	1.89	35.9	6.5
S950C60	1.32	0.32	0.4	0.67	0.31	1.82	42.7	6.04
S950C90	1.64	0.27	0.34	0.63	0.36	1.52	46.7	8.71
S950C120	2.09	0.22	0.27	0.56	0.46	1.18	53.7	9.1
A750C45	0.99	0.10	0.21	0.31	0.69	1.43	45.7	4.23
A750C60	1.09	0.09	0.19	0.29	0.70	1.41	47.5	5.71
A750C90	1.05	0.10	0.2	0.3	0.70	1.43	43.7	3.57
A900C0	1.18	0.10	0.19	0.3	0.73	1.39	46.4	5.49
A900C10	1.33	0.10	0.16	0.29	0.74	1.14	48.2	5.85
P700C50	0.78	0.14	0.27	0.4	0.60	1.30	68.5	6.6
P900C0	0.93	0.17	0.24	0.43	0.58	1.20	69	5.71
S700O0	0.5	0.28	0.54	0.7	0.28	1.98	32.2	6
S750O0	0.58	0.31	0.57	0.74	0.24	2.02	34.6	4.29
S800O0	0.57	0.30	0.49	0.65	0.35	1.82	30	4.98
S750O40	0.45	0.38	0.6	0.78	0.20	1.91	30.8	5.22
S750O56	0.46	0.28	0.5	0.67	0.33	1.89	36.7	4.65
A500O30	0.97	0.08	0.19	0.28	0.72	1.36	47	5.2
A500O60	0.96	0.09	0.2	0.28	0.69	1.32	46.3	5.14
A750O0	0.94	0.10	0.18	0.28	0.71	1.41	30.6	5.69
P400O50	0.6	0.10	0.18	0.27	0.73	1.02	73.5	-

Figure 7.4 CO_2 uptake (1 bar, 308 K) versus (a) volume of ultramicropores (0.4-0.7 nm), (b) volume of ultramicropores (<0.7 nm), (c) volume of micropores (<2 nm), (d) volume of mesopores, (e) total pore volume, (f) mesopore ratio, (g) external surface area and (h) BET (total) surface area of all materials. Stars, squares, circles and triangles represent commercial AC, Starbons®, Algibons and Pecbons, respectively; colours in black, red, blue and green represent non-activated, KOH activated, CO_2 activated and O_2 activated materials, respectively.

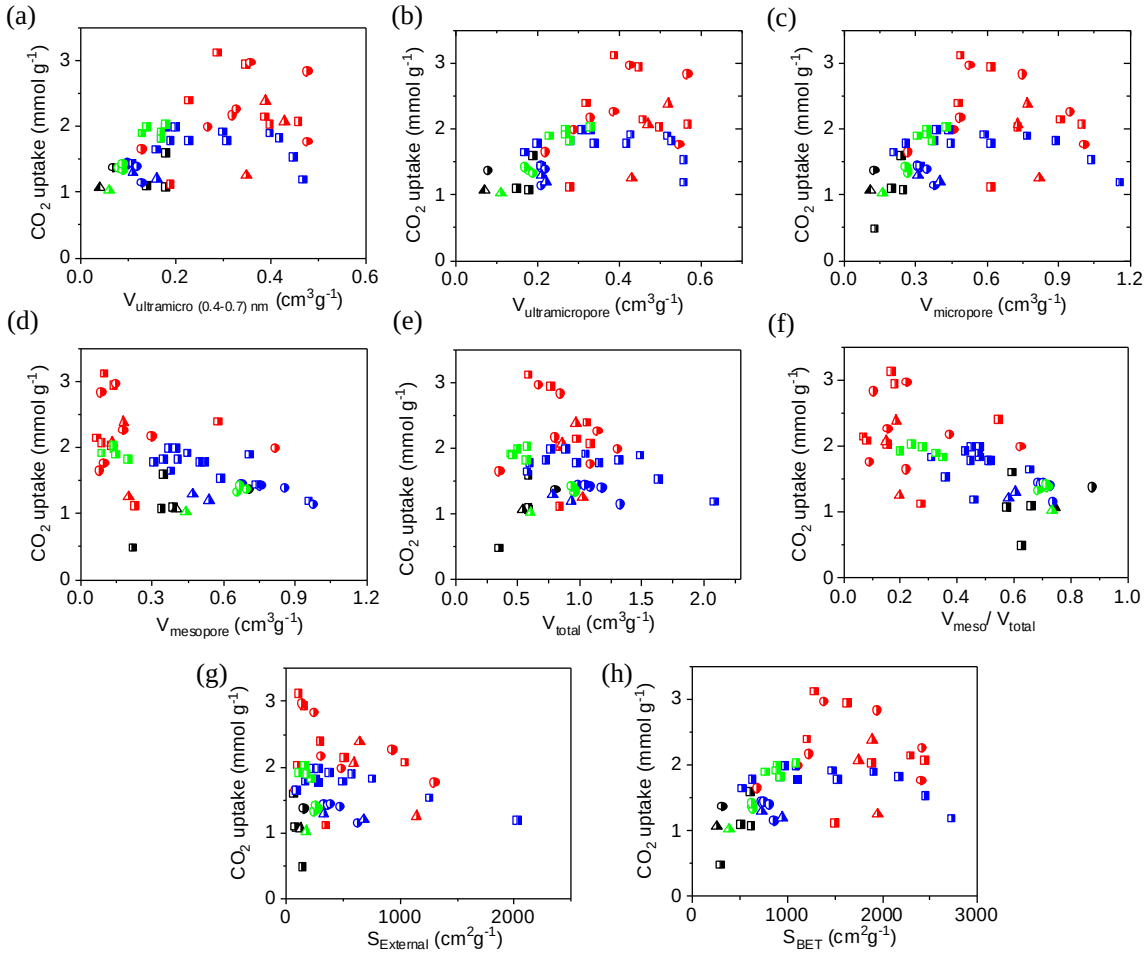

Figure 7.5 Experimental and kinetic models of predicted CO_2 uptake of samples at 308 K and 1 bar.

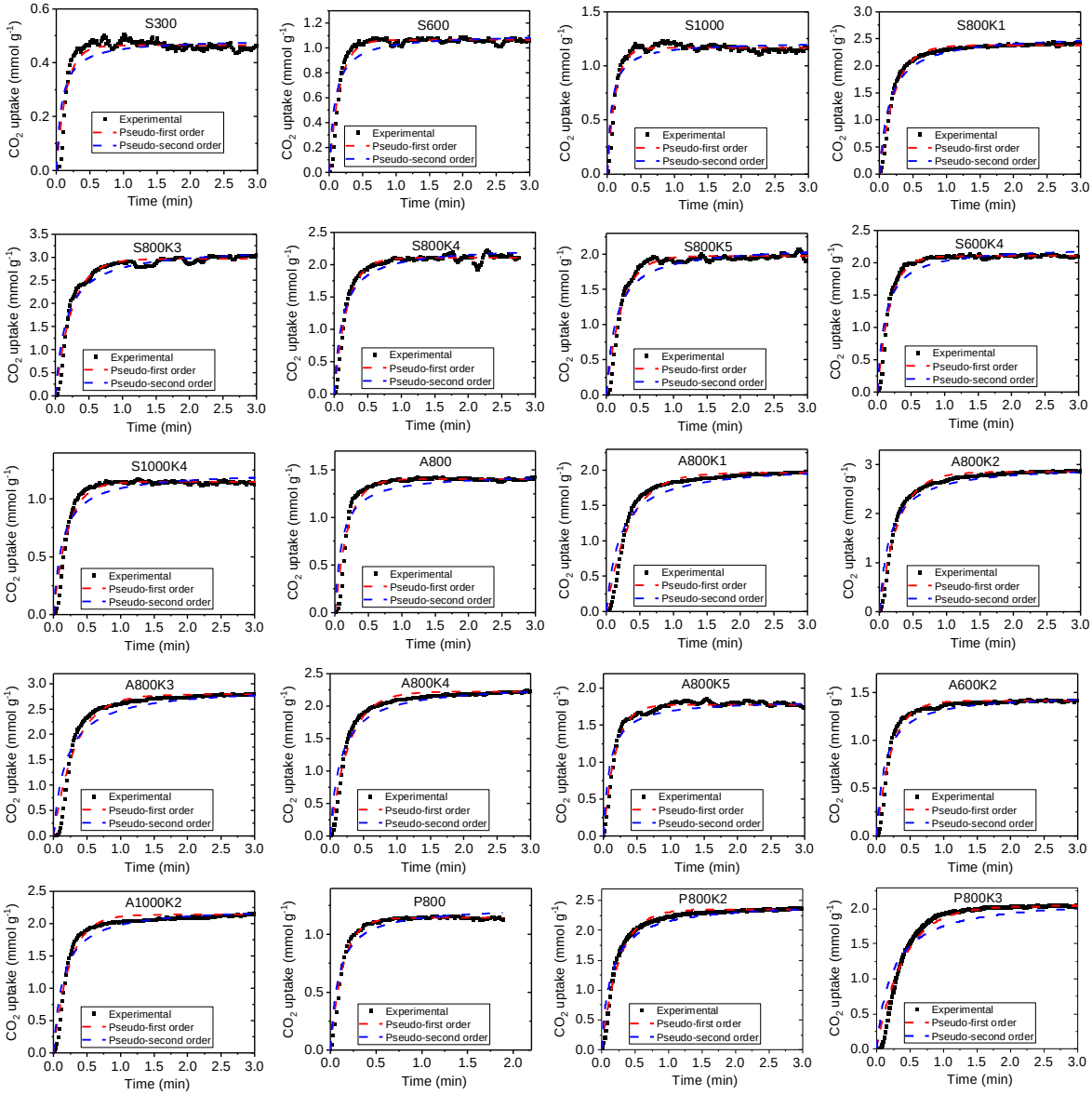

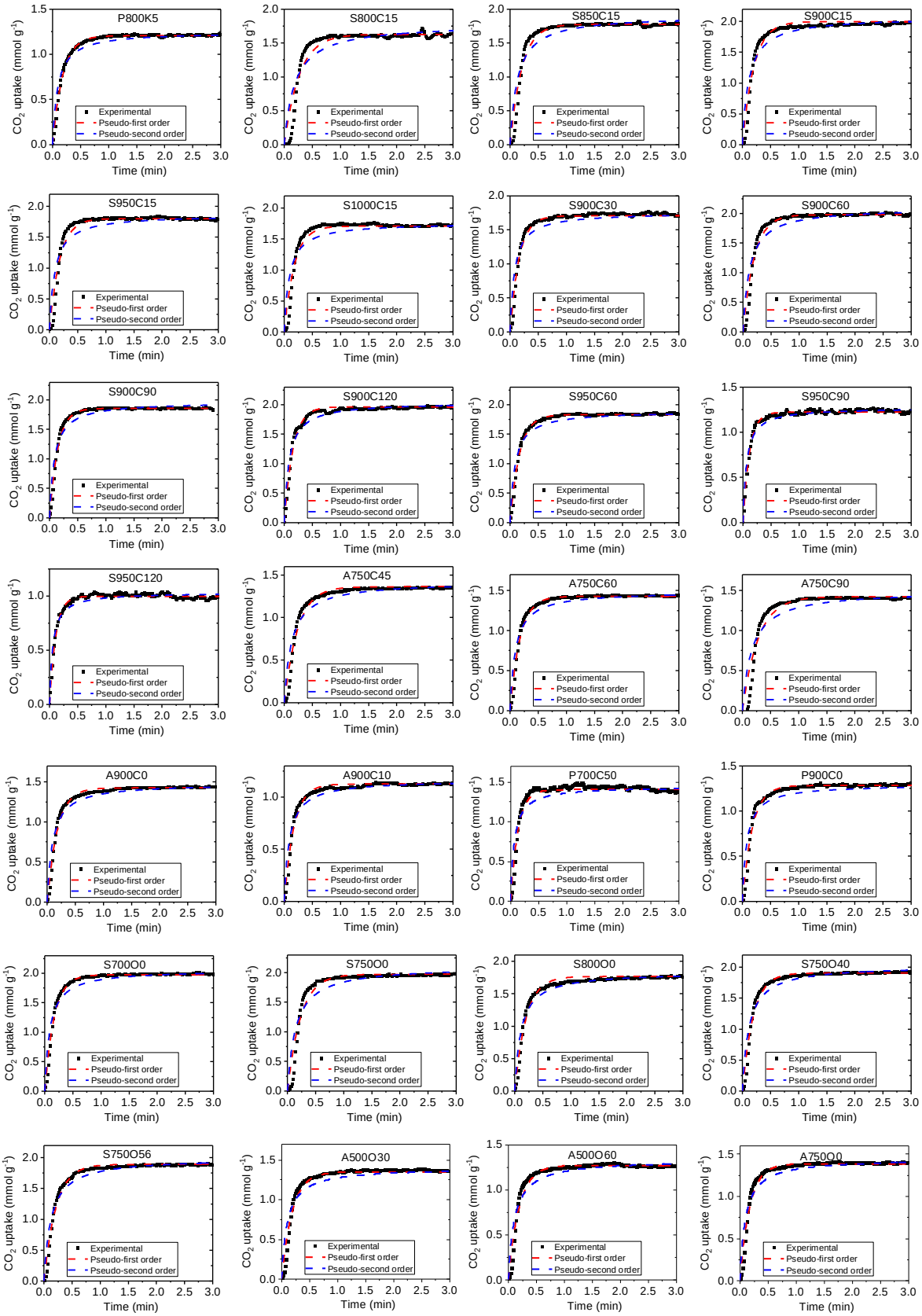
P800K5
S800C15
S850C15
S900C15
S950C15
S1000C15
S900C30
S900C60
S900C90
S900C120
S950C60
S950C90
S950C120
A750C45
A750C60
A750C90
A900C0
A900C10
P700C50
P900C0
S700O0
S750O0
S800O0
S750O40
S750O56
A500O30
A500O60
A750O0
CO2 uptake (mmol g-1)
Time (min)
Experimental
Pseudo-first order
Pseudo-second order

Table 7.8 Experimental and kinetic parameters for CO_2 uptake of samples at 308 K and 1 bar.

Sample	$q_{e-(exp)}$ (mmol g^{-1})	Pseudo 1 order				Pseudo 2 order			
		k_1 (min^{-1})	q_e (mmol g^{-1})	R^2	SSE	k_2 (g min^{-1} $mmol^{-1}$)	q_e (mmol g^{-1})	R^2	SSE
S300	0.44	6.815	0.464	0.908	0.129	25.752	0.487	0.782	0.306
S600	1.07	6.549	1.066	0.942	0.400	10.901	1.109	0.856	0.991
S800	1.62	8.847	1.592	0.989	0.118	9.5	1.674	0.929	0.715
S1000	1.09	8.315	1.168	0.959	0.259	13.134	1.218	0.856	0.914
S800K1	2.4	4.358	2.383	0.983	0.657	2.630	2.580	0.960	1.603
S800K2	3.22	3.296	3.127	0.977	2.049	1.481	3.398	0.959	3.710
S800K3	2.93	4.049	2.965	0.969	2.111	1.927	3.218	0.944	3.857
S800K4	2.14	5.247	2.105	0.977	0.640	3.600	2.279	0.933	1.817
S800K5	2.06	4.382	1.976	0.966	1.045	3.288	2.120	0.917	2.574
S600K4	2.02	5.510	2.103	0.975	0.710	4.028	2.248	0.913	2.443
S1000K4	1.11	4.738	1.150	0.967	0.332	6.158	1.236	0.890	1.095
A800	1.36	5.158	1.406	0.954	0.697	6.656	1.459	0.863	2.075
A800K1	1.98	2.922	1.965	0.974	1.146	2.386	2.081	0.926	3.262
A800K2	2.9	3.599	2.855	0.980	1.420	2.181	2.992	0.947	3.799
A800K3	2.82	3.059	2.789	0.961	3.494	1.788	2.943	0.905	8.537
A800K4	2.25	3.552	2.221	0.970	1.395	2.698	2.331	0.935	3.019
A800K5	1.75	5.683	1.778	0.969	0.609	6.060	1.842	0.901	1.926
A600K2	1.48	4.522	1.415	0.968	0.504	5.394	1.483	0.922	1.216
A1000K2	2.16	4.224	2.138	0.962	1.389	3.125	2.257	0.945	2.004
P800	1.07	7.328	1.144	0.986	0.079	9.207	1.241	0.937	0.368
P800K2	2.39	3.791	2.348	0.978	1.009	2.840	2.452	0.952	2.225
P800K3	2.06	2.459	2.033	0.975	1.462	1.978	2.154	0.895	6.057
P800K5	1.22	5.567	1.206	0.989	0.095	8.802	1.250	0.928	0.623
S800C15	1.64	3.738	1.628	0.920	2.188	3.042	1.783	0.844	4.267
S850C15	1.77	4.848	1.776	0.955	1.085	4.066	1.907	0.879	2.908
S900C15	1.98	4.929	1.997	0.953	1.405	4.270	2.073	0.917	2.493
S950C15	1.82	5.593	1.802	0.948	1.235	5.774	1.865	0.840	3.814
S1000C15	1.74	5.580	1.708	0.944	1.210	6.358	1.764	0.813	4.030
S900C30	1.74	6.286	1.704	0.971	0.485	7.415	1.752	0.876	2.105
S900C60	1.98	5.076	1.980	0.967	0.952	4.145	2.096	0.891	3.091
S900C90	1.86	6.900	1.856	0.985	0.253	6.026	1.968	0.924	1.311
S900C120	1.89	6.496	1.964	0.971	0.574	5.848	2.043	0.949	1.019
S950C60	1.82	6.036	1.832	0.982	0.342	6.364	1.893	0.913	1.677
S950C90	1.52	8.714	1.222	0.981	0.109	13.059	1.272	0.942	0.335
S950C120	1.04	9.102	0.996	0.977	0.085	17.909	1.033	0.915	0.312
A750C45	1.39	4.226	1.363	0.968	0.499	5.323	1.423	0.922	1.213
A750C60	1.41	5.706	1.427	0.984	0.200	7.182	1.488	0.917	1.032
A750C90	1.43	3.570	1.422	0.944	1.234	4.075	1.498	0.867	2.942
A900C0	1.39	5.488	1.425	0.979	0.264	7.027	1.481	0.927	0.929
A900C10	1.14	5.846	1.125	0.975	0.188	9.612	1.164	0.933	0.501
P700C50	1.3	6.604	1.400	0.949	0.531	11.082	1.441	0.822	1.854
P900C0	1.2	5.712	1.283	0.900	1.184	10.072	1.292	0.826	2.055
S700O0	1.98	5.999	1.974	0.985	0.344	5.476	2.058	0.917	1.866

S750O0	2.01	4.289	1.972	0.949	1.745	3.246	2.109	0.884	3.962
S800O0	1.82	4.982	1.766	0.962	0.806	4.947	1.836	0.946	1.158
S750O40	1.91	5.222	1.907	0.979	0.500	4.300	2.028	0.930	1.656
S750O56	1.89	4.649	1.892	0.980	0.506	4.039	1.995	0.945	1.403
A500O30	1.34	5.198	1.346	0.968	0.414	7.107	1.398	0.877	1.589
A500O60	1.32	5.143	1.270	0.963	0.433	6.727	1.334	0.902	1.137
A750O0	1.39	5.688	1.382	0.976	0.291	7.224	1.443	0.910	1.082

Table 7.9 CO_2 capture capacities (measured by adsorption isotherms) of S800 and KOH activated Starbons®.

	0.15 bar (mmol g^{-1})			1 bar (mmol g^{-1})			10 bar (mmol g^{-1})		
	273 K	298 K	323 K	273 K	298 K	323 K	273 K	298 K	323 K
S800	1.5	0.8	0.5	3.4	2.4	1.8	9.6	6.2	4.9
S800K2	2.2	1.1	0.6	6.2	4.0	2.7	12.7	9.8	8.0
S800K3	2.1	-	-	6.3	-	-	12.1	-	-
S800K5	1.4	-	-	5.9	-	-	20.3	-	-

Figure 7.6 Isotherm models fitted to the experimental nitrogen adsorption data of (a) S800 at 298 K, (b) S800K2 at 298 K, (c) S800K2 at 273 K and (d) S800K5 at 273 K.

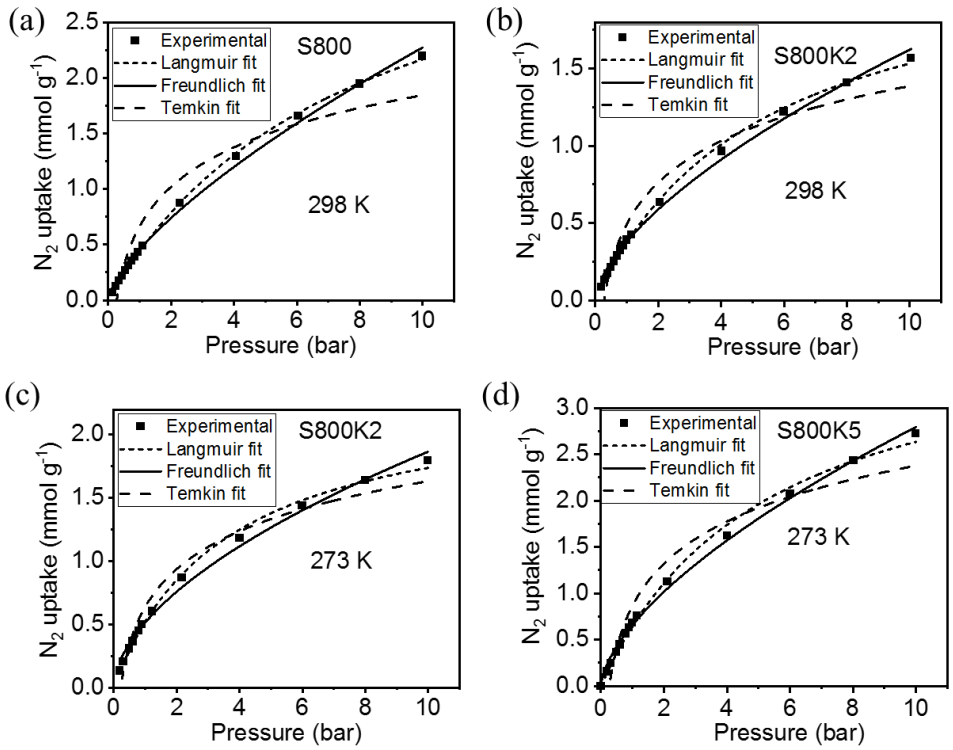

Table 7.10 N_2 adsorption isotherm parameters via Langmuir, Freundlich and Temkin fits.

Sample	T (K)	Langmuir			Freundlich			Temkin		
		q_m[a]	K_L[b]	R^2	K_F[c]	1/n	R^2	B[d]	K_T[e]	R^2
S800	298	3.9	0.128	0.999	0.455	0.698	0.996	0.512	3.655	0.905
S800K2	298	2.4	0.188	0.998	0.379	0.632	0.995	0.388	3.551	0.944
S800K2	273	2.4	0.283	0.997	0.514	0.561	0.993	0.396	4.37	0.961
S800K5	273	4	0.191	0.997	0.656	0.629	0.997	0.601	3.74	0.947

a) Units: mmol g^{-1}; b) Units: atm^{-1}; c) Units: mmol g^{-1} $atm^{-1/n}$; d) Units: KJ mol^{-1}; e) Units: atm^{-1}

7.3 Appendix 3: Data for Chapter 4

Table 7.11 Effect of initial concentration of methylene blue on the equilibrium adsorption capacities and removal efficiencies of methylene blue at 298 K.

Sample	C_0 (mg L^{-1})	Q_e (mg g^{-1})	R_e (%)
	25	49.3±0.3	98.7±0.6
	50	93.9±4.0	93.9±4
	70	106.5±4.0	76.1±2.8
	80	105.8±3.2	66.1±2.0
	90	105.9±7.7	58.8±4.3
S800	100	99.7±6.5	49.8±3.2
	100	197.6±0.9	98.8±0.43
	200	346.6±2.7	86.6±0.7
	300	347.3±5.0	57.9±0.8
	400	340.5±9.2	42.6±1.2
S800K1	500	345.4±21.8	34.5±2.1
	50	98.9±0.4	98.8±0.4
	100	192.3±4.6	96.2±2.3
	200	248.3±6.0	62.1±1.5
	300	238.7±15.0	39.8±2.5
S800K2	400	244.7±9.7	30.6±1.2
	100	191.2±3.3	95.6±1.6
	200	360.3±10.3	90.1±2.6
	300	491.1±23.7	81.9±4.0
	400	483.2±21.3	60.4±5.2
S800K3	500	489.2±36.6	48.9±3.7
	300	597.9±0.7	99.7±0.1
	400	771.8±16.5	96.5±2.1
	500	787.2±22.7	78.7±2.3
S800K4	600	811.0±36.9	67.6±3.1

	700	817.0±46	58.4±4
	200	398.4±0.9	99.6±0.2
	300	557.3±24	92.9±4
	400	638.9±21.4	82.4±2.7
S800K5	500	629.0±3.1	62.9±0.3
	200	394.4±0.8	98.6±0.2
	300	511.0±31.2	85.2±5.2
	400	510.5±24.8	63.8±3.1
	500	494.8±37.2	49.5±3.7
S950C30	600	515.9±5.3	43.0±0.4
	300	579.2±8	96.5±1.3
	400	655.9±6.1	82.0±0.8
	500	726.1±33.1	72.6±3.3
S950C60	600	725.8±13.4	60.5±1.1
	300	597.9±1.4	99.7±0.2
	400	782.5±18.4	97.8±2.3
	500	825.9±38.7	82.6±3.9
S950C90	600	891.0±43.1	74.3±3.6
	100	196.6±1.0	98.3±0.5
	125	245.9±2.2	98.4±0.9
	150	289.1±9.8	96.4±3.3
	200	308.9±1.9	77.2±0.5
S750O0	250	328.4±24.1	65.7±4.8
	100	184.5±9.0	92.3±4.5
	150	218.4±3.4	72.8±1.1
	200	230.5±6.3	57.6±1.6
AC	250	225.1±11.8	45.0±2.4

Table 7.12 Methylene blue adsorption capacity and textural property of Starbons® and commercial AC at 298 K.

Material	$V_{2\text{-}50\ nm}$ ($cm^3\ g^{-1}$)	$V_{>50\ nm}$ ($cm^3\ g^{-1}$)	$V_{<0.7\ nm}/V_{total}$	$V_{<0.8\ nm}/V_{total}$	$V_{<0.9\ nm}/V_{total}$	$V_{<1nm}/V_{total}$	$V_{<2\ nm}/V_{total}$	S_{micro}/S_{total}	$S_{external}/S_{total}$	MB adsorption capacity ($mg\ g^{-1}$)
AC	0.3	0.1	0.28	0.32	0.34	0.36	0.46	0.52	0.48	230.5
S800	0.09	0.26	0.32	0.34	0.36	0.37	0.41	0.88	0.12	105.9
S800K1	0.2	0.38	0.30	0.33	0.36	0.38	0.45	0.75	0.25	347.3
S800K2	0.04	0.06	0.66	0.71	0.75	0.76	0.83	0.91	0.09	248.3
S800K3	0.08	0.06	0.58	0.65	0.69	0.71	0.81	0.90	0.10	491.1
S800K4	0.06	0.01	0.47	0.57	0.63	0.67	0.93	0.77	0.23	817.0
S800K5	0.08	0.01	0.52	0.59	0.64	0.70	0.92	0.57	0.43	638.9
S950C30	0.15	0.13	0.49	0.53	0.56	0.60	0.68	0.76	0.24	515.9
S950C60	0.26	0.06	0.40	0.45	0.5	0.54	0.67	0.65	0.35	726.1
S950C90	0.36	0.06	0.34	0.39	0.43	0.47	0.63	0.49	0.51	891.0
S750O0	0.07	0.01	0.57	0.62	0.66	0.67	0.74	0.85	0.15	328.4

Figure 7.7 methylene blue adsorption capacity at 298 K versus (a,b) volume of pores with diameter (a) between 2-50 nm, (b) larger than 2 nm; (c-g) fraction of the volume of pores with diameter (c) less than 0.7 nm, (d) 0.8 nm, (e) 0.9 nm, (f) 1 nm, (g) 2 nm; (h,i) fraction of (h) micropore surface area and (i) external surface area of Starbons® and commercial activated carbon. Colours in black, red, blue, green and orange represent non-activated S800, KOH activated, CO_2 activated, O_2 activated Starbons® and commercial activated carbon, respectively.

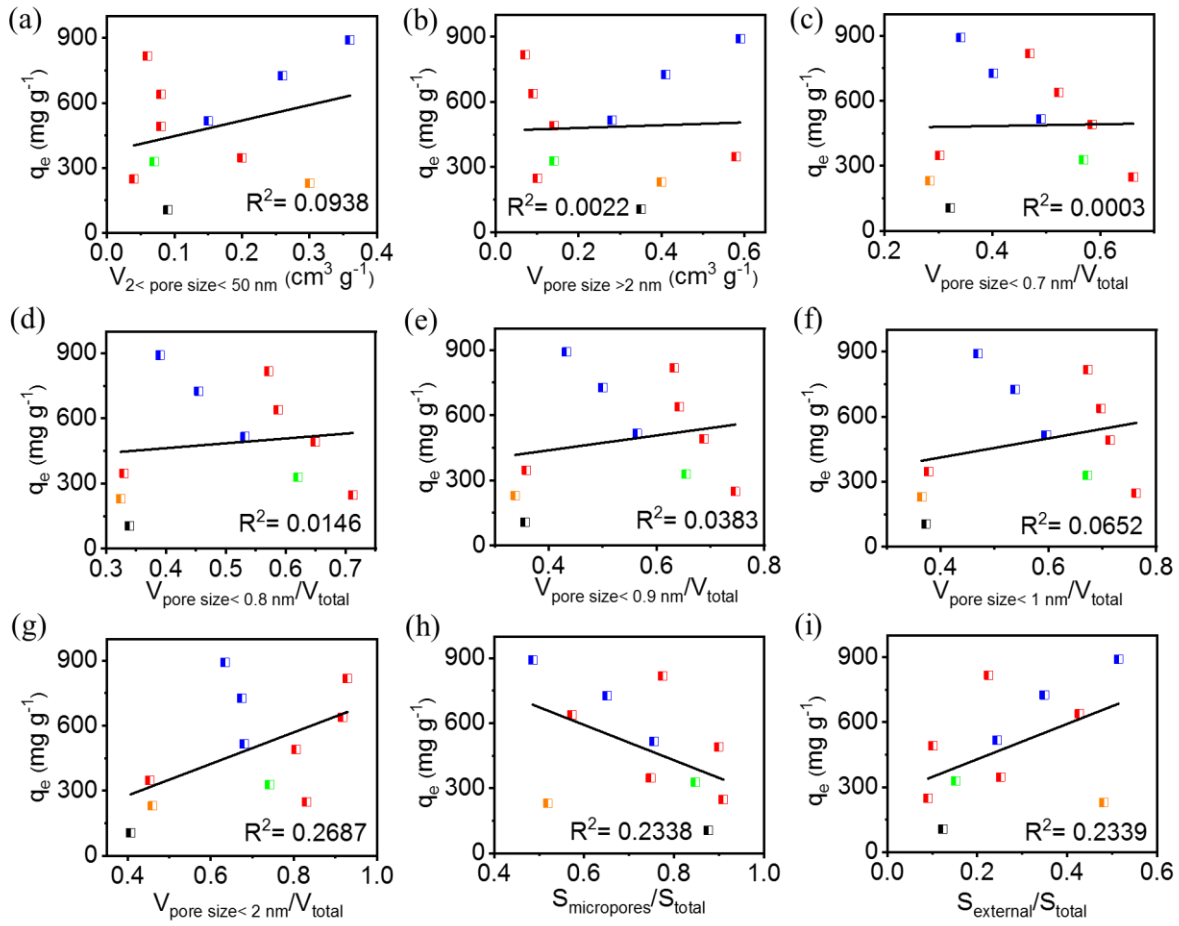

Figure 7.8 (a) Wide scan XPS spectra of S800K4 before and after MB adsorption; (b–d) high resolution spectra of S800K4 after MB adsorption in (b) N1s, (c) C1s and (d) O1s regions; (e–f) high resolution spectra of S800K4 in (e) C1s and (f) O1s regions.

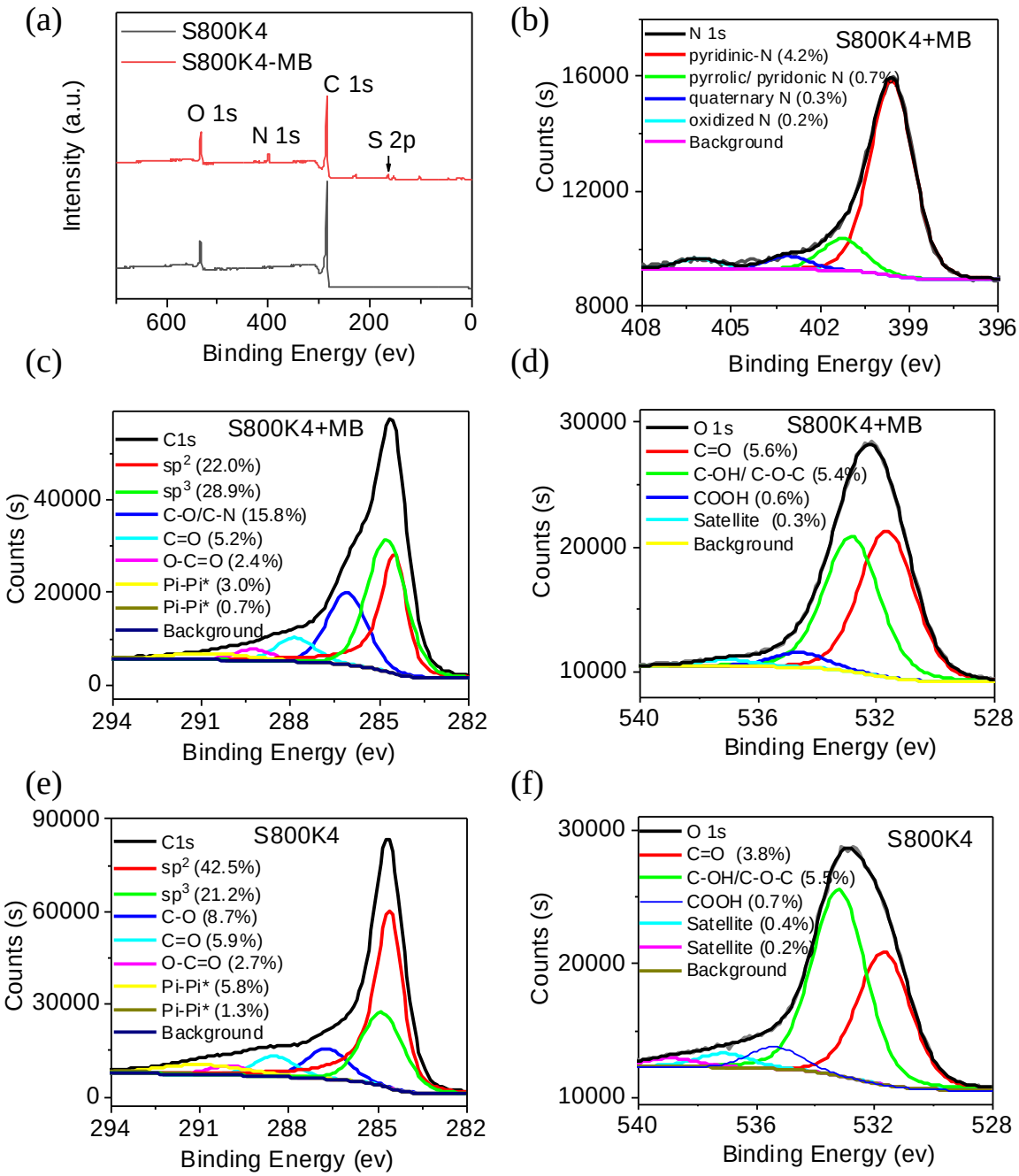

Figure 7.9 SEM-EDS of (a) S950C90 and (b) S950C90 adsorbed MB at a lower magnification.

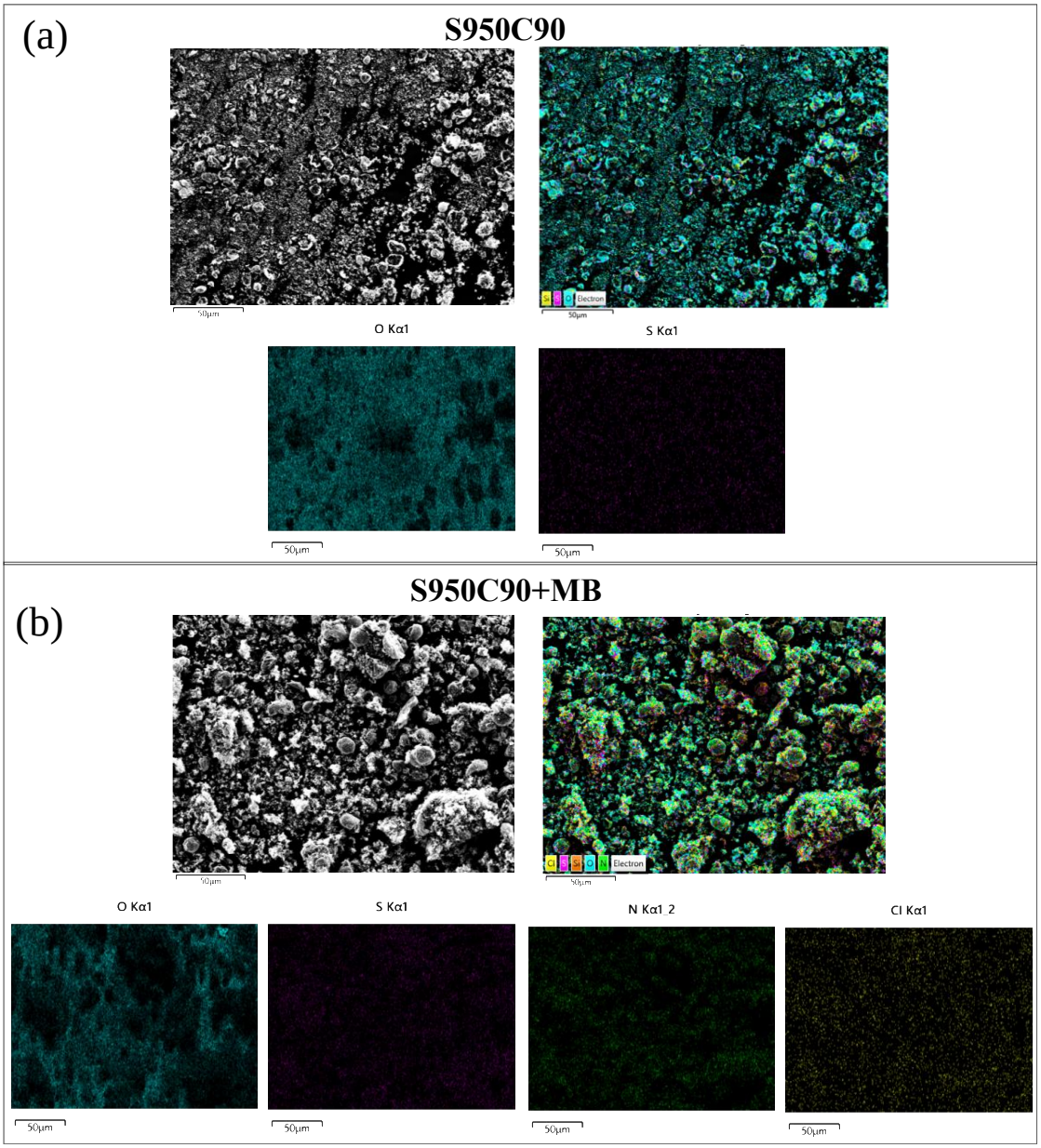

Abbreviations

AB	Acid blue 92
ACs	Activated carbons
Algibons	Starbons® derived from alginic acid
AMCS	Alginic acid-derived mesoporous carbon spheres
BET	Brunauer, Emmett and Teller
BE	Binding energy, ev
BJH	Barett, Joyner and Halenda
COFs	Covalent organic frameworks
CCS	Carbon dioxide capture and sequestration
DEA	Diethanolamine
DR	Dubinin-Radushkevich
DA	Dubinin-Astakov
DS	Dubinin-Stoeckli
DFT	Density functional theory
DSC	Differential scanning calorimetry
DTA	Differential thermal analysis
2D-NLDFT	Two-dimensional density functional theory
EISA	Evaporation-induced self-assembly
$E_{surface}$	Surface energy
EDX	Energy-dispersive X-ray spectroscopy
FTIR	Fourier-transform infrared spectroscopy
G	α-L-guluronic acid
HK	Horvath and Kawazoe
IUPAC	International Union of Pure and Applied Chemistry
IAST	Ideal adsorbed solution theory
KE	kinetic energy
LDFT	Local density functional theory
MOFs	Metal organic frameworks
M41S	Mesoporous aluminosilicate molecular sieve family
M	β-D-mannuronic acid
MEA	Monoethanolamine

MDEA	Methydiethanolamine
MV	Micropore volume
MB	Methylene blue
NLDFT	Nonlocal density functional theory
OMC	Ordered mesoporous carbon
POPs	Porous organic polymers
PGC	porous graphitic carbon
Pecbons	Starbons® derived from pectin
PTSA	p-Toluenesulfonic acid
PV	Pore volume
PD	Pore diameter
PSD	Pore size distributions
PSA	Pressure swing system
QSDFT	Quenched solid density functional theory
SDA	Structure-directing templates
$scCO_2$	Supercritical carbon dioxide
Starbons®	Derived from starch, alginic acid and pectin
S800SE	S800 prepared by the solvent exchange drying method
SA	Surface area
SAN	Small angle neutron
SAX	X-ray scattering
SEM	Scanning electron microscopy
SF	Saito and Foley
STA	Simultaneous thermal analysis, simultaneous application of TGA and DSC in one experiment
SSA	Specific surface area
SSE	Sum squares error
TBA	tert-butanol
TSA	Thermal swing system
TEM	Transmission electron microscopy
TGA	Thermogravimetric analysis
TG-FTIR	Thermogravimetric-Fourier transform infrared spectroscopy coupled analysis
UV-Vis	Ultraviolet-visible
XPS	X-ray photoelectron spectroscopy

C_0	Initial concentration of methylene blue, mg L^{-1}
C_t	Concentration of methylene blue after adsorption time t, mg L^{-1}
C_e	Concentration of methylene blue at equilibrium, mg L^{-1}
q_t	Quantity adsorbed after adsorption time t, mg g^{-1}
q_e	Quantity adsorbed at equilibrium, mg g^{-1}
q_0	Monolayer adsorption capacity, mg g^{-1}
q_m	Maximum adsorption capacity, mg g^{-1}
R_t	Percentage removal after adsorption time t, %
R_e	Percentage removal at equilibrium, %
t	Adsorption time, min
V	Volume of solution, L
m	Mass of adsorbent, g
k_1	Pseudo-first order constant, min^{-1}
k_2	Pseudo-second order constant, g mg^{-1} min^{-1}
α	Initial rate of adsorption, mg g^{-1} min^{-1}
β	Extent of surface coverage, g mg^{-1}
1/β	Available number of adsorption sites
h	Rate of adsorption, mg $g^{-1}min^{-1}$
b	Affinity of adsorbent toward adsorbate, L mg^{-1}
K_L	Langmuir isotherm constant, L mg^{-1}
K_F	Freundlich constant, mg g^{-1}(L $mg^{-1})^{1/n}$
n	Intensity of adsorption constant for Freundlich
K_T	Temkin isotherm equilibrium binding constant, L mg^{-1}
q_e	Adsorption capacity at equilibrum in gas phase, mmol g^{-1}
q_m	Maximum adsorption capacity in gas phase, mmol g^{-1}
k_1	Pseudo-first order constant in gas phase, min^{-1}
k_2	Pseudo-second order constant in gas phase, g $mmol^{-1}$ min^{-1}
K_L	Langmuir isotherm constant in gas phase, atm^{-1}
K_F	Freundlich constant in gas phase, mmol g^{-1} $atm^{-1/n}$
B	Temkin isotherm constant in gas phase, KJ mol^{-1}
K_T	Temkin isotherm equilibrium binding constant in gas phase, atm^{-1}
R^2	Linear regression correlation coefficient
R	Universal gas constant, 8.314 J mol^{-1} K^{-1}
ΔG°	Gibbs free energy, KJ mol^{-1}
ΔH°	Enthalpy, KJ mol^{-1}

$\Delta S°$	Entropy, J mol^{-1} K^{-1}
P	Equilibrium pressure, MPa
P_0	Saturation vapour pressure, MPa
P/P_0	Relative pressure
σ_m	Cross-sectional area, nm^2
S_{micro}	Micropore surface area, m^2g^{-1}
S_{BET}	BET specific surface area, m^2g^{-1}
V_{total}	Total pore volume, cm^3g^{-1}
$V_{ultramicro}$	Ultramicropore volume, cm^3g^{-1}
V_{micro}	Micropore volume, cm^3g^{-1}
V_{meso}	Mesopore volume, cm^3g^{-1}
Q_{st}	Isosteric enthalpy of adsorption, KJ mol^{-1}
ΔH_{ads}	Enthalpy of adsorption, KJ mol^{-1}
ΔH_{des}	Enthalpy of desorption, KJ mol^{-1}
pH_{zpc}	pH value of the solution when the charge on the surface of the adsorbent is zero

References

1. Davis, M. E., Ordered porous materials for emerging applications. *Nature* **2002,** *417* (6891), 813-821.
2. Wan, Y.; Zhao, D. Y., On the controllable soft-templating approach to mesoporous silicates. *Chem. Rev.* **2007,** *107* (7), 2821-2860.
3. Smith, J. V., Topochemistry of zeolites and related materials. 1. Topology and geometry. *Chem. Rev.* **1988,** *88* (1), 149-182.
4. Juarez, T.; Biener, J.; Weissmuller, J.; Hodge, A. M., Nanoporous Metals with Structural Hierarchy: A Review. *Adv. Eng. Mater.* **2017,** *19* (12), 1700389.
5. Furukawa, H.; Cordova, K. E.; O'Keeffe, M.; Yaghi, O. M., The Chemistry and Applications of Metal-Organic Frameworks. *Science* **2013,** *341* (6149), 1230444.
6. Cote, A. P.; Benin, A. I.; Ockwig, N. W.; O'Keeffe, M.; Matzger, A. J.; Yaghi, O. M., Porous, crystalline, covalent organic frameworks. *Science* **2005,** *310* (5751), 1166-1170.
7. Thomas, A., Functional Materials: From Hard to Soft Porous Frameworks. *Angew. Chem. Int. Ed.* **2010,** *49* (45), 8328-8344.
8. Slater, A. G.; Cooper, A. I., Function-led design of new porous materials. *Science* **2015,** *348*, 6238.
9. Sing, K. S. W.; Everett, D. H.; Haul, R. A. W.; Moscou, L.; Pierotti, R. A.; Rouquerol, J.; Siemieniewska, T., Reporting Physisorption Data for Gas Solid Systems with Special Reference to the Determination of Surface-Area and Porosity (Recommendations 1984). *Pure Appl. Chem.* **1985,** *57* (4), 603-619.
10. Zdravkov, B. D.; Cermak, J. J.; Sefara, M.; Janku, J., Pore classification in the characterization of porous materials: A perspective. *Open Chem.* **2007,** *5* (2), 385-395.
11. Herrero-Latorre, C.; Alvarez-Mendez, J.; Barciela-Garcia, J.; Garcia-Martin, S.; Pena-Crecente, R. M., Characterization of carbon nanotubes and analytical methods for their determination in environmental and biological samples: A review. *Anal. Chim. Acta* **2015,** *853*, 77-94.
12. Zhong, H.; Xu, F.; Li, Z. H.; Fu, R. W.; Wu, D. C., High-energy supercapacitors based on hierarchical porous carbon with an ultrahigh ion-accessible surface area in ionic liquid electrolytes. *Nanoscale* **2013,** *5* (11), 4678-4682.
13. Zhang, Z.; Luo, D.; Lui, G.; Li, G. R.; Jiang, G. P.; Cano, Z. P.; Deng, Y. P.; Du, X. J.; Yin, S.; Chen, Y. F.; Zhang, M. H.; Yan, Z. F.; Chen, Z. W., In-situ ion-activated carbon nanospheres with tunable ultramicroporosity for superior CO_2 capture. *Carbon* **2019,** *143*, 531-541.
14. Querejeta, N.; Gil, M. V.; Pevida, C.; Centeno, T. A., Standing out the key role of ultramicroporosity to tailor biomass-derived carbons for CO_2 capture. *J. CO_2 Util.* **2018,** *26*, 1-7.
15. Zhou, J.; Li, Z. H.; Xing, W.; Shen, H. L.; Bi, X.; Zhu, T. T.; Qiu, Z. P.; Zhuo, S. P., A New Approach to Tuning Carbon Ultramicropore Size at Sub-Angstrom Level for Maximizing Specific Capacitance and CO_2 Uptake. *Adv. Funct. Mater.* **2016,** *26* (44), 7955-7964.
16. Wickramaratne, N. P.; Jaroniec, M., Importance of small micropores in CO_2 capture by phenolic resin-based activated carbon spheres. *J. Mater. Chem. A* **2013,** *1* (1), 112-116.
17. Linares, N.; Silvestre-Albero, A. M.; Serrano, E.; Silvestre-Albero, J.; Garcia-Martinez, J., Mesoporous materials for clean energy technologies. *Chem. Soc. Rev.* **2014,** *43* (22), 7681-7717.

18. Yang, X. Y.; Chen, L. H.; Li, Y.; Rooke, J. C.; Sanchez, C.; Su, B. L., Hierarchically porous materials: synthesis strategies and structure design. *Chem. Soc. Rev.* **2017,** *46* (2), 481-558.
19. Wagner, T.; Haffer, S.; Weinberger, C.; Klaus, D.; Tiemann, M., Mesoporous materials as gas sensors. *Chem. Soc. Rev.* **2013,** *42* (9), 4036-4053.
20. Wu, Z. X.; Zhao, D. Y., Ordered mesoporous materials as adsorbents. *Chem. Commun.* **2011,** *47* (12), 3332-3338.
21. Nasreen, S.; Urooj, A.; Rafique, U.; Ehrman, S., Functionalized mesoporous silica: absorbents for water purification. *Desalination Water Treat.* **2016,** *57* (60), 29352-29362.
22. Diagboya, P. N. E.; Dikio, E. D., Silica-based mesoporous materials; emerging designer adsorbents for aqueous pollutants removal and water treatment. *Micropor. Mesopor. Mater.* **2018,** *266*, 252-267.
23. Serra, A.; Valles, E., Microemulsion-Based One-Step Electrochemical Fabrication of Mesoporous Catalysts. *Catalysts* **2018,** *8* (9), 395.
24. Singh, S.; Kumar, R.; Setiabudi, H. D.; Nanda, S.; Vo, D. V. N., Advanced synthesis strategies of mesoporous SBA-15 supported catalysts for catalytic reforming applications: A state-of-the-art review. *Appl. Catal. A-Gen.* **2018,** *559*, 57-74.
25. Walcarius, A., Mesoporous materials and electrochemistry. *Chem. Soc. Rev.* **2013,** *42* (9), 4098-4140.
26. Ren, Y.; Ma, Z.; Bruce, P. G., Ordered mesoporous metal oxides: synthesis and applications. *Chem. Soc. Rev.* **2012,** *41* (14), 4909-4927.
27. Li, W.; Zhao, D. Y., An overview of the synthesis of ordered mesoporous materials. *Chem. Commun.* **2013,** *49* (10), 943-946.
28. Pal, N.; Bhaumik, A., Soft templating strategies for the synthesis of mesoporous materials: Inorganic, organic-inorganic hybrid and purely organic solids. *Adv. Colloid Interface Sci.* **2013,** *189*, 21-41.
29. Beck, J. S.; Vartuli, J. C.; Roth, W. J.; Leonowicz, M. E.; Kresge, C. T.; Schmitt, K. D.; Chu, C. T. W.; Olson, D. H.; Sheppard, E. W.; Mccullen, S. B.; Higgins, J. B.; Schlenker, J. L., A New Family of Mesoporous Molecular-Sieves Prepared with Liquid-Crystal Templates. *J. Am. Chem. Soc.* **1992,** *114* (27), 10834-10843.
30. Sakamoto, Y.; Kaneda, M.; Terasaki, O.; Zhao, D. Y.; Kim, J. M.; Stucky, G.; Shim, H. J.; Ryoo, R., Direct imaging of the pores and cages of three-dimensional mesoporous materials. *Nature* **2000,** *408* (6811), 449-453.
31. Kleitz, F.; Choi, S. H.; Ryoo, R., Cubic Ia3d large mesoporous silica: synthesis and replication to platinum nanowires, carbon nanorods and carbon nanotubes. *Chem. Commun.* **2003,** (17), 2136-2137.
32. Han, L.; Che, S. N., Anionic surfactant templated mesoporous silicas (AMSs). *Chem. Soc. Rev.* **2013,** *42* (9), 3740-3752.
33. Fan, J.; Yu, C. Z.; Gao, T.; Lei, J.; Tian, B. Z.; Wang, L. M.; Luo, Q.; Tu, B.; Zhou, W. Z.; Zhao, D. Y., Cubic mesoporous silica with large controllable entrance sizes and advanced adsorption properties. *Angew. Chem. Int. Ed.* **2003,** *42* (27), 3146-3150.
34. Zhao, H. R.; Zhang, T.; Qi, R. R.; Dai, J. X.; Liu, S.; Fei, T.; Lu, G. Y., Organic-inorganic hybrid materials based on mesoporous silica derivatives for humidity sensing. *Sens. Actuators B Chem.* **2017,** *248*, 803-811.
35. Croissant, J. G.; Cattoen, X.; Man, M. W. C.; Durand, J. O.; Khashab, N. M., Syntheses and applications of periodic mesoporous organosilica nanoparticles. *Nanoscale* **2015,** *7* (48), 20318-20334.
36. Lu, A. H.; Schuth, F., Nanocasting: A versatile strategy for creating nanostructured porous materials. *Adv. Mater.* **2006,** *18* (14), 1793-1805.

37. Yonemoto, B. T.; Hutchings, G. S.; Jiao, F., A General Synthetic Approach for Ordered Mesoporous Metal Sulfides. *J. Am. Chem. Soc.* **2014,** *136* (25), 8895-8898.
38. Yang, D.; Lu, Z. Y.; Rui, X. H.; Huang, X.; Li, H.; Zhu, J. X.; Zhang, W. Y.; Lam, Y. M.; Hng, H. H.; Zhang, H.; Yan, Q. Y., Synthesis of Two-Dimensional Transition-Metal Phosphates with Highly Ordered Mesoporous Structures for Lithium-Ion Battery Applications. *Angew. Chem. Int. Ed.* **2014,** *53* (35), 9352-9355.
39. Wan, Y.; Shi, Y. F.; Zhao, D. Y., Supramolecular aggregates as templates: Ordered mesoporous polymers and carbons. *Chem. Mater.* **2008,** *20* (3), 932-945.
40. Xuan, W. M.; Zhu, C. F.; Liu, Y.; Cui, Y., Mesoporous metal-organic framework materials. *Chem. Soc. Rev.* **2012,** *41* (5), 1677-1695.
41. Meng, Y.; Gu, D.; Zhang, F. Q.; Shi, Y. F.; Yang, H. F.; Li, Z.; Yu, C. Z.; Tu, B.; Zhao, D. Y., Ordered mesoporous polymers and homologous carbon frameworks: Amphiphilic surfactant templating and direct transformation. *Angew. Chem. Int. Ed.* **2005,** *44* (43), 7053-7059.
42. Malenfant, P. R. L.; Wan, J. L.; Taylor, S. T.; Manoharan, M., Self-assembly of an organic-inorganic block copolymer for nano-ordered ceramics. *Nat. Nanotech.* **2007,** *2* (1), 43-46.
43. Zhao, D. Y.; Feng, J. L.; Huo, Q. S.; Melosh, N.; Fredrickson, G. H.; Chmelka, B. F.; Stucky, G. D., Triblock copolymer syntheses of mesoporous silica with periodic 50 to 300 angstrom pores. *Science* **1998,** *279* (5350), 548-552.
44. Shin, H. J.; Ryoo, R.; Liu, Z.; Terasaki, O., Template synthesis of asymmetrically mesostructured platinum networks. *J. Am. Chem. Soc.* **2001,** *123* (6), 1246-1247.
45. Rossinyol, E.; Arbiol, J.; Peiro, F.; Cornet, A.; Morante, J. R.; Tian, B.; Bo, T.; Zhao, D., Nanostructured metal oxides synthesized by hard template method for gas sensing applications. *Sens. Actuators B Chem.* **2005,** *109* (1), 57-63.
46. Thomas, A.; Goettmann, F.; Antonietti, M., Hard templates for soft materials: Creating nanostructured organic materials. *Chem. Mater.* **2008,** *20* (3), 738-755.
47. Dai, G. P.; Wang, X.; Liu, S. Q.; Liang, Y.; Liu, K., Template-free Fabrication of Hierarchical Macro-/mesoporous N-doped TiO_2/graphene Oxide Composites with Enhanced Visible-light Photocatalytic Activity. *J. Chin. Chem. Soc.* **2015,** *62* (2), 170-176.
48. Li, W.; Liu, M. B.; Feng, S. S.; Li, X. M.; Wang, J. X.; Shen, D. K.; Li, Y. H.; Sun, Z. K.; Elzatahry, A. A.; Lu, H. J.; Zhao, D. Y., Template-free synthesis of uniform magnetic mesoporous TiO_2 nanospindles for highly selective enrichment of phosphopeptides. *Mater. Horiz.* **2014,** *1* (4), 439-445.
49. Li, W.; Deng, Y. H.; Wu, Z. X.; Qian, X. F.; Yang, J. P.; Wang, Y.; Gu, D.; Zhang, F.; Tu, B.; Zhao, D. Y., Hydrothermal Etching Assisted Crystallization: A Facile Route to Functional Yolk-Shell Titanate Microspheres with Ultrathin Nanosheets-Assembled Double Shells. *J. Am. Chem. Soc.* **2011,** *133* (40), 15830-15833.
50. Itoi, H.; Muramatsu, H.; Inagaki, M., Constraint spaces in carbon materials. *RSC Adv.* **2019,** *9* (40), 22823-22840.
51. Stein, A.; Wang, Z. Y.; Fierke, M. A., Functionalization of Porous Carbon Materials with Designed Pore Architecture. *Adv. Mater.* **2009,** *21* (3), 265-293.
52. Li, B. W.; Xiong, H.; Xiao, Y., Progress on Synthesis and Applications of Porous Carbon Materials. *Int. J. Electrochem. Sci.* **2020,** *15* (2), 1363-1377.
53. Zhang, Z.; Cano, Z. P.; Luo, D.; Dou, H. Z.; Yu, A. P.; Chen, Z. W., Rational design of tailored porous carbon-based materials for CO_2 capture. *J. Mater. Chem. A* **2019,** *7* (37), 20985-21003.
54. Zhang, M.; He, L.; Shi, T.; Zha, R. H., Nanocasting and Direct Synthesis Strategies for Mesoporous Carbons as Supercapacitor Electrodes. *Chem. Mater.* **2018,** *30* (21), 7391-7412.

55. Titirici, M. M.; White, R. J.; Brun, N.; Budarin, V. L.; Su, D. S.; del Monte, F.; Clark, J. H.; MacLachlan, M. J., Sustainable carbon materials. *Chem. Soc. Rev.* **2015,** *44* (1), 250-290.
56. Xin, W.; Song, Y. H., Mesoporous carbons: recent advances in synthesis and typical applications. *RSC Adv.* **2015,** *5* (101), 83239-83285.
57. Ryoo, R.; Joo, S. H.; Jun, S., Synthesis of highly ordered carbon molecular sieves via template-mediated structural transformation. *J. Phys. Chem. B* **1999,** *103* (37), 7743-7746.
58. Benzigar, M. R.; Talapaneni, S. N.; Joseph, S.; Ramadass, K.; Singh, G.; Scaranto, J.; Ravon, U.; Al-Bahily, K.; Vinu, A., Recent advances in functionalized micro and mesoporous carbon materials: synthesis and applications. *Chem. Soc. Rev.* **2018,** *47* (8), 2680-2721.
59. White, R. J.; Budarin, V.; Luque, R.; Clark, J. H.; Macquarrie, D. J., Tuneable porous carbonaceous materials from renewable resources. *Chem. Soc. Rev.* **2009,** *38* (12), 3401-3418.
60. Li, W.; Liu, J.; Zhao, D. Y., Mesoporous materials for energy conversion and storage devices. *Nat. Rev. Mater.* **2016,** *1* (6), 1-17.
61. Bhanja, P.; Bhaumik, A., Materials with Nanoscale Porosity: Energy and Environmental Applications. *Chem. Rec.* **2019,** *19* (2-3), 333-346.
62. Rondeau-Gagne, S.; Morin, J. F., Preparation of carbon nanomaterials from molecular precursors. *Chem. Soc. Rev.* **2014,** *43* (1), 85-98.
63. Maciel, J. V.; Durigon, A. M. M.; Souza, M. M.; Quadrado, R. F. N.; Fajardo, A. R.; Dias, D., Polysaccharides derived from natural sources applied to the development of chemically modified electrodes for environmental applications: A review. *Trends Environ. Anal. Chem.* **2019,** *22, e00062*.
64. Parker, H. L.; Hunt, A. J.; Budarin, V. L.; Shuttleworth, P. S.; Miller, K. L.; Clark, J. H., The importance of being porous: polysaccharide-derived mesoporous materials for use in dye adsorption. *RSC. Adv.* **2012,** *2* (24), 8992-8997.
65. Blackburn, R. S., Natural polysaccharides and their interactions with dye molecules: Applications in effluent treatment. *Environ. Sci. Technol.* **2004,** *38* (18), 4905-4909.
66. Te Wierik, G.H.P.; Bergsma, J.; Arends-Scholte, A.W.; Boersma, T.; Eissens, A.C.; Lerk, C.F., A new generation of starch products as excipient in pharmaceutical tablets. I. Preparation and binding properties of high surface area potato starch products. *Int. J. Pharm.* **1996,** *134*(1-2), 27-36.
67. Glenn, G.M.; Irving, D.W., Starch-based microcellular foams. *Cereal Chem.* **1995,** *72*(2), 155-161.
68. White, R. J.; Budarin, V. L.; Clark, J. H., Pectin-Derived Porous Materials. *Chem. Eur. J.* **2010,** *16* (4), 1326-1335.
69. Shuttleworth, P. S.; Budarin, V.; White, R. J.; Gun'ko, V. M.; Luque, R.; Clark, J. H., Molecular-Level Understanding of the Carbonisation of Polysaccharides. *Chem. Eur. J.* **2013,** *19* (28), 9351-9357.
70. White, R. J.; Budarin, V. L.; Clark, J. H., Tuneable mesoporous materials from alpha-D-polysaccharides. *ChemSusChem* **2008,** *1* (5), 408-411.
71. Budarin, V.; Clark, J. H.; Hardy, J. J. E.; Luque, R.; Milkowski, K.; Tavener, S. J.; Wilson, A. J., Starbons: New starch-derived mesoporous carbonaceous materials with tunable properties. *Angew. Chem. Int. Ed.* **2006,** *45* (23), 3782-3786.
72. White, R. J.; Antonio, C.; Budarin, V. L.; Bergstrom, E.; Thomas-Oates, J.; Clark, J. H., Polysaccharide-Derived Carbons for Polar Analyte Separations. *Adv. Funct. Mater.* **2010,** *20* (11), 1834-1841.
73. Marriott, A. S.; Hunt, A. J.; Bergstrom, E.; Thomas-Oates, J.; Clark, J. H., Effect of rate of pyrolysis on the textural properties of naturally templated porous carbons from alginic acid. *J. Anal. Appl. Pyrolysis* **2016,** *121*, 62-66.

74. Borisova, A.; De Bruyn, M.; Budarin, V. L.; Shuttleworth, P. S.; Dodson, J. R.; Segatto, M. L.; Clark, J. H., A Sustainable Freeze-Drying Route to Porous Polysaccharides with Tailored Hierarchical Meso- and Macroporosity. *Macromol. Rapid Commun.* **2015,** *36* (8), 774-779.
75. Ni, N.; Tesconi, M.; Tabibi, S.E.; Gupta, S.; Yalkowsky, S.H., Use of pure t-butanol as a solvent for freeze-drying: a case study. *Int. J. Pharm.* **2001,** *226* (1-2), 39-46.
76. Guizard, C.; Leloup, J.; Deville, S., Crystal templating with mutually miscible solvents: a simple path to hierarchical porosity. *J. Am. Ceram. Soc.* **2014,** *97*(7), 2020-2023.
77. Zuin, V. G.; Budarin, V. L.; Shuttleworth, P. S.; Hunt, A. J.; Pluciennik, C.; Borisova, A.; Dodson, J.; Parker, H. L.; Clark, J. H., Polysaccharide-derived mesoporous materials (Starbon®) for sustainable separation of complex mixtures. *Faraday Discuss.* **2017,** *202*, 451-464.
78. Luque, R.; Clark, J. H., Biodiesel-Like Biofuels from Simultaneous Transesterification/Esterification of Waste Oils with a Biomass-Derived Solid Acid Catalyst. *ChemCatChem* **2011,** *3* (3), 594-597.
79. Luque, R.; Budarin, V.; Clark, J. H.; Macquarrie, D. J., Glycerol transformations on polysaccharide derived mesoporous materials. *Appl. Catal., B: Environ.* **2008,** *82* (3-4), 157-162.
80. Luque, R.; Budarin, V.; Clark, J. H.; Macquarrie, D. J., Microwave-assisted preparation of amides using a stable and reusable mesoporous carbonaceous solid acid. *Green Chem.* **2009,** *11* (4), 459-461.
81. Marriott, A. S.; Bergstrom, E.; Hunt, A. J.; Thomas-Oates, J.; Clark, J. H., A natural template approach to mesoporous carbon spheres for use as green chromatographic stationary phases. *RSC Adv.* **2014,** *4* (1), 222-228.
82. Parker, H. L.; Budarin, V. L.; Clark, J. H.; Hunt, A. J., Use of Starbon for the Adsorption and Desorption of Phenols. *ACS Sustain. Chem. Eng.* **2013,** *1* (10), 1311-1318.
83. Tony, M. A.; Parker, H. L.; Clark, J. H., Treatment of laundrette wastewater using Starbon and Fenton's reagent. *J. Environ. Sci. Heal. A* **2016,** *51* (11), 974-979.
84. Shannon, J. M.; Clark, J. H.; de Heer, M. I.; Ekblad, T.; Matharu, A. S., Kinetic and Desorption Study of Selected Bioactive Compounds on Mesoporous Starbons: A Comparison with Microporous-Activated Carbon. *ACS Omega* **2018,** *3* (12), 18361-18369.
85. Garcia, A. M.; Hunt, A. J.; Budarin, V. L.; Parker, H. L.; Shuttleworth, P. S.; Ellis, G. J.; Clark, J. H., Starch-derived carbonaceous mesoporous materials (Starbon®) for the selective adsorption and recovery of critical metals. *Green Chem.* **2015,** *17* (4), 2146-2149.
86. Dura, G.; Budarin, V. L.; Castro-Osma, J. A.; Shuttleworth, P. S.; Quek, S. C. Z.; Clark, J. H.; North, M., Importance of Micropore-Mesopore Interfaces in Carbon Dioxide Capture by Carbon-Based Materials. *Angew. Chem. Int. Ed.* **2016,** *55* (32), 9173-9177.
87. Milescu, R. A.; Dennis, M. R.; McElroy, C. R.; Macquarrie, D. J.; Matharu, A. S.; Smith, M. W.; Clark, J. H.; Budarin, V. L., The role of surface functionality of sustainable mesoporous materials Starbon® on the adsorption of toxic ammonia and sulphur gasses. *Sustain. Chem. Pharm.* **2020,** *15, 100230*.
88. Colmenares, J. C.; Lisowski, P.; Lomot, D., A novel biomass-based support (Starbon) for TiO2 hybrid photocatalysts: a versatile green tool for water purification. *RSC Adv.* **2018,** *8* (40), 22321-22321.
89. Garcia, A. M.; Budarin, V. L.; Zhou, Y. X.; De Bruyn, M.; Hunt, A. J.; Lari, L.; Lazarov, V. K.; Salavagione, H. J.; Morales, E.; Ellis, G. J.; Clark, J. H.; Shuttleworth, P. S., Monolithic mesoporous graphitic composites as super capacitors: from Starbons to Starenes®. *J. Mater. Chem. A* **2018,** *6* (3), 1119-1127.
90. Kim, S.; Escamilla-Perez, A. M.; De Bruyn, M.; Alauzun, J. G.; Louvain, N.; Brun, N.; Macquarrie, D.; Stievano, L.; Boury, B.; Monconduit, L.; Mutin, P. H., Sustainable

polysaccharide-derived mesoporous carbons (Starbon®) as additives in lithium-ion batteries negative electrodes. *J. Mater. Chem. A* **2017,** *5* (46), 24380-24387.
91. Kim, S.; De Bruyn, M.; Alauzun, J. G.; Louvain, N.; Brun, N.; Macquarrie, D. J.; Stievano, L.; Boury, B.; Mutin, P. H.; Monconduit, L., Alginic acid-derived mesoporous carbonaceous materials (Starbon®) as negative electrodes for lithium-ion batteries: Importance of porosity and electronic conductivity. *J. Power Sources* **2018,** *406*, 18-25.
92. Gadipelli, S.; Guo, Z. X., Graphene-based materials: Synthesis and gas sorption, storage and separation. *Prog. Mater. Sci.* **2015,** *69*, 1-60.
93. Liu, L.; Deng, Q.-F.; Ma, T.-Y.; Lin, X.-Z.; Hou, X.-X.; Liu, Y.-P.; Yuan, Z.-Y., Ordered mesoporous carbons: citric acid-catalyzed synthesis, nitrogen doping and CO_2 capture. *J Mater. Chem.* **2011,** *21* (40), 16001-16009.
94. Xia, Y.; Zhu, Y.; Tang, Y., Preparation of sulfur-doped microporous carbons for the storage of hydrogen and carbon dioxide. *Carbon* **2012,** *50* (15), 5543-5553.
95. Zhang, Y.; Li, B.; Williams, K.; Gao, W.-Y.; Ma, S., A new microporous carbon material synthesized via thermolysis of a porous aromatic framework embedded with an extra carbon source for low-pressure CO_2 uptake. *Chem. Commun.* **2013,** *49* (87), 10269-10271.
96. Zhao, Y.; Yao, K. X.; Teng, B.; Zhang, T.; Han, Y., A perfluorinated covalent triazine-based framework for highly selective and water–tolerant CO_2 capture. *Energy Environ. Sci.* **2013,** *6* (12), 3684-3692.
97. Srinivas, G.; Krungleviciute, V.; Guo, Z.-X.; Yildirim, T., Exceptional CO_2 capture in a hierarchically porous carbon with simultaneous high surface area and pore volume. *Energy Environ. Sci.* **2014,** *7* (1), 335-342.
98. Zhao, Y.; Zhao, L.; Yao, K. X.; Yang, Y.; Zhang, Q.; Han, Y., Novel porous carbon materials with ultrahigh nitrogen contents for selective CO_2 capture. *J. Mater. Chem.* **2012,** *22* (37), 19726-19731.
99. Zhou, J.; Li, W.; Zhang, Z.; Xing, W.; Zhuo, S., Carbon dioxide adsorption performance of N-doped zeolite Y templated carbons. *RSC Adv.* **2012,** *2* (1), 161-167.
100. Sun, J. K.; Xu, Q., Functional materials derived from open framework templates/precursors: synthesis and applications. *Energy Environ. Sci.* **2014,** *7* (7), 2071-2100.
101. Liu, B.; Shioyama, H.; Akita, T.; Xu, Q., Metal-organic framework as a template for porous carbon synthesis. *J. Am. Chem. Soc.* **2008,** *130* (16), 5390-5391.
102. Liu, X. L.; Wang, C.; Wu, Q. H.; Wang, Z., Porous carbon derived from a metal-organic framework as an efficient adsorbent for the solid-phase extraction of phthalate esters. *J Sep. Sci.* **2015,** *38* (22), 3928-3935.
103. Yang, T.; Lua, A.C., Characteristics of activated carbons prepared from pistachio-nut shells by physical activation. *J. Colloid Interface Sci.* **2003,** *267* (2), 408-417.
104. Román, S.; González, J.; González-García, C.; Zamora, F., Control of pore development during CO2 and steam activation of olive stones. *Fuel Process. Technol.* **2008,** *89* (8), 715-720.
105. Li, Y.; Ben, T.; Zhang, B.; Fu, Y.; Qiu, S., Ultrahigh gas storage both at low and high pressures in KOH-activated carbonized porous aromatic frameworks. *Sci. Rep.* **2013,** *3*, 2420.
106. Xu, C.; Stromme, M., Sustainable Porous Carbon Materials Derived from Wood-Based Biopolymers for CO_2 Capture. *Nanomaterials* **2019,** *9* (1), 103.
107. Jiang, W.; Xing, X. J.; Zhang, X. W.; Mi, M. X., Prediction of combustion activation energy of NaOH/KOH catalyzed straw pyrolytic carbon based on machine learning. *Renew. Energy* **2019,** *130*, 1216-1225.
108. Tao, J.; Huo, P. L.; Fu, Z. H.; Zhang, J.; Yang, Z.; Zhang, D. F., Characterization and phenol adsorption performance of activated carbon prepared from tea residue by NaOH activation. *Environ. Technol.* **2019,** *40* (2), 171-181.

109. Tay, T.; Ucar, S.; Karagoz, S., Preparation and characterization of activated carbon from waste biomass. *J. Hazard. Mater.* **2009,** *165* (1-3), 481-485.
110. Morris, E. A.; Weisenberger, M. C.; Abdallah, M. G.; Vautard, F.; Grappe, H.; Ozcan, S.; Paulauskas, F. L.; Eberle, C.; Jackson, D.; Mecham, S. J.; Naskar, A. K., High performance carbon fibers from very high molecular weight polyacrylonitrile precursors. *Carbon* **2016,** *101*, 245-252.
111. Cheng, L. L.; Guo, P. Z.; Wang, R. Y.; Ming, L. F.; Leng, F. F.; Li, H. L.; Zhao, X. S., Electrocapacitive properties of supercapacitors based on hierarchical porous carbons from chestnut shell. *Colloids Surf. A Physicochem. Eng. Asp.* **2014,** *446*, 127-133.
112. Hulicova-Jurcakova, D.; Puziy, A. M.; Poddubnaya, O. I.; Suarez-Garcia, F.; Tascon, J. M. D.; Lu, G. Q., Highly Stable Performance of Supercapacitors from Phosphorus-Enriched Carbons. *J. Am. Chem. Soc.* **2009,** *131* (14), 5026-5027.
113. Bhomick, P. C.; Supong, A.; Karmaker, R.; Baruah, M.; Pongener, C.; Sinha, D., Activated carbon synthesized from biomass material using single-step KOH activation for adsorption of fluoride: Experimental and theoretical investigation. *Korean J. Chem. Eng.* **2019,** *36* (4), 551-562.
114. Singh, G.; Kim, I. Y.; Lakhi, K. S.; Srivastava, P.; Naidu, R.; Vinu, A., Single step synthesis of activated bio-carbons with a high surface area and their excellent CO_2 adsorption capacity. *Carbon* **2017,** *116*, 448-455.
115. Mahamad, M. N.; Zaini, M. A. A.; Zakaria, Z. A., Preparation and characterization of activated carbon from pineapple waste biomass for dye removal. *Int. Biodeterior. Biodegradation.* **2015,** *102*, 274-280.
116. Deng, J.; Li, M. M.; Wang, Y., Biomass-derived carbon: synthesis and applications in energy storage and conversion. *Green Chem.* **2016,** *18* (18), 4824-4854.
117. Wang, J.; Kaskel, S., KOH activation of carbon-based materials for energy storage. *J Mater. Chem.* **2012,** *22* (45), 23710-23725.
118. Li, S.; Han, K.; Li, J.; Li, M.; Lu, C., Preparation and characterization of super activated carbon produced from gulfweed by KOH activation. *Micropor. Mesopor. Mater.* **2017,** *243*, 291-300.
119. Li, D.; Ma, T.; Zhang, R.; Tian, Y.; Qiao, Y., Preparation of porous carbons with high low-pressure CO_2 uptake by KOH activation of rice husk char. *Fuel* **2015,** *139*, 68-70.
120. Sevilla, M.; Mokaya, R., Energy storage applications of activated carbons: supercapacitors and hydrogen storage. *Energy Environ. Sci.* **2014,** *7* (4), 1250-1280.
121. Sevilla, M.; Díez, N.; Fuertes, A.B., More sustainable chemical activation strategies for the production of porous carbons. *ChemSusChem*, 2021, *14* (1), 94-117.
122. Du, S.-h.; Wang, L.-q.; Fu, X.-t.; Chen, M.-m.; Wang, C.-y., Hierarchical porous carbon microspheres derived from porous starch for use in high-rate electrochemical double-layer capacitors. *Bioresour. Technol.* **2013,** *139*, 406-409.
123. Zhang, Y. X.; Yu, S.; Lou, G. B.; Shen, Y. L.; Chen, H.; Shen, Z. H.; Zhao, S. Y.; Zhang, J. Z.; Chai, S. G.; Zou, Q. C., Review of macroporous materials as electrochemical supercapacitor electrodes. *J. Mater. Sci.* **2017,** *52* (19), 11201-11228.
124. Liang, Y.; Wu, D.; Fu, R., Carbon microfibers with hierarchical porous structure from electrospun fiber-like natural biopolymer. *Sci. Rep.* **2013,** *3*, 1119-1123.
125. Armandi, M.; Bonelli, B.; Geobaldo, F.; Garrone, E., Nanoporous carbon materials obtained by sucrose carbonization in the presence of KOH. *Micropor. Mesopor. Mater.* **2010,** *132* (3), 414-420.
126. Liu, X.; Sun, Y.; Liu, J.; Sun, C.; Liu, H.; Xue, Q.; Snape, C. Potassium and zeolitic structure modified ultra-microporous adsorbent materials from a renewable feedstock with favorable surface chemistry for CO_2 capture. ACS Appl. Mater. Interfaces. 2017, *9* (32), 26826-26839.

127. Hao, P.; Zhao, Z. H.; Tian, J.; Li, H. D.; Sang, Y. H.; Yu, G. W.; Cai, H. Q.; Liu, H.; Wong, C. P.; Umar, A., Hierarchical porous carbon aerogel derived from bagasse for high performance supercapacitor electrode. *Nanoscale* **2014,** *6* (20), 12120-12129.
128. Wang, J.; Heerwig, A.; Lohe, M. R.; Oschatz, M.; Borchardt, L.; Kaskel, S., Fungi-based porous carbons for CO_2 adsorption and separation. *J. Mater. Chem.* **2012,** *22* (28), 13911-13913.
129. Zhao, Y.; Liu, X.; Han, Y., Microporous carbonaceous adsorbents for CO_2 separation via selective adsorption. *RSC Adv.* **2015,** *5* (38), 30310-30330.
130. Sevilla, M.; Fuertes, A. B.; Mokaya, R., High density hydrogen storage in superactivated carbons from hydrothermally carbonized renewable organic materials. *Energy Environ. Sci.* **2011,** *4* (4), 1400-1410.
131. Wang, S.; Nam, H.; Nam, H., Preparation of activated carbon from peanut shell with KOH activation and its application for H_2S adsorption in confined space. *J. Environ. Chem. Eng.* **2020,** *8* (2), 103683.
132. Gonzalez-Serrano, E.; Cordero, T.; Rodriguez-Mirasol, J.; Cotoruelo, L.; Rodriguez, J. J., Removal of water pollutants with activated carbons prepared from H_3PO_4 activation of lignin from kraft black liquors. *Water Res.* **2004,** *38* (13), 3043-3050.
133. Phan, N. H.; Rio, S.; Faur, C.; Le Coq, L.; Le Cloirec, P.; Nguyen, T. H., Production of fibrous activated carbons from natural cellulose (jute, coconut) fibers for water treatment applications. *Carbon* **2006,** *44* (12), 2569-2577.
134. Zu, G. Q.; Shen, J.; Zou, L. P.; Wang, F.; Wang, X. D.; Zhang, Y. W.; Yao, X. D., Nanocellulose-derived highly porous carbon aerogels for supercapacitors. *Carbon* **2016,** *99*, 203-211.
135. Rashidi, N. A.; Yusup, S., An overview of activated carbons utilization for the post-combustion carbon dioxide capture. *J. CO_2 Util.* **2016,** *13*, 1-16.
136. Yang, K. B.; Peng, J. H.; Srinivasakannan, C.; Zhang, L. B.; Xia, H. Y.; Duan, X. H., Preparation of high surface area activated carbon from coconut shells using microwave heating. *Bioresour. Technol.* **2010,** *101* (15), 6163-6169.
137. Hao, W. M.; Bjorkman, E.; Lilliestrale, M.; Hedin, N., Activated carbons prepared from hydrothermally carbonized waste biomass used as adsorbents for CO_2. *Appl. Energ.* **2013,** *112*, 526-532.
138. Savova, D.; Apak, E.; Ekinci, E.; Yardim, F.; Petrov, N.; Budinova, T.; Razvigorova, M.; Minkova, V., Biomass conversion to carbon adsorbents and gas. *Biomass Bioenergy* **2001,** *21* (2), 133-142.
139. Gonzalez, A. S.; Plaza, M. G.; Rubiera, F.; Pevida, C., Sustainable biomass-based carbon adsorbents for post-combustion CO_2 capture. *Chem. Eng. J.* **2013,** *230*, 456-465.
140. Plaza, M. G.; Gonzalez, A. S.; Pis, J. J.; Rubiera, F.; Pevida, C., Production of microporous biochars by single-step oxidation: Effect of activation conditions on CO_2 capture. *Appl. Energy* **2014,** *114*, 551-562.
141. Gonzalez, J. F.; Roman, S.; Gonzalez-Garcia, C. M.; Nabais, J. M. V.; Ortiz, A. L., Porosity Development in Activated Carbons Prepared from Walnut Shells by Carbon Dioxide or Steam Activation. *Ind. Eng. Chem. Res.* **2009,** *48* (16), 7474-7481.
142. Lopez, G.; Olazar, M.; Artetxe, M.; Amutio, M.; Elordi, G.; Bilbao, J., Steam activation of pyrolytic tyre char at different temperatures. *J. Anal. Appl. Pyrol.* **2009,** *85* (1-2), 539-543.
143. San Miguel, G.; Fowler, G. D.; Sollars, C. J., A study of the characteristics of activated carbons produced by steam and carbon dioxide activation of waste tyre rubber. *Carbon* **2003,** *41* (5), 1009-1016.
144. Salvador, F.; Sanchez-Montero, M. J.; Montero, J.; Izquierdo, C., Activated Carbon Fibers Prepared from a Phenolic Fiber by Supercritical Water and Steam Activation. *J. Phys. Chem. C* **2008,** *112* (50), 20057-20064.

145. Bai, Y. H.; Lv, P.; Yang, X. H.; Gao, M. Q.; Zhu, S. H.; Yan, L. J.; Li, F., Gasification of coal char in H_2O/CO_2 atmospheres: Evolution of surface morphology and pore structure. *Fuel* **2018,** *218*, 236-246.
146. Zhu, S. H.; Bai, Y. H.; Luo, K.; Hao, C. H.; Bao, W. R.; Li, F., Impacts of CO_2 on char structure and the gasification reactivity. *J. Anal. Appl. Pyrol.* **2017,** *128*, 13-17.
147. Bessant, G.; Walker Jr, P., Activation of anthracite: Using carbon dioxide versus air. *Carbon* **1994,** *32* (6), 1171-1176.
148. Walker Jr, P.; Rusinko Jr, F.; Austin, L. G., Gas reactions of carbon In "*Advances in catalysis"*, Elsevier: 1959; Vol. XI, 133-221.
149. Demiral, H.; Demiral, I.; Karabacakoglu, B.; Tumsek, F., Production of activated carbon from olive bagasse by physical activation. *Chem. Eng. Res. Des.* **2011,** *89* (2a), 206-213.
150. Lua, A. C.; Guo, J., Activated carbon prepared from oil palm stone by one-step CO_2 activation for gaseous pollutant removal. *Carbon* **2000,** *38* (7), 1089-1097.
151. Chang, C. F.; Chang, C. Y.; Tsai, W. T., Effects of burn-off and activation temperature on preparation of activated carbon from corn cob agrowaste by CO_2 and steam. *J. Colloid Interface Sci.* **2000,** *232* (1), 45-49.
152. Duan, X. H.; Srinivasakannan, C.; Peng, J. H.; Zhang, L. B.; Zhang, Z. Y., Comparison of activated carbon prepared from Jatropha hull by conventional heating and microwave heating. *Biomass Bioenergy* **2011,** *35* (9), 3920-3926.
153. Tam, M. S.; Antal, M. J., Preparation of activated carbons from macadamia nutshell and coconut shell by air activation. *Ind. Eng. Chem. Res.* **1999,** *38* (11), 4268-4276.
154. Parra, J.; Pis, J.; De Sousa, J.; Pajares, J. A.; Bansal, R., Effect of coal preoxidation on the development of microporosity in activated carbons. *Carbon* **1996,** *34* (6), 783-787.
155. Gomez-Serrano, V.; Pastor-Villegas, J.; Duran-Valle, C.; Valenzuela-Calahorro, C., Heat treatment of rockrose char in air. Effect on surface chemistry and porous texture. *Carbon* **1996,** *34* (4), 533-538.
156. Gómez-Serrano, V.; Piriz-Almeida, F.; Durán-Valle, C. J.; Pastor-Villegas, J., Formation of oxygen structures by air activation. A study by FT-IR spectroscopy. *Carbon* **1999,** *37* (10), 1517-1528.
157. Dawson, E. A.; Parkes, G. M. B.; Barnes, P. A.; Chinn, M. J., An investigation of the porosity of carbons prepared by constant rate activation in air. *Carbon* **2003,** *41* (8), 1689-1691.
158. Feng, B.; Bhatia, S. K., Variation of the pore structure of coal chars during gasification. *Carbon* **2003,** *41* (3), 507-523.
159. Ganan, J.; Gonzalez, J. F.; Gonzalez-Garcia, C. M.; Ramiro, A.; Sabio, E.; Roman, S., Air-activated. carbons from almond tree pruning: Preparation and characterization. *Appl. Surf. Sci.* **2006,** *252* (17), 5988-5992.
160. Osswald, S.; Portet, C.; Gogotsi, Y.; Laudisio, G.; Singer, J. P.; Fischer, J. E.; Sokolov, V. V.; Kukushkina, J. A.; Kravchik, A. E., Porosity control in nanoporous carbide-derived carbon by oxidation in air and carbon dioxide. *J. Solid State Chem.* **2009,** *182* (7), 1733-1741.
161. Wang, H.; Shan, L.; Lv, Q.; Cai, S.; Quan, G.; Yan, J., Production of hierarchically porous carbon from natural biomass waste for efficient organic contaminants adsorption. *J. Clean. Prod.* **2020,** 263, 121352.
162. Manan, Z. A.; Nawi, W. N. R. M.; Alwi, S. R. W.; Klemeš, J. J., Advances in Process Integration research for CO_2 emission reduction–A review. *J. Clean. Prod.* **2017,** *167*, 1-13.
163. Stern, N., Stern review report on the economics of climate change. *Energy Environ.* **2006,** *17* (6), 977-981.
164. Haszeldine, R. S., Carbon capture and storage: how green can black be? *Science* **2009,** *325* (5948), 1647-1652.

165. Orr Jr, F. M., CO_2 capture and storage: are we ready? *Energy Environ. Sci.* **2009,** *2* (5), 449-458.
166. Mason, J. A.; McDonald, T. M.; Bae, T.-H.; Bachman, J. E.; Sumida, K.; Dutton, J. J.; Kaye, S. S.; Long, J. R., Application of a high-throughput analyzer in evaluating solid adsorbents for post-combustion carbon capture via multicomponent adsorption of CO_2, N_2, and H_2O. *J. Am. Chem. Soc.* **2015,** *137* (14), 4787-4803.
167. Goeppert, A.; Czaun, M.; Prakash, G. S.; Olah, G. A., Air as the renewable carbon source of the future: an overview of CO_2 capture from the atmosphere. *Energy Environ. Sci.* **2012,** *5* (7), 7833-7853.
168. Jacobson, M. Z., Review of solutions to global warming, air pollution, and energy security. *Energy Environ. Sci.* **2009,** *2* (2), 148-173.
169. Rochelle, G. T., Amine scrubbing for CO_2 capture. *Science* **2009,** *325* (5948), 1652-1654.
170. Wang, R.; Liu, S.; Li, Q.; Zhang, S.; Wang, L.; An, S., CO_2 capture performance and mechanism of blended amine solvents regulated by N-methylcyclohexyamine. *Energy* **2021**, *215*, 119209.
171. D'Alessandro, D. M.; Smit, B.; Long, J. R., Abscheidung von Kohlendioxid: Perspektiven für neue Materialien. *Angew. Chem. Int. Ed.* **2010,** *122* (35), 6194-6219.
172. D'Alessandro, D. M.; Smit, B.; Long, J. R., Carbon dioxide capture: prospects for new materials. *Angew. Chem. Int. Ed.* **2010,** *49* (35), 6058-6082.
173. Tuinier, M.; van Sint Annaland, M.; Kramer, G. J.; Kuipers, J., Cryogenic CO_2 capture using dynamically operated packed beds. *Chem. Eng. Sci.* **2010,** *65* (1), 114-119.
174. Song, C. F.; Liu, Q. L.; Deng, S.; Li, H. L.; Kitamura, Y., Cryogenic-based CO_2 capture technologies: State-of-the-art developments and current challenges. *Renew. Sustain. Energy Rev.* **2019,** *101*, 265-278.
175. Figueroa, J. D.; Fout, T.; Plasynski, S.; McIlvried, H.; Srivastava, R. D., Advances in CO2 capture technology—the US Department of Energy's Carbon Sequestration Program. *Int. J. Greenhouse Gas Control* **2008,** *2* (1), 9-20.
176. Aaron, D.; Tsouris, C., Separation of CO_2 from flue gas: a review. *Sep. Sci. Technol.* **2005,** *40* (1-3), 321-348.
177. Choi, S.; Drese, J. H.; Jones, C. W., Adsorbent materials for carbon dioxide capture from large anthropogenic point sources. *ChemSusChem* **2009,** *2* (9), 796-854.
178. Hudson, M. R.; Queen, W. L.; Mason, J. A.; Fickel, D. W.; Lobo, R. F.; Brown, C. M., Unconventional, highly selective CO_2 adsorption in zeolite SSZ-13. *J. Am. Chem. Soc.* **2012,** *134* (4), 1970-1973.
179. Wong-Foy, A. G.; Matzger, A. J.; Yaghi, O. M., Exceptional H2 saturation uptake in microporous metal− organic frameworks. *J. Am. Chem. Soc.* **2006,** *128* (11), 3494-3495.
180. Sumida, K.; Rogow, D. L.; Mason, J. A.; McDonald, T. M.; Bloch, E. D.; Herm, Z. R.; Bae, T.-H.; Long, J. R., Carbon dioxide capture in metal–organic frameworks. *Chem. Rev.* **2011,** *112* (2), 724-781.
181. An, J.; Geib, S. J.; Rosi, N. L., High and selective CO2 uptake in a cobalt adeninate metal−organic framework exhibiting pyrimidine-and amino-decorated pores. *J. Am. Chem. Soc.* **2009,** *132* (1), 38-39.
182. Ding, Y.; Alpay, E., Equilibria and kinetics of CO_2 adsorption on hydrotalcite adsorbent. *Chem. Eng. Sci.* **2000,** *55*(17), 3461-3474.
183. Balsamo, M.; Rodríguez-Reinoso, F.; Montagnaro, F.; Lancia, A.; Erto, A., Highlighting the role of activated carbon particle size on CO_2 capture from model flue gas. *Ind. Eng. Chem. Res.* **2013,** *52*(34), 12183-12191.

184. Liu, J.; Liu, X.; Sun, Y.; Sun, C.; Liu, H.; Stevens, L.A.; Li, K.; Snape, C.E., High density and super ultra-microporous-activated carbon macrospheres with high volumetric capacity for CO_2 capture. *Adv. Sustain. Syst.* **2018**, *2*(2), 1700115.
185. Oschatz, M.; Leistner, M.; Nickel, W.; Kaskel, S., Advanced structural analysis of nanoporous materials by thermal response measurements. *Langmuir* **2015,** *31* (13), 4040-4047.
186. Murge, P.; Dinda, S.; Roy, S., Zeolite-based sorbent for CO_2 capture: preparation and performance evaluation. *Langmuir.* **2019,** *35* (46), 14751-14760.
187. Ke, Q.; Sun, T.; Wei, X.; Guo, Y.; Xu, S. Wang, S., Economical synthesis strategy of RHO zeolites with fine-tuned composition and porosity for enhanced trace CO_2 capture. *Chem. Eng. J.* **2019,** 359, 344-353.
188. Li, Z.; Liu, P.; Ou, C.; Dong, X., Porous Metal–Organic Frameworks for Carbon Dioxide Adsorption and Separation at Low Pressure. *ACS Sustain. Chem. Eng.* **2020,** *8* (41), 15378-15404.
189. Ding, M.; Flaig, R.W.; Jiang, H.L.; Yaghi, O.M., Carbon capture and conversion using metal–organic frameworks and MOF-based materials. *Chem. Soc. Rev.* **2019,** *48* (10), 2783-2828.
190. Cui, X.; Bustin, R. M.; Dipple, G., Selective transport of CO_2, CH_4, and N_2 in coals: insights from modeling of experimental gas adsorption data. *Fuel.* **2004,** *83* (3), 293-303.
191. Ra, E. J.; Kim, T. H.; Yu, W. J.; An, K. H.; Lee, Y. H., Ultramicropore formation in PAN/camphor-based carbon nanofiber paper. *Chem. Commun.* **2010,** *46* (8), 1320-1322.
192. Sarker, A.I.; Aroonwilas, A.; Veawab, A., Equilibrium and kinetic behaviour of CO_2 adsorption onto zeolites, carbon molecular sieve and activated carbons. *Energy Procedia* **2017,** 114, 2450-2459.
193. Pérez-Ramírez, J.; Christensen, C. H.; Egeblad, K.; Christensen, C. H.; Groen, J. C., Hierarchical zeolites: enhanced utilisation of microporous crystals in catalysis by advances in materials design. *Chem. Soc. Rev.* **2008,** *37* (11), 2530-2542.
194. Choma, J.; Górka, J.; Jaroniec, M.; Zawislak, A., Development of microporosity in mesoporous carbons. *Top. Catal.* **2010,** *53* (3-4), 283-290.
195. Antar, M.; Lyu, D.; Nazari, M.; Shah, A.; Zhou, X.; Smith, D.L., Biomass for a sustainable bioeconomy: An overview of world biomass production and utilization. *Renew. Sust. Energ. Rev*. **2021,** 139, 110691.
196. Li, Y.; Wang, J.; Fan, S.; Wang, F.; Shen, Z.; Duan, H.; Xu, J.; Huang, Y., Nitrogen-doped hierarchically porous carbon spheres for low concentration CO_2 capture. *J. Energy Chem.* **2021,** 53, 168-174.
197. Shi, J.; Cui, H.; Xu, J.; Yan, N.; Zhang, C.; You, S., Fabrication of nitrogen doped and hierarchically porous carbon flowers for CO_2 adsorption. *J. CO_2 Util.* **2021,** 51, 101617.
198. Estevez, L.; Barpaga, D.; Zheng, J.; Sabale, S.; Patel, R.L.; Zhang, J.G.; McGrail, B.P.; Motkuri, R.K., Hierarchically porous carbon materials for CO_2 capture: the role of pore structure. *Ind. Eng. Chem. Res.* **2018,** *57* (4), 1262-1268.
199. Dutta, S.; Bhaumik, A.; Wu, K.C.W., Hierarchically porous carbon derived from polymers and biomass: effect of interconnected pores on energy applications. *Energy Environ. Sci.* **2014,** *7* (11), 3574-3592.
200. Yagub, M. T.; Sen, T. K.; Afroze, S.; Ang, H. M., Dye and its removal from aqueous solution by adsorption: A review. *Adv. Colloid Interface Sci.* **2014,** *209*, 172-184.
201. SokolowskaGajda, J.; Freeman, H. S.; Reife, A., Synthetic dyes based on environmental considerations. Part 2. Iron complexed formazan dyes. *Dyes Pigm.* **1996,** *30* (1), 1-20.
202. Kabdasli, I.; Tunay, O.; Orhon, D., Wastewater control and management in a leather tanning district. *Water Sci. Technol.* **1999,** *40* (1), 261-267.

203. Bensalah, N.; Alfaro, M. A. Q.; Martinez-Huitle, C. A., Electrochemical treatment of synthetic wastewaters containing Alphazurine A dye. *Chem. Eng. J.* **2009,** *149* (1-3), 348-352.
204. Wrobel, D.; Boguta, A.; Ion, R. M., Mixtures of synthetic organic dyes in a photoelectrochemical cell. *J. Photochem. Photobiol. A Chem.* **2001,** *138* (1), 7-22.
205. Singh, R. L.; Singh, P. K.; Singh, R. P., Enzymatic decolorization and degradation of azo dyes - A review. *Int. Biodeterior. Biodegradation* **2015,** *104*, 21-31.
206. Ngulube, T.; Gumbo, J. R.; Masindi, V.; Maity, A., An update on synthetic dyes adsorption onto clay-based minerals: A state-of-art review. *J. Environ. Manage.* **2017,** *191*, 35-57.
207. Katheresan, V.; Kansedo, J.; Lau, S. Y., Efficiency of various recent wastewater dye removal methods: A review. *J. Environ. Chem. Eng.* **2018,** *6* (4), 4676-4697.
208. Barton, S. S., The Adsorption of Methylene-Blue by Active-Carbon. *Carbon* **1987,** *25* (3), 343-350.
209. Wong, Y. C.; Szeto, Y. S.; Cheung, W. H.; McKay, G., Adsorption of acid dyes on chitosan- equilibrium isotherm analyses. *Process Biochem.* **2004,** *39* (6), 693-702.
210. Forgacs, E.; Cserhati, T.; Oros, G., Removal of synthetic dyes from wastewaters: a review. *Environ. Int.* **2004,** *30* (7), 953-971.
211. Singh, K.; Arora, S., Removal of Synthetic Textile Dyes from Wastewaters: A Critical Review on Present Treatment Technologies. *Crit. Rev. Env. Sci. Tec.* **2011,** *41* (9), 807-878.
212. Singh, N. B.; Nagpal, G.; Agrawal, S.; Rachna, Water purification by using Adsorbents: A Review. *Environ. Technol. Inno.* **2018,** *11*, 187-240.
213. Ali, H., Biodegradation of Synthetic Dyes-A Review. *Water Air Soil Pollut.* **2010,** *213* (1-4), 251-273.
214. De Gisi, S.; Lofrano, G.; Grassi, M.; Notarnicola, M., Characteristics and adsorption capacities of low-cost sorbents for wastewater treatment: A review. *Sustain. Mater. Technol.* **2016,** *9*, 10-40.
215. Kyzas, G. Z.; Matis, K. A., Nanoadsorbents for pollutants removal: A review. *J. Mol. Liq.* **2015,** *203*, 159-168.
216. Joshi, M.; Bansal, R.; Purwar, R., Colour removal from textile effluents. *Indian J. Fibre. Text.* **2004,** *29* (2), 239-259.
217. Dabrowski, A., Adsorption - from theory to practice. *Adv. Colloid Interface Sci.* **2001,** *93* (1-3), 135-224.
218. Tan, X. F.; Liu, S. B.; Liu, Y. G.; Gu, Y. L.; Zeng, G. M.; Hua, X. J.; Wang, X.; Liu, S. H.; Jiang, L. H., Biochar as potential sustainable precursors for activated carbon production: Multiple applications in environmental protection and energy storage. *Bioresour. Technol.* **2017,** *227*, 359-372.
219. Montoya-Suarez, S.; Colpas-Castillo, F.; Meza-Fuentes, E.; Rodriguez-Ruiz, J.; Fernandez-Maestre, R., Activated carbons from waste of oil-palm kernel shells, sawdust and tannery leather scraps and application to chromium(VI), phenol, and methylene blue dye adsorption. *Water Sci. Technol.* **2016,** *73* (1), 21-27.
220. Srinivasan, A.; Viraraghavan, T., Decolorization of dye wastewaters by biosorbents: A review. *J. Environ. Manage.* **2010,** *91* (10), 1915-1929.
221. Adegoke, K. A.; Bello, O. S., Dye sequestration using agricultural wastes as adsorbents. *Water Resour. Ind.* **2015,** *12*, 8-24.
222. Rafatullah, M.; Sulaiman, O.; Hashim, R.; Ahmad, A., Adsorption of methylene blue on low-cost adsorbents: A review. *J. Hazard. Mater.* **2010,** *177* (1-3), 70-80.
223. Dawood, S.; Sen, T. K.; Phan, C., Synthesis and Characterisation of Novel-Activated Carbon from Waste Biomass Pinecone and Its Application in the Removal of Congo Red Dye from Aqueous Solution by Adsorption. *Water Air Soil Pollut.* **2014,** *225* (1), 1-16.

224. Rajapaksha, A. U.; Vithanage, M.; Ahmad, M.; Seo, D. C.; Cho, J. S.; Lee, S. E.; Lee, S. S.; Ok, Y. S., Enhanced sulfamethazine removal by steam-activated invasive plant-derived biochar. *J. Hazard. Mater.* **2015,** *290*, 43-50.
225. Liu, W. J.; Jiang, H.; Yu, H. Q., Development of Biochar-Based Functional Materials: Toward a Sustainable Platform Carbon Material. *Chem. Rev.* **2015,** *115* (22), 12251-12285.
226. Mousavi, D.V.; Ahmadipouya, S.; Shokrgozar, A.; Molavi, H.; Rezakazemi, M.; Ahmadijokani, F.; Arjmand, M., Adsorption performance of UiO-66 towards organic dyes: Effect of activation conditions. *J. Mol. Liq.* **2021,** 321, 114487.
227. Wang, B. Y.; Li, C. P.; Liang, H., Bioleaching of heavy metal from woody biochar using Acidithiobacillus ferrooxidans and activation for adsorption. *Bioresour. Technol.* **2013,** *146*, 803-806.
228. Spagnoli, A. A.; Giannakoudakis, D. A.; Bashkova, S., Adsorption of methylene blue on cashew nutshell-based carbons activated with zinc chloride: The role of surface and structural parameters. *J. Mol. Liq.* **2017,** *229*, 465-471.
229. Sun, L.; Chen, D. M.; Wan, S. G.; Yu, Z. B., Performance, kinetics, and equilibrium of methylene blue adsorption on biochar derived from eucalyptus saw dust modified with citric, tartaric, and acetic acids. *Bioresour. Technol.* **2015,** *198*, 300-308.
230. Qi, C. L.; Xu, L. H.; Zhang, M. X.; Zhang, M., Fabrication and application of hierarchical porous carbon for the adsorption of bulky dyes. *Micropor. Mesopor. Mater.* **2019,** *290*, 109651.
231. Chen, L.; Ji, T.; Brisbin, L.; Zhu, J. H., Hierarchical Porous and High Surface Area Tubular Carbon as Dye Adsorbent and Capacitor Electrode. *ACS. Appl. Mater. Inter.* **2015,** *7* (22), 12230-12237.
232. Zhang, Y. L.; Ji, G. Z.; Li, C. J.; Wang, X. X.; Li, A. M., Templating synthesis of hierarchical porous carbon from heavy residue of tire pyrolysis oil for methylene blue removal. *Chem. Eng. J.* **2020,** *390*, 124398.
233. Albadarin, A. B.; Collins, M. N.; Naushad, M.; Shirazian, S.; Walker, G.; Mangwandi, C., Activated lignin-chitosan extruded blends for efficient adsorption of methylene blue. *Chem. Eng. J.* **2017,** *307*, 264-272.
234. Han, Z. X.; Zhu, Z.; Wu, D. D.; Wu, J.; Liu, Y. R., Adsorption Kinetics and Thermodynamics of Acid Blue 25 and Methylene Blue Dye Solutions on Natural Sepiolite. *Synth. React. Inorg. Me* **2014,** *44* (1), 140-147.
235. Tumsek, F.; Avci, O., Investigation of Kinetics and Isotherm Models for the Acid Orange 95 Adsorption from Aqueous Solution onto Natural Minerals. *J. Chem. Eng. Data* **2013,** *58* (3), 551-559.
236. Anirudhan, T. S.; Ramachandran, M., Adsorptive removal of basic dyes from aqueous solutions by surfactant modified bentonite clay (organoclay): Kinetic and competitive adsorption isotherm. *Proc. Saf. Environ. Prot.* **2015,** *95*, 215-225.
237. Chaari, I.; Moussi, B.; Jamoussi, F., Interactions of the dye, CI direct orange 34 with natural clay. *J Alloy. Comp.* **2015,** *647*, 720-727.
238. Yan, L. G.; Qin, L. L.; Yu, H. Q.; Li, S.; Shan, R. R.; Du, B., Adsorption of acid dyes from aqueous solution by CTMAB modified bentonite: Kinetic and isotherm modeling. *J. Mol. Liq.* **2015,** *211*, 1074-1081.
239. Chinoune, K.; Bentaleb, K.; Bouberka, Z.; Nadim, A.; Maschke, U., Adsorption of reactive dyes from aqueous solution by dirty bentonite. *Appl. Clay Sci.* **2016,** *123*, 64-75.
240. Elmoubarki, R.; Mahjoubi, F. Z.; Tounsadi, H.; Moustadraf, J.; Abdennouri, M.; Zouhri, A.; El Albani, A.; Barka, N., Adsorption of textile dyes on raw and decanted Moroccan clays: Kinetics, equilibrium and thermodynamics. *Water Resour. Ind.* **2015,** *9*, 16-29.
241. Makhoukhi, B.; Djab, M.; Didi, M. A., Adsorption of Telon dyes onto bis-imidazolium modified bentonite in aqueous solutions. *J. Environ. Chem. Eng.* **2015,** *3* (2), 1384-1392.

242. Zhao, Y. F.; Abdullayev, E.; Vasiliev, A.; Lvov, Y., Halloysite nanotubule clay for efficient water purification. *J. Colloid Interface Sci.* **2013,** *406*, 121-129.
243. Yu, X. B.; Wei, C. H.; Wu, H. Z., Effect of molecular structure on the adsorption behavior of cationic dyes onto natural vermiculite. *Sep. Purif. Technol.* **2015,** *156*, 489-495.
244. Ho, Y. S.; McKay, G., Pseudo-second order model for sorption processes. *Process Biochem.* **1999,** *34* (5), 451-465.
245. Wu, F. C.; Tseng, R. L.; Juang, R. S., Initial behavior of intraparticle diffusion model used in the description of adsorption kinetics. *Chem. Eng. J.* **2009,** *153* (1-3), 1-8.
246. Bos, M.J.; Kreuger, T.; Kersten, S.R.A.; Brilman, D.W.F., Study on transport phenomena and intrinsic kinetics for CO_2 adsorption in solid amine sorbent. *Chem. Eng. J.* **2019,** 377, 120374.
247. Limousin, G.; Gaudet, J. P.; Charlet, L.; Szenknect, S.; Barthes, V.; Krimissa, M., Sorption isotherms: A review on physical bases, modeling and measurement. *Appl. Geochem.* **2007,** *22* (2), 249-275.
248. Allen, S. J.; Mckay, G.; Porter, J. F., Adsorption isotherm models for basic dye adsorption by peat in single and binary component systems. *J. Colloid Interface Sci.* **2004,** *280* (2), 322-333.
249. Foo, K. Y.; Hameed, B. H., Insights into the modeling of adsorption isotherm systems. *Chem. Eng. J.* **2010,** *156* (1), 2-10.
250. Parshetti, G. K.; Chowdhury, S.; Balasubramanian, R., Biomass derived low-cost microporous adsorbents for efficient CO_2 capture. *Fuel* **2015,** *148*, 246-254.
251. Langmuir, I., Chemical reactions at low pressures. *J. Am. Chem. Soc.* **1915,** *37*, 1139-1167.
252. Vijayaraghavan, K.; Padmesh, T. V. N.; Palanivelu, K.; Velan, M., Biosorption of nickel (II) ions onto Sargassum wightii: Application of two-parameter and three-parameter isotherm models. *J. Hazard. Mater.* **2006,** *133* (1-3), 304-308.
253. A brief introduction to the state key laboratory for physical chemistry of solid surfaces. *Prog. Nat. Sci.* **1997,** *7* (4), 509-512.
254. Temkin, M.; Pyzhev, V., Kinetics of ammonia synthesis on promoted iron catalysts. *Acta Physicochim. URSS* **1940,** *12* (3), 327-356.
255. Kim, Y. H.; Kim, C. M.; Choi, I. H.; Rengaraj, S.; Yi, J. H., Arsenic removal using mesoporous alumina prepared via a templating method. *Environ. Sci. Technol.* **2004,** *38* (3), 924-931.
256. Fan, S. S.; Wang, Y.; Wang, Z.; Tang, J.; Tang, J.; Li, X. D., Removal of methylene blue from aqueous solution by sewage sludge-derived biochar: Adsorption kinetics, equilibrium, thermodynamics and mechanism. *J. Environ. Chem. Eng.* **2017,** *5* (1), 601-611.
257. Fu, J. W.; Chen, Z. H.; Wang, M. H.; Liu, S. J.; Zhang, J. H.; Zhang, J. N.; Han, R. P.; Xu, Q., Adsorption of methylene blue by a high-efficiency adsorbent (polydopamine microspheres): Kinetics, isotherm, thermodynamics and mechanism analysis. *Chem. Eng. J.* **2015,** *259*, 53-61.
258. Meynen, V.; Cool, P.; Vansant, E. F., Verified syntheses of mesoporous materials. *Micropor. Mesopor. Mater.* **2009,** *125* (3), 170-223.
259. Nasir, S.; Hussein, M. Z.; Zainal, Z.; Yusof, N. A.; Zobir, S. A. M.; Alibe, I. M., Potential Valorization of By-product Materials from Oil Palm: A review of Alternative and Sustainable Carbon Sources for Carbon-based Nanomaterials Synthesis. *Bioresources* **2019,** *14* (1), 2352-2388.
260. Inagaki, M., Pores in carbon materials-Importance of their control. *New Carbon Mater.* **2009,** *24* (3), 193-222.

261. Gonzalez-Garcia, P., Activated carbon from lignocellulosics precursors: A review of the synthesis methods, characterization techniques and applications. *Renew. Sustain. Energy Rev.* **2018,** *82*, 1393-1414.
262. Thommes, M.; Cychosz, K. A., Physical adsorption characterization of nanoporous materials: progress and challenges. *Adsorption* **2014,** *20* (2-3), 233-250.
263. Rouquerol, J.; Avnir, D.; Fairbridge, C. W.; Everett, D. H.; Haynes, J. H.; Pernicone, N.; Ramsay, J. D. F.; Sing, K. S. W.; Unger, K. K., Recommendations for the Characterization of Porous Solids. *Pure Appl. Chem.* **1994,** *66* (8), 1739-1758.
264. Rouquerol, J.; Baron, G.; Denoyel, R.; Giesche, H.; Groen, J.; Klobes, P.; Levitz, P.; Neimark, A. V.; Rigby, S.; Skudas, R.; Sing, K.; Thommes, M.; Unger, K., Liquid intrusion and alternative methods for the characterization of macroporous materials (IUPAC Technical Report). *Pure Appl. Chem.* **2012,** *84* (1), 107-136.
265. Thommes, M.; Kaneko, K.; Neimark, A. V.; Olivier, J. P.; Rodriguez-Reinoso, F.; Rouquerol, J.; Sing, K. S. W., Physisorption of gases, with special reference to the evaluation of surface area and pore size distribution (IUPAC Technical Report). *Pure Appl. Chem.* **2015,** *87* (9-10), 1051-1069.
266. Ravikovitch, P. I.; Vishnyakov, A.; Russo, R.; Neimark, A. V., Unified approach to pore size characterization of microporous carbonaceous materials from N_2, Ar, and CO_2 adsorption isotherms. *Langmuir* **2000,** *16* (5), 2311-2320.
267. Furmaniak, S.; Terzyk, A. P.; Gauden, P. A.; Harris, P. J. F.; Kowalczyk, P., The influence of carbon surface oxygen groups on Dubinin-Astakhov equation parameters calculated from CO_2 adsorption isotherm. *J. Phys. Condens. Matter* **2010,** *22* (8), 085003.
268. Rouquerol, J.; Llewellyn, P.; Rouquerol, F., Is the BET equation applicable to microporous adsorbents? *Characterization of Porous Solids Vii - Proceedings of the 7th International Symposium on the Characterization of Porous Solids (Cops-Vii), Aix-En-Provence, France, 26-28 May 2005,* **2006,** *160*, 49-56.
269. Characterisation of porous solids and powders. *Powder Metall.* **2006,** *49* (2), 102-102.
270. Jura, G.; Harkins, W. D., A new adsorption isotherm which is valid over a very wide range of pressure. *J. Chem. Phys.* **1943,** *11* (9), 430-431.
271. Gil, A.; Grange, P., Application of the Dubinin-Radushkevich and Dubinin-Astakhov equations in the characterization of microporous solids. *Colloid Surface A* **1996,** *113* (1-2), 39-50.
272. Horvath, G.; Kawazoe, K., Method for the Calculation of Effective Pore-Size Distribution in Molecular-Sieve Carbon. *J. Chem. Eng. Japan.* **1983,** *16* (6), 470-475.
273. Rouquerol, J.; Rouquerol, F.; Llewellyn, P.; Maurin, G.; Sing, K. S., *Adsorption by powders and porous solids: principles, methodology and applications*. Academic press: 2013.
274. Thommes, M., Physical Adsorption Characterization of Nanoporous Materials. *Chem. Ing. Tech.* **2010,** *82* (7), 1059-1073.
275. Jaroniec, M.; Solovyov, L. A., Improvement of the Kruk-Jaroniec-Sayari method for pore size analysis of ordered silicas with cylindrical mesopores. *Langmuir* **2006,** *22* (16), 6757-6760.
276. Monson, P. A., Understanding adsorption/desorption hysteresis for fluids in mesoporous materials using simple molecular models and classical density functional theory. *Micropor. Mesopor. Mater.* **2012,** *160*, 47-66.
277. Seaton, N. A.; Walton, J. P. R. B.; Quirke, N., A New Analysis Method for the Determination of the Pore-Size Distribution of Porous Carbons from Nitrogen Adsorption Measurements. *Carbon* **1989,** *27* (6), 853-861.
278. Lastoskie, C.; Gubbins, K. E.; Quirke, N., Pore-Size Distribution Analysis of Microporous Carbons - a Density-Functional Theory Approach. *J. Phys. Chem.* **1993,** *97* (18), 4786-4796.

279. Olivier, J. P.; Conklin, W. B.; Vonszombathely, M., Determination of Pore-Size Distribution from Density-Functional Theory- a Comparison of Nitrogen and Argon Results. *Stud. Surf. Sci. Catal.* **1994,** *87*, 81-89.
280. Landers, J.; Gor, G.Y.; Neimark, A.V., Density functional theory methods for characterization of porous materials. *Colloids Surf. A Physicochem. Eng. Asp.* **2013,** 437, 3-32.
281. Jagiello, J.; Olivier, J. P., 2D-NLDFT adsorption models for carbon slit-shaped pores with surface energetical heterogeneity and geometrical corrugation. *Carbon* **2013,** *55*, 70-80.
282. Neimark, A. V.; Lin, Y. Z.; Ravikovitch, P. I.; Thommes, M., Quenched solid density functional theory and pore size analysis of micro-mesoporous carbons. *Carbon* **2009,** *47* (7), 1617-1628.
283. Gor, G. Y.; Thommes, M.; Cychosz, K. A.; Neimark, A. V., Quenched solid density functional theory method for characterization of mesoporous carbons by nitrogen adsorption. *Carbon* **2012,** *50* (4), 1583-1590.
284. Wedler, C.; Span, R., Micropore Analysis of Biomass Chars by CO_2 Adsorption: Comparison of Different Analysis Methods. *Energy Fuels*, **2021,** *35* (10), 8799-8806.
285. Belmabkhout, Y.; Frere, M.; De Weireld, G., High-pressure adsorption measurements. A comparative study of the volumetric and gravimetric methods. *Meas. Sci. Technol.* **2004,** *15* (5), 848-858.
286. Mohammad, S.; Fitzgerald, J.; Robinson, R. L.; Gasem, K. A. M., Experimental Uncertainties in Volumetric Methods for Measuring Equilibrium Adsorption. *Energy Fuels* **2009,** *23* (5-6), 2810-2820.
287. Abunowara, M.; Bustam, M.; Sufian, S.; Eldemerdash, U., Measurement techniques for carbon dioxide sorption capacity on various coal samples: critical review. *Earth Environ. Sci.* **2016,** *36* (1), 012059.
288. Wang, S.; Qin, J. Q.; Zhao, Y. J.; Duan, L. L.; Wang, J. X.; Gao, W. J.; Wang, R. C.; Wang, C. Y.; Pal, M.; Wu, Z. S.; Li, W.; Zhao, D. Y., Ultrahigh Surface Area N-Doped Hierarchically Porous Carbon for Enhanced CO_2 Capture and Electrochemical Energy Storage. *ChemSusChem* **2019,** *12* (15), 3541-3549.
289. Rouquerol, J.; Rouquerol, F.; Llewellyn, P.; Denoyel, R., Surface excess amounts in high-pressure gas adsorption: Issues and benefits. *Colloid Surface A* **2016,** *496*, 3-12.
290. Ozawa, T., Thermal analysis - review and prospect. *Thermochim. Acta* **2000,** *355* (1-2), 35-42.
291. Coats, A. W.; Redfern, J. P., Thermogravimetric Analysis. *Analyst* **1963,** *88* (105), 906-924.
292. Yu, J. P.; Wang, P. Y.; Ni, F. L.; Cizdziel, J.; Wu, D. X.; Zhao, Q. L.; Zhou, Y., Characterization of microplastics in environment by thermal gravimetric analysis coupled with Fourier transform infrared spectroscopy. *Mar. Pollut. Bull.* **2019,** *145*, 153-160.
293. Liu, Z.; Qi, N.; Luan, Y. N.; Sun, X. Y., Thermogravimetry-Infrared Spectroscopy Analysis of the Pyrolysis of Willow Leaves, Stems, and Branches. *Adv. Mater. Sci. Eng.* **2015,** *2015*, 303212.
294. Ren, X. Y.; Guo, J.; Li, S. Y.; Chang, J. M., Thermogravimetric Analysis-Fourier Transform Infrared Spectroscopy Study on the Effect of Extraction Pretreatment on the Pyrolysis Properties of Eucalyptus Wood Waste. *ACS Omega* **2020,** *5* (36), 23364-23371.
295. Materazzi, S., Thermogravimetry infrared spectroscopy (TG-FTIR) coupled analysis. *Appl. Spectrosc. Rev.* **1997,** *32* (4), 385-404.
296. Biliaderis, C. G., Differential Scanning Calorimetry in Food Research - a Review. *Food Chem.* **1983,** *10* (4), 239-265.

297. Lopez-Capel, E.; Bol, R.; Manning, D. A. C., Application of simultaneous thermal analysis mass spectrometry and stable carbon isotope analysis in a carbon sequestration study. *Rapid Comm. Mass Spect.* **2005,** *19* (22), 3192-3198.
298. Arvelakis, S.; Jensen, P. A.; Dam-Johansen, M., Simultaneous thermal analysis (STA) on ash from high-alkali biomass. *Energy Fuels* **2004,** *18* (4), 1066-1076.
299. Dutour, S.; Nokerman, J.; Limborg-Noetinger, S.; Frere, M., Simultaneous determination of mass and calorimetric adsorption data of volatile organic compounds on microporous media in the low relative pressure range. *Meas. Sci. Technol.* **2004,** *15* (1), 185-194.
300. Wu, D.; Gassensmith, J. J.; Gouvea, D.; Ushakov, S.; Stoddart, J. F.; Navrotsky, A., Direct Calorimetric Measurement of Enthalpy of Adsorption of Carbon Dioxide on CD-MOF-2, a Green Metal-Organic Framework. *J. Am. Chem. Soc.* **2013,** *135* (18), 6790-6793.
301. Fadley, C. S., X-ray photoelectron spectroscopy: Progress and perspectives. *J. Electron Spectrosc. Relat. Phenom.* **2010,** *178*, 2-32.
302. Mane, A.; Patil, V., X-ray photoelectron spectroscopy of nanofillers and their polymer nanocomposites. In *Spectrosc. Polym. Nanocomposites* **2016,** 452-467.
303. Chusuei, C. C.; Brookshier, M. A.; Goodman, D. W., Correlation of relative X-ray photoelectron spectroscopy shake-up intensity with CuO particle size. *Langmuir* **1999,** *15* (8), 2806-2808.
304. Picollo, M.; Aceto, M.; Vitorino, T., UV-Vis spectroscopy. *Physic. Sci. Rev.* **2019,** *4* (4).
305. Hardesty, J. H.; Attili, B., Spectrophotometry and the Beer-Lambert Law: An Important Analytical Technique in Chemistry. *Collin College, Department of Chemistry* **2010,** 1-6.
306. Fredriksson, H.; Silverio, J.; Andersson, R.; Eliasson, A.-C.; Åman, P., The influence of amylose and amylopectin characteristics on gelatinization and retrogradation properties of different starches. *Carbohydr. Polym.* **1998,** *35* (3-4), 119-134.
307. Attard, J.; Milescu, R.; Budarin, V.; Matharu, A. S.; Clark, J. H., Unexpected nitrile formation in bio-based mesoporous materials (Starbons®). *Chem. Commun.* **2018,** *54* (6), 686-688.
308. Zhang, S.; Li, X.; Zhou, J.; Li, L.; Bao, L.; Li, X., The Critical Role of Oxygen-Containing Functional Groups in the Etching Behavior of Activators to Carbon Materials. *ACS Sustain. Chem. Eng.* **2021,** *9*(4), 1646-1655.
309. Singh, G.; Lakhi, K. S.; Sathish, C. I.; Ramadass, K.; Yang, J. H.; Vinu, A., Oxygen-Functionalized Mesoporous Activated Carbons Derived from Casein and Their Superior CO_2 Adsorption Capacity at Both Low- and High-Pressure Regimes. *ACS Appl. Nano Mater.* **2019,** *2* (3), 1604-1613.
310. Plaza, M. G.; Thurecht, K. J.; Pevida, C.; Rubiera, F.; Pis, J. J.; Snape, C. E.; Drage, T. C., Influence of oxidation upon the CO_2 capture performance of a phenolic-resin-derived carbon. *Fuel Process. Technol.* **2013,** *110*, 53-60.
311. Liu, L.; Cao, Y.; Liu, Q. C., Kinetics studies and structure characteristics of coal char under pressurized CO_2 gasification conditions. *Fuel* **2015,** *146*, 103-110.
312. Hurt, R. H.; Sarofim, A. F.; Longwell, J. P., The Role of Microporous Surface-Area in the Gasification of Chars from a Sub-Bituminous Coal. *Fuel* **1991,** *70* (9), 1079-1082.
313. Jribi, S.; Miyazaki, T.; Saha, B. B.; Pal, A.; Younes, M. M.; Koyama, S.; Maalej, A., Equilibrium and kinetics of CO_2 adsorption onto activated carbon. *Int. J. Heat. Mass. Tran.* **2017,** *108*, 1941-1946.
314. Oschatz, M.; Antonietti, M., A search for selectivity to enable CO_2 capture with porous adsorbents. *Energy Environ. Sci.* **2018,** *11* (1), 57-70.
315. Liu, X.; Sun, C. G.; Liu, H.; Tan, W. H.; Wang, W. L.; Snape, C., Developing hierarchically ultra-micro/mesoporous biocarbons for highly selective carbon dioxide adsorption. *Chem. Eng. J.* **2019,** *361*, 199-208.

316. Nuhnen, A.; Janiak, C., A practical guide to calculate the isosteric heat/enthalpy of adsorption via adsorption isotherms in metal-organic frameworks, MOFs. *Dalton Trans.* **2020,** *49* (30), 10295-10307.
317. Belmabkhout, Y.; Guillerm, V.; Eddaoudi, M., Low concentration CO_2 capture using physical adsorbents: Are metal–organic frameworks becoming the new benchmark materials? *Chem. Eng. J.* **2016,** *296*, 386-397.
318. Singh, J.; Basu, S.; Bhunia, H., Dynamic CO_2 adsorption on activated carbon adsorbents synthesized from polyacrylonitrile (PAN): Kinetic and isotherm studies. *Micropor. Mesopor. Mater.* **2019,** *280*, 357-366.
319. Montagnaro, F.; Silvestre-Albero, A.; Silvestre-Albero, J.; Rodriguez-Reinoso, F.; Erto, A.; Lancia, A.; Balsamo, M., Post-combustion CO_2 adsorption on activated carbons with different textural properties. *Micropor. Mesopor. Mater.* **2015,** 209, 157-164
320. Wang, Y. X.; Hu, X. D.; Hao, J.; Ma, R.; Guo, Q. J.; Gao, H. F.; Bai, H. C., Nitrogen and Oxygen Codoped Porous Carbon with Superior CO_2 Adsorption Performance: A Combined Experimental and DFT Calculation Study. *Ind. Eng. Chem. Res.* **2019,** *58* (29), 13390-13400.
321. Tiwari, D.; Bhunia, H.; Bajpai, P. K., Development of chemically activated N-enriched carbon adsorbents from urea-formaldehyde resin for CO_2 adsorption: Kinetics, isotherm, and thermodynamics. *J. Environ. Manage.* **2018,** *218*, 579-592.
322. Kaur, B.; Gupta, R. K.; Bhunia, H., Chemically activated nanoporous carbon adsorbents from waste plastic for CO_2 capture: Breakthrough adsorption study. *Micropor. Mesopor. Mater.* **2019,** *282*, 146-158.
323. Goel, C.; Bhunia, H.; Bajpai, P. K., Prediction of Binary Gas Adsorption of CO_2/N_2 and Thermodynamic Studies on Nitrogen Enriched Nanostructured Carbon Adsorbents. *J. Chem. Eng. Data* **2017,** *62* (1), 214-225.
324. Ramadass, K.; Sathish, C.; MariaRuban, S.; Kothandam, G.; Joseph, S.; Singh, G.; Kim, S.; Cha, W.; Karakoti, A.; Belperio, T., Carbon Nanoflakes and Nanotubes from Halloysite Nanoclays and their Superior Performance in CO_2 Capture and Energy Storage. *ACS Appl. Mater. Inter.* **2020,** *12* (10), 11922-11933.
325. Yue, L. M.; Rao, L. L.; Wang, L. L.; Sun, Y.; Wu, Z. Z.; DaCosta, H.; Hu, X., Enhanced CO2 Adsorption on Nitrogen-Doped Porous Carbons Derived from Commercial Phenolic Resin. *Energy Fuels* **2018,** *32* (2), 2081-2088.
326. Hao, G.P.; Li, W.C.; Qian, D.; Wang, G.H.; Zhang, W.P.; Zhang, T.; Wang, A.Q.; Schüth, F.; Bongard, H.J.; Lu, A.H., Structurally designed synthesis of mechanically stable poly (benzoxazine-co-resol)-based porous carbon monoliths and their application as high-performance CO_2 capture sorbents. *J. Am. Chem. Soc.* **2011,** *133*(29), 11378-11388.
327. Liu, X.; Liu, J.; Sun, C.; Liu, H.; Wang, W.; Smith, E.; Jiang, L.; Chen, X.; Snape, C., Design and development of 3D hierarchical ultra-microporous CO_2-sieving carbon architectures for potential flow-through CO_2 capture at typical practical flue gas temperatures. *J. Mater. Chem. A.* **2020,** *8*(33), 17025-17035.
328. Ashourirad, B.; Arab, P.; Islamoglu, T.; Cychosz, K.A.; Thommes, M.; El-Kaderi, H.M., A cost-effective synthesis of heteroatom-doped porous carbons as efficient CO_2 sorbents. *J. Mater. Chem. A.* **2016,** *4*(38), 14693-14702.
329. Liu, X.; Wang, S.; Sun, C.; Liu, H.; Stevens, L.; Dwomoh, P.K.; Snape, C., Synthesis of functionalized 3D microporous carbon foams for selective CO2 capture. *Chem. Eng. J.* **2020,** *402*, 125459.
330. Adeniran, B.; Masika, E.; Mokaya, R., A family of microporous carbons prepared via a simple metal salt carbonization route with high selectivity for exceptional gravimetric and volumetric post-combustion CO2 capture. *J. Mater. Chem. A.* **2014,** *2*(35), 14696-14710.

331. Xu, Y.; Yang, Z. X.; Zhang, G. J.; Zhao, P. Y., Excellent CO_2 adsorption performance of nitrogen-doped waste biocarbon prepared with different activators. *J. Clean. Prod.* **2020,** *264*, 121645.
332. Myers, A. L.; Prausnitz, J. M., Thermodynamics of Mixed-Gas Adsorption. *AICHE J.* **1965,** *11* (1), 121-127.
333. To, J. W. F.; He, J. J.; Mei, J. G.; Haghpanah, R.; Chen, Z.; Kurosawa, T.; Chen, S. C.; Bae, W. G.; Pan, L. J.; Tok, J. B. H.; Wilcox, J.; Bao, Z. N., Hierarchical N-Doped Carbon as CO_2 Adsorbent with High CO_2 Selectivity from Rationally Designed Polypyrrole Precursor. *J. Am. Chem. Soc.* **2016,** *138* (3), 1001-1009.
334. Kim, Y. K.; Kim, G. M.; Lee, J. W., Highly porous N-doped carbons impregnated with sodium for efficient CO_2 capture. *J. Mater. Chem. A* **2015,** *3* (20), 10919-10927.
335. Wang, S.; Tian, Z. Q.; Dai, S.; Jiang, D. E., Optimal Size of a Cylindrical Pore for Post-Combustion CO_2 Capture. *J. Phys. Chem. C* **2017,** *121* (40), 22025-22030.
336. Sekizkardes, A. K.; Islamoglu, T.; Kahveci, Z.; El-Kaderi, H. M., Application of pyrene-derived benzimidazole-linked polymers to CO_2 separation under pressure and vacuum swing adsorption settings. *J. Mater. Chem. A* **2014,** *2* (31), 12492-12500.
337. Ashourirad, B.; Sekizkardes, A. K.; Altarawneh, S.; El-Kaderi, H. M., Exceptional Gas Adsorption Properties by Nitrogen-Doped Porous Carbons Derived from Benzimidazole-Linked Polymers. *Chem. Mater.* **2015,** *27* (4), 1349-1358.
338. Zhang, P. X.; Zhong, Y.; Ding, J.; Wang, J.; Xu, M.; Deng, Q.; Zeng, Z. L.; Deng, S. G., A new choice of polymer precursor for solvent-free method: Preparation of N-enriched porous carbons for highly selective CO_2 capture. *Chem. Eng. J.* **2019,** *355*, 963-973.
339. Patel, H.A.; Byun, J.; Yavuz, C.T., Carbon dioxide capture adsorbents: chemistry and methods. *ChemSusChem*, **2017,** *10* (7), 1303-1317.
340. Wang, R. T.; Wang, P. Y.; Yan, X. B.; Lang, J. W.; Peng, C.; Xue, Q. J., Promising Porous Carbon Derived from Celtuce Leaves with Outstanding Supercapacitance and CO_2 Capture Performance. *ACS Appl. Mater. Inter.* **2012,** *4* (11), 5800-5806.
341. Sevilla, M.; Fuertes, A. B., Sustainable porous carbons with a superior performance for CO_2 capture. *Energ. Environ. Sci.* **2011,** *4* (5), 1765-1771.
342. Idrees, M.; Rangari, V.; Jeelani, S., Sustainable packaging waste-derived activated carbon for carbon dioxide capture. *J. CO_2 Util.* **2018,** *26*, 380-387.
343. Liu, Z.; Zhang, Z.; Jia, Z.; Zhao, L.; Zhang, T.; Xing, W.; Komarneni, S.; Subhan, F.; Yan, Z., New strategy to prepare ultramicroporous carbon by ionic activation for superior CO_2 capture. *Chem. Eng. J.* **2018,** *337*, 290-299.
344. Li, Y.; Li, D.; Rao, Y.; Zhao, X.; Wu, M., Superior CO_2, CH_4, and H_2 uptakes over ultrahigh-surface-area carbon spheres prepared from sustainable biomass-derived char by CO_2 activation. *Carbon* **2016,** *105*, 454-462.
345. Serafin, J.; Narkiewicz, U.; Morawski, A. W.; Wróbel, R. J.; Michalkiewicz, B., Highly microporous activated carbons from biomass for CO_2 capture and effective micropores at different conditions. *J. CO_2 Util.* **2017,** *18*, 73-79.
346. Deng, S.; Wei, H.; Chen, T.; Wang, B.; Huang, J.; Yu, G., Superior CO_2 adsorption on pine nutshell-derived activated carbons and the effective micropores at different temperatures. *Chem. Eng. J.* **2014,** *253*, 46-54.
347. Hong, S. M.; Jang, E.; Dysart, A. D.; Pol, V. G.; Lee, K. B., CO_2 Capture in the Sustainable Wheat-Derived Activated Microporous Carbon Compartments. *Sci. Rep.* **2016,** *6* (1), 1-10.
348. Xu, C.; Ruan, C.Q.; Li, Y.; Lindh, J.; Strømme, M., High-Performance Activated Carbons Synthesized from Nanocellulose for CO_2 Capture and Extremely Selective Removal of Volatile Organic Compounds. *Adv. Sustain. Syst.* **2018,** *2*(2), 1700147.

349. Li, D.; Chen, J.; Fan, Y.; Deng, L.; Shan, R.; Chen, H.; Yuan, H.; Chen, Y., Biomass-tar-Enabled nitrogen-doped highly ultramicroporous carbon as an efficient absorbent for CO_2 capture. *Energy Fuels* **2019,** *33* (9), 8927-8936.
350. Dilokekunakul, W.; Teerachawanwong, P.; Klomkliang, N.; Supasitmongkol, S.; Chaemchuen, S., Effects of nitrogen and oxygen functional groups and pore width of activated carbon on carbon dioxide capture: Temperature dependence. *Chem. Eng. J.* **2020,** *389*, 124413.
351. Heo, Y. J.; Park, S. J., H_2O_2/steam activation as an eco-friendly and efficient top-down approach to enhancing porosity on carbonaceous materials: the effect of inevitable oxygen functionalities on CO_2 capture. *Green Chem.* **2018,** *20* (22), 5224-5234.
352. Heo, Y.-J.; Park, S.-J., A role of steam activation on CO_2 capture and separation of narrow microporous carbons produced from cellulose fibers. *Energy* **2015,** *91*, 142-150.
353. Ge, M. T.; Liu, H. Z., A silsesquioxane-based thiophene-bridged hybrid nanoporous network as a highly efficient adsorbent for wastewater treatment. *J. Mater. Chem. A* **2016,** *4* (42), 16714-16722.
354. Bai, L. Z.; Li, Z. P.; Zhang, Y.; Wang, T.; Lu, R. H.; Zhou, W. F.; Gao, H. X.; Zhang, S. B., Synthesis of water-dispersible graphene-modified magnetic polypyrrole nanocomposite and its ability to efficiently adsorb methylene blue from aqueous solution. *Chem. Eng. J.* **2015,** *279*, 757-766.
355. Fu, J. W.; Xin, Q. Q.; Wu, X. C.; Chen, Z. H.; Yan, Y.; Liu, S. J.; Wang, M. H.; Xu, Q., Selective adsorption and separation of organic dyes from aqueous solution on polydopamine microspheres. *J. Colloid Interface Sci.* **2016,** *461*, 292-304.
356. Zhang, Z. Y.; Xu, X. C., Wrapping carbon nanotubes with poly (sodium 4-styrenesulfonate) for enhanced adsorption of methylene blue and its mechanism. *Chem. Eng. J.* **2014,** *256*, 85-92.
357. El Qada, E. N.; Allen, S. J.; Walker, G. M., Adsorption of Methylene Blue onto activated carbon produced from steam activated bituminous coal: A study of equilibrium adsorption isotherm. *Chem. Eng. J.* **2006,** *124* (1-3), 103-110.
358. Shi, L.; Zhang, G.; Wei, D.; Yan, T.; Xue, X.; Shi, S.; Wei, Q., Preparation and utilization of anaerobic granular sludge-based biochar for the adsorption of methylene blue from aqueous solutions. *J. Mol. Liq.* **2014,** *198*, 334-340.
359. Unur, E., Functional nanoporous carbons from hydrothermally treated biomass for environmental purification. *Micropor. Mesopor. Mater.* **2013,** *168*, 92-101.
360. Tu, W.; Liu, Y.; Xie, Z.; Chen, M.; Ma, L.; Du, G.; Zhu, M., A novel activation-hydrochar via hydrothermal carbonization and KOH activation of sewage sludge and coconut shell for biomass wastes: Preparation, characterization and adsorption properties. *J. Colloid Interface Sci.* **2021,** *593*, 390-407.
361. Danish, M.; Ahmad, T.; Hashim, R.; Said, N.; Akhtar, M. N.; Mohamad-Saleh, J.; Sulaiman, O., Comparison of surface properties of wood biomass activated carbons and their application against rhodamine B and methylene blue dye. *Surf. Interfaces* **2018,** *11*, 1-13.
362. Islam, M. A.; Ahmed, M.; Khanday, W.; Asif, M.; Hameed, B., Mesoporous activated coconut shell-derived hydrochar prepared via hydrothermal carbonization-NaOH activation for methylene blue adsorption. *J. Environ. Manage.* **2017,** *203*, 237-244.
363. Cazetta, A. L.; Vargas, A. M.; Nogami, E. M.; Kunita, M. H.; Guilherme, M. R.; Martins, A. C.; Silva, T. L.; Moraes, J. C.; Almeida, V. C., NaOH-activated carbon of high surface area produced from coconut shell: Kinetics and equilibrium studies from the methylene blue adsorption. *Chem. Eng. J.* **2011,** *174* (1), 117-125.
364. Jain, A.; Jayaraman, S.; Balasubramanian, R.; Srinivasan, M., Hydrothermal pre-treatment for mesoporous carbon synthesis: enhancement of chemical activation. *J. Mater. Chem. A* **2014,** *2* (2), 520-528.

365. Chen, L.; Ji, T.; Mu, L.; Shi, Y.; Wang, H.; Zhu, J., Pore size dependent molecular adsorption of cationic dye in biomass derived hierarchically porous carbon. *J. Environ. Manage.* **2017,** *196*, 168-177.
366. Alatalo, S. M.; Makila, E.; Repo, E.; Heinonen, M.; Salonen, J.; Kukk, E.; Sillanpaa, M.; Titirici, M. M., Meso- and microporous soft templated hydrothermal carbons for dye removal from water. *Green Chem.* **2016,** *18* (4), 1137-1146.
367. Sanchez-Sanchez, A.; Suarez-Garcia, F.; Martinez-Alonso, A.; Tascon, J. M. D., Aromatic polyamides as new precursors of nitrogen and oxygen-doped ordered mesoporous carbons. *Carbon* **2014,** *70*, 119-129.
368. Yang, D. S.; Bhattacharjya, D.; Inamdar, S.; Park, J.; Yu, J. S., Phosphorus-Doped Ordered Mesoporous Carbons with Different Lengths as Efficient Metal-Free Electrocatalysts for Oxygen Reduction Reaction in Alkaline Media. *J. Am. Chem. Soc.* **2012,** *134* (39), 16127-16130.
369. Wang, L. F.; Yang, R. T., Significantly Increased CO_2 Adsorption Performance of Nanostructured Templated Carbon by Tuning Surface Area and Nitrogen Doping. *J. Phys. Chem. C* **2012,** *116* (1), 1099-1106.
370. Qi, S.-C.; Wu, J.-K.; Lu, J.; Yu, G.-X.; Zhu, R.-R.; Liu, Y.; Liu, X.-Q.; Sun, L.-B., Underlying mechanism of CO_2 adsorption onto conjugated azacyclo-copolymers: N-doped adsorbents capture CO_2 chiefly through acid–base interaction? *J. Mater. Chem. A* **2019,** *7* (30), 17842-17853.
371. Xing, W.; Liu, C.; Zhou, Z.; Zhang, L.; Zhou, J.; Zhuo, S.; Yan, Z.; Gao, H.; Wang, G.; Qiao, S. Z., Superior CO_2 uptake of N-doped activated carbon through hydrogen-bonding interaction. *Energy Environ. Sci.* **2012,** *5* (6), 7323-7327.
372. Sun, Q.; Dai, Z. F.; Meng, X. J.; Xiao, F. S., Porous polymer catalysts with hierarchical structures. *Chem. Soc. Rev.* **2015,** *44* (17), 6018-6034.
373. Liang, H. W.; Zhuang, X. D.; Bruller, S.; Feng, X. L.; Mullen, K., Hierarchically porous carbons with optimized nitrogen doping as highly active electrocatalysts for oxygen reduction. *Nat. Commun.* **2014,** *5* (1), 1-7.
374. Abuelnoor, N.; AlHajaj, A.; Khaleel, M.; Vega, L.F.; Abu-Zahra, M.R., Activated Carbons from Biomass-Based Sources for CO_2 Capture Applications. *Chemosphere* **2021,** 131111.
375. Liu, R.S.; Shi, X.D.; Wang, C.T.; Gao, Y.Z.; Xu, S.; Hao, G.P.; Chen, S.; Lu, A.H., Advances in Post-Combustion CO_2 Capture by Physical Adsorption: From Materials Innovation to Separation Practice. *ChemSusChem*, **2021,** *14* (6), 1428-1471.
376. https://www.starbons.com/
377. El Qada, E.N.; Allen, S.J.; Walker, G.M., Influence of preparation conditions on the characteristics of activated carbons produced in laboratory and pilot scale systems. *Chem. Eng. J.* **2008,** *142* (1), 1-13.
378. Sawant, S.Y.; Munusamy, K.; Somani, R.S.; John, M.; Newalkar, B.L.; Bajaj, H.C., Precursor suitability and pilot scale production of super activated carbon for greenhouse gas adsorption and fuel gas storage. *Chem. Eng. J.* **2017,** *315*, 415-425.
379. Majchrzak-Kucęba I.; Wawrzyńczak, D.; Zdeb, J.; Smółka, W.; Zajchowski, A., Treatment of Flue Gas in a CO_2 Capture Pilot Plant for a Commercial CFB Boiler. *Energies* **2021,** *14* (9), 2458.
380. Dai, X.D.; Liu, X.M.; Qian, L.; Qiao, K.; Yan, Z.F, Pilot preparation of activated carbon for natural gas storage. *Energy & fuels* **2008,** *22* (5), 3420-3423.